Measurement of associated Wgamma production and search for anomalous WWgamma couplings with the CMS detector

Đurić, Senka

Abstract

The Large Hadron Collider (LHC) has recently delivered collisions at a center of mass energy of 7 TeV and has therefore allowed for the first time to test the validity of the Standard Model (SM) at TeV scale. The precise measurement of electroweak processes constitute a central part of this program. Diboson processes, in which pairs of electroweak bosons are produced, provide in particular a good opportunity to test SM at these energies. They also allow to seek indirectly for new physics through the search for anomalous triple gauge couplings. This thesis presents a measurement of the inclusive cross section of the $pp \to W\gamma \to \mu\nu\gamma$ process for phase spaces $E_T^{\gamma} > 15/60/90$ GeV and $\Delta R(\mu,\gamma) > 0.7$ using 5.0 fb^{-1} of data collected with the CMS detector in 2011. A search for anomalous triple gauge boson $WW\gamma$ coupling is performed, resulting in limits on the allowed values of the parameters $\Delta\kappa^{\gamma}$ and λ^{γ}.

Acknowledgements

This thesis would not have been possible without the support of many people. First I would like to thank my supervisors Vuko Brigljević and Krešo Kadija for their patience and guidance. I have also received a very useful guidance, comments and help from Yurii Maravin and Chia-Ming Kuo. Thanks to my colleagues as CERN, Poter, Kuan-Hsin, Irakli, Lindsey, Anthony and Jan for making this measurement a very nice working experience.

My colleagues at Ruđer Bošković Institute, Srećko, Jelena, Lucija, Tanja and Darko, are responsible for providing a pleasant working environment.

I would specially like to thank my parents, Nada and Željko Pintarić, and my brother, Siniša Pintarić, who have been supporting me since the very beginnings. A special thank to my husband Jadranko for his love, support, understanding and patience.

Last but not least I want to thank my friends in Croatia: Jasna, Strah, Silva, Iva, and friends at CERN, who have made my stays at CERN not only about work but good time as well: Jose, Ljiljana, Pooja, Tia, Carley, Oldrich, Georges, Jonatan, Luis, Serkan, Darren, Umut, Oscar, Lindsey, Carlo, Alberto, Keti, Yurii, Roko and Tomislav. I am grateful for their friendship and support in all the ups and (especially) the downs.

“It’s a dangerous business, Frodo, going out your door. You step onto the road, and if you don’t keep your feet, there’s no knowing where you might be swept off to.”

J.R.R. Tolkien

Contents

Abstract . . . .

Acknowledgements . . . .

List of Tables . . . .

List of Figures . . . .

1 Introduction **1**

2 $W\gamma$ production at the LHC **3**

2.1 The Standard Model of Particle Physics 3

2.2 The process $pp \to W\gamma + X \to l\nu\gamma + X$ in proton proton collisions 10

2.3 Radiation Amplitude Zero 12

2.4 Triple Gauge Couplings 14

3 The Large Hadron collider and the Compact Muon Solenoid detector **17**

3.1 The Large Hadron Collider 17

3.2 The Compact Muon Solenoid Experiment 21

3.2.1 Coordinate system 21

3.2.2 Magnet 23

3.2.3 Tracker 23

3.2.4 Electromagnetic and hadron calorimeter 25

3.2.5 Muon system 28

3.2.6 Reconstruction of objects . . . 30
3.2.7 Data and simulation . . . 34

4 Measurement of $W\gamma$ cross section **35**

4.1 Data samples . . . 36
4.2 Trigger and event selection . . . 37
4.2.1 Trigger selection . . . 37
4.2.2 Muon selection . . . 37
4.2.3 Photon selection . . . 38
4.2.4 Photon energy scale and resolution . . . 40
4.2.5 Neutrino selection . . . 42
4.2.6 Wγ event selection . . . 42
4.2.7 Selection efficiency and acceptance . . . 43
4.3 Backgrounds . . . 75
4.3.1 Background from jets misidentified as photons . . . 76
4.3.2 Background from electrons misidentified as photons . . . 91
4.3.3 Summary of backgrounds . . . 92
4.4 Systematic uncertainties . . . 93
4.4.1 Uncertainties on signal yield . . . 93
4.4.2 Uncertainties on acceptance and efficiency . . . 93
4.4.3 Uncertainties on efficiency correction factor . . . 94
4.4.4 Uncertainties on background yield . . . 95
4.4.5 Uncertainties on luminosity . . . 97
4.4.6 Summary of systematic uncertainties . . . 99
4.5 Results . . . 103

4.6 Combined results with electron channel . . . 114

5 Observation of $W\gamma$ radiation amplitude zero 118

5.1 Results . . . 118

5.2 Combined results with electron channel . . . 119

6 Triple gauge coupling measurement 122

6.1 Likelihood Formalism . . . 122

6.2 Signal simulation . . . 124

6.3 Results . . . 124

6.4 Combined results with electron channel . . . 125

7 Comparison with other results 130

8 Conclusion 134

9 Prošireni sažetak: Mjerenje zajedničke produkcije W bozona i fotona i potraga za anomalnim vezanjem WW foton CMS detektorom 135

9.1 Uvod . . . 135

9.2 $W\gamma$ proces na LHC-u . . . 137

9.2.1 Standardni Model . . . 137

9.2.2 $W\gamma$ proces . . . 144

9.2.3 Radijacijska amplituda vrijednosti nula . . . 145

9.2.4 Trostruka baždarna vezanja . . . 147

9.3 LHC akcelerator i CMS detektor . . . 150

9.3.1 LHC ubrzivač . . . 150

9.3.2 CMS detektor . . . 150

9.4 Mjerenje $W\gamma$ udarnog presjeka . . . 161

9.4.1 Podaci . . . 162
9.4.2 Selekcija događaja . . . 162
9.4.3 Pozadinski događaji . . . 167
9.4.4 Rezultati . . . 177
9.4.5 Kombinacija rezultata s elektronskim kanalom . . . 188
9.5 Opažanje radijacijske amplitude vrijednosti nula u $W\gamma$ procesu . . . 192
9.5.1 Rezultati . . . 192
9.5.2 Kombinacija rezultata s elektronskim kanalom . . . 192
9.6 Trostuka baždarna vezanja . . . 195
9.6.1 Statistički uvod . . . 195
9.6.2 Simulacija signala . . . 197
9.6.3 Rezultati . . . 197
9.6.4 Kombinacija rezultata s elektronskim kanalom . . . 197
9.7 Usporedba s drugim rezultatima . . . 203
9.8 Zaključak . . . 207

Bibliography **208**

Curriculum vitae **211**

List of Tables

2.1 Branching ratios for W^+ decay [1]. 11

4.1 Muon identification and isolation requirements. 38

4.2 A_{eff} values used for PU correction for photon selected in barrel and endcap. 40

4.3 Photon identification and isolation requirements. 40

4.4 A summary of the derived photon energy scale estimates. 42

4.5 Data and simulation yields in $W\gamma \to \mu\nu\gamma$ channel for 2011A (2.3 fb^{-1}), 2011B (2.7 fb^{-1}) and 2011A+2011B combined (5.0 fb^{-1}). 43

4.6 Definition of selected probes and the passing criterion. 46

4.7 Summary of measured efficiencies of a muon with Wγ-selection. Simulation is adapted to the different pile-up scenarios for Run 2011A and Run 2011B. 48

4.8 Summary of the M_T^W efficiencies in using corrected recoil, simulation, and a recoil/simulation ratio wrt N_{Vtx} for 2011A runs. 70

4.9 Summary of the M_T^W efficiencies in using corrected recoil, simulation, and a recoil/simulation ratio wrt N_{Vtx} for 2011B runs. 70

4.10 Summary of probabilities for the two particle case. 86

4.11 Background from jets misidentified as photons for $W\gamma \to \mu\nu\gamma$ estimated with 'template method' for 2011A and 2011B. 88

4.12 Background from jets misidentified as photons for $W\gamma \to \mu\nu\gamma$ estimated with 'template method' for 2011A+2011B combined. 90

4.13 Summary of background contributions in $W\gamma \to \mu\mu\gamma$ final state for 2011A and 2011B data set. The quoted fake photon background yield is determined by the 'template method'. 92

4.14 Summary of background contributions in $W\gamma \to \mu\mu\gamma$ final state for 2011A+2011B data sets combined. The quoted fake photon background yield is determined by the 'template method'. 92

4.15 Systematic uncertainties on the background from jets misidentified as photons for $W\gamma \to \mu\nu\gamma$ for 2011A data set. 99

4.16 Systematic uncertainties on the background from jets misidentified as photons for $W\gamma \to \mu\nu\gamma$ for 2011B data set. 100

4.17 Systematic uncertainties on the background from jets misidentified as photons for $W\gamma \to \mu\nu\gamma$ for 2011A+2011B combined data set. 101

4.18 Summary of systematic uncertainties for the $W\gamma \to \mu\nu\gamma$ cross section measurement. 102

4.19 Parameters used to calculate the $W\gamma \to \mu\nu\gamma$ cross section in 2011A and 2011B data sets. 111

4.20 Parameters used to calculate the $W\gamma \to \mu\nu\gamma$ cross section in 2011A+2011B data sets combined. 111

4.21 Summary of systematic uncertainties for the Wγ cross section measurement ($E_T(\gamma) > 60.$ GeV and $E_T(\gamma) > 90.$ GeV) for 2011A+2011B data set. 112

4.22 Summary of parameters for the $W\gamma$ cross section measurement for photon $E_T >$ 60 GeV and $E_T > 90$ GeV. 113

4.23 The summary of the cross section measurements and predictions for $E_{\mathrm{T}}^{\gamma} >$60 and 90 GeV for $W\gamma$. 114

6.1 1D 95% confidence level observed limits for $WW\gamma$ coupling. Electron and muon channel combined. 128

7.1 1D limits on aTGC parameters from ATLAS experiment measurements using 1 fb^{-1} of data. 132

7.2 Summary of limits on aTGC parameters from different experiments. 132

9.1 Omjeri grananja W^+ raspada [1]. 145

9.2 Selekcija miona. 163

9.3 Selekcija fotona. 164

9.4 Broj selektiranih $W\gamma \to \mu\nu\gamma$ događaja u podacima i simulaciji za uzorak podataka 2011A (2.3 fb^{-1}), 2011B (2.7 fb^{-1}) i ukupni uzorak 2011A+2011B (5.0 fb^{-1}). . . 165

9.5 Broj pozadinskih događaja koji čine pogrešno identificiranih mlazeva određeni metodom predložaka za uzorke 2011A i 2011B. 173

9.6 Broj pozadinskih događaja koji dolaze iz pogrešno identificiranih mlazeva određeni metodom predložaka za uzorak 2011A+2011B. 175

9.7 Procjenjene pozadine u $W\gamma \to \mu\nu\gamma$ konačnom stanju za uzorke 2011A i 2011B. . . 176

9.8 Procjenjene pozadine u $W\gamma \to \mu\nu\gamma$ konačnom stanju za uzorak 2011A+2011B. . . 176

9.9 Parametri korišteni pri određivanju udarnog presjeka $W\gamma \to \mu\nu\gamma$ za uzorke 2011A i 2011B. 185

9.10 Parametri korišteni pri određivanju udarnog presjeka $W\gamma \to \mu\nu\gamma$ za uzorak 2011A+2011B. 185

9.11 Parametri korišteni pri mjerenju udarnog presjeka $W\gamma \to \mu\nu\gamma$ za $E_T^\gamma > 60$ GeV-a i $E_T^\gamma > 90$ GeV-a za uzorak 2011A+2011B. 186

9.12 Prikaz mjerenih vrijednosti $W\gamma$ udarnog presjeka u mionskom i elektronskom kanalu. 188

9.13 Jednodimenzionalne 95% C.L. mjerene granice na parametre $WW\gamma$ vezanja uključujući kombinirane rezultate za elektronski i mionski kanal. 197

9.14 Jednodimenzionalne 95% C.L. granice na parametre $WW\gamma$ vezanja ATLAS eksperimenta, dobivene analizom podataka integriranog luminoziteta $1 fb^{-1}$. 203

9.15 Rezultati mjerenja aTGC parametara u različitim eksperimentima. 205

List of Figures

2.1 Feynman diagrams of the Wγ production via final (a) and initial (b) state radiation and via WWγ triple gauge coupling (c). 11

2.2 The differential cross section for the photon-lepton pseudorapidity difference for $pp \to W^+\gamma \to l^+\nu\gamma$ at $\sqrt{s} = 14$TeV in the SM. (a) The inclusive NLO differential cross section (solid line), together with the O(α_s) 0-jet (dotted line), and the (LO) 1-jet (dashed line) exclusive differential cross sections. (b) The NLO $W^+\gamma$+0-jet exclusive differential cross section (dotted line) compared with the Born differential cross section (dash-dotted line) [2]. 13

2.3 Simulated E_T^γ distribution for the $W\gamma$ process for different values of aTGC parameters. Process is simulated with the SHERPA generator [3] interfaced with PYTHIA [4]. 15

3.1 The integrated luminosity both delivered by the LHC to CMS and recorded by CMS in 2010-2012. The difference between delivered and recorded luminosities corresponds to a downtime less than 10% for the CMS detector. 18

3.2 Overview of the CERN accelerator complex. 19

3.3 A schematic view of the construction of an LHC main dipole. 20

3.4 A perspective view of the CMS detector with the major subsystems indicated. . . . 22

3.5 Schematic cross section through the CMS tracker. 25

3.6 Features of the CMS ECAL. 26

3.7 Features of the CMS HCAL. 27

3.8 CMS muon system. 29

3.9 Muon momentum resolution. 31

3.10 The CMS detector transverse section with simple particle topologies indicated. . . 32

4.1 Left: The invariant mass of the $\mu\mu\gamma$ system for $Z \to \mu\mu\gamma$ data events fit to a model. The photon is required to be in the barrel and have transverse energy between 15 and 20 GeV. The photon energy scale and resolution and the fraction of signal events are floated in the fit. Right: The photon energy scale as a function of the photon transverse energy for the simulation (simulation truth) and for a fit to the simulation (simulation fit) and to the data (data fit). 41

4.2 Muon tracking efficiency depending on P_{T}^{μ}, η^{μ}, and number of primary vertices together with data-simulation ratio. 47

4.3 Muon tracking efficiency depending on P_{T}^{μ} and η^{μ}. 48

4.4 Efficiency of muon reconstruction in muon system depending on P_{T}^{μ}, η^{μ}, and number of primary vertices together with data-simulation ratio. 49

4.5 Efficiency of muon reconstruction in muon system depending on P_{T}^{μ} and η^{μ}. . . . 50

4.6 Muon matching efficiency depending on P_{T}^{μ}, η^{μ}, and number of primary vertices together with data-simulation ratio. 51

4.7 Muon matching efficiency depending on P_{T}^{μ} and η^{μ}. 52

4.8 Isolation efficiency depending on P_{T}^{μ}, η^{μ}, and number of primary vertices together with data-simulation ratio. 53

4.9 Isolation efficiency depending on P_{T}^{μ} and η^{μ}. 54

4.10 Muon trigger efficiency depending on P_{T}^{μ}, η^{μ}, and number of primary vertices together with data-simulation ratio. 55

4.11 Muon trigger efficiency depending on P_{T}^{μ} and η^{μ}. 56

4.12 Ratio of photon selection efficiencies using electron 'tag-and-probe' in data and simulation (black) and the ratio of simulation truth photon efficiencies to simulation truth elecron efficiencies using photon selection criteria (red) as a function of the photon transverse energy. 58

4.13 Efficiency of photon selection criteria as a function of photon transverse momentum (left) and pseudorapidity (right). 58

4.14 Efficiencies for photon selection criteria depending on E_T^{γ} and number of primary vertices measured in data. 59

4.15 Efficiencies for photon selection criteria depending on E_T^{γ} and number of primary vertices measured in simulation. 60

4.16 Efficiency correction factor for photon selection criteria depending on E_T^{γ} and number of primary vertices. 61

4.17 The fitting results of u_1 response (top) and resolution (bottom) for 2011A data set. Left column shows the results for $1 \leq N_{Vtx} \leq 3$. Middle column shows the results for $4 \leq N_{Vtx} \leq 5$. Right column shows the results for $6 \leq N_{Vtx} \leq 7$. 62

4.18 The fitting results of u_1 response (top) and resolution (bottom) for 2011A data set. Left column shows the results for $8 \leq N_{Vtx} \leq 9$. Middle column shows the results for $10 \leq N_{Vtx} \leq 11$. Right column shows the results for $12 \leq N_{Vtx}$ 63

4.19 The fitting results of u_2 response (top) and resolution (bottom) for 2011A data set. Left column shows the results for $1 \leq N_{Vtx} \leq 3$. Middle column shows the results for $4 \leq N_{Vtx} \leq 5$. Right column shows the results for $6 \leq N_{Vtx} \leq 7$. 64

4.20 The fitting results of u_2 response (top) and resolution (bottom) for 2011A data set. Left column shows the results for $8 \leq N_{Vtx} \leq 9$. Middle column shows the results for $10 \leq N_{Vtx} \leq 11$. Right column shows the results for $12 \leq N_{Vtx}$. 65

4.21 The fitting results of u_1 response (top) and resolution (bottom) for 2011B data set. Left column shows the results for $1 \leq N_{Vtx} \leq 3$. Middle column shows the results for $4 \leq N_{Vtx} \leq 5$. Right column shows the results for $6 \leq N_{Vtx} \leq 7$. 66

4.22 The fitting results of u_1 response (top) and resolution (bottom) for 2011B data set. Left column shows the results for $8 \leq N_{Vtx} \leq 9$. Middle column shows the results for $10 \leq N_{Vtx} \leq 11$. Right column shows the results for $12 \leq N_{Vtx}$. 67

4.23 The fitting results of u_1 response (top) and resolution (bottom) for simulated Z. Left column shows the results for $1 \leq N_{Vtx} \leq 3$. Middle column shows the results for 4 $\leq N_{Vtx} \leq 5$. Right column shows the results for $6 \leq N_{Vtx} \leq 7$. 68

4.24 The fitting results of u_1 response (top) and resolution (bottom) for simulated Z. Left column shows the results for $8 \leq N_{Vtx} \leq 9$. Middle column shows the results for $10 \leq N_{Vtx} \leq 11$. Right column shows the results for $12 \leq N_{Vtx}$. 71

4.25 Comparison of the true $W\gamma \to \mu\nu\gamma$ simulated M_T^W distribution with the predicted simulated distribution from the u_i recoil fits. The filled histogram is the true simulated M_T^W, and the dots show the M_T^W shape that is predicted by the recoil fits. Plots correspond to (top-left) $1 \leq N_{Vtx} \leq 3$, (top-midle) $4 \leq N_{Vtx} \leq 5$, (top-right) $6 \leq N_{Vtx} \leq 7$, (bottom-left) $8 \leq N_{Vtx} \leq 9$, (bottom-midle) $10 \leq N_{Vtx} \leq 11$, (bottom-right) $12 \leq N_{Vtx}$, for 2011A. 72

4.26 Comparison of the true $W\gamma \to \mu\nu\gamma$ simulated M_T^W distribution with the predicted simulated distribution from the u_i recoil fits. The filled histogram is the true simulated M_T^W, and the dots show the M_T^W shape that is predicted by the recoil fits. Plots correspond to (top-left) $1 \leq N_{Vtx} \leq 3$, (top-midle) $4 \leq N_{Vtx} \leq 5$, (top-right) $6 \leq N_{Vtx} \leq 7$, (bottom-left) $8 \leq N_{Vtx} \leq 9$, (bottom-midle) $10 \leq N_{Vtx} \leq 11$, (bottom-right) $12 \leq N_{Vtx}$, for 2011B. 73

4.27 Efficiencies and efficiency correction factors for M_T^W cut. Upper (lower) plot corresponds to 2011A (2011B). 74

4.28 The $\sigma_{i\eta i\eta}$ distributions for barrel (left) and endcap (right). The difference of mean values between simulation (filled green histograms) and data (black dots) are accounted for by shifting the simulation signal shapes. 78

4.29 The $\sigma_{i\eta i\eta}$ distributions for barrel (left) and endcap (right) in different E_{T}^{γ} bins ($15-20$ GeV, $20-25$ GeV, and $25-30$ GeV). Data FSR photon is shown in black dots, simulated FSR photon is shown in filled green histogram, and photon from simulation $W\gamma$ is shown in red histogram. 79

4.30 The correlation between $<\sigma_{i\eta i\eta}>$ and Iso_{TRK} for each E_{T}^{γ} bin in the barrel region. 80

4.31 The correlation between $<\sigma_{i\eta i\eta}>$ and Iso_{TRK} for each E_{T}^{γ} bin in the endcap region. 80

4.32 The $\sigma_{i\eta i\eta}$ distributions for the selected $W\gamma \to \mu\nu\gamma$ events in data (black squares) with photon candidates identified in the barrel (upper plot) and in the endcap (lower plot) for 2011A+2011B with the E_{T}^{γ} of 15-20 GeV. The unbinned fit result is shown by the blue solid line, and the background component is shown in red. 82

4.33 Above: Comparison of the fake rates for $W + jet$, $\gamma + jet$ and $jet + jet$ in simulation. The $\gamma + jet$ and $W + jet$ fake rates are not identical. Instead the $W + jet$ fake rate lies between that of $\gamma + jet$ and $jet + jet$. Below: Correction factors to adjust the $\gamma + jet$ and $jet + jet$ fake rate curves to emulate the $W + jet$ fake rate. 85

4.34 R_p as a function of photon candidate E_{T}^{γ} for barrel ECAL in $\gamma + jet$ and multijet QCD sample ($jet + jet$). The difference in R_p values between two processes is due to the fact that jets in $\gamma + jet$ process are dominated by quark fragmentation, while those in $jet + jet$ are dominated by gluon fragmentation. 86

4.35 Estimated background from jets misidentified as photons for $W\gamma \to \mu\nu\gamma$ for the barrel (left) and endcap (right) photon candidates, for 2011A (top), 2011B (middle) and 2011A+2011B combined (bottom). The 'template method' fit results are shown in red, the 'ratio method' results in blue, and background prediction from simulation as filled histograms. 89

4.36 The uncertainty on background 'template' for barrel (left) and endcap (right). The change in the estimated number of background events due to anti-isolation requirement (sideband bias) is given as a function of E_{T}^{γ} as red circles, while the contamination from genuine photons are given as blue dots. The overall effect is given as red dots. 95

4.37 Template method background yields using different background templates as the function of upper $\Delta\phi(MET, \gamma)$ cut value. 98

4.38 Muon candidate trensverse momentum (P_T^{μ}), pseudorapidity (η^{μ}), missing transverse energy (MET), invariant transverse mass of W (M_T^W), photon transverse energy E_T^{γ}, pseudorapidity (η^{γ}), $\Delta R(\mu,\gamma)$, number of good vertices, number of selected jets, $W\gamma$ candidate transverse momentum ($P_T^{W\gamma}$) , event yields after event selection and $\Delta\phi(leading\,jet,\gamma)$ overlaid distributions of the $W\gamma \to \mu\nu\gamma$ candidates in data, signal simulation, and background simulation for 2011A data set. 105

4.39 Muon candidate trensverse momentum (P_T^{μ}), pseudorapidity (η^{μ}), missing transverse energy (MET), invariant transverse mass of W (M_T^W), photon transverse energy E_T^{γ}, pseudorapidity (η^{γ}), $\Delta R(\mu,\gamma)$, number of good vertices, number of selected jets, $W\gamma$ candidate transverse momentum ($P_T^{W\gamma}$) , event yields after event selection and $\Delta\phi(leading\,jet,\gamma)$ overlaid distributions of the $W\gamma \to \mu\nu\gamma$ candidates in data, signal simulation, and background simulation for 2011B data set. 106

4.40 Muon candidate trensverse momentum (P_T^{μ}), pseudorapidity (η^{μ}), missing transverse energy (MET), invariant transverse mass of W (M_T^W), photon transverse energy E_T^{γ}, pseudorapidity (η^{γ}), $\Delta R(\mu,\gamma)$, number of good vertices, number of selected jets, $W\gamma$ candidate transverse momentum ($P_T^{W\gamma}$) , event yields after event selection and $\Delta\phi(leading\,jet,\gamma)$ overlaid distributions of the $W\gamma \to \mu\nu\gamma$ candidates in data, signal simulation, and background simulation for 2011A+2011B data sets combined. 107

4.41 The ratio of data shape to simulation shape for muon candidate trensverse momentum (P_T^{μ}), pseudorapidity (η^{μ}), missing transverse energy (MET), invariant transverse mass of W (M_T^W), photon transverse energy E_T^{γ}, pseudorapidity (η^{γ}), $\Delta R(\mu,\gamma)$, number of good vertices, number of selected jets, $W\gamma$ candidate transverse momentum ($P_T^{W\gamma}$) , event yields after event selection and $\Delta\phi(leading\,jet,\gamma)$ of the $W\gamma \to \mu\nu\gamma$ candidates for 2011A data set. 108

4.42 The ratio of data shape to simulation shape for muon candidate trensverse momentum (P_T^{μ}), pseudorapidity (η^{μ}), missing transverse energy (MET), invariant transverse mass of W (M_T^W), photon transverse energy E_T^{γ}, pseudorapidity (η^{γ}), $\Delta R(\mu,\gamma)$, number of good vertices, number of selected jets, $W\gamma$ candidate transverse momentum ($P_T^{W\gamma}$) , event yields after event selection and $\Delta\phi(leading\,jet,\gamma)$ of the $W\gamma \to \mu\nu\gamma$ candidates for 2011B data set. 109

4.43 The ratio of data shape to simulation shape for muon candidate trensverse momentum (P_T^{μ}), pseudorapidity (η^{μ}), missing transverse energy (MET), invariant transverse mass of W (M_T^W), photon transverse energy E_T^{γ}, pseudorapidity (η^{γ}), $\Delta R(\mu,\gamma)$, number of good vertices, number of selected jets, $W\gamma$ candidate transverse momentum ($P_T^{W\gamma}$) , event yields after event selection and $\Delta\phi(leading\,jet,\gamma)$ of the $W\gamma \to \mu\nu\gamma$ candidates for 2011A+2011B data sets combined. 110

4.44 Measured cross sections for $W\gamma \to \mu\nu\gamma$ (left) and the ratio of measured cross section to MCFM prediction for $W\gamma \to \mu\nu\gamma$ (right). 113

4.45 Measured cross sections for $W\gamma \to e\nu\gamma$ (left) and the ratio of measured cross section to MCFM prediction for $W\gamma \to e\nu\gamma$ (right). 115

4.46 Measured cross sections for $W\gamma \to l\nu\gamma$ (left) and the ratio of measured cross section to MCFM prediction for $W\gamma \to l\nu\gamma$ (right). Measurements in electron and muon channel are combined. 115

4.47 A summary of the measured cross sections and their combination for the Wγ analysis. 117

4.48 The summary of all cross section measurements and comparisons to theory for the Wγ measurement. 117

5.1 Charge-signed η distribution in data, signal simulation, and background simulation for $W\gamma \to \mu\nu\gamma$ for 2011A (left), 2011B (middle) and 2011A+2011B combined (right). 120

5.2 The ratio of data shape to simulated shape for charge-signed η distribution, for $W\gamma \to \mu\nu\gamma$ for 2011A (left), 2011B (middle) and 2011A+2011B combined (right). 120

5.3 Charge-signed η distribution in data, signal simulation, and background simulation combined for $W\gamma \to \mu\nu\gamma$ and $W\gamma \to e\nu\gamma$ for 2011A+2011B data sets combined. Yield from signal simulation is scaled to data signal yield. The right plot is background subtracted, uncertainties include statistic and systematic uncertainties. . . . 121

6.1 Photon E_{T}^{γ} distribution for data (black circles), background (blue filled histogram), simulated signal (black histogram), simulated signal with aTGC close to the excluded region $\Delta\kappa^{\gamma} = 0.4$ and $\lambda_{\gamma} = 0.0$ (red histogram). The last bin includes overflows. 125

6.2 2D 95% confidence level expected and observed contours for $WW\gamma$ coupling. . . . 126

6.3 1D 95% confidence level expected and observed limits for $\Delta\kappa^{\gamma}\, WW\gamma$ coupling. . . 126

6.4 1D 95% confidence level expected and observed limits for $\lambda^{\gamma}\, WW\gamma$ coupling. . . 127

6.5 2D 95% confidence level expected and observed contours for $WW\gamma$ coupling. Electron and muon channel combined. 127

6.6 1D 95% confidence level expected and observed limits for $\Delta\kappa^{\gamma}\, WW\gamma$ coupling. Electron and muon channel combined. 128

6.7 1D 95% confidence level expected and observed limits for $\lambda^{\gamma}\, WW\gamma$ coupling. Electron and muon channel combined. 129

7.1 Measurements of $W\gamma$ cross section with ATLAS detector using 1 fb^{-1} of data. . . . 131

7.2 Measurements of $W\gamma$ cross section with ATLAS detector using 5 fb^{-1} of data. Left plot shows the results for inclusive and right plot for exclusive measurement. . . . 131

7.3 1D limits on aTGC parameters from ATLAS experiment measurements using 5 fb^{-1} of data. 133

7.4 One-dimensional limits on aTGC parameters from different experiments. 133

9.1 Feynmanovi dijagrami koji doprinose Wγ produkciji: emisija fotona iz konačnog (a) i početnog (b) stanja i WWγ trostruko baždarno vezanje (c). 144

9.2 Diferencijalni udarni presjek razlike pseudorapiditeta fotona i leptona za proces $pp \to W^+\gamma \to l^+\nu\gamma$ pri $\sqrt{s} = 14$ TeV-a u SM. Inkluzivni NLO diferencijalni udarni presjek (puna linija), ekskluzivni diferencijalni udarni presjek događaja sa jednim mlazom (isprekidana linija), ekskluzivni diferencijalni udarni presjek događaja sa nula mlazeva (točkasta linija). 147

9.3 Simulirana raspodjela E_T^γ za $W\gamma$ proces, za različite vrijednosti aTGC parametara. . 149

9.4 Shematski prikaz akceleratorskog sustava LHC-a. 151

9.5 Shematski prikaz dipolnog magneta u LHC-u. 152

9.6 CMS detektor. 153

9.7 Presjek detektora tragova u CMS eksperimentu. 155

9.8 Prikaz elektromagnetskog kalorimetra u CMS eksperimentu. 156

9.9 Shematski prikaz hadronskog kalorimetra. 156

9.10 Mionski sustav eksperimenta CMS. 157

9.11 Rezolucija količine gibanja miona. 158

9.12 Transverzalni presjek CMS detektora s odgovarajućim potpisom različitih čestica. . 159

9.13 $\sigma_{i\eta i\eta}$ raspodjele za centralni (lijevo) i bočne dijelove detektora (desno) za simulirane (zeleni histogram) i mjerene događaje (točke) za uzorak 2011A (gore) i 2011B (dolje). 169

9.14 $\sigma_{i\eta i\eta}$ raspodjele za selektirane $W\gamma \to \mu\nu\gamma$ događaje u podacima (crne točke) za fotonske kandidate transverzalne enrgije $15 \leq E_{\mathrm{T}}^{\gamma} \leq 20$ GeV-a u centralnom (gore) i bočnim dijelovima detektora (dolje) za uzorak 2011A+2011B. Rezultati prilagodbe prikazani su plavom linijom dok je doprinos pozadine prikazan crvenom linijom. . 171

9.15 Broj pozadinskih događaja koje čine iz pogrešno identificirani mlazevi, za centralni (lijevo) i bočne dijelove detektora (desno). Rezultati dobiveni metodom predložaka i metodom omjera prikazani su crvenom odnosno plavom bojom. Zelenom bojom prikazan je broj pozadinskih događaja doiven iz simulacije. 174

9.16 Raspodjela transverzalnog impulsa miona (P_T^{μ}), pseudorapiditeta miona (η^{μ}), nedostajuće transverzalne energije (MET), transverzalne mase W bozona (M_T^W), tranverzalne energije fotona (E_T^{γ}), pseudorapiditeta fotona (η^{γ}), prostorne udaljenosti fotona i miona ($dR(\gamma,\mu)$), broja primarnih vrhova u događaju (Number of good vertices), broja mlazeva u događaju (Number of selected jets), transverzalnog impulsa $W\gamma$ sustava ($P_T^{W\gamma}$), broja događaja koji prolaze niz selekcijskih zahtjeva i razlike u kutu ϕ između mlaza i fotona ($\Delta\phi(jet,\gamma)$) za događaje koji zadovoljavaju $W\gamma \to \mu\nu\gamma$ selekciju za simulirane (histogrami) i mjerene događaje (točke) za uzorak 2011A. 179

9.17 Raspodjela transverzalnog impulsa miona (P_T^{μ}), pseudorapiditeta miona (η^{μ}), nedostajuće transverzalne energije (MET), transverzalne mase W bozona (M_T^W), tranverzalne energije fotona (E_T^{γ}), pseudorapiditeta fotona (η^{γ}), prostorne udaljenosti fotona i miona ($dR(\gamma,\mu)$), broja primarnih vrhova u događaju (Number of good vertices), broja mlazeva u događaju (Number of selected jets), transverzalnog impulsa $W\gamma$ sustava ($P_T^{W\gamma}$), broja događaja koji prolaze niz selekcijskih zahtjeva i razlike u kutu ϕ između mlaza i fotona ($\Delta\phi(jet,\gamma)$) za događaje koji zadovoljavaju $W\gamma \to \mu\nu\gamma$ selekciju za simulirane (histogrami) i mjerene događaje (točke) za uzorak 2011B. 180

9.18 Raspodjela transverzalnog impulsa miona (P_T^{μ}), pseudorapiditeta miona (η^{μ}), nedostajuće transverzalne energije (MET), transverzalne mase W bozona (M_T^W), tranverzalne energije fotona (E_T^{γ}), pseudorapiditeta fotona (η^{γ}), prostorne udaljenosti fotona i miona ($dR(\gamma,\mu)$), broja primarnih vrhova u događaju (Number of good vertices), broja mlazeva u događaju (Number of selected jets), transverzalnog impulsa $W\gamma$ sustava ($P_T^{W\gamma}$), broja događaja koji prolaze niz selekcijskih zahtjeva i razlike u kutu ϕ između mlaza i fotona ($\Delta\phi(jet,\gamma)$) za događaje koji zadovoljavaju $W\gamma \to \mu\nu\gamma$ selekciju za simulirane (histogrami) i mjerene događaje (točke) za uzorak 2011A+2011B. 181

9.19 Omjeri raspodjela transverzalnog impulsa miona (P_T^{μ}), pseudorapiditeta miona (η^{μ}), nedostajuće transverzalne energije (MET), transverzalne mase W bozona (M_T^W), tranverzalne energije fotona (E_T^{γ}), pseudorapiditeta fotona (η^{γ}), prostorne udaljenosti fotona i miona ($dR(\gamma,\mu)$), broja primarnih vrhova u događaju (Number of good vertices), broja mlazeva u događaju (Number of selected jets), transverzalnog impulsa $W\gamma$ sustava ($P_T^{W\gamma}$), broja događaja koji prolaze niz selekcijskih zahtjeva i razlike u kutu ϕ između mlaza i fotona ($\Delta\phi(jet,\gamma)$) za događaje koji zadovoljavaju $W\gamma \to \mu\nu\gamma$ selekciju za mjerene i simulirane događaje za uzorak 2011A. 182

9.20 Omjeri raspodjela transverzalnog impulsa miona (P_T^{μ}), pseudorapiditeta miona (η^{μ}), nedostajuće transverzalne energije (MET), transverzalne mase W bozona (M_T^W), tranverzalne energije fotona (E_T^{γ}), pseudorapiditeta fotona (η^{γ}), prostorne udaljenosti fotona i miona ($dR(\gamma,\mu)$), broja primarnih vrhova u događaju (Number of good vertices), broja mlazeva u događaju (Number of selected jets), transverzalnog impulsa $W\gamma$ sustava ($P_T^{W\gamma}$), broja događaja koji prolaze niz selekcijskih zahtjeva i razlike u kutu ϕ između mlaza i fotona ($\Delta\phi(jet,\gamma)$) za događaje koji zadovoljavaju $W\gamma \to \mu\nu\gamma$ selekciju za mjerene i simulirane događaje za uzorak 2011B. 183

9.21 Omjeri raspodjela transverzalnog impulsa miona (P_T^{μ}), pseudorapiditeta miona (η^{μ}), nedostajuće transverzalne energije (MET), transverzalne mase W bozona (M_T^W), tranverzalne energije fotona (E_T^{γ}), pseudorapiditeta fotona (η^{γ}), prostorne udaljenosti fotona i miona ($dR(\gamma,\mu)$), broja primarnih vrhova u događaju (Number of good vertices), broja mlazeva u događaju (Number of selected jets), transverzalnog impulsa $W\gamma$ sustava ($P_T^{W\gamma}$), broja događaja koji prolaze niz selekcijskih zahtjeva i razlike u kutu ϕ između mlaza i fotona ($\Delta\phi(jet,\gamma)$) za događaje koji zadovoljavaju $W\gamma \to \mu\nu\gamma$ selekciju za mjerene i simulirane događaje za uzorak 2011A+2011B. 184

9.22 Mjereni udarni presjek $W\gamma \to \mu\nu\gamma$ (lijevo) te omjer mjerenog udarnog presjeka i udarnog presjeka predviđenog MCFM generatorom (desno). 187

9.23 Mjereni udarni presjek $W\gamma \to e\nu\gamma$ (lijevo) te omjer mjerenog udarnog presjeka i udarnog presjeka predviđenog MCFM generatorom (desno). 189

9.24 Mjereni udarni presjek $W\gamma \to l\nu\gamma$ (lijevo) te omjer mjerenog udarnog presjeka i udarnog presjeka predviđenog MCFM generatorom (desno) za kombinirani mionski i elektronski kanal. 189

9.25 Pregled mjerenih udarnih presjeka $W\gamma$ procesa. 191

9.26 Mjereni i teorijski predviđeni udarni presjeci za $W\gamma$ proces. 191

9.27 $Q_l \times \Delta\eta$ raspodjela za događaje koji zadovoljavaju $W\gamma \to \mu\nu\gamma$ selekciju za simulirane (histogrami) i mjerene događaje (točke) za uzorak 2011A (lijevo), uzrak 2011B (sredina) i uzorak 2011A+2011B (desno). 193

9.28 Omjer $Q_l \times \Delta\eta$ raspodjele za događaje koji zadovoljavaju $W\gamma \to \mu\nu\gamma$ selekciju za mjerene i simulirane događaje za uzorak 2011A (lijevo), uzorak 2011B (sredina) i uzorak 2011A+2011B (desno). 193

9.29 $Q_l \times \Delta\eta$ raspodjele dobivene kombiniranjem elektronskog i mionskog kanala za događaje koji zadovoljavaju $W\gamma \to l\nu\gamma$ selekciju za simulirane (histogrami) i mjerene događaje (točke) za uzorak 2011A+2011B. Broj simuliranih događaja u signalu skaliran je na mjereni broj događaja u signalu. Na desnoj raspodjeli oduzet je doprinos pozadine. Pogreške uključuju statističke i sistematske pogreške. 194

9.30 Raspodjela transverzalne mase fotona (E_{T}^{γ}) za događaje koji zadovoljavaju $W\gamma \to \mu\nu\gamma$ selekciju za pozadinu (puni histogram), simulirane $W\gamma$ događaje (crni isprekidani histogram), simulirani aTGC signal za vrijednosti parametara $\Delta\kappa^{\gamma} = 0.4$ i $\lambda_{\gamma} = 0.0$ (crveni histogram) i mjerene događaje (točke) za uzorak 2011A+2011B. Posljednji bin uključuje događaje s velikim E_{T}^{γ} vrijednostima. 198

9.31 Dvodimenzionalne 95% C.L. očekivane i mjerene granice na parametre $WW\gamma$ vezanja. 199

9.32 Jednodimenzionalne 95% C.L. očekivane i mjerene granice na parametar $\Delta\kappa^{\gamma}$ $WW\gamma$ vezanja. 199

9.33 Jednodimenzionalne 95% C.L. očekivane i mjerene granice na parametar λ_{γ} $WW\gamma$ vezanja. 200

9.34 Dvodimenzionalne 95% C.L. očekivane i mjerene granice na parametre $WW\gamma$ vezanja. Kombinirani rezultati za elektronski i mionski kanal. 200

9.35 Jednodimenzionalne 95% C.L. očekivane i mjerene granice na parametar $\Delta\kappa^{\gamma}$ $WW\gamma$ vezanja. Kombinirani rezultati za elektronski i mionski kanal. 201

9.36 Jednodimenzionalne 95% C.L. očekivane i mjerene granice na parametar λ^{γ} $WW\gamma$ vezanja. Kombinirani rezultati za elektronski i mionski kanal. 202

9.37 Rezultati mjerenja $W\gamma$ udarnog presjeka ATLAS detektorom koristeći podatke koji odgovaraju integriranom luminozitetu 1 fb^{-1}. 204

9.38 Rezultati inkluzivnog (lijevo) i ekskluzivnog (desno) mjerenja $W\gamma$ udarnog presjeka ATLAS detektorom koristeći podatke koji odgovaraju integriranom luminozitetu 5 fb^{-1}. 204

9.39 Jednodimenzionalne 95% C.L. granice na parametre $WW\gamma$ vezanja ATLAS eksperimenta. Rezultati su prikazani za mjerenje koristeći podatke integriranog luminoziteta $5fb^{-1}$. 206

9.40 Rezultati mjerenja aTGC parametara u različitim eksperimentima. 206

Chapter 1

Introduction

Particle physics is for decades trying to give an answer to several questions related to fundamental structure of matter . What is the physics beyond Standard Model (SM) like? What is dark matter, dark energy, nature of gravity? Is there a Higgs boson? The latest question was the one that triggered the construction of several important experiments. At the Fermilab proton-antiproton collider two detectors, D0 and CDF, were operating from 1985. to 2011. and provided many important observations and discoveries at an energy of about 2 TeV. However Higgs boson was not discovered. Several years ago the Large Hadron Collider (LHC) at CERN started colliding protons at center of mass energy of 7 TeV. Two general purpose detectors, ATLAS and CMS, are trying to give a long anticipated answer to the question about the Higgs boson existence.

The ability to precisely measure the outgoing particles of SM Higgs decay was one of the most important design requirements for the ATLAS and CMS detectors. Therefore their design allows a precise measurement of leptons and photons.

Besides the search for the Higgs boson and physics beyond SM (new physiscs) measurements of SM processes constitute an important task at the LHC. Besides checking the validity of the SM at high energy some of these measurements also provide the ability of indirect search for new physics. Diboson processes like Wγ provide an opportunity to measure a cross section and search for new physics through the measurement of triple gauge boson couplings (TGC). In presence of new (yet

undiscovered) particles the TGC would be stronger therefore resulting in anomalous TGC (aTGC). These couplings are the least well measured properties in the electroweak sector of the SM.

Chapter 2

$W\gamma$ production at the LHC

2.1 The Standard Model of Particle Physics

The Standard model [5] combines all our current knowledge of physics of elementary particles and their interactions. Thoroughly tested by measurements for decades it has been proven correct at all energies available in the laboratory. With the start of proton-proton collisions at the Large hadron collider (LHC) at an energy of 7 TeV, the first task was to check the SM predictions.

The electroweak theory, the combined theory of the electromagnetic and weak interactions, is the most exciting part of the Standard Model. It includes the only massive force mediators, spontaneous symmetry breaking with Higgs mechanism and V-A structure.

It is known that a renormalizable theory is a theory with local gauge invariance. The lagrangian of the electroweak theory is required to be invariant under $SU(2)_L \otimes U(1)_Y$ transformations, where L stands for left-handed and Y is the weak hypercharge.

The Lagrangian for a free fermion is:

$$\begin{aligned}\mathscr{L}_1 &= \overline{\Psi}(i\gamma^\mu\partial_\mu - m)\Psi, \\ &= (\overline{L}+\overline{R})(i\gamma^\mu\partial_\mu - m)(L+R), \\ &= \overline{L}(i\gamma^\mu\partial_\mu)L + \overline{R}(i\gamma^\mu\partial_\mu)R - m(\overline{L}R + \overline{R}L)\end{aligned} \tag{2.1}$$

where Ψ is the fermion wave function [6] and m is the fermion mass. Ψ has left-handed (L) and right-handed (R) components that transform differently under $SU(2)_L \otimes U(1)_Y$ transformation:

$$\begin{aligned}L \rightarrow L' &= e^{i\overrightarrow{\alpha}(x)\cdot\overrightarrow{T} + i\beta(x)Y}L, \\ R \rightarrow R' &= e^{i\beta(x)Y}R\end{aligned} \tag{2.2}$$

where $\overrightarrow{T}$ and Y are generators of the $SU(2)_L$ and $U(1)_Y$ groups. L is an isospin doublet while R is an isospin singlet, in case of leptons these are:

$$\begin{aligned}L &= \begin{pmatrix}\nu_e \\ e^-\end{pmatrix}_L, \begin{pmatrix}\nu_\mu \\ \mu^-\end{pmatrix}_L, \begin{pmatrix}\nu_\tau \\ \tau^-\end{pmatrix}_L \\ R &= \left(e^-\right)_R, \left(\mu^-\right)_R, \left(\tau^-\right)_R.\end{aligned} \tag{2.3}$$

The Lagrangian 2.1 is required to be invariant under local $SU(2)_L \otimes U(1)_Y$ transformations. Unlike in quantum electrodynamics, where $U(1)$ local invariance is required, here the fermion mass term of the Lagrangian is not invariant and is removed for now. One achieves invariance of the remaining Lagrangian terms with the use of the 'covariant derivative' D_μ where four vector boson fields $\overrightarrow{W}^\mu$ and B^μ are introduced:

$$\text{for } L\text{: } D_\mu = \partial_\mu + ig\overrightarrow{T}\cdot\overrightarrow{W}_\mu + ig'\frac{Y}{2}B_\mu, \tag{2.4}$$

$$\text{for } R\text{: } D_\mu = \partial_\mu + ig'\frac{Y}{2}B_\mu. \tag{2.5}$$

Using these derivatives the Lagrangian becomes gauge invariant:

$$\begin{aligned}\mathscr{L}_1 = \overline{L}\gamma^\mu(i\partial_\mu - g\overrightarrow{T}\cdot\overrightarrow{W}_\mu - ig'\frac{Y}{2}B_\mu)L \\ + \overline{R}\gamma^\mu(i\partial_\mu - ig'\frac{Y}{2}B_\mu)R\end{aligned} \tag{2.6}$$

The Lagragian 2.6 includes terms for the fermion kinetic energy, interaction with vector bosons W^1, W^2,W^3 and B asociated with vector fields $\overrightarrow{W}^\mu$ and B^μ. Since additional vector fields are included in the Lagrangian the invariant kinetic energy of bosons needs to be included:

$$\mathscr{L}_2 = -\frac{1}{4}\overrightarrow{W}_{\mu\nu}\overrightarrow{W}^{\mu\nu} - \frac{1}{4}B_{\mu\nu}B^{\mu\nu} \tag{2.7}$$

where

$$\overrightarrow{W}_{\mu\nu} = \partial_\mu\overrightarrow{W}_\nu - \partial_\nu\overrightarrow{W}_\mu - g\overrightarrow{W}_\mu \times \overrightarrow{W}_\nu, \tag{2.8}$$

and

$$B_{\mu\nu} = \partial_\mu B_\nu - \partial_\nu B_\mu. \tag{2.9}$$

The final term in 2.8 arise from the non-Abelian character of the group.

Ferminos have non zero masses as well as the electroweak bosons $W^\pm$ and Z, while γ is massless. The Higgs mechanism [7, 8, 9] is used to provide masses to both bosons and fermions, while at the same time keeping the Lagrangian gauge invariant. In the procedure few choices are made that result with the desired properties. Four real scalar fields Φ_i are introduced. The Lagrangian of the scalar field is:

$$\mathscr{L}_3 = (\partial_\mu\Phi)^\dagger(\partial^\mu\Phi) - V(\Phi) \tag{2.10}$$

where $V(\Phi)$ is the potential of the field. The potential is chosen to have the form:

$$V(\Phi) = \mu^2 \Phi^\dagger \Phi + \lambda (\Phi^\dagger \Phi)^2. \tag{2.11}$$

To achieve local $SU(2)_L \otimes U(1)_Y$ invariance of the Lagrangian 2.10 the Φ_i must belong to $SU(2)_L \otimes U(1)_Y$ multiplets and the 'covariant derivative' 2.4 has to be used. The fields are chosen to form an isospin doublet:

$$\Phi = \begin{pmatrix} \phi^+ \\ \phi^0 \end{pmatrix} \tag{2.12}$$

where

$$\phi^+ = \frac{\phi_1 + i\phi_2}{\sqrt{2}} \tag{2.13}$$

$$\phi^0 = \frac{\phi_3 + i\phi_4}{\sqrt{2}} \tag{2.14}$$

If the constants μ and λ fulfill $\mu^2 < 0$ and $\lambda > 0$, the potential has a 'Mexican-hat' shape, the point $\Phi = 0$ is unstable and there is a continuum of minimum values where:

$$\Phi^\dagger \Phi = -\frac{\mu^2}{2\lambda}. \tag{2.15}$$

Choosing one minimum point gives the vacuum a preferred direction in isospin space, and the symmetry is spontaneously broken. A minimum (vacuum value) is chosen at this point:

$$\begin{aligned} &\phi_1 = \phi_2 = \phi_4, \phi_3^2 = -\frac{\mu^2}{\lambda} \equiv v^2, \\ &\Phi_0 = \frac{1}{\sqrt{2}} \begin{pmatrix} 0 \\ v \end{pmatrix} \end{aligned} \tag{2.16}$$

This choice of Φ_0 breaks $SU(2)$ and $U(1)_Y$ gauge symmetries while $U(1)_{em}$ is unbroken. This results in massive $W^{\pm}$ and Z vector bosons and a massless photon.

Using 'covariant derivative' the Lagrangian 2.10 takes gauge invariant form:

$$\begin{aligned}\mathscr{L}_3 &= \Phi^{\dagger}(\partial_\mu - ig\overrightarrow{T}\cdot\overrightarrow{W}_\mu - ig'\frac{Y}{2}B_\mu)(\partial^\mu + ig\overrightarrow{T}\cdot\overrightarrow{W}^\mu + ig'\frac{Y}{2}B^\mu)\Phi - V(x) \\ &= \frac{1}{2}\begin{pmatrix}0 & v\end{pmatrix}(\partial_\mu - ig\overrightarrow{T}\cdot\overrightarrow{W}_\mu - ig'\frac{1}{2}B_\mu)(\partial^\mu + ig\overrightarrow{T}\cdot\overrightarrow{W}^\mu + ig'\frac{1}{2}B^\mu)\begin{pmatrix}0\\ v\end{pmatrix} - V(x)\end{aligned} \tag{2.17}$$

where a chosen vacuum point 2.16 and a corresponding weak hypercharge value $Y = 1$ are used. The relevant term for boson masses is:

$$\begin{aligned}\mathscr{L}_3^{\text{boson mass term}} =& \frac{1}{2}\begin{pmatrix}0 & v\end{pmatrix}(-ig\overrightarrow{T}\cdot\overrightarrow{W}_\mu - ig'\frac{1}{2}B_\mu)(ig\overrightarrow{T}\cdot\overrightarrow{W}^\mu + ig'\frac{1}{2}B^\mu)\begin{pmatrix}0\\ v\end{pmatrix} \\ =& \frac{1}{8}\begin{pmatrix}0 & v\end{pmatrix}\begin{pmatrix}gW_\mu^3 + g'B_\mu & gW_\mu^1 - igW_\mu^2 \\ gW_\mu^1 + igW_\mu^2 & -gW_\mu^3 + g'B_\mu\end{pmatrix} \\ & \begin{pmatrix}gW^{\mu 3} + g'B^\mu & gW^{\mu 1} - igW^{\mu 2} \\ gW^{\mu 1} + igW^{\mu 2} & -gW^{\mu 3} + g'B^\mu\end{pmatrix}\begin{pmatrix}0\\ v\end{pmatrix} \\ =& \frac{(vg)^2}{8}[(W_\mu^1)^2 + (W_\mu^2)^2] + \frac{(v)^2}{8}[-gW_\mu^3 + g'B_\mu]^2.\end{aligned} \tag{2.18}$$

For a charged vector boson a term of form $M_X^2X^2$ is expected and for a neutral boson of form $\frac{1}{2}M_X^2X^2$. Mixing of fields $\overrightarrow{W}^\mu$ and B^μ is needed to recognize the physical vector bosons $W^{\pm}$, Z and the photon. This is achieved using the following identities:

$$
\begin{aligned}
W_\mu^+ &= \frac{1}{\sqrt{2}}(W_\mu^1 - iW_\mu^2),\\
W_\mu^- &= \frac{1}{\sqrt{2}}(W_\mu^1 + iW_\mu^2),\\
Z_\mu &= \frac{1}{\sqrt{g^2+g'^2}}(gW_\mu^3 - g'B_\mu),\\
A_\mu &= \frac{1}{\sqrt{g^2+g'^2}}(g'W_\mu^3 + gB_\mu).
\end{aligned}
\tag{2.19}
$$

The mass term can now be written as:

$$
\mathscr{L}_3^{\text{boson mass term}} = \frac{(vg)^2}{4}W_\mu^+ W^{\mu-} + \frac{(v)^2}{8}(g^2+g'^2)(Z_\mu)^2 + 0(A_\mu)^2, \tag{2.20}
$$

where the boson masses are recognized:

$$
\begin{aligned}
M_W &= \frac{vg}{2},\\
M_Z &= \frac{v}{2}\sqrt{g^2+g'^2},\\
M_A &= 0.
\end{aligned}
\tag{2.21}
$$

The Higgs mechanism is also used to generate fermion masses. The $SU(2)_L \otimes U(1)_Y$ gauge invariant term in the Lagrangian representing the interaction of the Higgs field to fermions can be written as:

$$
\mathscr{L}_4 = -G_e(\overline{R}\Phi^\dagger L + \overline{L}\Phi R) \tag{2.22}
$$

The symmetry is spontaneously broken by choosing the vacuum point 2.16 and expanding around it:

$$
\Phi(x) = \frac{1}{\sqrt{2}}\begin{pmatrix} 0 \\ v+h(x). \end{pmatrix} \tag{2.23}
$$

To generate the electron mass equation 2.3 is used:

$$\begin{aligned}\mathscr{L}_4 &= -\frac{G_e}{\sqrt{2}}[v(\overline{e_R}e_L + \overline{e_L}e_R) + h(x)(\overline{e_R}e_L + \overline{e_L}e_R)] \\ &= -\frac{G_e}{\sqrt{2}}[v(\overline{e}e) + h(x)(\overline{e}e)].\end{aligned} \tag{2.24}$$

To recognize the mass of electron the following is chosen:

$$G_e = \sqrt{2}\frac{m_e}{v} \tag{2.25}$$

then

$$\mathscr{L}_4 = -m_e\overline{e}e - \frac{m_e}{v}h(x)\overline{e}e \tag{2.26}$$

where the first term is the electron mass term and the second describes the coupling of the Higgs field to electrons. Quark masses are generated in the same way.

Summing up all parts the total electroweak Lagrangian is:

$$\begin{aligned}\mathscr{L}_{total} =& \Phi^\dagger(\partial_\mu - ig\overrightarrow{T}\cdot\overrightarrow{W}_\mu - ig'\frac{Y}{2}B_\mu)(\partial^\mu + ig\overrightarrow{T}\cdot\overrightarrow{W}^\mu + ig'\frac{Y}{2}B^\mu)\Phi - V(x) \\ &- G_1(\overline{R}\Phi^\dagger L + \overline{L}\Phi R) - G_2(\overline{R}\Phi_c^\dagger L + \overline{L}\Phi_c R) \\ &+ \overline{L}\gamma^\mu(i\partial_\mu - g\overrightarrow{T}\cdot\overrightarrow{W}_\mu - ig'\frac{Y}{2}B_\mu)L \\ &+ \overline{R}\gamma^\mu(i\partial_\mu - ig'\frac{Y}{2}B_\mu)R \\ &- \frac{1}{4}\overrightarrow{W}_{\mu\nu}\overrightarrow{W}^{\mu\nu} - \frac{1}{4}B_{\mu\nu}B^{\mu\nu}\end{aligned} \tag{2.27}$$

where Φ_c is the new Higgs doublet used to generate masses of upper members of L doublets:

$$\Phi_c = \begin{pmatrix} -\overline{\phi^0} \\ \phi^- \end{pmatrix}. \tag{2.28}$$

The first therm in equation 2.27 represents $W^{\pm}$, Z, γ and Higgs masses and couplings, the second term lepton and quark masses and coupling to Higgs, the third and fourth terms lepton and quark kinetic energies and their interaction with vector bosons and the final two terms represent vector bosons kinetic energies and self-interactions. Due to the last term in 2.7 triple gauge couplings (TGC) $WW\gamma$ and WWZ are allowed. Using identities 2.19 the part in the Lagrangian describing TGC is:

$$\mathscr{L}_{TGC} = -ig_{WWV}[V^{\mu}(W^-_{\mu\nu}W^{+\nu} - W^+_{\mu\nu}W^{-\nu}) + W^+_{\mu}W^-_{\nu}V^{\mu\nu}] \tag{2.29}$$

where V^{μ} is A^{μ} or Z^{μ}, $g_{WWZ} = ecot\theta_W$ and $g_{WW\gamma} = e$. It can be seen that the allowed TGCs in SM are $WW\gamma$ and WWZ.

2.2 The process $pp \rightarrow W\gamma + X \rightarrow l\nu\gamma + X$ in proton proton collisions

The production of gauge-boson pairs provide the test of the non-Abelian gauge symmetry of the SM. Deviation from the SM predictions may come either from the presence of anomalous couplings or the production of new heavy particles and their decays into vector boson pairs. Vector-boson pair production also gives the most important background for a number of new physics signals.

Wγ production in proton-proton collision at leading order (LO) includes the three processes shown in Figure 2.1. These include initial state radiation, final state radiation and the process via triple gauge boson coupling. There is one additional process that dominates at very high energies, photon bremstrahlung where $q_1 g \rightarrow V q_2$ is followed by photon radiation from the final state quark. This process is eliminated by requiring the photon to be isolated.

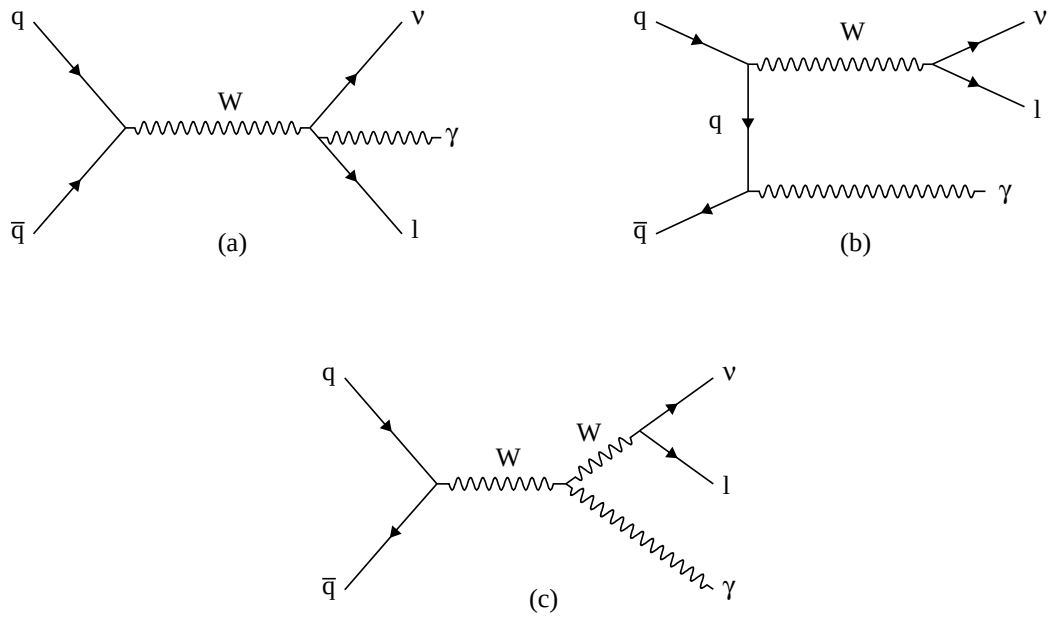

Figure 2.1: Feynman diagrams of the Wγ production via final (a) and initial (b) state radiation and via WWγ triple gauge coupling (c).

Table 2.1: Branching ratios for W^+ decay [1].

Decay mode	Fraction
$l^+\nu$	10.80 ± 0.09 %
$e^+\nu$	10.75 ± 0.13 %
$\mu^+\nu$	10.57 ± 0.15 %
hadrons	67.60 ± 0.27 %

The production mechanism at LO is through quark-antiquark anihilation and at NLO mainly quark-gluon fusion. At LHC the NLO corrections are large due to large quark-gluon parton density at high energies.

Finally, W can decay leptonically or hadronically with the branching ratios shown in table 2.1.

2.3 Radiation Amplitude Zero

A pronounced feature of Wγ production in hadronic collisions is the so-called radiation amplitude zero (RAZ), the phenomena that all contributing helicity amplitudes vanish for a defined angle of the outgoing photon in the center of mass frame.

It is known that all SM helicity amplitudes of the parton-level subprocess $q_1\bar{q_2} \rightarrow W^{\pm}\gamma$ vanish in the centre of mass frame for $\cos\theta^* = -\frac{Q_1+Q_2}{Q_1-Q_2}$ [10, 11], where θ^* is the scattering angle of the photon with respect to the quark q_1 direction, and Q_i (i = 1; 2) are the quark charges in units of the proton electric charge e. In proton-proton collisions the dominant production process for $W^+\gamma$ is $u\bar{d} \rightarrow W^+\gamma$ where amplitudes vanish for $\cos\theta^* = -\frac{1}{3}$, and the dominant production process for $W^-\gamma$ is $d\bar{u} \rightarrow W^-\gamma$ where amplitudes vanish for $\cos\theta^* = \frac{1}{3}$.

This zero is difficult to observe for numerous reasons. In a realistic experimental environment it is always approximate or becomes a dip. Other contributing processes, higher order QCD corrections, finite W width and final state radiation are filling the dip. Detector resolution effects further dilute the RAZ signal. It is also not possible to reconstruct the center of mass frame at a hadron collider since the longitudinal momentum of the neutrino cannot be determined without ambiguities. Since it is not possible to perform the measurement in the center of mass frame, a sensitive variable in the laboratory frame must be found. Since W and γ are back to back in the center of mass frame, dip is also expected in the W rapidity distribution and the same is true for the W and γ rapidity difference $y(\gamma)^* - y(W)^*$. [1] Since the rapidity difference is invariant under the longitudinal boost, the rapidity difference in the laboratory frame, $y(\gamma) - y(W)$, also has a dip. Since the neutrino longitudinal momentum is not measured in the detector we cannot reconstruct the W rapidity. In the SM the dominant helicity in $W^{\pm}\gamma$ production is $\lambda_W = \pm 1$ [12]. This means that the lepton from the W decay tends to be emitted in the direction of the parent W, reflecting thus most of the kinematic properties of the W. Therefore the correlation of W and γ rapidities is mostly present in lepton and γ rapidities. In the limit of massless particles the rapidity and pseudorapidity are equal so

[1] Rapidity is defined as $y = \frac{1}{2}\ln\frac{E+p_Z}{E-p_Z}$. Where E is the energy of particle and p_Z is the component of momentum along the beam axis.

it is expected that the RAZ dip is also present in the pseudorapidity difference $\eta(\gamma) - \eta(l)$. [2] The pseudorapidity is precisely measured variable at CMS detector.

At the LHC we expect to see the RAZ in $W\gamma$ production as a dip at value 0 in $\eta(\gamma) - \eta(l)$ distribution as shown in Figure 2.2 [2].

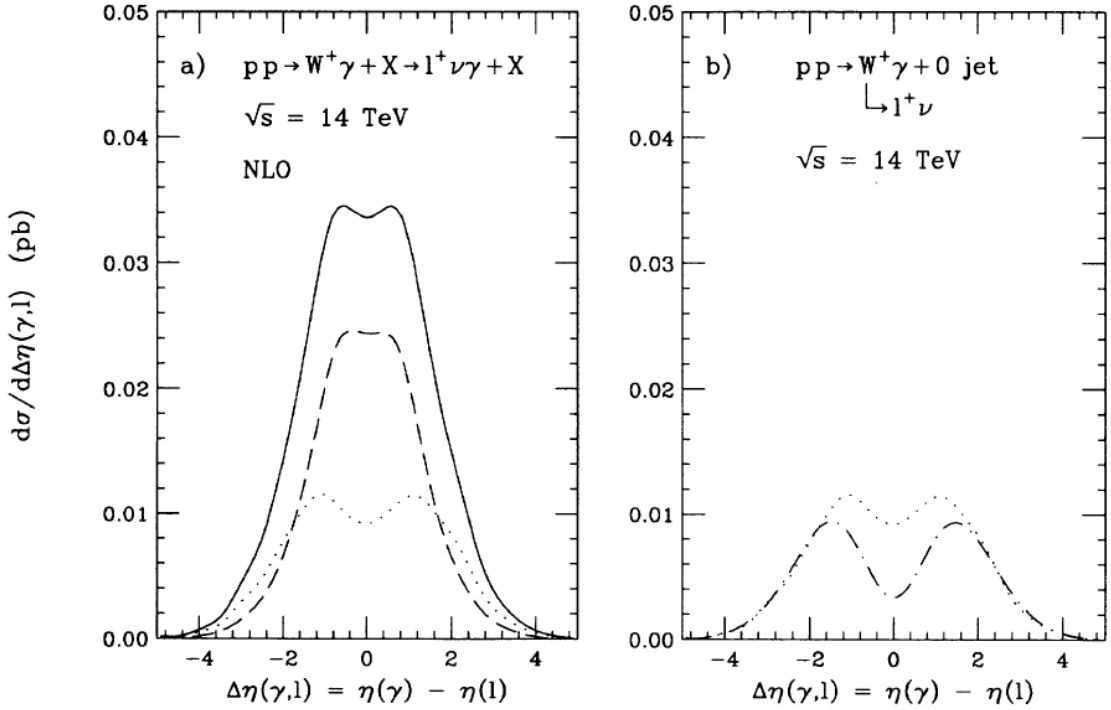

Figure 2.2: The differential cross section for the photon-lepton pseudorapidity difference for $pp \to W^+\gamma \to l^+\nu\gamma$ at $\sqrt{s} = 14$TeV in the SM. (a) The inclusive NLO differential cross section (solid line), together with the O(α_s) 0-jet (dotted line), and the (LO) 1-jet (dashed line) exclusive differential cross sections. (b) The NLO $W^+\gamma$+0-jet exclusive differential cross section (dotted line) compared with the Born differential cross section (dash-dotted line) [2].

The RAZ can also be expressed as the relativistic generalization of the absence of electric and magnetic dipole radiation for nonrelativistic collisions of particles with the same charge-to-mass ratio and g factor [13].

Additional selection on $W\gamma$ events can be imposed in order to make RAZ more visible in the data. Higher order QCD correction contributions that tend to fill in the dip can be reduced by imposing

[2] Pesudorapidity is defined as $\eta = -\ln\tan(\theta/2) = \frac{1}{2}\ln\frac{|\vec{p}|+p_Z}{|\vec{p}|-p_Z}$. Where θ is the angle between the particle momentum $\vec{p}$ and the beam axis, p_Z is the component of momentum along the beam axis.

the jet veto, removing events with jet above some P_T threshold. Process where the γ is a result of lepton radiation, final state radiation, also diminish the RAZ dip. These events can successfully be removed by imposing the lower cut on transverse mass of three objects $M_T^{(l,\nu,\gamma)}$.

RAZ is also sensitive to the presence of anomalous triple gauge couplings. If they are present they also change the shape of $\eta(\gamma) - \eta(l)$ distribution by filling the RAZ dip. However this is not the variable most sensitive to anomalous couplings in the $W\gamma$ channel.

2.4 Triple Gauge Couplings

If the particle spectrum of the SM has to be enlarged with new particles (as in the Minimal Supersymmetric Standard Model (MSSM) [14]) with mass values of $\geq 0.5 - 1$ TeV, their presence would be manifested as small anomalous couplings at low energy.

Triple gauge boson couplings (TGC) are a consequence of the non-Abelian nature of the SM electroweak sector $SU(2)_L \otimes U(1)_Y$ and are uniquely predicted. Many extensions of the SM predict additional processes with multiple bosons in the final state. Therefore, any deviation of the observed value from the SM prediction could be an early sign of new physics at high energies. A measurement of TGCs can thus be sensitive to new phenomena at high energies which would require more energy or luminosity to be observed directly.

The most general Lorentz invariant effective Lagrangian that describes WWV coupling has 14 independent parameters [15, 16], 7 parameters for WWZ and 7 for $WW\gamma$ vertex. Assuming C and P conservation, only six independent couplings remain with a given effective Lagrangian:

$$\frac{\mathscr{L}_{TGC}}{g_{WWV}} = ig_1^V(W^-_{\mu\nu}W^{+\mu}V^\nu - W^-_\mu V_\nu W^{+\mu\nu}) + i\kappa_V W^-_\mu W^+_\nu V^{\mu\nu} + \frac{i\lambda_V}{M_W^2}W^-_{\delta\mu}W^{+\mu}_\nu V^{\nu\delta}, \qquad (2.30)$$

where $V = \gamma$ or Z, $g_{WW\gamma} = -e$, $g_{WWZ} = -e\cot\theta_W$ and θ_W is the weak mixing angle. Assuming electromagnetic gauge invariance, $g_1^\gamma = 1$, the remaining parameters that describe WWV coupling are g_1^Z, κ_Z, κ_γ, λ_Z and λ_γ. Comparison with 2.29 reveals that in the SM $\lambda_Z = \lambda_\gamma = 0$ and $g_1^Z = \kappa_Z = \kappa_\gamma = 1$.

These five couplings are further reduced to three independent couplings if one requires the Lagrangian to be $SU(2)_L \otimes U(1)_Y$ invariant:

$$\Delta\kappa_Z = \Delta g_1^Z - \Delta\kappa_\gamma \cdot \tan^2\theta_W, \quad \lambda = \lambda_\gamma = \lambda_Z. \tag{2.31}$$

In this study $\Delta\kappa_\gamma$ and λ_γ are measured from $W\gamma$ production.

All anomalous couplings violate the partial wave unitarity at high energies. Thus, all Tevatron studies of TGC define the $\hat{s}$-dependence of the TGCs that preserve unitarity at high energies as following:

$$\alpha(\hat{s}) = \frac{\alpha_0}{(1+\hat{s}/\Lambda_{NP}^2)^n}. \tag{2.32}$$

Here, α_0 is a low-energy approximation of the coupling $\alpha(\hat{s})$, where $\hat{s}$ is the square of the invariant mass of the diboson system, and Λ_{NP} is the form factor scale, an energy at which new physics cancels divergences in the TGC vertex. In this study TGCs without form-factor scaling are measured, as this allows to provide results without any particular bias that can arise due to the choice of the form-factor energy dependence.

As a signature of aTGC in the $W\gamma$ final state one expects to observe a higher yield of events with high E_T^γ as shown in Fig. 2.3.

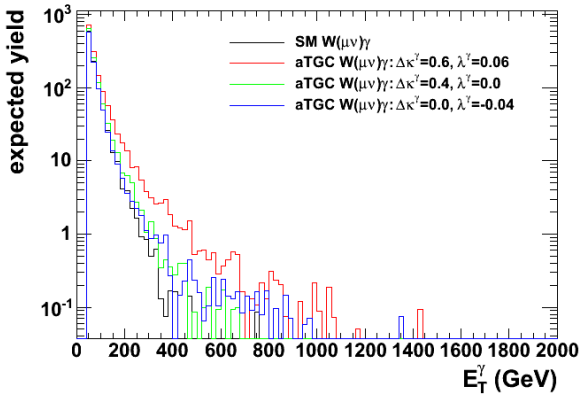

Figure 2.3: Simulated E_T^γ distribution for the $W\gamma$ process for different values of aTGC parameters. Process is simulated with the SHERPA generator [3] interfaced with PYTHIA [4].

Different models of physics beyond the Standard Model result with different contributions to aTGC parameters. Additional generation of heavy quarks and leptons would contribute with $\approx 10^{-3}$, while the Minimal Supersymmetric Standard Model (MSSM) would result in the following upper bounds [14]:

$$\begin{aligned} |\Delta\kappa_\gamma| &\leq 2 \times 10^{-2}, \\ |\Delta\kappa_Z| &\leq 2 \times 10^{-2}, \\ |\lambda_\gamma| &\leq 6 \times 10^{-3}, \\ |\lambda_Z| &\leq 6 \times 10^{-3}. \end{aligned} \tag{2.33}$$

Chapter 3

The Large Hadron collider and the Compact Muon Solenoid detector

3.1 The Large Hadron Collider

The Large Hadron Collider (LHC) [17] is the most powerful collider in the world . The LHC was installed in the existing LEP tunnel, a 26.7 km ring consisting of eight straight sections connected by eight arcs, housed at a depth of 45 m to 170 m near the France-Switzerland border.

The two general purpose experiments, CMS and ATLAS, study Standard Model physics processes and perform searches for physics beyond the Standard Model.

The LHC started colliding protons in 2009 at a center of mass energy of 1.18 TeV. Collisions continued in 2010 and 2011 at a center of mass energy of 7 TeV. During 2012 the energy of collisions was enhanced to 8 TeV.

Since protons have higher mass they loose less energy than electrons via synchrotron radiation what allows to reach higher energies. The main production process of Higgs boson in high energy proton-(anti)proton collisions is gluon fusion. Since gluon density functions are identical in proton and antiproton and producing high intensity antiproton beams is much more challenging and expensive,

proton-proton collisions were the better choice. The pp design of the LHC allows it to achieve instantaneous luminosities beyond those seen in the Tevatron $p\overline{p}$ collisions.

The instantaneous luminosity for a symmetric colliding beam experiment such as the LHC is given as:

$$\mathscr{L} = \frac{nN^2 f}{A_{eff}} \tag{3.1}$$

where n is the number of bunches per beam, N the number of particles per bunch, f the revolution frequency , and A_{eff} the effective cross-sectional area of the beams. The beams are focused to 16 μm in each of the transverse directions (σ_x and σ_y) which can be used to calculate the value of A_{eff} = $4\pi\sigma_x\sigma_y$. The total integrated luminosity delivered in 2011 is shown in Figure 3.1.

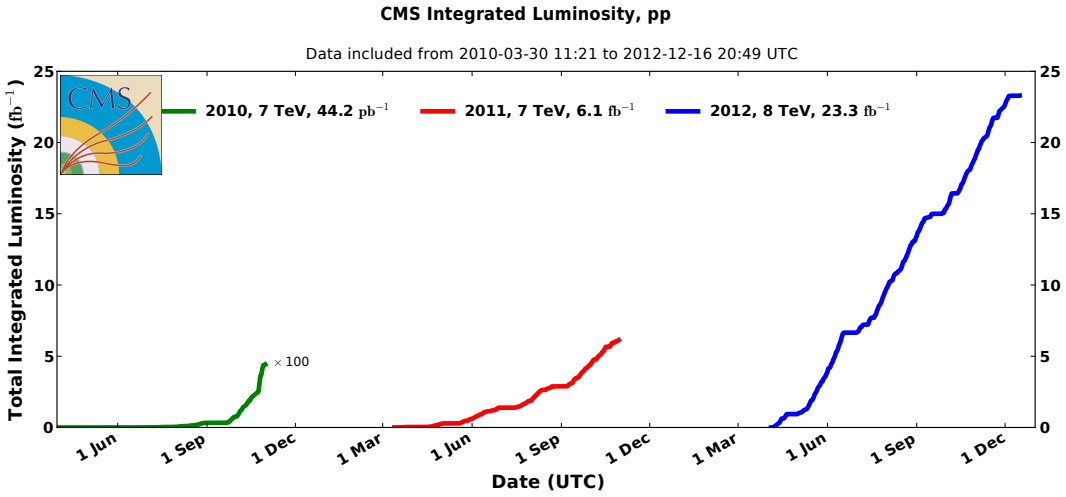

Figure 3.1: The integrated luminosity both delivered by the LHC to CMS and recorded by CMS in 2010-2012. The difference between delivered and recorded luminosities corresponds to a downtime less than 10% for the CMS detector.

The CERN accelerator complex includes a series of components which progressively accelerate the proton beams to higher energies. The LEP injection chain is used to accelerate the protons to an energy of 450 GeV before entering the main ring. The first stage uses the Linac2 to boost the protons to 50 MeV in a series of radio frequency (RF) cavities, next the Proton Synchrotron Booster

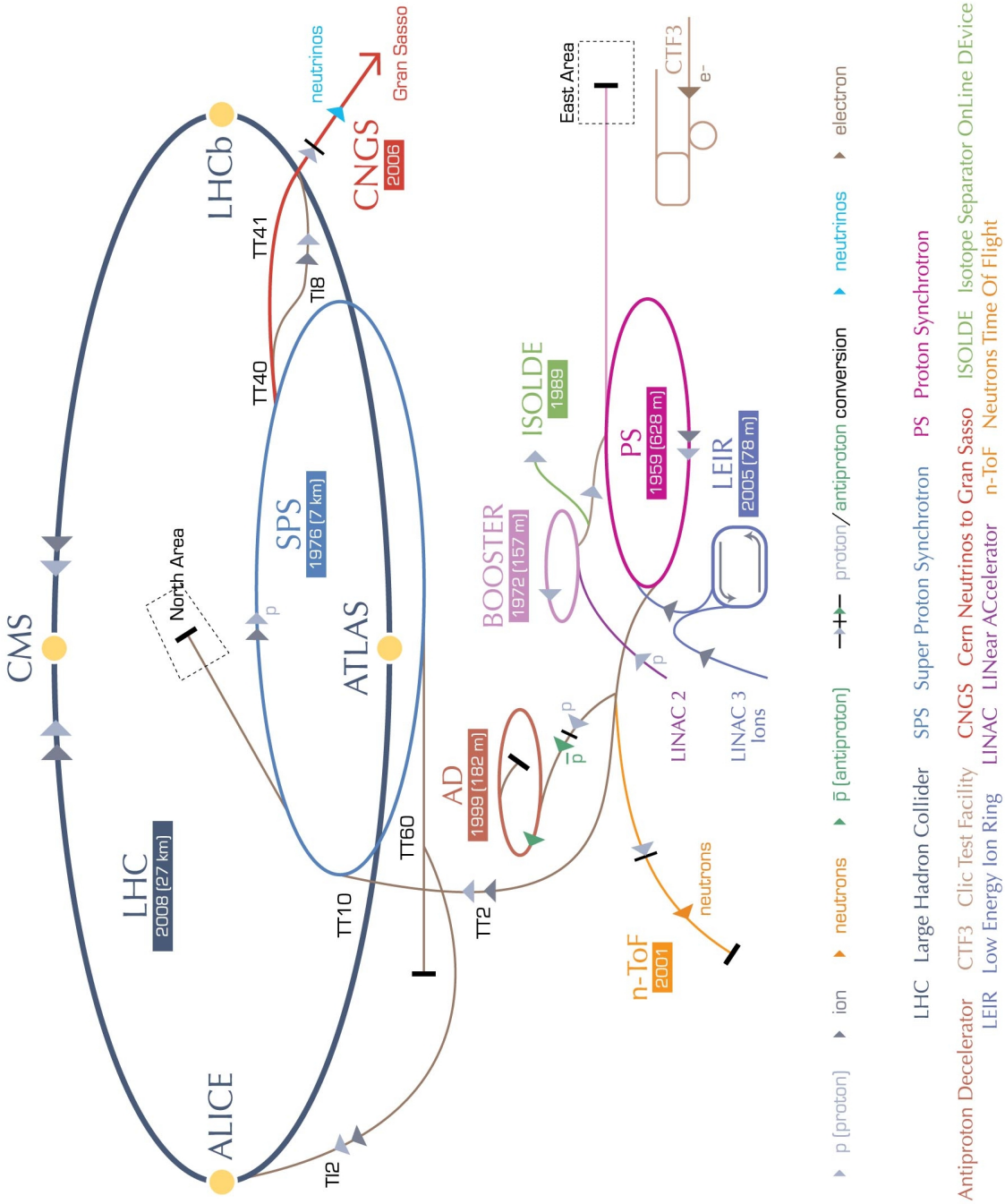

Figure 3.2: Overview of the CERN accelerator complex.

(PSB) accelerates to 1.4 GeV and then the Proton Synchrotron (PS) to 24 GeV. The Super Proton Synchrotron (SPS) accelerates protons up to a full injection energy of 450 GeV. Once they reach the LHC, the bunched charged particles are accelerated by 400 MHz RF cavities resulting in high energy bunches of protons with 25 ns gaps. In 2011 LHC running, every other RF bucket contains a proton bunch, resulting in a bunch spacing of 50 ns. A schematic of accelerator stages is shown in Figure 3.1.

The use of the existing LEP tunnel for the LHC accelerator created the design challenges for the LHC, specifically in terms of the size and power of magnets needed to direct the LHC proton beams. Since the same magnetic field can not be used to bend the counter circulating proton beams in the same direction the magnets have unique twin-bore design shown in Figure 3.1 producing oppositely-directed fields. To adequately bend the 7 TeV proton beam the dipole magnets with magnetic field of 8 T achieved by superconductors carrying the current of 11850A are used.

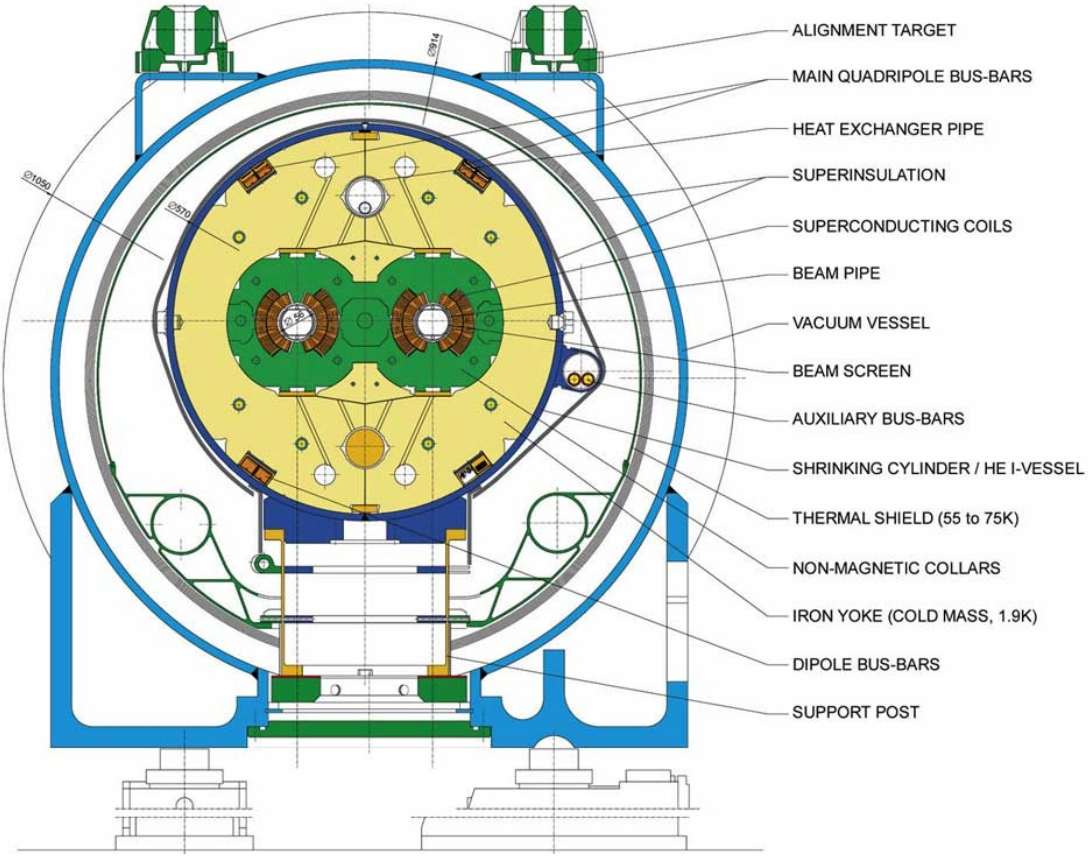

Figure 3.3: A schematic view of the construction of an LHC main dipole.

3.2 The Compact Muon Solenoid Experiment

The central feature of the Compact Muon Solenoid (CMS) apparatus is a superconducting solenoid of 6 m internal diameter, providing a magnetic field of 3.8 T. Within the superconducting solenoid volume are a silicon pixel and strip tracker, a lead tungstate crystal electromagnetic calorimeter (ECAL), and a brass/scintillator hadron calorimeter (HCAL). Muons are measured in gas-ionization detectors embedded in the steel return yoke outside the solenoid. Extensive forward calorimetry complements the coverage provided by the barrel and endcap detectors.

Layered design of CMS shown in Figure 3.4 with multiple calorimeter and tracking detectors arranged to complement one another provides a nuanced view of collision events. A short descriptions of the different subdetectors is given in the following subsections. A detailed description of CMS can be found in [18].

3.2.1 Coordinate system

The CMS detector has a cylindrical shape around the beam axis of 14.6m diameter and 21.6m length, and consists of the barrel part in the middle and two endcaps on the sides. A right handed Cartesian coordinate system is used within the CMS detector with the origin located at the assumed interaction point at the center of the detector. The x-axis points horizontally towards the center of the LHC ring, the y-axis points vertically outwards from the earth's center, and the z-axis is oriented horizontally along the anticlockwise beam direction.

In the transverse (x-y) plane, the azimuthal angle ϕ is measured from the x axis and the radial coordinate is denoted as $r = \sqrt{x^2 + y^2}$. The polar angle θ is measured from the z axis but more often the pseudorapidity η is used.

In inelastic collision of protons two partons (one from every proton) carrying a particular fraction of proton momentum interact. This interaction is referred to as the hard process. The parton momentum is longitudinal with negligible transverse component. Due to momentum conservation the total momentum of particles originating from the hard process is also longitudinal. The particle

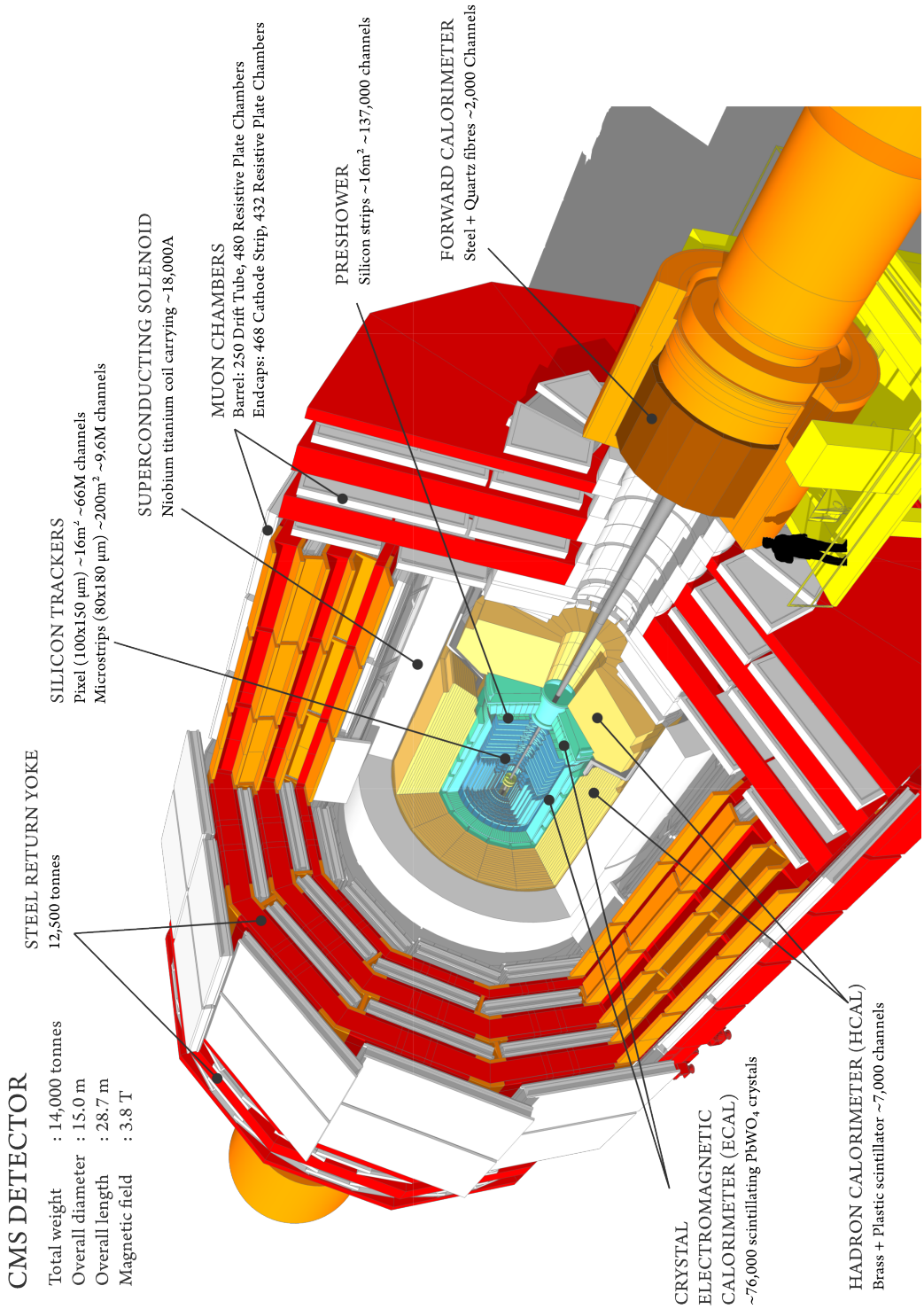

Figure 3.4: A perspective view of the CMS detector with the major subsystems indicated.

trajectories are therefore often described in the transverse plane. A particle escaping the detection creates an inbalance in the total transverse energy measurement, also called missing transverse energy.

3.2.2 Magnet

The choice of the magnetic field configuration was an important aspect driving the detector design and layout. One of the design requirements of CMS is unambiguous determination of the sign for muons up to momenta of about 1 TeV. This requires a momentum resolution of $\Delta p/p \approx 10\%$ at p = 1 TeV. Large bending power is needed to measure precisely the momentum of charged particles. Superconducting technology is used. A 13-m-long solenoid with 5.9 m inner diameter produces a longitudinal homogenous magnetic field of 3.8T over a volume of more than 300 m^2. The return field saturates the iron yoke, providing a consistent 2T field throughout the outer muon system, allowing large lever arm measurement of the transverse momentum for muons. The capabilities and geometry of the magnet have guided the design of each of the CMS subsystems.

3.2.3 Tracker

The closest subdetector to the interaction point is the tracker, which is entirely based on silicon semiconductor technology. A very fine granularity in the innermost part is essential to identify the different vertices in a bunch crossing. Vertices correspond to the interaction points of the proton collisions or the displaced decay of a short-lived particles.

The sensors are constructed as reversed-biased p-n diodes, which yield a detectable current when the bias voltage across the diode is lowered by the ionization depositions caused by passing charged particle.

The tracker can be divided into three regions containing detectors with different characteristics for regions with different particle fluxes.

Closest to the interaction point where the particle flux is the highest, $\approx 10^7$/s at r $\approx$ 10 cm, pixel detectors are placed. To achieve an optimal vertex position resolution, a design with an "almost" square pixel shape of 100×150 μm^2 along the (r,ϕ) and the z coordinates respectively is used. The position resolution is $\approx$ 10 μm in the r-ϕ plane and 20 μm along z. There are 3 layers of hybrid pixel detectors at radii of 4, 7, and 11 cm.

In the intermediate region (20 $\leq$ r $\leq$ 55 cm), the particle flux is low enough to enable the use of silicon microstrip detectors with a minimum cell size of 10 cm $\times$ 80 μm.

In the outermost region (55 cm $\leq$ r $\leq$ 110 cm) of the inner tracker, the particle flux has dropped sufficiently to allow use of larger-pitch silicon microstrips with a maximum cell size of 25 cm $\times$ 180 μm.

The layout of the complete CMS tracking detector is shown in Figure 3.5.

The total area of the pixel detector is $\approx 1m^2$, while the area of the silicon strip detectors is 200 m^2, providing coverage up to $\mid \eta \mid \leq$ 2.5.

The tracker transverse momentum resolution up to $\mid \eta \mid \leq$ 1.6 is:

$$\frac{\sigma_{P_T}}{P_T} = (15P_T \oplus 0.5)\%(TeV) \tag{3.2}$$

while the resolution at $\mid \eta \mid =$ 2.5 is equal:

$$\frac{\sigma_{P_T}}{P_T} = (60P_T \oplus 0.5)\%(TeV) \tag{3.3}$$

The first term corresponds to the measurement of curvature of particle track which is less precise for high-momentum tracks since they become more straight. The second term corresponds to interaction with the tracker material such as multiple scattering.

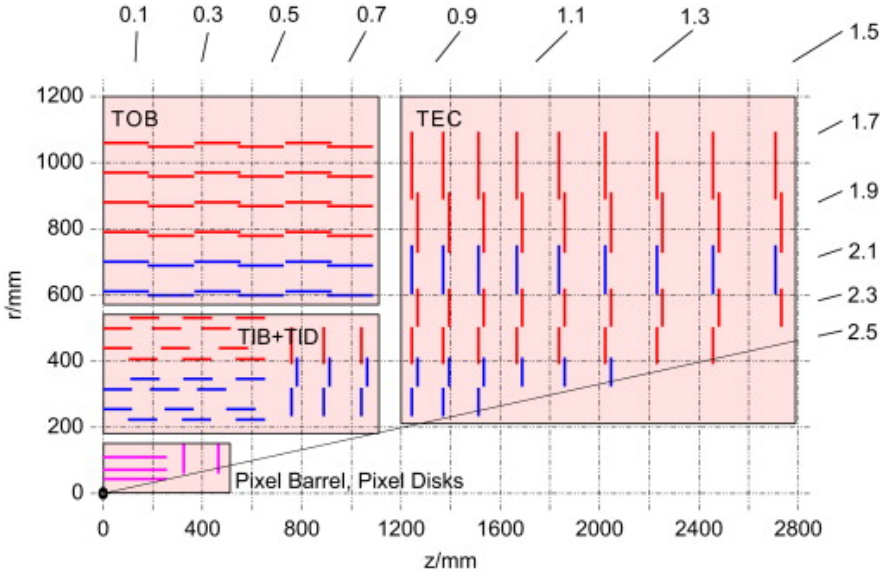

Figure 3.5: Schematic cross section through the CMS tracker.

3.2.4 Electromagnetic and hadron calorimeter

The Electromagnetic Calorimeter (ECAL) is designed to detect and precisely measure the energy of electrons and photons. Placing the ECAL inside the magnet, one avoids the significant degradation seen is previous hadron collider experiment due to interactions with the magnet material. This requires the ECAL to be compact, and therefore made with high transparent and dense interacting material. These conditions fulfill lead tungstate ($PbWO_4$). It has high density (8.28 g/cm^{-3}), short radiation length (0.89 cm) and small Moliere radius (2.2 cm). This enables the absorption of electron and photon showers with reasonably short crystals. Crystals of a length of 25.8 radiation lengths are used in the barrel and 24.7 radiation lengths in the endcaps. In 23 cm long crystals, all but the most energetic electrons and photons deposit all of their energy via bremsstralung and electromagnetic pair production. A good shower separation is ensured with a typical crystal cross section 2.2cm$\times$2.2cm. The readout electronics are collecting the scintillation light emitted in the electromagnetic shower.

The Electromagnetic Calorimeter (ECAL) is a hermetic, homogeneous calorimeter comprising 61200 lead tungstate (PbWO4) crystals in the central barrel part in the range $\mid \eta \mid \leq 1.4442$, closed

by 7324 crystals in each endcap in the range $1.566 \leq |\eta| \leq 3.0$. Figure 3.6 is a schematic showing various features of the CMS ECAL.

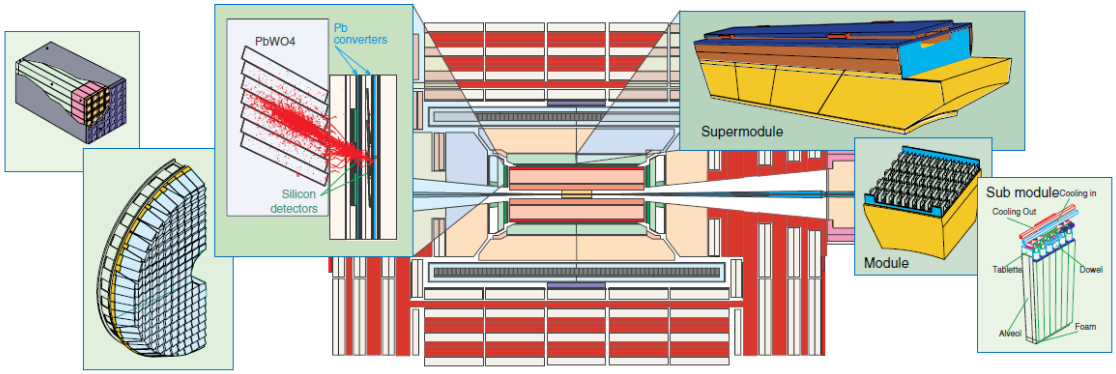

Figure 3.6: Features of the CMS ECAL.

The ECAL energy resolution is given by:

$$\left(\frac{\sigma_E}{E}\right)^2 = \left(\frac{2.8\%}{\sqrt{E/GeV}}\right)^2 + \left(\frac{0.12}{E/GeV}\right)^2 + (0.3\%)^2 \tag{3.4}$$

where the first term corresponds to statistical fluctuations and intrinsic shower fluctuations, the second term corresponds to electronic noise and pileup energy (energy deposition coming from additional soft interactions) and the final term corresponds to intrinsic detector non-uniformities and calibration uncertainties.

Radiation damage is manifested as a change in crystal transparency, resulting in non-uniform scintillation light transmittance as a function of time. This is monitored and corrected for using a laser calibration system that records the change in transparency.

The ECAL is surrounded by a hadron calorimeter (HCAL) which is designed to detect particles which primarily interact with atomic nuclei via the strong force. Strongly interacting particles typically start showering in the ECAL, so a full picture of a particle energy comes from combining information from both calorimeters. The HCAL consists of three sub-systems, shown in Figure 3.7.

The HCAL barrel (HB) provides coverage up to $|\eta| \leq 1.305$, the HCAL endcap (HE) in the range $1.305 \leq |\eta| \leq 3.0$ and the HCAL forward (HF) in the range $3.0 \leq |\eta| \leq 5.0$. The forward calorimeters ensure full geometric coverage and therefore play a large role in the the measurement of the transverse energy in the event. HB and HE are made up of interleaved layers of brass radiator and scintillating tiles while HF is made of steel plates embedded with quartz fibers to better withstand the high radiation doses in that region.

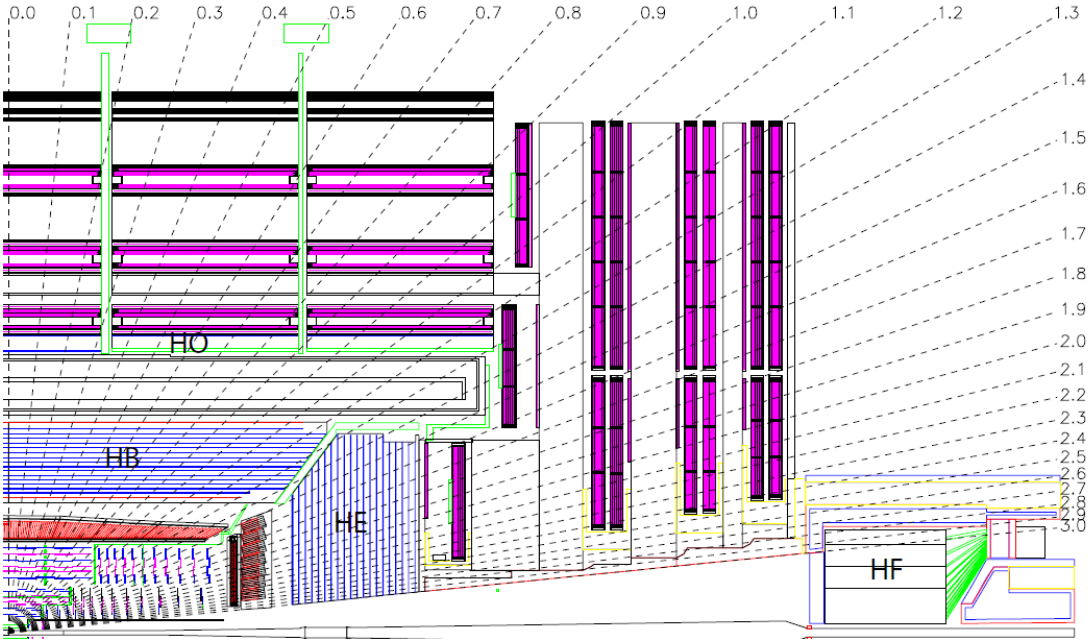

Figure 3.7: Features of the CMS HCAL.

In the case of the HB and HE, brass acts as a non-ferromagnetic absorber with 5.82 interaction lengths of material to encourage development of hadronic showers. The particles produced in nuclear interactions of hadronic particles with the brass pass through the scintillating material and produce light. The collected light is used as an estimate of the energy of the shower. In the case of HF, Cherenkov radiation from the particles in the evolving shower traversing quartz fibers is used as energy estimate.

The energy resolution for HB and HE can be expressed as:

$$\left(\frac{\sigma_E}{E}\right)^2 = \left(\frac{90\%}{\sqrt{E/GeV}}\right)^2 + (4.5\%)^2 \tag{3.5}$$

while for HF the resolution is:

$$\left(\frac{\sigma_E}{E}\right)^2 = \left(\frac{172\%}{\sqrt{E/GeV}}\right)^2 + (9.0\%)^2 \tag{3.6}$$

The first term in equations corresponds to statistical fluctuations and intrinsic shower fluctuations (considerably larger than that of the ECAL), and the constant term is due to uncertainties in the calibration.

3.2.5 Muon system

A good measurement of muons was a driving factor in the overall design of CMS. Muons produced in proton collisions in the center of CMS are measured in the inner tracker and in the muon chambers placed outside of magnet.

The muon system consist of three types of gaseous particle detectors optimized for different environments and goals – drift tubes (DTs) in the barrel ($|\eta| \leq 1.2$), cathode strip chambers (CSCs) in the endcaps ($|\eta| \leq 2.4$), and resistive plate chambers (RPCs) covering nearly the entire barrel and endcap regions ($|\eta| \leq 1.6$). The muon system is shown in Figure 3.8.

RPCs provide a fast response with good time resolution but with a coarser position resolution than the DTs or CSCs. RPCs can therefore identify unambiguously the correct bunch crossing.

The DT chambers consist of multiple drift tubes filled with a gas mixture ionized by the passage of charged particles. Each tube contains an anode wire held at high voltage and two cathode strips on either side. As the particles traverse the drift tube, they ionize the gas in the tube, and the ionized

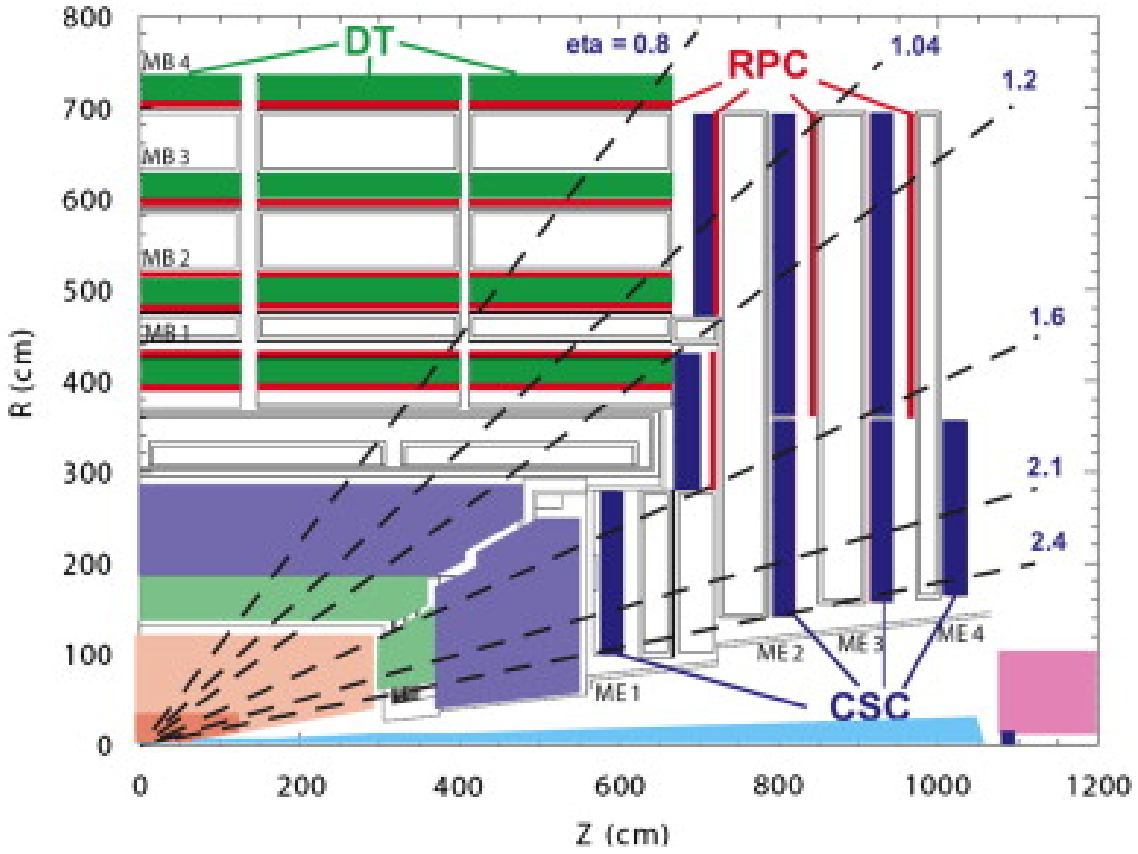

Figure 3.8: CMS muon system.

atoms are collected by the anode creating an electronic pulse. Each DT chamber consists of three superlayers, each composed in turn of four layers of rectangular drift cells staggered by half a cell. The two outer superlayers are oriented with the wires parallel to the beam to provide tracking in the r-ϕ plane in which the muon bends due to the magnetic field. The third superlayer, present only in the first three stations, measures the z coordinate. The spatial resolution of a DT chamber is 100 μm in the r-ϕ plane, and 150 μm in the z direction, the drift time is up to 386 ns and the timing resolution is 3.8 ns.

Each CSC is trapezoidal in shape and consists of 6 gas gaps, each gap having a plane of radial cathode strips and a plane of anode wires running almost perpendicularly to the strips. The gas ionization and subsequent electron avalanche caused by a charged particle traversing each plane of a chamber produces a charge on the anode wire and an image charge on a group of cathode strips.

The spatial resolution provided by each chamber from the strips is typically about 200 μm, while the angular resolution in ϕ is of order 10 mrad.

RPCs are located both in the barrel and in the endcaps Their spatial resolution is limited, but their time resolution is excellent ($\approx$ 1 ns) and smaller than the 25 ns LHC bunch spacing. Therefore RPC detectors are used to identify unambiguously the bunch crossing and to provide prompt trigger decision. An RPC consists of parallel electrode plates, yielding a constant and uniform electric field across a gap filled with ionizing gas. The RPCs are constructed of two highly resistive electrodes and a layer of readout strips immersed in a thin layer of inert gas. As charged particles pass the gas is ionized and releases electrons which then, due to the electric field in the RPC, ionize more atoms, releasing more electrons in an 'avalanche'. These avalanches of electrons are collected on a cathode pad and used to deduce the timing and position of the incident particle.

Measurement of the momentum of muons using only the muon system is essentially determined by the muon bending angle at the exit of the 4T coil, taking the interaction point as the origin of the muon. The resolution of this measurement is dominated by multiple scattering in the material before the first muon station up to P_T values of 200 GeV. For larger P_T the chamber spatial resolution starts to dominate. For low-momentum muons the momentum resolution is dominated by resolution in the silicon tracker. However, the muon trajectory beyond the return yoke extrapolates back to the beam-line due to the compensation of the bend before and after the coil when multiple scattering and energy loss can be neglected. This fact can be used to improve the muon momentum resolution at high momentum when combining the inner tracker and muon detector measurements. The muon momentum resolution is shown in Figure 3.9.

3.2.6 Reconstruction of objects

Reconstruction is the operation of constructing physics quantities from the raw detector signals collected in the experiment. The reconstruction process can be divided into 3 steps, corresponding to local reconstruction within an individual detector module, global reconstruction within a whole detector, and combination of these reconstructed objects to produce higher-level objects.

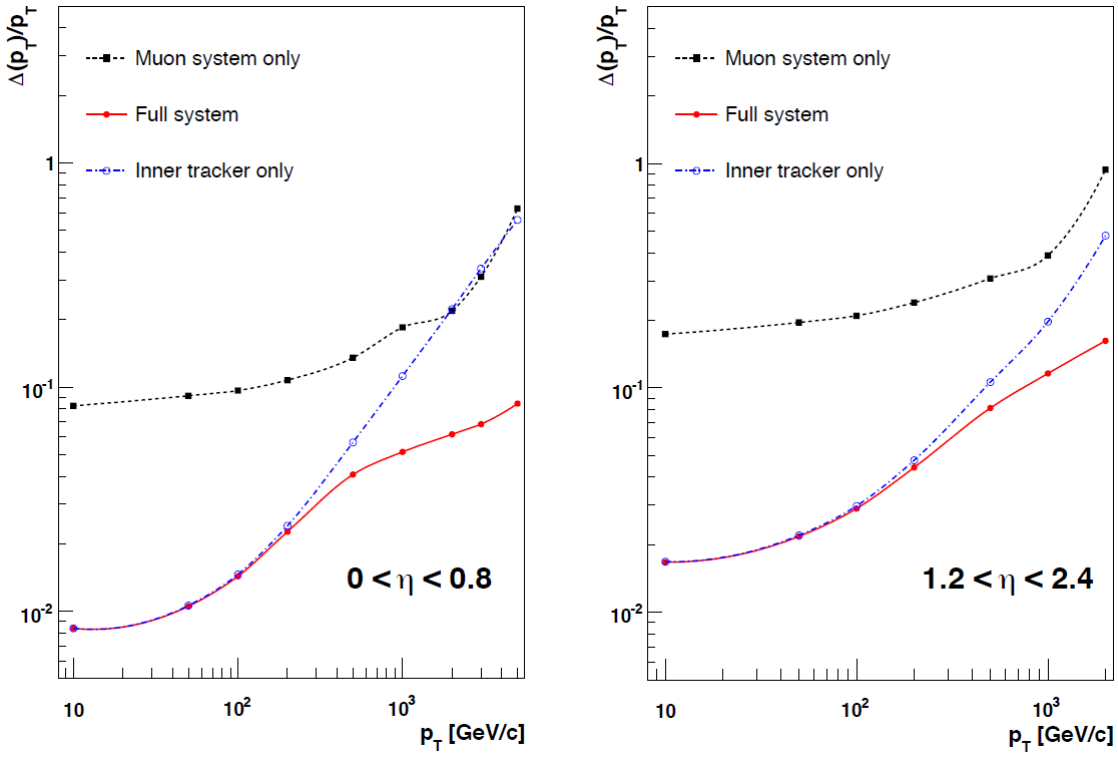

Figure 3.9: Muon momentum resolution.

Different particles provide different signatures in CMS detector sub-systems as shown in Figure 3.10. A muon will be measured in the tracker and in moun system loosing very little energy in the calorimeters. An electron (and positron) will leave a track in the tracker and loose all its energy in ECAL, while a photon will be measured only in ECAL. Accordingly, different sub-systems participate in a reconstruction process.

Reconstruction of muons

The muons (and antimuons) are detected in the range $|\eta| < 2.4$ by spatially matching the tracks from the inner tracker and the outer muon system resulting in a P_T resolution of 1-5% for muons with P_T up to 1 TeV. The reconstruction algorithm is described in detail in [19].

Muon objects are the association of two tracks, one in the silicon tracker (or tracker track), and a second one in the muon systems (or standalone track). Starting from standalone track as input a

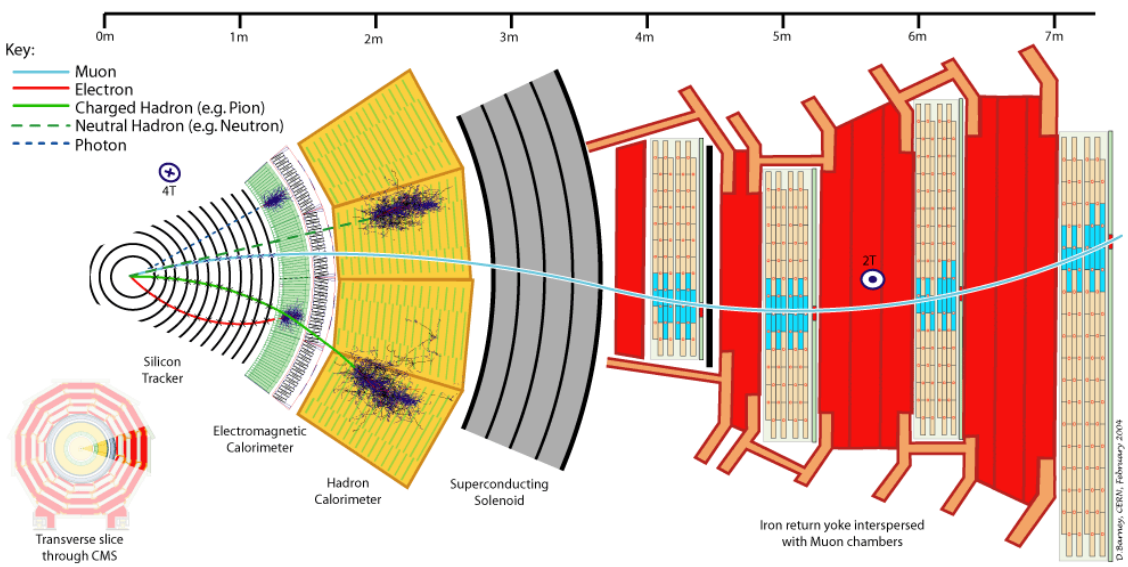

Figure 3.10: The CMS detector transverse section with simple particle topologies indicated.

matching tracker track is found and a global-muon track is fitted combining hits from the tracker track and standalone track. Compatibility in terms of momentum, position, and direction are considered in matching stand-alone muons to tracker tracks.

The CMS solenoid subjects the tracker to a 3.8T longitudinal magnetic field, and the muon chambers to a return field in the opposite direction, of value $\approx$ 2T. Hence the trajectory of a muon is curved in opposite orientations in the tracker and in the muon chambers.

The degree of curvature gives the muon transverse momentum, while the orientation of the curvature determines its charge. For a global muon, these parameters are mainly based on the tracker information, because of the very precise inner tracking system. However the combination of these two systems becomes important for muons with high momentum where the reduced bending of the muon tracks limits the resolution of the inner tracking measurement.

Reconstruction of photons

Photon reconstruction begins with energy deposited in the ECAL. Since ECAL crystals in CMS have a Moliere radius of 2.2 cm (the same as the physical width of their front face), a photon with

1 GeV of energy deposits 95% of its energy into an array of 5×5 crystals. Material between the interaction region and the ECAL cause roughly half of direct photons to convert into e^+e^- pairs, resulting in a deposit of energy more spread along ϕ (due to the presence of the magnetic field from the solenoid). The ECAL crystal arrays have different geometry in the barrel and endcap, and in addition, the magnetic field is different, so energy deposits is grouped together in Super Cluster (SC) by different algorithms: a "Hybrid Clustering Algorithm" in the barrel, and a "Multi5×5" algorithm in the endcap [20].

For both algorithms the center of the photon shower is determined from a log-weighted energy sum:

$$x = \frac{\sum x_i W_i}{\sum W_i}, \text{ where } W_i = max\left(0, 4.7 + log\frac{E_i}{\sum E_j}\right) \tag{3.7}$$

where E_i is the energy of the i^{th} crystal in the SC.

The direction of the momentum of a photon candidate is determined by connecting a line from the primary vertex to the position of the SC. Identification of photons is enhanced by the use of tracking information as photons that do not convert leave no signal in the silicon detectors. Since there is no alternate measurement of the particle's momentum to compare to it is significantly harder to identify real photons since there is a large background both from jets and from electrons.

Reconstruction of missing transverse energy (MET)

Neutrinos are not detected directly, but give rise to experimentally observed imbalance of transverse energy, MET. This quantity is computed using a Particle Flow technique [21], an algorithm designed to reconstruct a complete list of distinct particles using all the subcomponents of the CMS detector. The MET for each event is then determined as the negative vector sum of the transverse momenta of all reconstructed particles in each event.

Trigger at CMS (on-line event pre-selection)

Data are selected online using a two-level trigger system. The first level (L1), consisting of custom made hardware processors, selects events in less than 1 μs, while the high-level trigger (HLT) processor farm further decreases the event rate from around 100 kHz to about 300 Hz before data storage. At the HLT events are accepted if they match at least one of hundreds of differet "interesting" signatures in the detector. In this work the one requiring high P_T muon in event is used.

3.2.7 Data and simulation

To predict the results of colliding protons involves modeling of subatomic makeup of a proton, the calculation of scattering amplitudes, the decay of unstable particles, and the hadronization of quarks and gluons into jets. Next the response of the detector to these final state particles must be modeled. Knowledge of detector materials and positions of these materials is necessary for accurate modeling of the detector response.

“Monte Carlo” techniques [22] are generally used. Here a random number generator is interfaced with the equations governing a certain process in order to produce a large number of simulated collision events. The simulation of proton-proton collisions happens in several steps, each being specialized to emulate a particular aspect of particle collisions. The first stage is a matrix element calculation which describes the differential cross section for a given hard scattering process. Next stage takes the colored partons (quarks) and gluons produced in the hard scattering interaction along with any radiated gluons and describes how they hadronize into colorless composite particles in a parton showering process. Following stage describes the underlying event consisting of soft interactions of the spectator partons which did not directly participate in the hard scattering. These programs rely on parameterizations tuned first by input from previous colliders extrapolated to LHC energies and later retuned based on data from initial LHC runs [23]. A detailed description of the CMS detector and magnetic field is used as input to the GEANT4 package [24, 25], a software toolkit for simulating the passage of particles through CMS detector.

Chapter 4

Measurement of $W\gamma$ cross section

In this work the cross section for the process $pp \to W\gamma \to \mu\nu\gamma$ at a center of mass energy of 7 TeV is measured. As the $W\gamma$ cross section diverges at LO for soft photons or those that are spatially close to the charged lepton, the measurement is restricted to the following kinematic range:

- The transverse photon energy must be larger than 15 GeV.
- The muon and the photon must be spatially separated by $\Delta R(\mu,\gamma) \equiv \sqrt{(\Delta\phi(\mu,\gamma))^2 + (\Delta\eta(\mu,\gamma))^2} > 0.7$.

This measurement uses data collected during 2011 by the CMS detector corresponding to an integrated luminosity of 5 fb^{-1}.

The $W\gamma \to \mu\nu\gamma$ final state is characterized by a prompt, energetic, and isolated muon, significant missing energy due to a neutrino, and a prompt isolated photon. Besides $W\gamma$, there are several other processes with identical final state particles or with different outgoing particles giving similar signature in the detector. In order to reduce these backgrounds, the selection criteria described in Section 4.2 are applied. The backgrounds and the methods used to derive their contribution are described in Section 4.3.

The cross section is extracted using the expression:

$$\sigma = \frac{N_{\text{sig}}}{A \cdot \varepsilon \cdot \mathscr{L}} \tag{4.1}$$

where N_{sig} is the number of observed signal events, A is the geometric and kinematic acceptance, ε is the selection efficiency for events in the acceptance, and $\mathscr{L}$ is the integrated luminosity.

The product $A \cdot \varepsilon_{gen}$ is derived from the simulation. To account for differences in efficiency between data and simulation a correction factor, $\rho_{\text{eff}} = \varepsilon/\varepsilon_{\text{gen}}$, is used. The correction factor is derived by measuring the efficiency in the same way on data and simulation as described in Section 4.2.7. The product $A \cdot \varepsilon$ is replaced by the product $\mathscr{F} \cdot \rho_{\text{eff}}$, where $\mathscr{F} \equiv A \cdot \varepsilon_{\text{gen}}$:

$$\sigma = \frac{N_{\text{sig}}}{A \cdot \sum_i \varepsilon^i_{gen} \cdot \sum_i \frac{\varepsilon^i}{\varepsilon^i_{gen}} \cdot \mathscr{L}} = \frac{N_{\text{sig}}}{\mathscr{F} \cdot \rho_{eff} \cdot \mathscr{L}}. \tag{4.2}$$

Since the efficiency depends on a particle kinematic the efficiency is derived as the sum over all events. $\mathscr{F}$ is defined as $\frac{N_{\text{accept}}}{N_{\text{gen,kin}}}$, where N_{accept} is the number of events passing all selection cuts, and $N_{\text{gen,kin}}$ is the number of generated events with $E_T^{\gamma} > 15$ GeV, $\Delta R(\mu, \gamma) > 0.7$.

Sources of systematic uncertainties are described in Section 4.4.

4.1 Data samples

The used data set corresponds to luminosity of 5 fb^{-1} collected with the CMS detector at center of mass energy of 7 TeV during 2011. The LHC beam conditions were rather different in two runs taken during 2011, resulting in low- and high-pile-up (PU) periods. The average number of PU interactions for the low-PU data set is 4.9 interactions per collision, while the high-PU set has an average of 7.8 interactions. The former data set corresponds to about 2.2 fb^{-1} of integrated luminosity and is referred to as 2011A in the text, the latter corresponds to 2.7 fb^{-1} and is referred to as 2011B. The combined data set are referred to as 2011A+2011B. The measurements are performed

using the combined 2011A+2011B data set. To check the compatibility of results measurements using 2011A and 2011B separately are also performed. The data set contains only certified CMS data, which are recorded while all CMS subdetectors were operating properly.

4.2 Trigger and event selection

The selection is chosen such to minimize the background contribution while efficiently selecting the signal. However in some cases, it is not possible to apply the most ideal selection criteria due to trigger pre-selection applied online during data taking.

4.2.1 Trigger selection

The $W\gamma \to \mu\nu\gamma$ events are selected by using the unprescaled muon trigger with the lowest available P_T threshold. An isolated single muon trigger with a threshold of 30 GeV is used during 2011A and 2011B. The restriction of the triggering region to $|\eta| < 2.1$ is used to reduce the trigger rate from misidentified muons in the forward regions of the detector.

4.2.2 Muon selection

The muon identification scheme defined in [19] is used, with a minor alteration of cuts on the distance of closest approach of the muon track to the primary vertex. Muon candidates are required to pass the GlobalMuon and TrackerMuon reconstruction algorithm, to have hits in the pixel system, not more than a few missing hits in the tracking system, a good χ^2 of the overall fit of the tracks in the tracker and muon sub-detectors and more than one chamber with matched muon segments. To ensure that the muon is produced from the primary interaction vertex in the event, the muon's charged track is required to have a distance of closest approach to the z-axis 0.02 cm and to have z-coordinate within 0.1 cm from the primary vertex [26]. Cosmic ray muon contamination is sig-

Table 4.1: Muon identification and isolation requirements.

Description	criterion
Kinematical	$p_{\mathrm{T}} > 35$ GeV and $\lvert\eta\rvert < 2.1$
Number of pixel hits	> 0
Number of tracker hits	> 10
χ^2/n.d.f	< 10
Number of muon hits	> 0
Number of chambers with matched segments	> 1
Vertex d_0	< 0.02 cm
Vertex d_z	< 0.1 cm
Combined relative isolation ; $\Delta R = 0.3$	< 0.1

nificantly reduced by these cuts. Further cross-checks of timing and cosmic tagger information [26] indicate negligible contribution from cosmic background.

To suppress energetic pions misidentified as muons, as well as muons produced in jets, a relative isolation requirement is used. A sum of all energies and track momenta, not associated with the muon candidate, in a cone of $\Delta R = 0.3$ around the muon candidate normalized to the muon p_{T} is required to be below 10%.

Muons are required to have transverse momentum larger than 35 GeV and to be within $\lvert\eta\rvert < 2.1$.

The summary of muon kinematical requirements as well as identification criteria is given in Table 4.1.

4.2.3 Photon selection

Photon candidates are reconstructed as Super Clusters (SC) with $E_{\mathrm{T}}^{\gamma} > 15$ GeV in the fiducial volume of the ECAL detector. The efficiency of reconstructing a SC from a photon electromagnetic deposit in the ECAL is measured in simulation and is found to be very close to 100%.

A shower shape variable measures the width of the photon SC in the η direction, denoted as $\sigma_{i\eta i\eta}$ and defined as:

$$\sigma^2_{i\eta i\eta} = \frac{\sum(\eta_i - \bar{\eta})^2 w_i}{\sum w_i},\ \bar{\eta} = \frac{\sum \eta_i w_i}{\sum w_i},\ w_i = \max(0, 4.7 + \log(E_i/E_{5\times5})), \tag{4.3}$$

where the sum runs over the 5×5 crystal matrix around the most energetic crystal in the SC.

The rate of jets reconstructed as photons is greatly reduced by requiring stringent photon identification criteria, including isolation and shower shape requirements:

- The ratio of HCAL to ECAL energies in a cone size of $\Delta R = 0.15$ around the seed crystal must be below 0.05.
- $\sigma_{i\eta i\eta}$ must be below 0.011 in the barrel and below 0.030 in the endcap.

To reduce the background from misidentified electrons, photon candidate must have no associated hit in the pixel detector (pixel seed veto).

High pile-up conditions during the 2011 LHC run require the photon isolation criteria to be robust against PU modeling in simulation. The sum of all the tracks transverse momenta found in the annulus of $0.05 < \Delta R < 0.4$, I_{TRK}, around the photon candidate is required not to exceed 2 GeV + $0.001 \cdot E_T^\gamma + A_{eff} \cdot \rho$, where ρ is the median background energy density per unit area, computed using the FASTJET package [27], and A_{eff} is an effective area correction, which ensures that the isolation requirement does not exhibit a pile-up dependence. The photon candidate is also required to be isolated in the ECAL by summing the transverse energy deposited in the ECAL in an annulus $0.06 < \Delta R < 0.40$, excluding a rectangular strip of $\Delta\eta \times \Delta\phi = 0.04 \times 0.40$ to reduce the effect of counting the fragments of the converted photon shower. The ECAL isolation, I_{ECAL}, is required to be less than 4.2 GeV $+ 0.006 \cdot E_T^\gamma + A_{eff} \cdot \rho$. Finally the HCAL isolation I_{HCAL}, has to be below 2.2 GeV $+ 0.0025 \cdot E_T^\gamma + A_{eff} \cdot \rho$. The values of A_{eff} are tabulated for all three isolation criteria separately for barrel and endcap in Table 4.2.

The summary of photon identification criteria is given in Table 4.3.

Table 4.2: A_{eff} values used for PU correction for photon selected in barrel and endcap.

Isolation	barrel	endcap
Tracker (I_{TRK})	0.0167	0.032
ECAL (I_{ECAL})	0.183	0.090
HCAL (I_{HCAL})	0.062	0.180

Table 4.3: Photon identification and isolation requirements.

Description	criterion
Kinematical	$p_T > 15$ GeV
	$\|\eta\| < 1.4442$ for barrel ($1.566 < \|\eta\| < 2.5$ for endcap)
HCAL/ECAL energy ; $\Delta R < 0.15$	< 0.05
$\sigma_{i\eta i\eta}$	$< 0.011(0.03)$
Associated track	Pixel seed veto
I_{TRK} ; $\Delta R < 0.4$	$< 2.0 + 0.001 \cdot E_T + 0.0167(0.032) \cdot \rho$
I_{ECAL} ; $\Delta R < 0.4$	$< 4.2 + 0.006 \cdot E_T + 0.183(0.090) \cdot \rho$
I_{HCAL} ; $\Delta R < 0.4$	$< 2.2 + 0.0025 \cdot E_T + 0.062(0.180) \cdot \rho$

4.2.4 Photon energy scale and resolution

The known width and peak position of the Z boson can be exploited to measure the photon energy resolution and to determine the absolute photon energy scale using the data itself using the $Z \to \mu\mu\gamma$ decay. This process is the only source of pure energetic photons in the hadron collider environment. Requiring the $\mu\mu\gamma$ invariant mass to be within 30 GeV of the Z boson pole mass reduces the Z+jets background to a negligible level.

The photon energy scale s is defined as the mode of the distribution of the photon energy response $x = E^{\gamma}/E^{\gamma}_{\text{true}} - 1$, where E^{γ} and E^{γ}_{true} are the reconstructed and true photon energies, respectively. The photon energy resolution r is defined as half of the shortest interval containing 68.3% of the photon energy response distribution.

The photon energy scale and resolution are measured in the simulation and in data. In simulation the photon energy is corrected to match the resolution in data and to have the perfect energy scale, i.e. s=0, while in data only the energy scale is corrected. These corrections are performed by shifting the measured value of photon energy in every event.

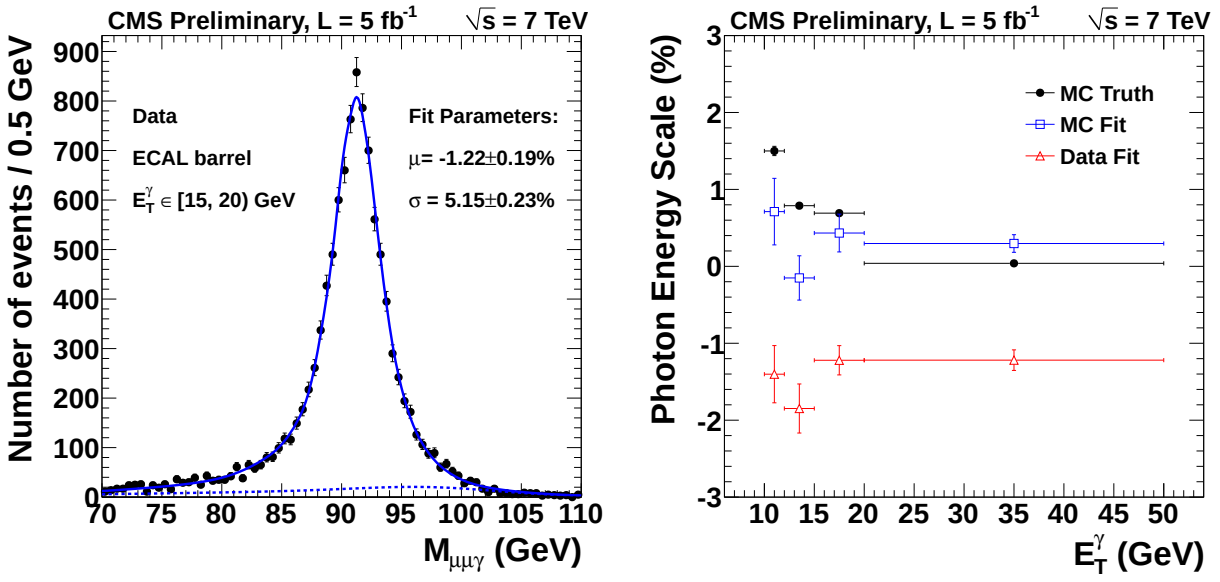

Figure 4.1: Left: The invariant mass of the $\mu\mu\gamma$ system for $Z \rightarrow \mu\mu\gamma$ data events fit to a model. The photon is required to be in the barrel and have transverse energy between 15 and 20 GeV. The photon energy scale and resolution and the fraction of signal events are floated in the fit. Right: The photon energy scale as a function of the photon transverse energy for the simulation (simulation truth) and for a fit to the simulation (simulation fit) and to the data (data fit).

To estimate the scale and resolution in both data and simulation the model as the function of the scale and resolution in sensitive observable, photon energy response for the simulation and Z mass peak for the data, is build. This model is used in the fit to extract the scale and resolution.

To estimate the scale and resolution in the simulation, the energy responses from simulated $Z \rightarrow \mu\mu\gamma$ events were used. The resolution and scale were varied in the simulation to build the corresponding model. The observed distribution was smoothed using a kernel density estimator [28] to define the input photon energy response line shape $f_0(x)$ with scale s_0 and resolution r_0. The estimates of the scale and resolution and their uncertainties are obtained from fitting the modeled photon energy response to the analogous photon energy spectrum from the simulated event sample.

For data E_{true} is not known. The invariant mass spectrum of $\mu\mu\gamma$ is used therefore to estimate the scale and resolution. The model of the invariant mass density is derived using the simulation in the similar way as described above for the energy response. The energy scale and resolution are derived with an unbinned maximum likelihood fit of the model on the data.

Figure 4.1 shows an example fit to the $\mu\mu\gamma$ mass in data and a comparison of the extracted photon energy scale in data and simulation with the true energy scale in simulation as a function of photon transverse energy.

Table 4.4: A summary of the derived photon energy scale estimates.

E_{T}^{γ} bin	Simulation true %	Data fit %
Barrel / Endcap		
$10 \leq E_{\mathrm{T}}^{\gamma} \leq 12$	1.35 / 2.94	-1.40 / -1.84
$12 \leq E_{\mathrm{T}}^{\gamma} \leq 15$	0.76 / 0.75	-1.85 / -0.87
$15 \leq E_{\mathrm{T}}^{\gamma} \leq 20$	0.65 / 1.58	-1.22 / -1.68
$20 \leq E_{\mathrm{T}}^{\gamma} \leq 50$	0.08 / 0.15	-1.22 / -0.15

4.2.5 Neutrino selection

To identify W boson candidates the transverse mass is used, M_T^{W}, defined as:

$$M_T^{\mathrm{W}} = \sqrt{2 \times p_{\mathrm{T}}(\mu) \times \mathrm{MET} \times (1 - \cos\Delta\phi(\mu, \mathrm{MET}))}. \tag{4.4}$$

The M_T^{W} is computed using the transverse momentum and the azimuthal angle of a muon and a MET.

4.2.6 Wγ event selection

Events are selected by requiring at least one muon with $p_{\mathrm{T}} > 35$ GeV that satisfies selection criteria described in Section 4.2.2. Events that have more than one muon candidate are rejected if the next-to-leading muon has $p_{\mathrm{T}} > 10$ GeV and $|\eta| < 2.4$. This reduces the Drell-Yan background. Selected events are required to have $M_T^W > 70$, due to the M_T^W requirement used at trigger level for the electron channel. The consistency between electron and muon channel was required. A photon candidate with $E_{\mathrm{T}} > 15$ GeV within the ECAL fiducial region needs further to be present. The

photon candidate is required to pass the photon selection described in Section 4.2.3. If more then one photon is passing the selection the leading photon, photon with the highest E_{T}^{γ} , is chosen.

5014 events are selected in the data with 2.3 fb^{-1} of integrated luminosity (2011A), and 5795 events are selected in data with 2.7 fb^{-1} of integrated luminosity (2011B). Expected yields for the signal and background processes from simulation are given in Table 4.5.

Table 4.5: Data and simulation yields in $W\gamma \to \mu\nu\gamma$ channel for 2011A (2.3 fb^{-1}), 2011B (2.7 fb^{-1}) and 2011A+2011B combined (5.0 fb^{-1}).

	cross section(pb)	Events (2011A)	Events (2011B)	Events (2011A+2011B)
$W\gamma \to \mu\nu\gamma$	137.3	2097.4 ± 33.3	2252.5 ± 34.0	4341.7 ± 55.9
$W\gamma \to \tau\nu\gamma$	21.41	11.9 ± 1.9	18.0 ± 2.4	28.8 ± 3.5
W+jets	31314	1701.4 ± 54.0	2261.3 ± 62.2	3945.9 ± 95.9
Z+jets	3048	59.4 ± 4.9	78.4 ± 5.5	138.2 ± 8.6
$Z+\gamma \to ll\gamma$	41.37	154.7 ± 10.5	195.5 ± 11.6	349.2 ± 18.3
$t\bar{t}$+jets	157.5	54.8 ± 3.4	59.0 ± 3.4	114.2 ± 5.6
$t\bar{t}\gamma$	0.444	17.2 ± 0.6	19.4 ± 0.6	36.7 ± 1.0
Incl. μ QCD	84679.3	0.0 ± 0.0	0.0 ± 0.0	0.0 ± 0.0
$\gamma + jets$	by $\hat{P_T}$	0.0 ± 0.0	0.0 ± 0.0	0.0 ± 0.0
WW	5.7	14.8 ± 0.6	15.7 ± 0.6	30.5 ± 1.0
WZ	0.6	0.2 ± 0.0	0.2 ± 0.0	0.4 ± 0.0
ZZ	0.06	0.0 ± 0.0	0.0 ± 0.0	0.0 ± 0.0
simulation (Total)		4111.9 ± 64.6	4900.0 ± 72.2	8985.6 ± 113.0
data		5014	5795	10809

4.2.7 Selection efficiency and acceptance

The efficiency and acceptance used to derive the $W\gamma$ cross section are not derived separatelly but as a product, $\mathscr{F} = A \cdot \varepsilon_{gen}$, using the $W\gamma$ simulation. The efficiency represents the probability that a genuine $W\gamma$ event with outgoing particles within detector acceptance will pass the full selection while the acceptance represents the probability that a genuine $W\gamma$ event will not be reconstructed in the detector due to the limited detector acceptance. In order not to rely on the simulation for the efficiency, the efficiency is determined for both data and simulation and an efficiency correction factor $\rho_{eff} = \sum_i \frac{\varepsilon^i}{\varepsilon^i_{gen}} = \sum_i \frac{\varepsilon^i_{data}}{\varepsilon^i_{gen}}$ is applied to $\mathscr{F}$.

'Tag-and-probe' method for efficiency determination

The 'tag-and-probe' method [19] is often used in CMS analysis to derive the efficiency of lepton selection criteria. To ensure that the efficiency of genuine leptons is measured, the Z resonance was used as a source of pure, energetic leptons. The events containing two opposite charge leptons whose invariant mass is close to the Z resonance are selected. One lepton, the 'tag' lepton, is required to pass stringent lepton identification requirements. A second lepton, the 'probe' lepton, is required to pass loose identification requirements and is used to determine the efficiency of some studied selection criteria. The 'probe' lepton selection is such that it does not bias the efficiency of the selection criteria that is being measured.

Some events with reconstructed di-lepton mass close to Z resonance are not events where a Z boson is produced but are a background. The amount of background is determined by performing a fit on the di-lepton mass spectrum using signal and background model shapes. The fit is performed on selected events with 'tag' and 'probe' leptons and results in a number of signal events, $N_{\text{signal}}^{\text{loose}}$, and a number of background events, $N_{\text{bkg}}^{\text{loose}}$. The selection criteria that is being studied is then applied on the 'probe' lepton and the fit is performed again on selected events resulting in a number of signal events, $N_{\text{signal}}^{\text{tight}}$, and a number of background events, $N_{\text{bkg}}^{\text{tight}}$. The efficiency of the selection criteria on lepton is:

$$\varepsilon_{\text{selection criteria}} = \frac{N_{\text{signal}}^{\text{tight}}}{N_{\text{signal}}^{\text{loose}} + N_{\text{signal}}^{\text{tight}}}. \tag{4.5}$$

The efficiency of all muon selection criteria are derived applying 'tag-and-probe' method on $Z \rightarrow \mu\mu$ events. For photons, $Z \rightarrow ee$ events are used, where electrons are treated as photons.

Efficiency of muon selection

The efficiency of muon selection requirements is measured using the 'tag-and-probe' technique.

The signal shape used in 'tag-and-probe' invariant mass fit is described by a Breit-Wigner distribution convoluted with a Crystal Ball function where its width is fixed to the width of the Z boson as determined by the PDG global average. The Breit-Wigner function is numerically convoluted with the Crystal Ball function to account for detector resolution and final state radiation effects in the measured distribution. The background is described by a Landau function.

The signal model is a Breit–Wigner convoluted with a Crystal Ball function in order to properly describe resolution effects.

The overall single muon identification efficiency is factorized as a product of efficiencies of several consecutively applied requirements:

$$\varepsilon_{tot} = \varepsilon_{TRK} \cdot \varepsilon_{SA} \cdot \varepsilon_{ID} \cdot \varepsilon_{ISO} \cdot \varepsilon_{trigger}, \tag{4.6}$$

where individual efficiencies are defined below:

- ε_{TRK}: the efficiency of reconstructing a track in the Tracker with the required number of pixel and tracker hits,
- ε_{SA}: the efficiency of reconstructing a track in the muon system, *i.e.*, a stand-alone (SA) muon with at least two muon stations and one matched chamber hit,
- ε_{ID}: the efficiency of passing the GlobalMuon and TrackerMuon algorithms with the required cuts on d_0, d_z and χ^2/n.d.f,
- ε_{ISO}: the efficiency of passing the required isolation,
- $\varepsilon_{trigger}$: the efficiency of satisfying the requirements of the muon trigger.

As the requirements are applied sequentially, the efficiency for both data and simulation are estimated with respect to the previously applied criteria. ε_{TRK} is approximated by the efficiency of reconstructing a track given a stand-alone muon.

The 'tag' is defined as a muon that satisfies all muon selection criteria and is matched to a object triggering an isolated single muon trigger with a p_{T} threshold of 24 GeV. The 'probe' is defined to

estimate each of the individual efficiencies defined by Eq. 4.6 with definitions and passing criteria summarized in Table 4.6. All 'probes' (P) together with the 'tag' (T) are required to have an invariant mass 50 GeV$< M_{TP} <$ 150 GeV and opposite charge.

Table 4.6: Definition of selected probes and the passing criterion.

ε	Probe definition	Passing criteria
TRK	SA muon	Track in Tracker
SA	Track in Tracker	SA muon
ID	Track in Tracker and SA muon	Global/Tracker muon
ISO	Global/Tracker muon	Isolated Global/Tracker muon
Trigger	Isolated Global/Tracker muon	Isolated Global/Tracker muon matched to trigger

The results for the overall muon identification efficiency of the selected probes are given in Table 4.7 for both data and simulation.

The same method is used to get results for the efficiencies as a function of p_{T} and η of the probe and as a function of the number of primary vertices in the event. The latter gives the direct estimate of the pile-up dependence. The results are shown in Figs. 4.2 - 4.11.

The difference between efficiency derived using 'tag-and-probe' method on the simulation and simulation truth counting efficiency of 1.5% is assigned as systematic uncertainty.

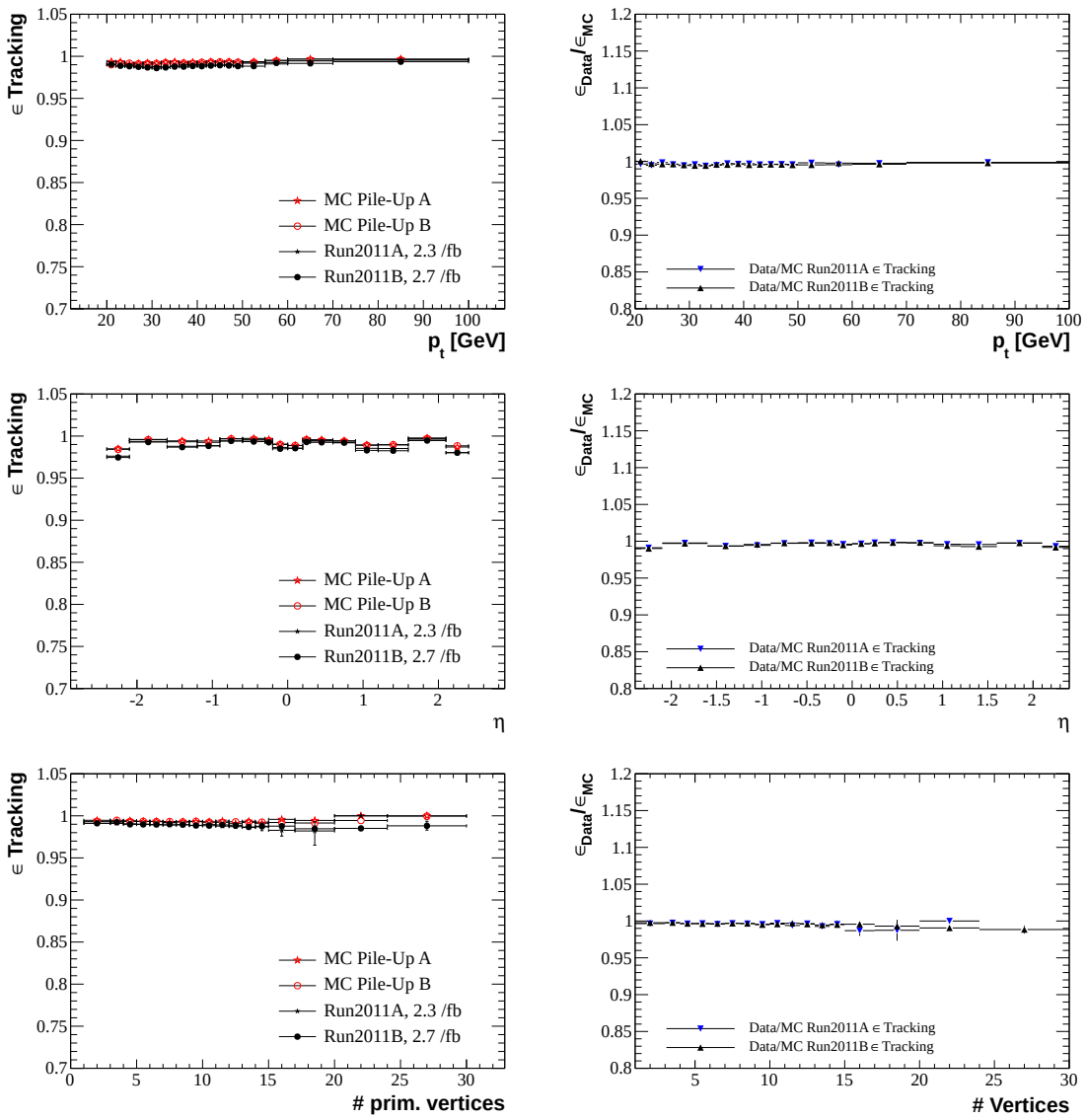

Figure 4.2: Muon tracking efficiency depending on P_{T}^{μ}, η^{μ}, and number of primary vertices together with data-simulation ratio.

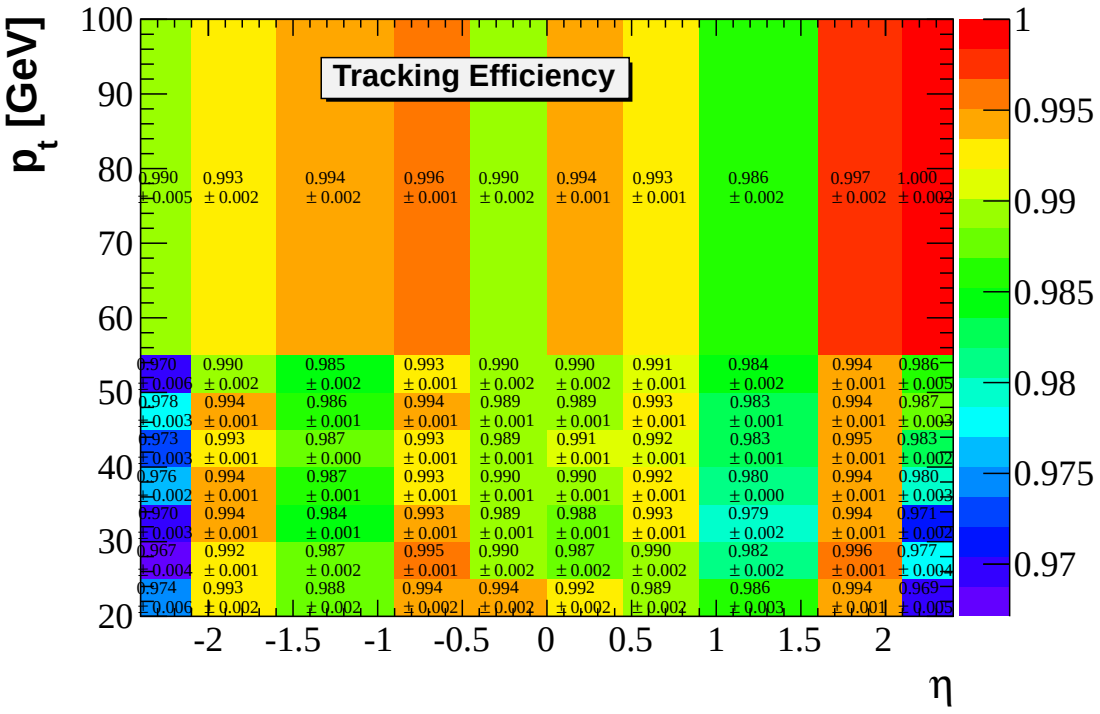

Figure 4.3: Muon tracking efficiency depending on P_{T}^{μ} and η^{μ}.

Table 4.7: Summary of measured efficiencies of a muon with Wγ-selection. Simulation is adapted to the different pile-up scenarios for Run 2011A and Run 2011B.

Efficiency	Data [%]	Simulation [%]	Data/Simulation [%]
Run 2011A			
ε_{TRK}	99.19 ± 0.01	99.50 ± 0.01	99.69 ± 0.01
ε_{SA}	97.46 ± 0.01	97.49 ± 0.01	99.97 ± 0.01
ε_{ID}	99.26 ± 0.01	99.48 ± 0.01	99.78 ± 0.01
ε_{ISO}	98.80 ± 0.01	99.02 ± 0.01	99.77 ± 0.01
$\varepsilon_{TRK}\varepsilon_{SA}\varepsilon_{ID}\varepsilon_{ISO}$	94.97 ± 0.01	95.59 ± 0.01	99.36 ± 0.01
$\varepsilon_{trigger}$	86.09 ± 0.03	86.39 ± 0.01	99.65 ± 0.03
Run 2011B			
ε_{TRK}	99.07 ± 0.01	99.42 ± 0.01	99.67 ± 0.01
ε_{SA}	95.88 ± 0.01	97.50 ± 0.01	98.33 ± 0.01
ε_{ID}	99.33 ± 0.01	99.51 ± 0.01	99.82 ± 0.01
ε_{ISO}	98.74 ± 0.01	99.03 ± 0.01	99.71 ± 0.01
$\varepsilon_{TRK}\varepsilon_{SA}\varepsilon_{ID}\varepsilon_{ISO}$	93.32 ± 0.01	95.53 ± 0.01	97.68 ± 0.01
$\varepsilon_{trigger}$	83.56 ± 0.01	84.49 ± 0.01	98.90 ± 0.01

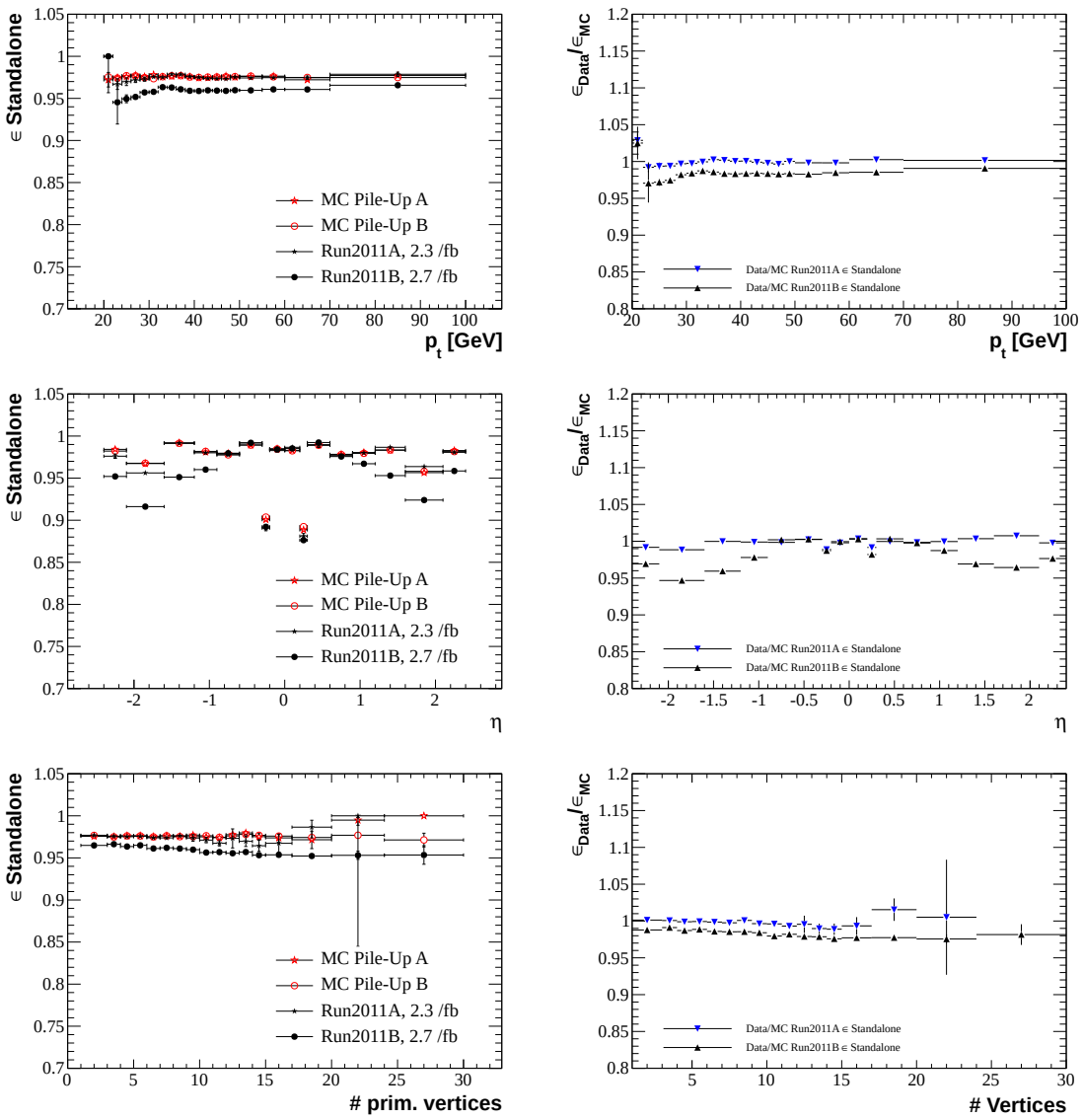

Figure 4.4: Efficiency of muon reconstruction in muon system depending on P_{T}^{μ}, η^{μ}, and number of primary vertices together with data-simulation ratio.

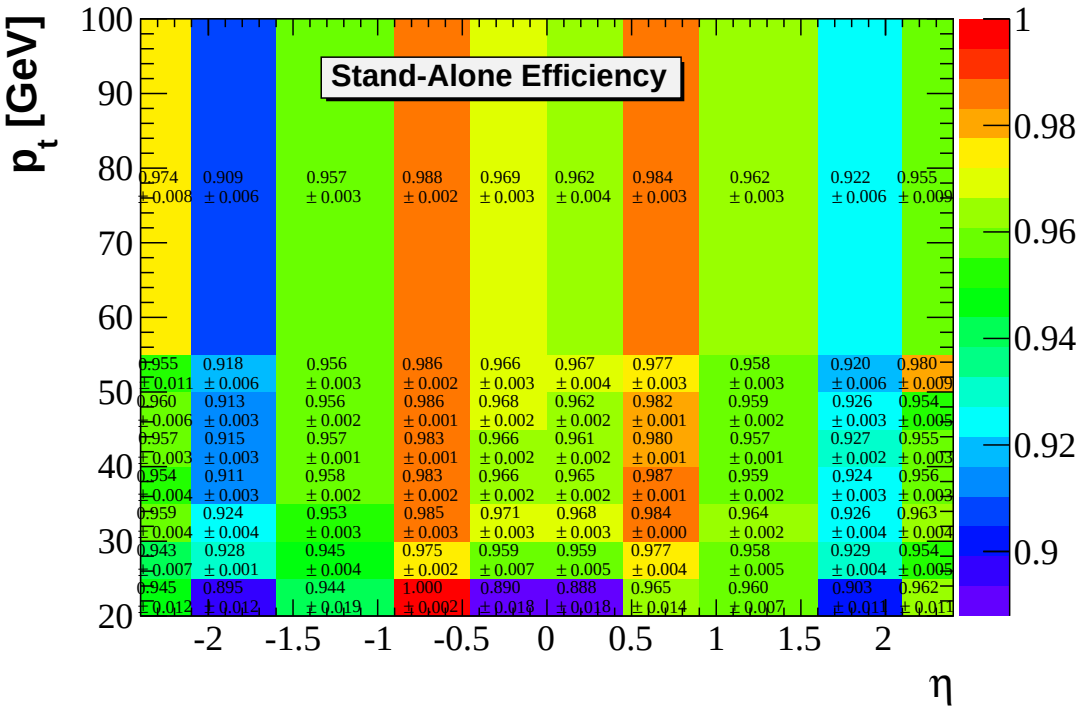

Figure 4.5: Efficiency of muon reconstruction in muon system depending on P_{T}^{μ} and η^{μ}.

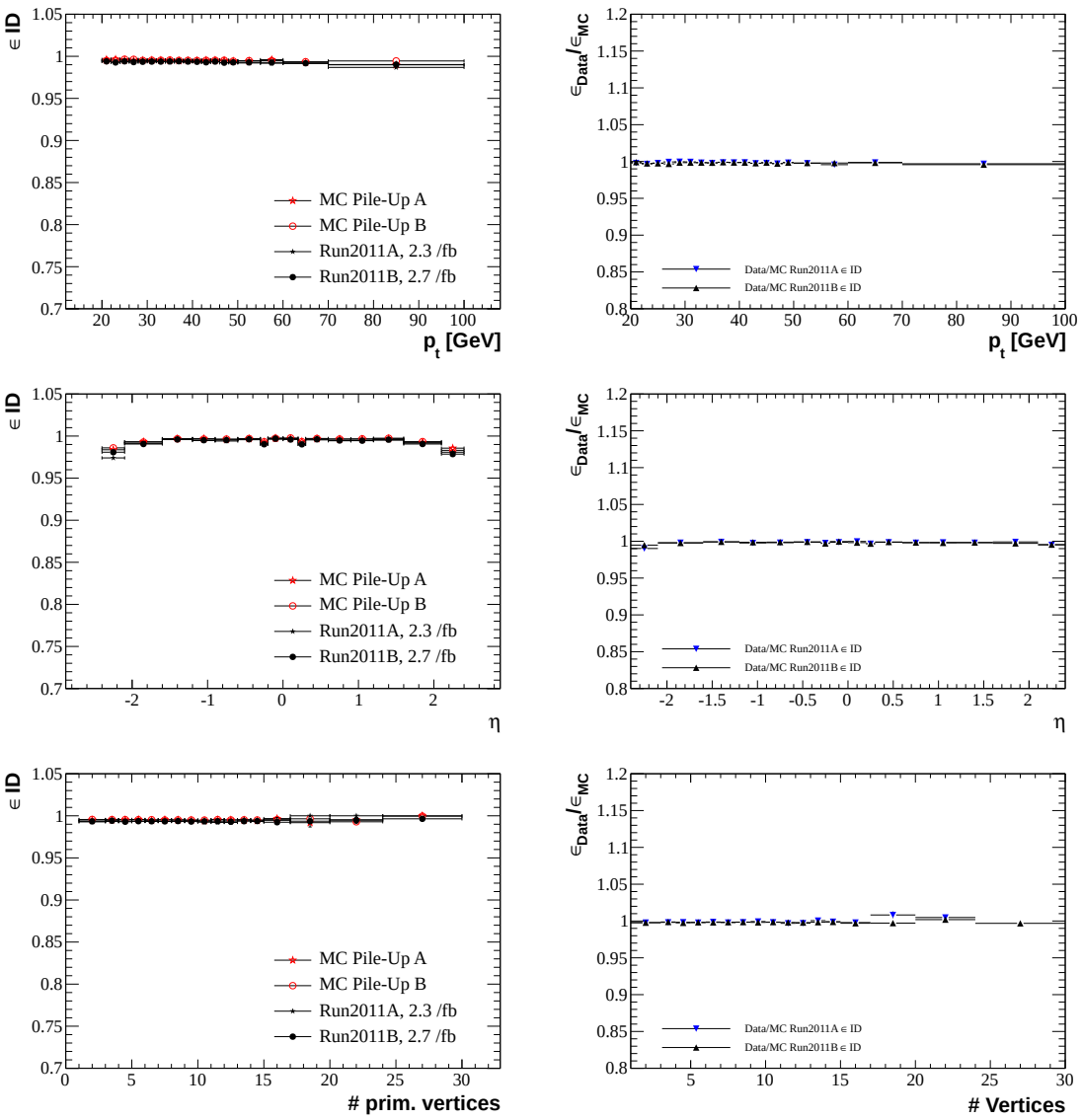

Figure 4.6: Muon matching efficiency depending on P_{T}^{μ}, η^{μ}, and number of primary vertices together with data-simulation ratio.

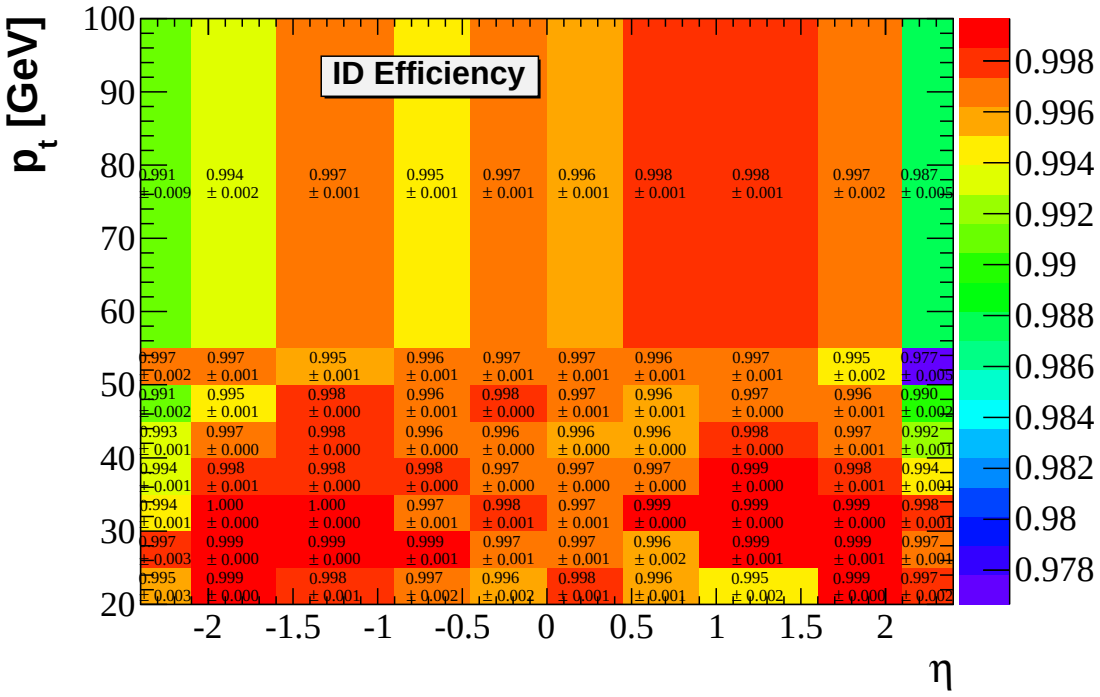

Figure 4.7: Muon matching efficiency depending on P_{T}^{μ} and η^{μ}.

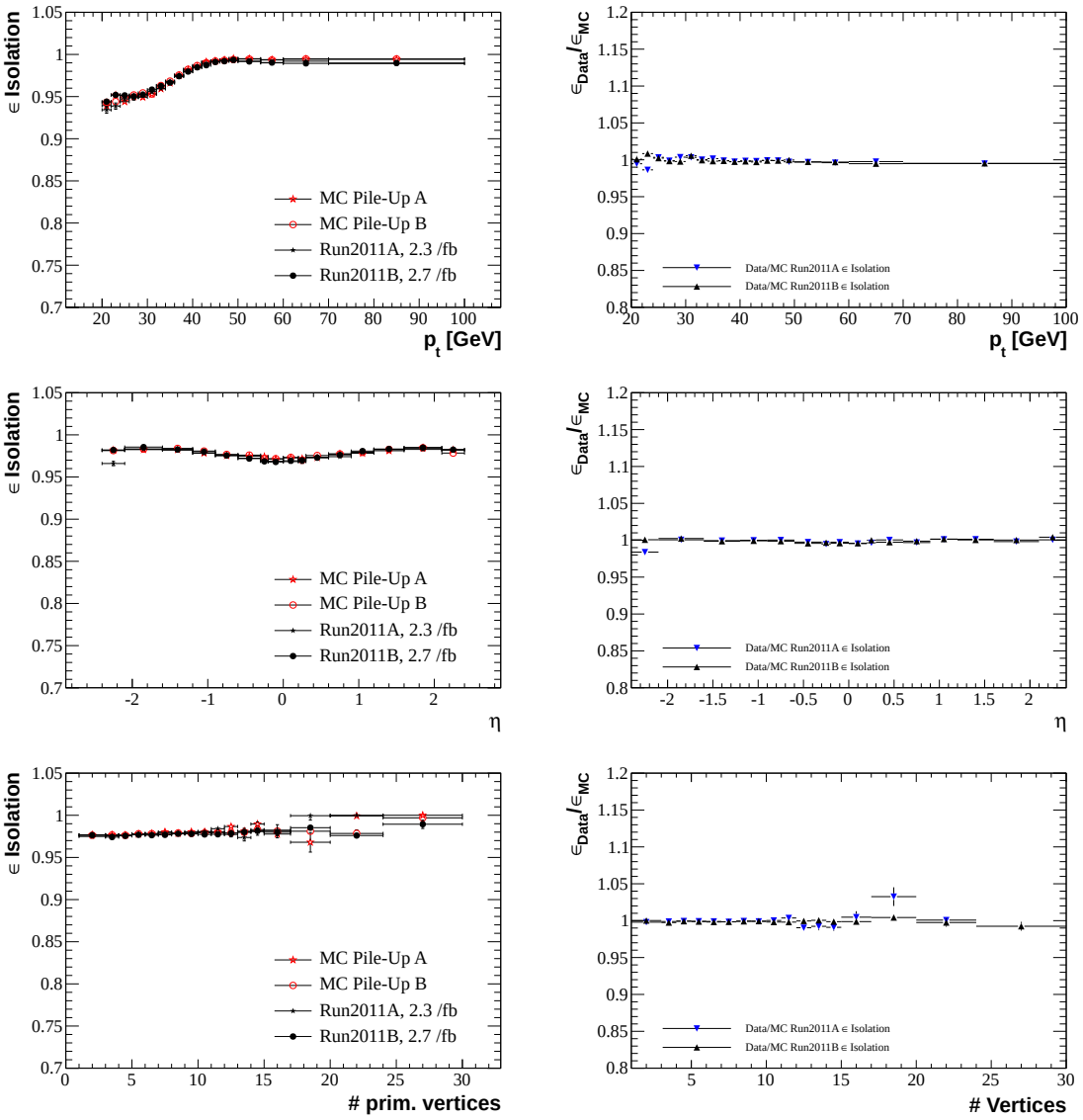

Figure 4.8: Isolation efficiency depending on P_{T}^{μ}, η^{μ}, and number of primary vertices together with data-simulation ratio.

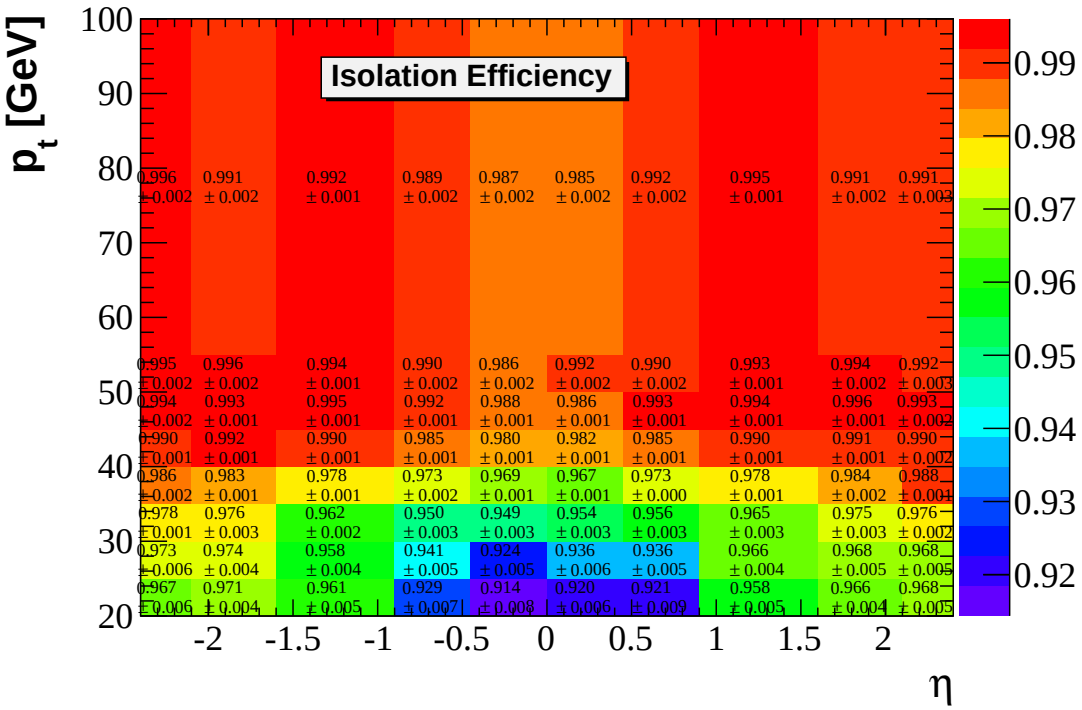

Figure 4.9: Isolation efficiency depending on P_{T}^{μ} and η^{μ}.

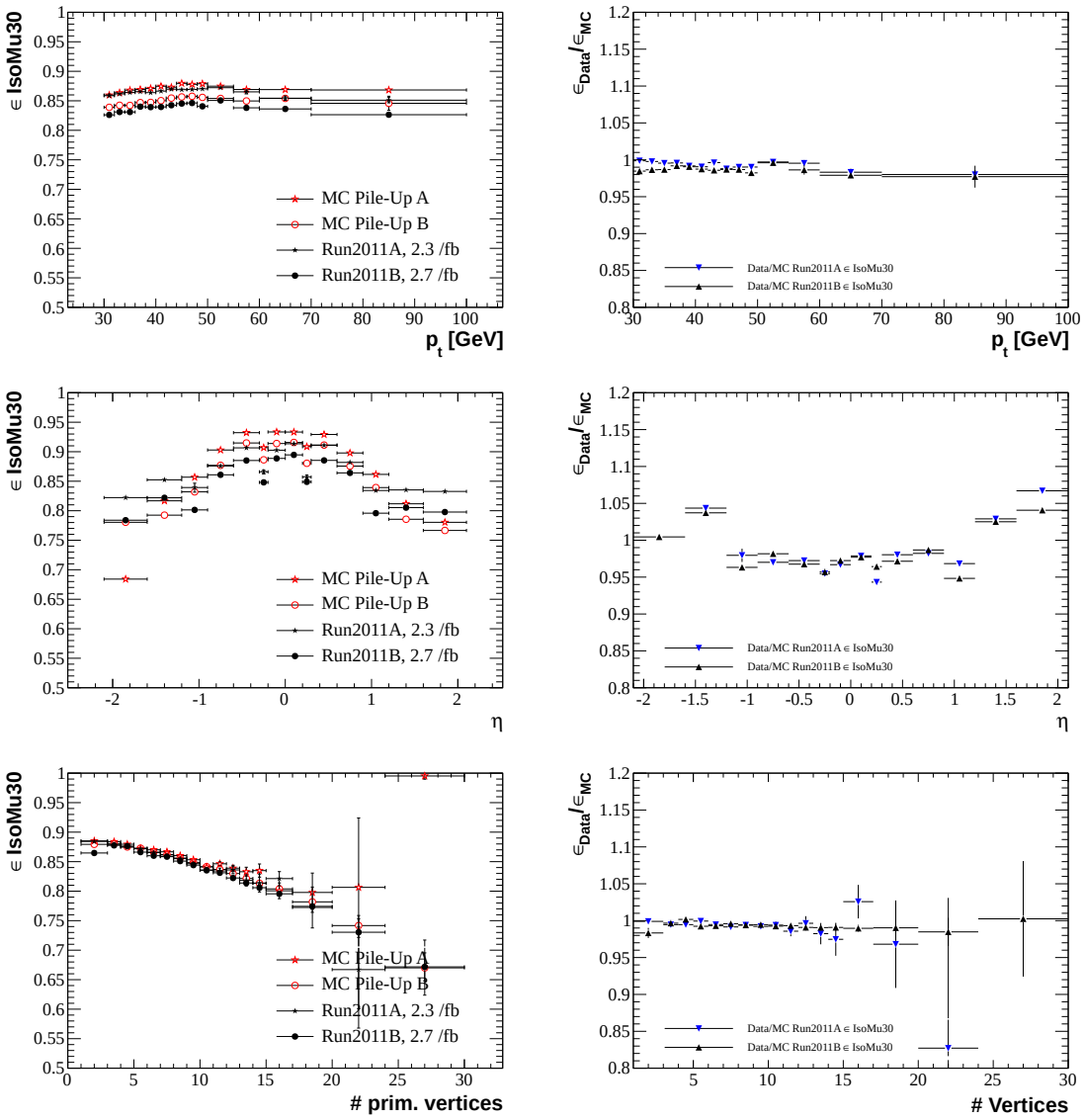

Figure 4.10: Muon trigger efficiency depending on P_{T}^{μ}, η^{μ}, and number of primary vertices together with data-simulation ratio.

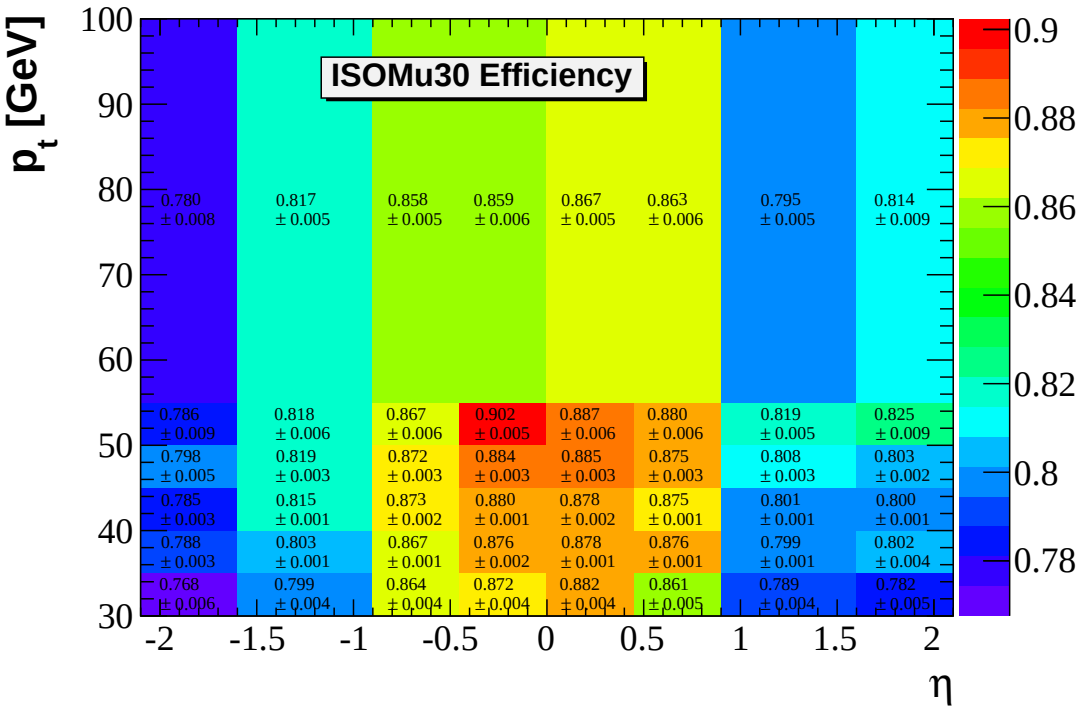

Figure 4.11: Muon trigger efficiency depending on P_{T}^{μ} and η^{μ}.

Efficiency of photon selection

The efficiency of photon selection is factorized as:

$$\varepsilon_{tot} = \varepsilon_{\text{selection}} \cdot \varepsilon_{\text{pixelSeed}}, \tag{4.7}$$

where $\varepsilon_{\text{pixelSeed}}$ is the efficiency of photon to have no associated hitsin the pixel detector, and $\varepsilon_{\text{selection}}$ is the efficiency of photon requiring all other selection criteria described in Section 4.2.3. The efficiencies $\varepsilon_{\text{pixelSeed}}$ and $\varepsilon_{\text{selection}}$ are derived by applying the 'tag-and-probe' method on $Z \rightarrow \mu\mu\gamma$ and $Z \rightarrow ee$ events, respectively.

Since there exists no pure source of photons with high statistics in data, the photon selection efficiency is estimated using electrons from Z decays. The ratio of efficiencies for selecting photons to that of electrons with the same criteria obtained from simulation is shown in Figure 4.12. They agree within 3%. It is also found that the selection criteria in data and simulation agree to better than 3% accuracy in both transverse momentum and pseudorapidity dependence as shown in Figure 4.13.

The invariant mass of the di-electron pair is required to be consistent with the Z boson mass, *i.e.* within 50 and 150 GeV. Both 'tag' and 'probe' electrons must have HCAL over ECAL energy less then 0.15, $E_{\text{T}}^{\gamma} > 20$ GeV and positioned in the ECAL fiducial region. The model for the 'tag-and-probe' fit is the convolution of a Breit-Wigner and a Crystal Ball function for signal and an 'exponential decay + error function' for background.

The efficiencies in data and simulation are shown in Figs. 4.14 and 4.15 respectively. Corresponding efficiency correction factors (ρ_{eff}) are shown in Figure 4.16

The difference between efficiency derived using 'tag-and-probe' method on the simulation and simulation truth counting efficiency, amounts to 0.5%, is assigned as systematic uncertainty.

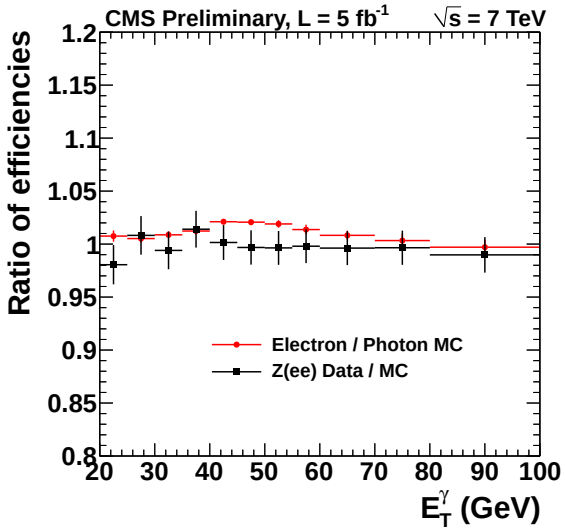

Figure 4.12: Ratio of photon selection efficiencies using electron 'tag-and-probe' in data and simulation (black) and the ratio of simulation truth photon efficiencies to simulation truth elecron efficiencies using photon selection criteria (red) as a function of the photon transverse energy.

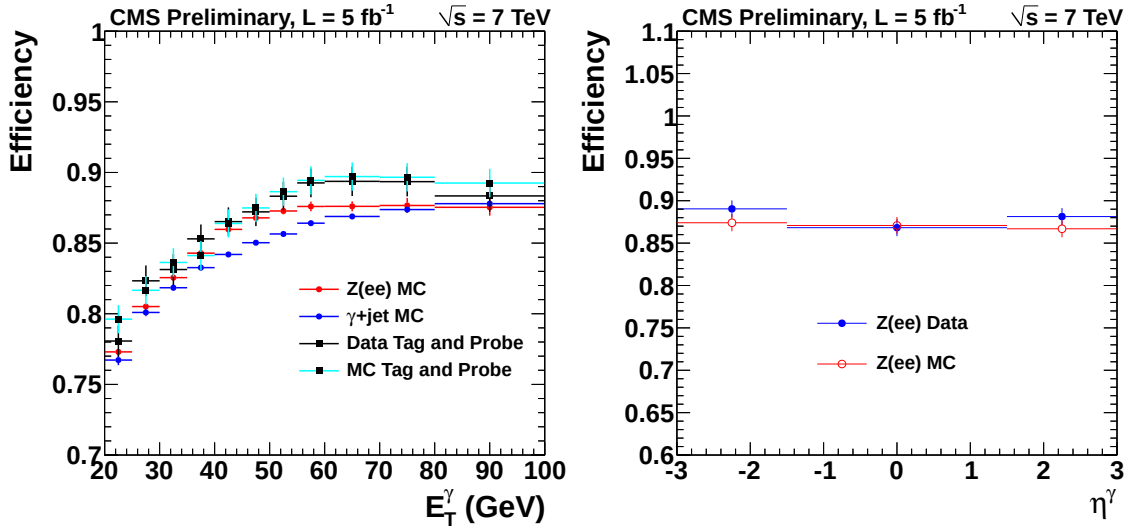

Figure 4.13: Efficiency of photon selection criteria as a function of photon transverse momentum (left) and pseudorapidity (right).

The efficiency of the requirement of the pixel hit veto is calculated using a source of photons from final state radiation $Z \rightarrow \mu\mu\gamma$ events. The requirement of no associated pixel hits in data is 97% and 89% efficient in barrel and endcap, respectively.

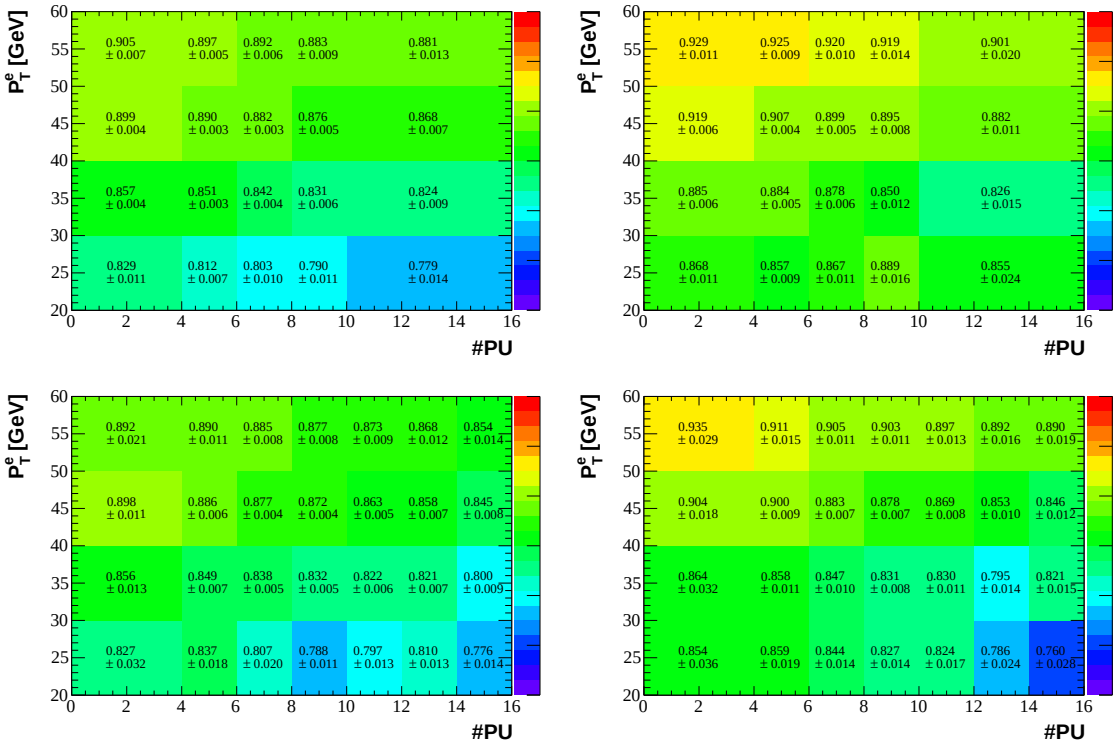

Figure 4.14: Efficiencies for photon selection criteria depending on E_T^γ and number of primary vertices measured in data.

Efficiency of M_T^W selection

The efficiency of M_T^W selection is measured using the signal simulation. The difference between the simulation and data is applied as correction for every simulated event. Accuracy of M_T^W measurement is dominated by the quality of MET measurement. We therefore need to compare the MET measurement between data and simulation. The measurement of MET is driven by the quality of the measurement of visible particles in the detector, which is mainly limited by the measurement of the hadronic component of the final state. The performance of this measurement can be studied in events where the transverse energy of the hadronic component is precisely known. This is the case for $Z + jets$ events, in which the momentum of the Z is precisely measured due to the excellent measurement of leptons.

Z bosons can be selected without significant background and P_T^Z can be accurately reconstructed. All additonal contributions to event with measured $Z \rightarrow ll$ are expected to sum into $\vec{P}_T$ pointing in

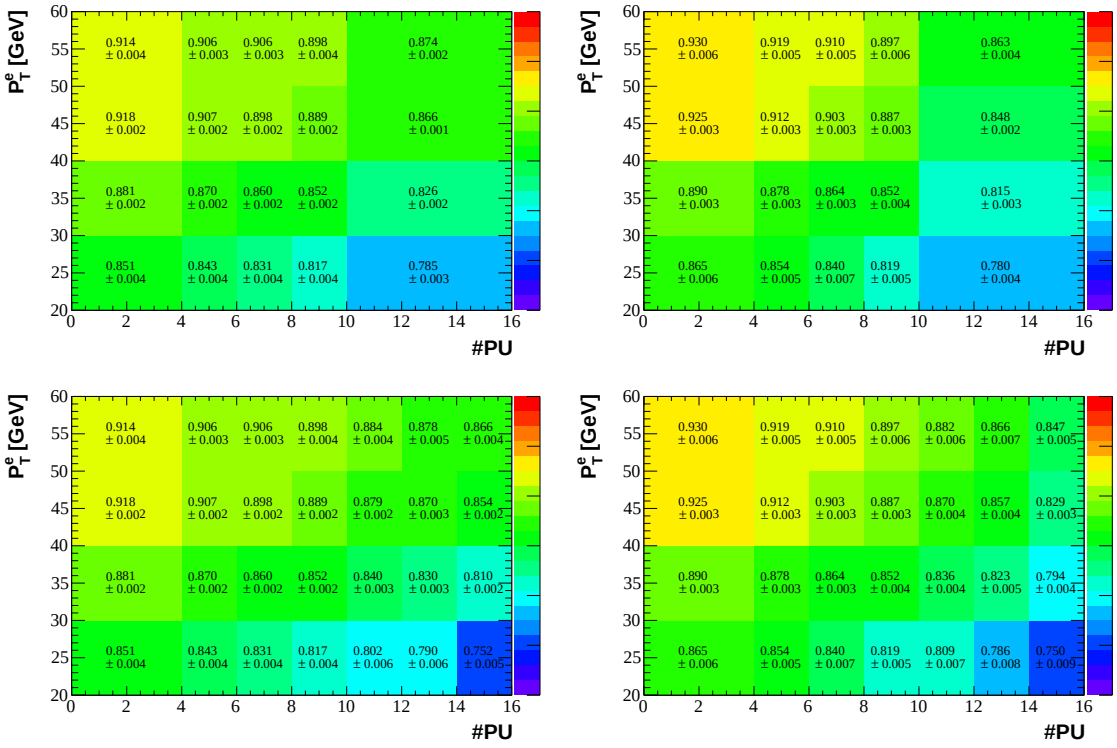

Figure 4.15: Efficiencies for photon selection criteria depending on E_T^γ and number of primary vertices measured in simulation.

the opposite direction, $\vec{P}_T = -\vec{P}_T^Z$. These additional contributions are compared in selected $Z \to \mu\mu$ events in data and simulation, as the function of P_T^Z, and provide the necessary correction.

The efficiency of the M_T^W selection is estimated by $W\gamma$ simulation applying the hadronic recoil correction which takes into account the difference in MET scale and resolution between data and simulation using the method fully described in [29]. The recoil modeling is applied on $Z \to \mu\mu$ events in data and simulation.

The method calibrates the recoil response and resolution with $Z \to \mu\mu$ events in data and simulation as a function of P_T^Z. This information is combined with $W\gamma$ simulation to derive corrections to the METv based on $P_T^{W\gamma}$, as well as the associated systematic uncertainties.

The transverse recoil vector ($\vec{u}$) for Z events is determined from the reconstructed METv and $\vec{P}_T^Z$:

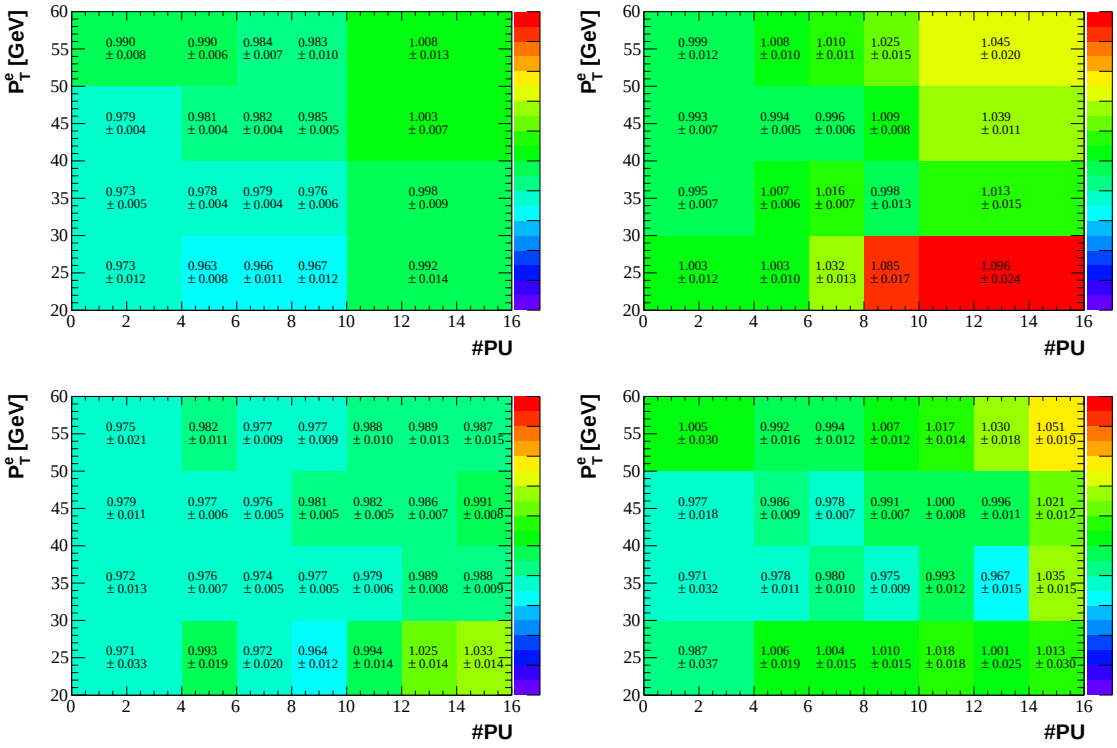

Figure 4.16: Efficiency correction factor for photon selection criteria depending on E_T^γ and number of primary vertices.

$$\vec{u} = -M\vec{E}T - \vec{P}_T^Z = -M\vec{E}T - \vec{P}_T^{l_1} - \vec{P}_T^{l_2} \tag{4.8}$$

The reference vector is defined as $\vec{P}_T^Z$ reconstructed by 2 leptons, $\vec{P}_T^{l_1} + \vec{P}_T^{l_2}$, for data and simulated true $\vec{P}_T^{Z^{gen}}$ for the simulation. Axes oriented parallel (u_1) and perpendicular (u_2), to the reference vector's direction are defined. In ideal case: $< u_1 >= P_T^Z$ and $< u_2 >= 0$.

A Gaussian fit to u_1 and u_2 spectra is performed in different P_T^Z bins in both data and simulation to get the response (expected value) and resolution (variance). The recoil response function is obtained by fitting a linear function, $a + b \cdot P_T^Z$, to the response, and the recoil resolution function by fitting a quadratic function, $a + b \cdot P_T^Z + c \cdot (P_T^Z)^2$, to the resolution. Figures 4.17 to 4.22 and Figures 4.23 to 4.24 show the fitted distributions of u_1 and u_2 in Z events for data and simulation for different values of the number of vertices in the event (N_{Vtx}).

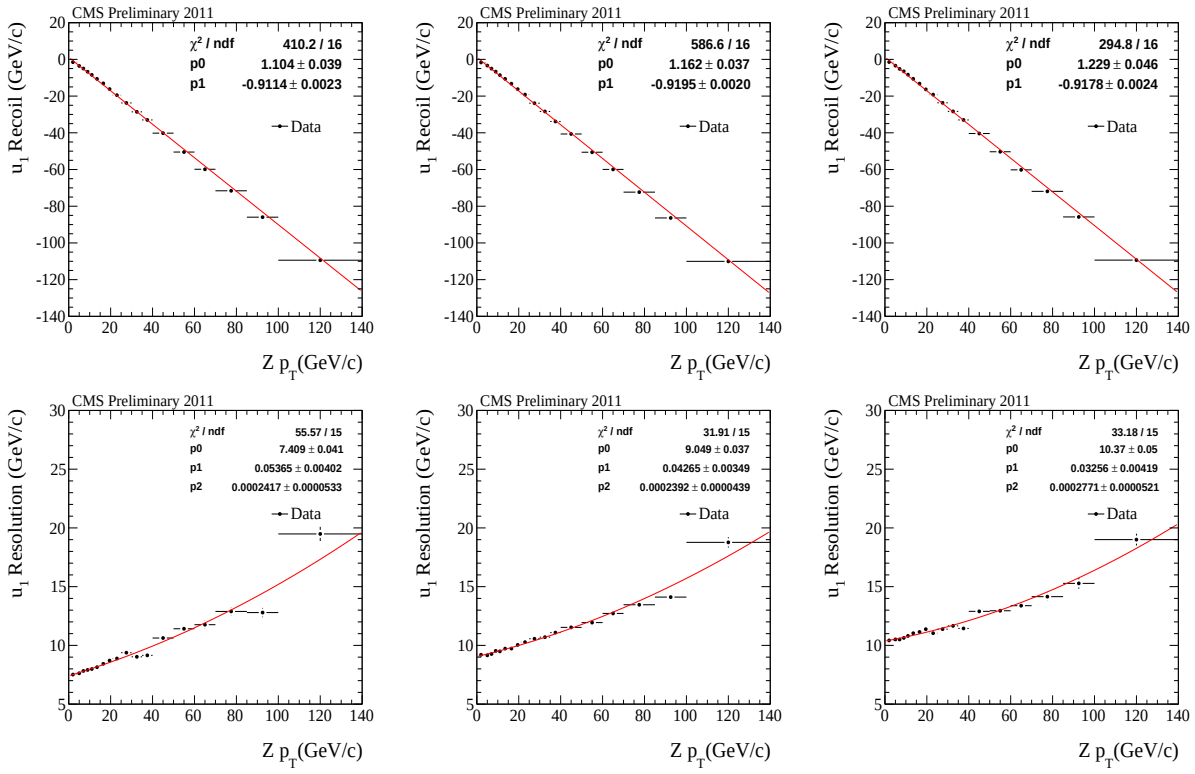

Figure 4.17: The fitting results of u_1 response (top) and resolution (bottom) for 2011A data set. Left column shows the results for $1 \leq N_{Vtx} \leq 3$. Middle column shows the results for $4 \leq N_{Vtx} \leq 5$. Right column shows the results for $6 \leq N_{Vtx} \leq 7$.

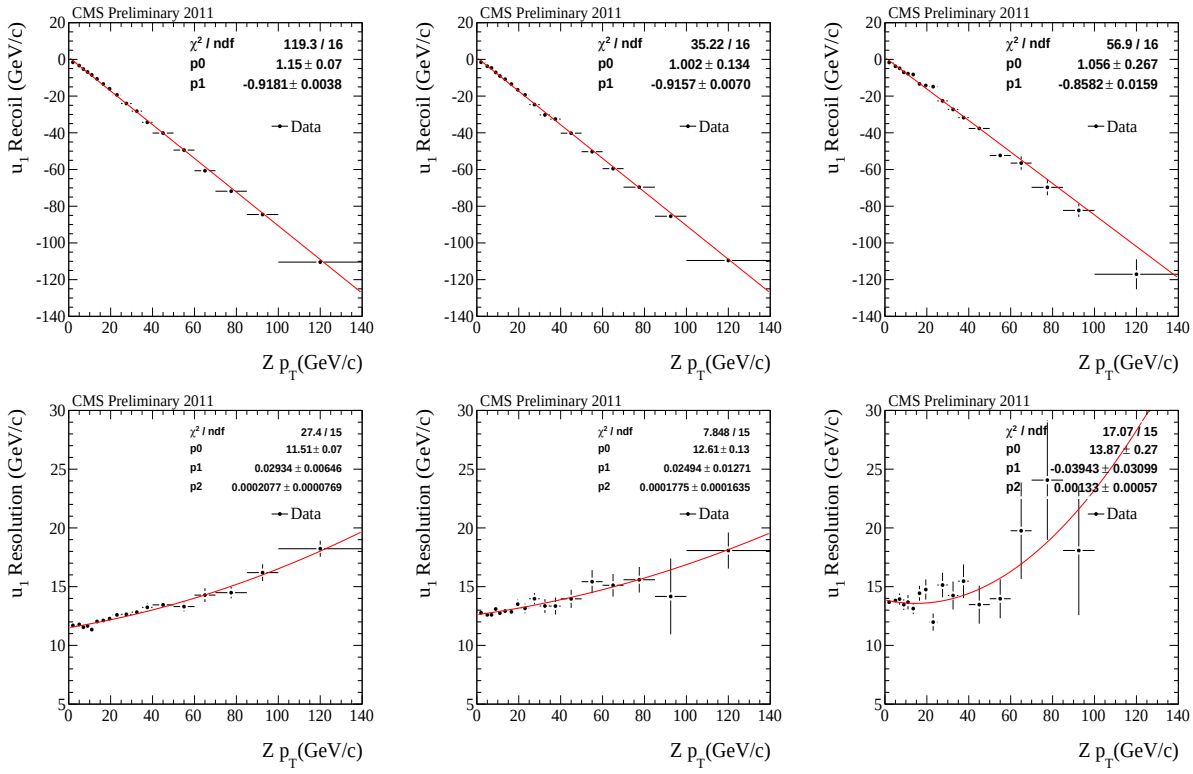

Figure 4.18: The fitting results of u_1 response (top) and resolution (bottom) for 2011A data set. Left column shows the results for $8 \leq N_{Vtx} \leq 9$. Middle column shows the results for $10 \leq N_{Vtx} \leq 11$. Right column shows the results for $12 \leq N_{Vtx}$

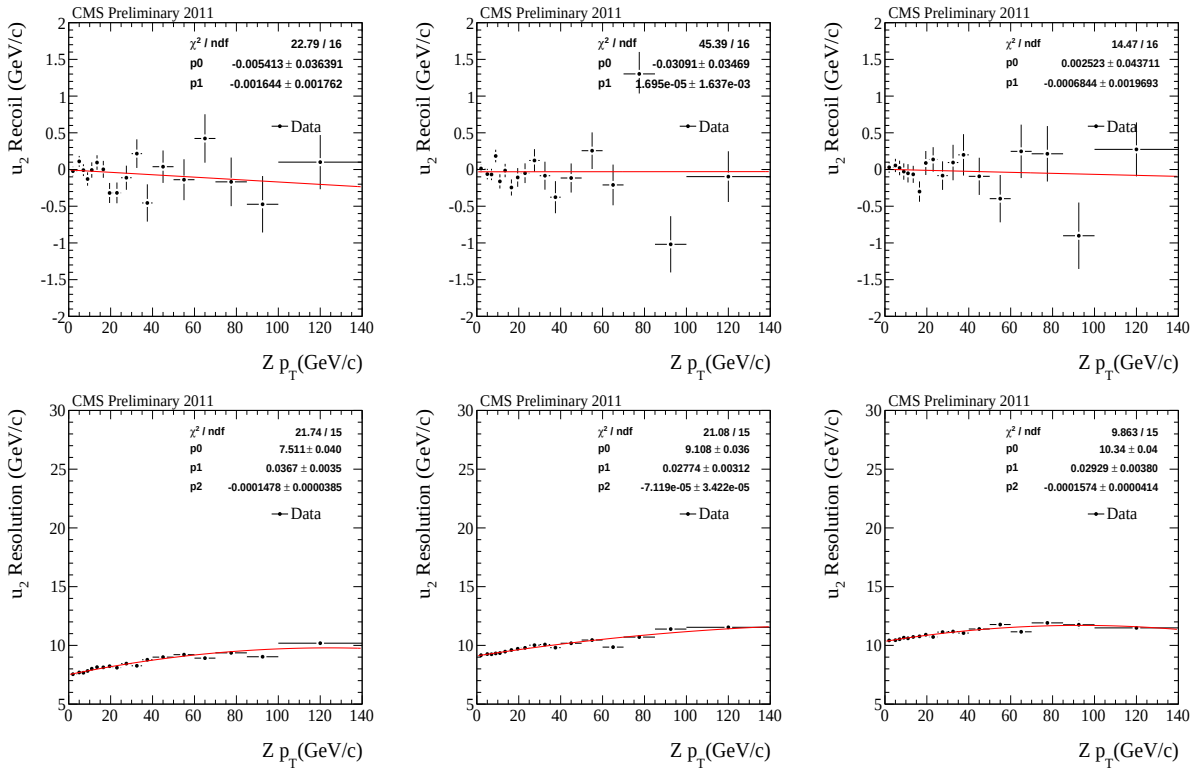

Figure 4.19: The fitting results of u_2 response (top) and resolution (bottom) for 2011A data set. Left column shows the results for $1 \leq N_{Vtx} \leq 3$. Middle column shows the results for $4 \leq N_{Vtx} \leq 5$. Right column shows the results for $6 \leq N_{Vtx} \leq 7$.

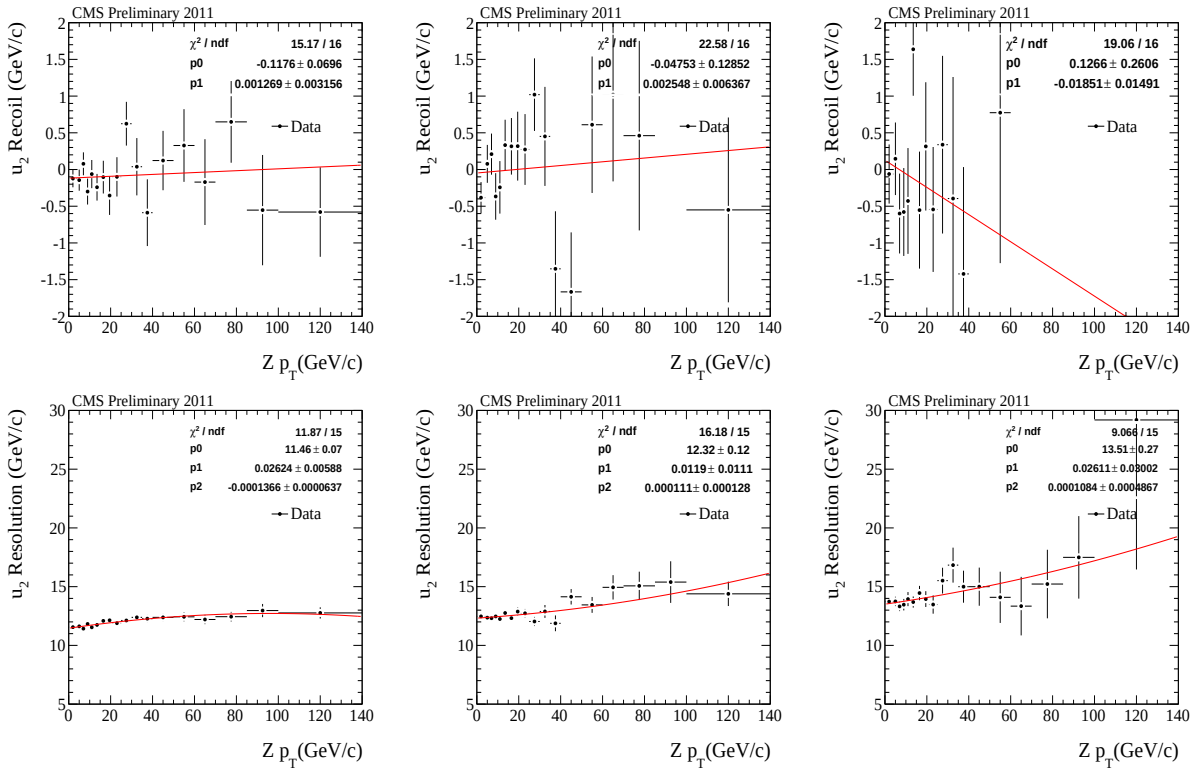

Figure 4.20: The fitting results of u_2 response (top) and resolution (bottom) for 2011A data set. Left column shows the results for $8 \leq N_{Vtx} \leq 9$. Middle column shows the results for $10 \leq N_{Vtx} \leq 11$. Right column shows the results for $12 \leq N_{Vtx}$.

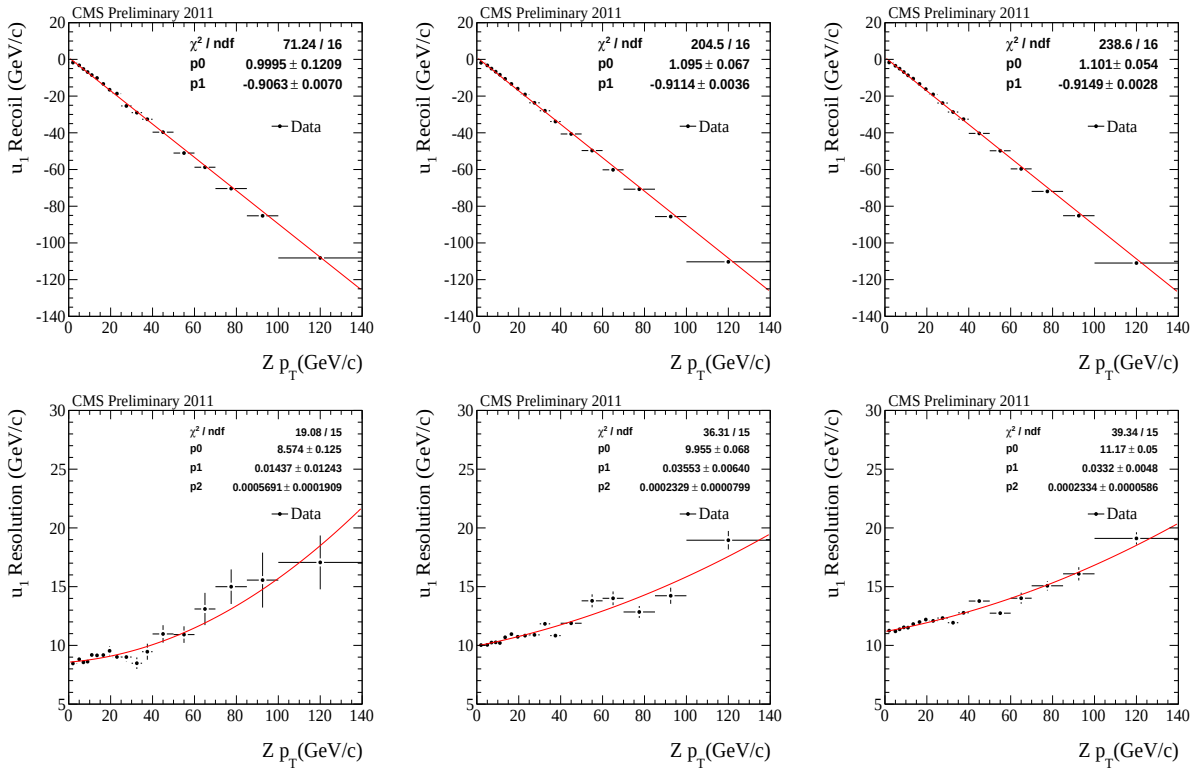

Figure 4.21: The fitting results of u_1 response (top) and resolution (bottom) for 2011B data set. Left column shows the results for $1 \leq N_{Vtx} \leq 3$. Middle column shows the results for $4 \leq N_{Vtx} \leq 5$. Right column shows the results for $6 \leq N_{Vtx} \leq 7$.

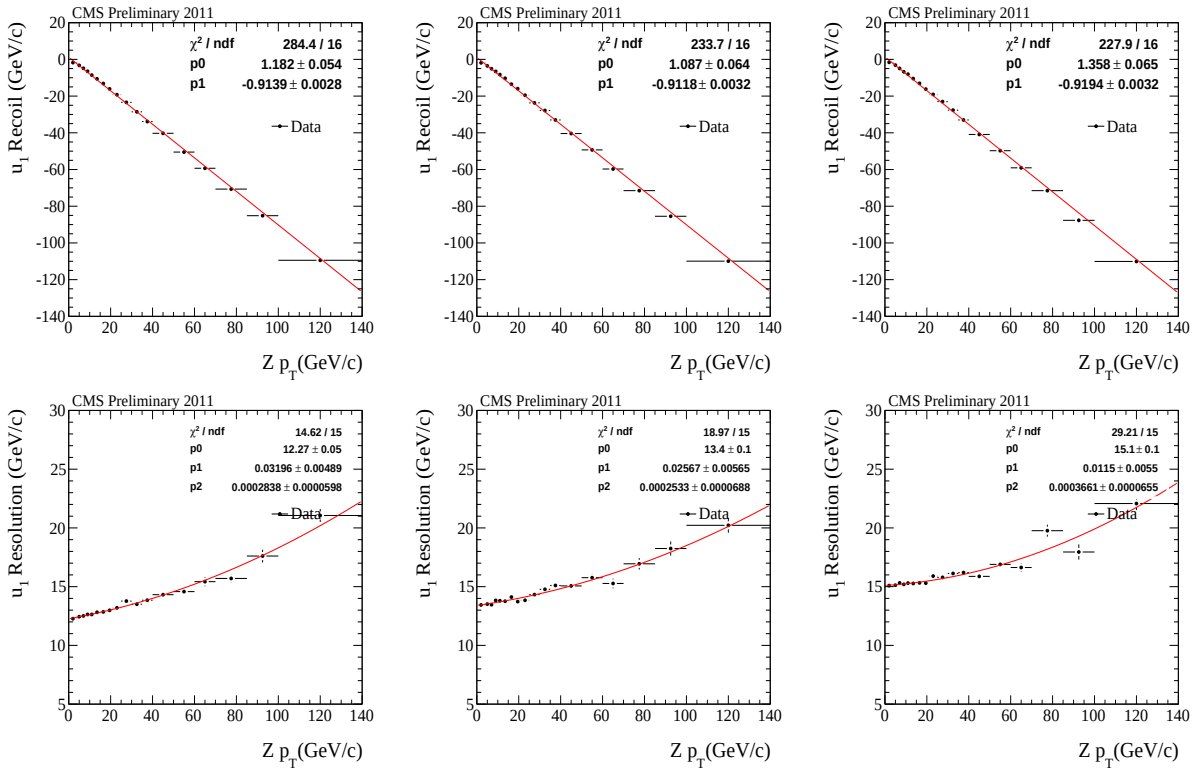

Figure 4.22: The fitting results of u_1 response (top) and resolution (bottom) for 2011B data set. Left column shows the results for $8 \leq N_{Vtx} \leq 9$. Middle column shows the results for $10 \leq N_{Vtx} \leq 11$. Right column shows the results for $12 \leq N_{Vtx}$.

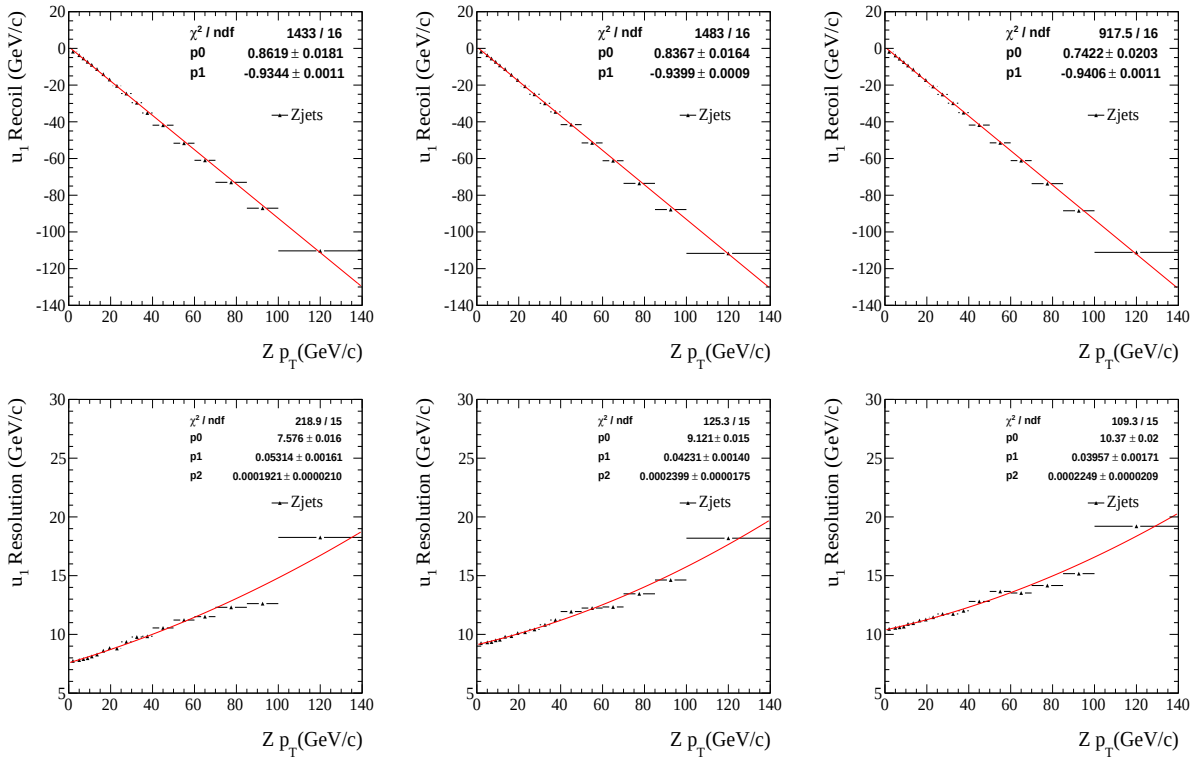

Figure 4.23: The fitting results of u_1 response (top) and resolution (bottom) for simulated Z. Left column shows the results for $1 \leq N_{Vtx} \leq 3$. Middle column shows the results for $4 \leq N_{Vtx} \leq 5$. Right column shows the results for $6 \leq N_{Vtx} \leq 7$.

The transverse recoil vector for simulated $W\gamma$ events is determined from the reconstructed $\vec{MET}$ and P_T of the lepton and γ:

$$\vec{u} = -\vec{MET} - \vec{P}_T^{l} - \vec{P}_T^{\gamma} \tag{4.9}$$

The reference vector is $\vec{P}_T^{W\gamma^{gen}} = \vec{P}_T^{\nu^{gen}} + \vec{P}_T^{l^{gen}} + \vec{P}_T^{\gamma^{gen}}$, abtained from simulation truth particles.

The reason to subtract the contribution of the photon from the recoil is to isolate the purely hadronic component. This can also avoid the miscalculation of the recoil if it is a FSR event.

The corrected function of the recoil response and resolution can be obtained by 3 fitted distributions (Z from data, Z from simulation, and $W\gamma$ from simulation):

$$f_{d_i}(P_T^{W\gamma}) = \frac{f_{d_i}^{\text{Z,data}}(P_T^Z)}{f_{d_i}^{\text{Z,simulation}}(P_T^Z)} \times f_{d_i}^{\text{W}\gamma\text{,simulation}}(P_T^{W\gamma}) \tag{4.10}$$

where $d_i = u_i, \sigma_i$ and $i = 1, 2$.

Using the corrected recoil response and resolution curves a corrected MET distribution in $W\gamma$ simulation is generated by the following steps:

1. For every simulated $W\gamma$ event, look up the u_1 and u_2 response $(f_{u_i}(P_T^{W\gamma}))$ and resolution $(f_{\sigma i}(P_T^{W\gamma}))$ from the corrected curves.
2. Randomly sample Gaussian PDFs defined with these values to determine new recoil components for each event, $u_i{}' = Gauss(f_{u_i}(P_T^{W\gamma}), f_{\sigma_i}(P_T^{W\gamma}))$
3. Combine the new $u_i{}'$ components to reconstruct a corrected recoil vector $\vec{u}_i{}'$. Add the lepton $(\vec{P}_T^{l})$ and photon vector $(\vec{P}_T^{\gamma})$ back in to determine the corrected $\vec{MET}$.
4. Using the corrected $\vec{MET}$, the corrected M_T^W is calculated.

A "closure test" is performed to show that these parameters describe the original M_T^W shape well in the same sample. The comparison between the M_T^W obtained from the recoil method and the

original M_T^W shape is shown in Fig . 4.25 and 4.26. The difference in efficiency between the original and recoil M_T^W, and due to fitting errors, are assigned as systematic uncertainty.

The M_T^W efficiencies are summarized in Tables 4.8 and 4.9 and in Figure 4.27.

Table 4.8: Summary of the M_T^W efficiencies in using corrected recoil, simulation, and a recoil/simulation ratio wrt N_{Vtx} for 2011A runs.

Efficiency	Recoil Prediction	Simulation	Prediction/Simulation
$0 < N_{Vtx} <= 3$	$56.1 \pm 0.3\%$	$55.2 \pm 0.2\%$	1.016 ± 0.006
$3 < N_{Vtx} <= 5$	$55.8 \pm 0.3\%$	$54.3 \pm 0.5\%$	1.027 ± 0.005
$5 < N_{Vtx} <= 7$	$55.4 \pm 0.3\%$	$54.0 \pm 0.3\%$	1.026 ± 0.006
$7 < N_{Vtx} <= 9$	$55.6 \pm 0.5\%$	$54.7 \pm 0.1\%$	1.017 ± 0.009
$9 < N_{Vtx} <= 11$	$55.3 \pm 0.6\%$	$53.9 \pm 0.8\%$	1.026 ± 0.012
$11 < N_{Vtx}$	$56.5 \pm 1.1\%$	$53.5 \pm 0.3\%$	1.057 ± 0.021

Table 4.9: Summary of the M_T^W efficiencies in using corrected recoil, simulation, and a recoil/simulation ratio wrt N_{Vtx} for 2011B runs.

Efficiency	Recoil Prediction	Simulation	Prediction/Simulation
$0 < N_{Vtx} <= 3$	$55.8 \pm 0.5\%$	$54.9 \pm 0.2\%$	1.018 ± 0.010
$3 < N_{Vtx} <= 5$	$56.2 \pm 0.3\%$	$54.3 \pm 0.5\%$	1.036 ± 0.006
$5 < N_{Vtx} <= 7$	$55.4 \pm 0.4\%$	$53.7 \pm 0.2\%$	1.031 ± 0.007
$7 < N_{Vtx} <= 9$	$55.5 \pm 0.4\%$	$54.5 \pm 0.3\%$	1.017 ± 0.008
$9 < N_{Vtx} <= 11$	$54.8 \pm 0.6\%$	$53.6 \pm 0.2\%$	1.022 ± 0.011
$11 < N_{Vtx}$	$54.8 \pm 0.8\%$	$53.7 \pm 0.5\%$	1.020 ± 0.015

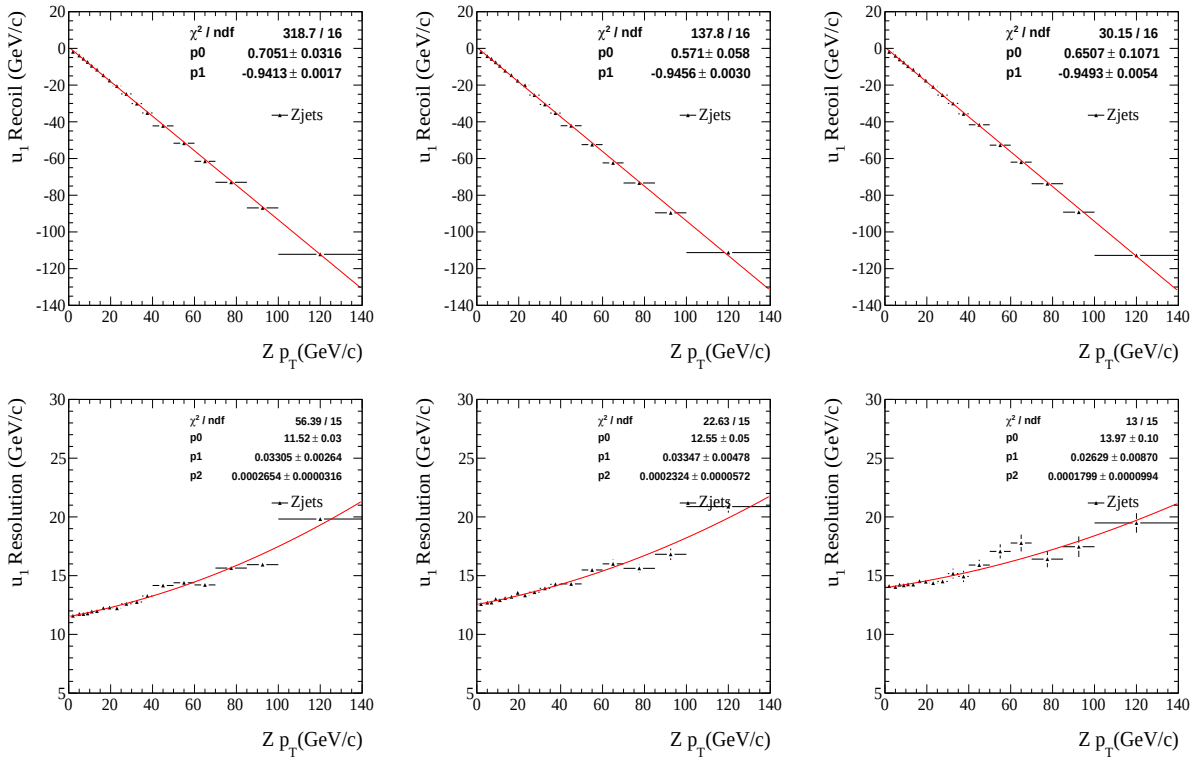

Figure 4.24: The fitting results of u_1 response (top) and resolution (bottom) for simulated Z. Left column shows the results for $8 \leq N_{Vtx} \leq 9$. Middle column shows the results for $10 \leq N_{Vtx} \leq 11$. Right column shows the results for $12 \leq N_{Vtx}$.

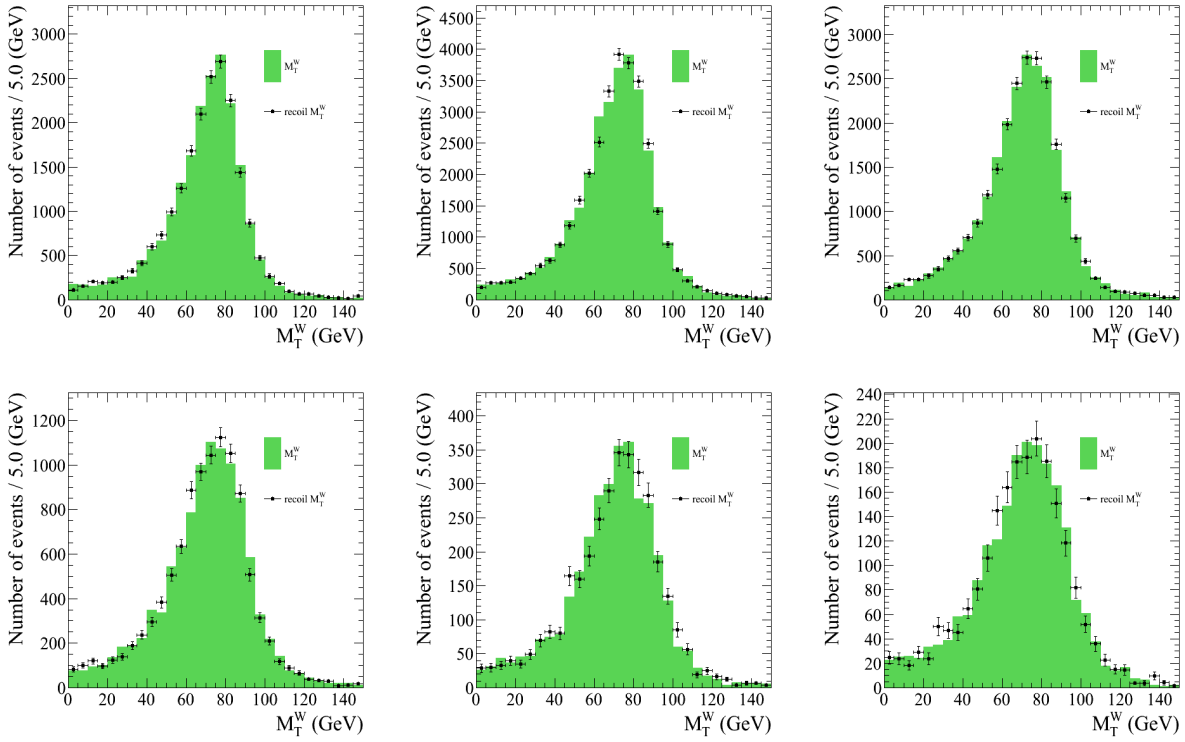

Figure 4.25: Comparison of the true $W\gamma \to \mu\nu\gamma$ simulated M_T^W distribution with the predicted simulated distribution from the u_i recoil fits. The filled histogram is the true simulated M_T^W, and the dots show the M_T^W shape that is predicted by the recoil fits. Plots correspond to (top-left) $1 \leq N_{Vtx} \leq 3$, (top-midle) $4 \leq N_{Vtx} \leq 5$, (top-right) $6 \leq N_{Vtx} \leq 7$, (bottom-left) $8 \leq N_{Vtx} \leq 9$, (bottom-midle) $10 \leq N_{Vtx} \leq 11$, (bottom-right) $12 \leq N_{Vtx}$, for 2011A.

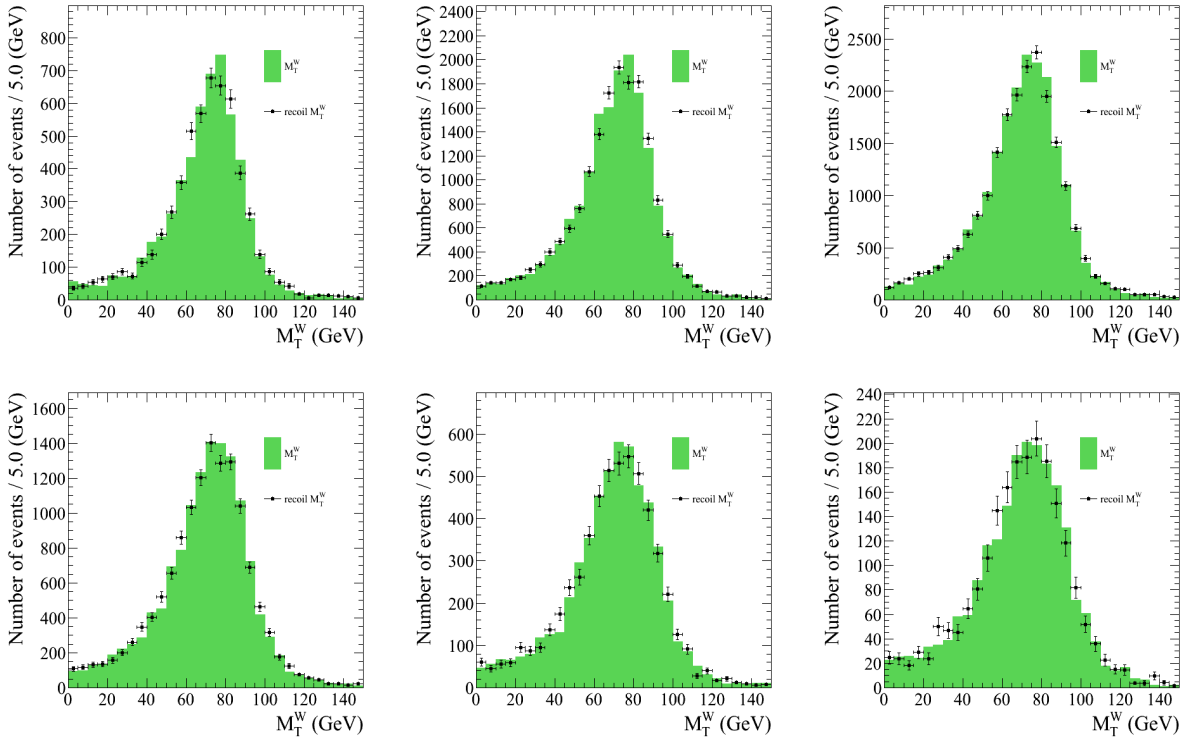

Figure 4.26: Comparison of the true $W\gamma \to \mu\nu\gamma$ simulated M_T^W distribution with the predicted simulated distribution from the u_i recoil fits. The filled histogram is the true simulated M_T^W, and the dots show the M_T^W shape that is predicted by the recoil fits. Plots correspond to (top-left) $1 \leq N_{Vtx} \leq 3$, (top-midle) $4 \leq N_{Vtx} \leq 5$, (top-right) $6 \leq N_{Vtx} \leq 7$, (bottom-left) $8 \leq N_{Vtx} \leq 9$, (bottom-midle) $10 \leq N_{Vtx} \leq 11$, (bottom-right) $12 \leq N_{Vtx}$, for 2011B.

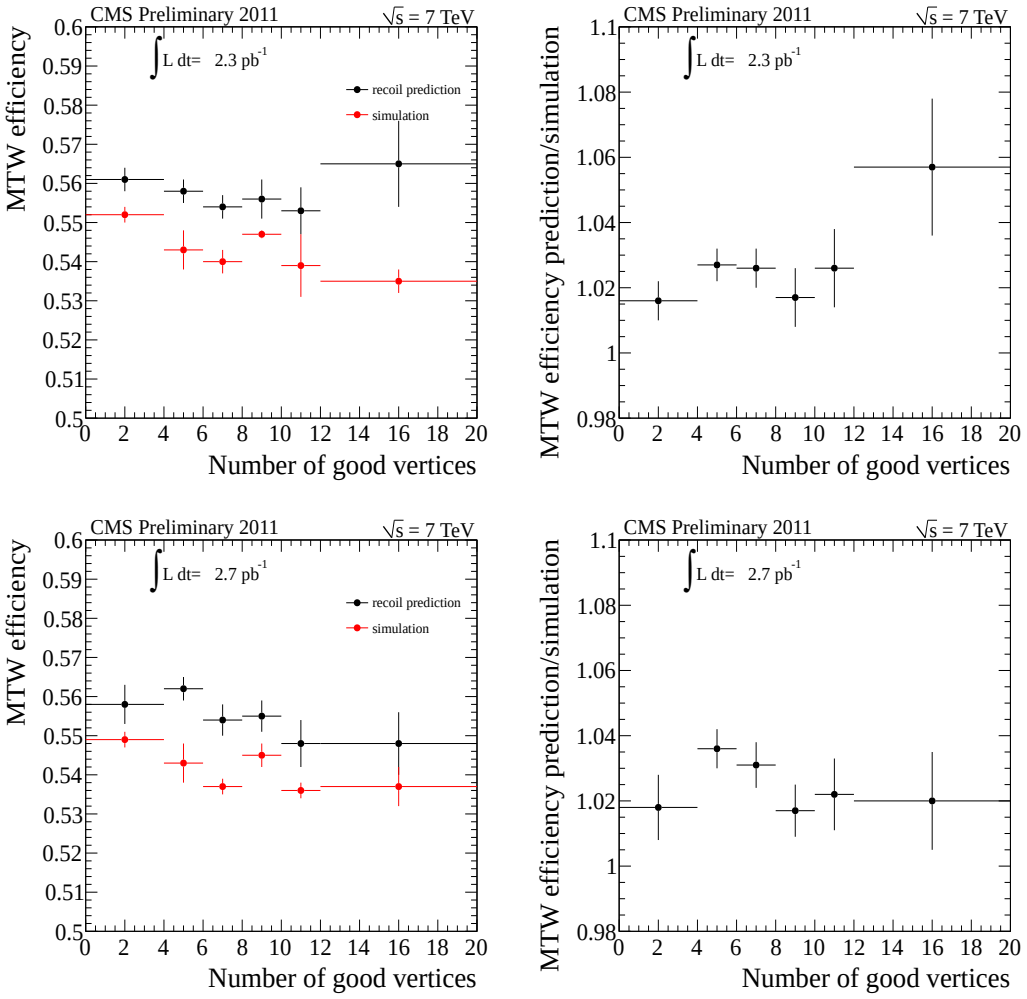

Figure 4.27: Efficiencies and efficiency correction factors for M_T^W cut. Upper (lower) plot corresponds to 2011A (2011B).

4.3 Backgrounds

The largest background to $W\gamma$ production is from events in which a jet that has a large fraction of electromagnetic energy is misidentified as a photon. The following background processes fall into this category:

- W+jets where the jet is misidentified as a photon.
- Z+jets where one of the leptons from the Z boson decay is outside acceptance and a jet is misidentified as a photon.
- $t\bar{t}$+jets where one of the W bosons from the $t\bar{t}$-pair decays into a lepton and a jet is misidentified as a photon.

This background is estimated in data with two methods,the 'template method' and the 'ratio method', as described in Sec. 4.3.1.

Multibosons processes can also be background if an electron is misidentified as a photon. For the $W\gamma \rightarrow \mu\nu\gamma$ channel this background source is small and is estimated in data, as described in Sec. 4.3.2.

Other backgrounds to the $W\gamma$ process are from

- Misidentified leptons from γ+jet production,
- W$\gamma \rightarrow \tau\nu\gamma$ where the τ decays to $\mu\nu\gamma$,
- Zγ events,
- $t\bar{t}\gamma$ events.

All these backgrounds are estimated to be negligible compared to the $W + jets$ contribution and are estimated from the simulation.

4.3.1 Background from jets misidentified as photons

The dominant background comes from events with misidentified photons, mostly originating from the jets in $W + jets$ events. The background from these sources is estimated in data, using two methods described below.

'Template method'

The 'template method' uses the $\sigma_{i\eta i\eta}$ distribution as discriminating variable to determine the number of genuine photons from misidentified jets passing full selection criteria by performing a two-component extended maximum likelihood fit of signal and background $\sigma_{i\eta i\eta}$ 'templates' to data. The signal and background distributions, or 'templates', are taken as input for the fit and the background yield is extracted from the fit.

Signal and background templates are obtained in bins of E_{T}^{γ}: $15-20$ GeV, $20-25$ GeV, $25-30$ GeV, $30-35$ GeV, $35-40$ GeV, $40-60$ GeV, $60-90$ GeV, and $90-500$ GeV for 2011A and 2011B separately, and $90-120$ GeV and $120-500$ GeV for 2011A and 2011B analyzed together. Template shapes for photons reconstructed in the barrel ($|\eta| < 1.4442$) and the endcap ($1.556 < |\eta| < 2.5$) are made separately for each E_{T}^{γ} bin.

The signal shape is obtained from photon candidates in $W\gamma$ simulation. The simulation of electromagnetic shower is cross checked with data using $Z \rightarrow ee$ events. Events are required to have at least two electron candidates with $p_{\mathrm{T}} > 20$ GeV and pass selection criteria but without $\sigma_{i\eta i\eta}$ requirement. Both electron candidates must be identified in the ECAL fiducial volume and have invariant mass between 60 and 120 GeV. A 'tag' electron candidate, is required to pass the stringent electron trigger criteria , while no trigger requirements are applied on the other electron candidate, a 'probe'. The purity of this selection is estimated to be 99% for both barrel and endcap regions.

The comparison of the $\sigma_{i\eta i\eta}$ distributions for the 'probe' in data and simulation is shown in Figure 4.28. The mean of the $\sigma_{i\eta i\eta}$ distribution in data is smaller than that in simulation by 0.9×10^{-4} (0.8×10^{-4}) and 2.1×10^{-4} (1.9×10^{-4}) for barrel and endcap in 2011A (2011B), respectively.

These effects were accounted for by shifting the $\sigma_{i\eta i\eta}$ template distributions in simulation by this difference.

The $\sigma_{i\eta i\eta}$ distributions are additionaly checked using FSR photons from the $Z \rightarrow \mu\mu\gamma$ process in data. The comparison of the $\sigma_{i\eta i\eta}$ distributions between data FSR photons, simulated FSR photons and simulated photons from the $W\gamma$ process is shown in Figure 4.29. As expected from the $Z \rightarrow ee$ comparison the mean of the $\sigma_{i\eta i\eta}$ distribution in data is smaller than in simulation. The $\sigma_{i\eta i\eta}$ distributions from FSR simulated photons and signal photons from $W\gamma$ simulation are in agreement.

The background 'templates' are made from jet-enriched data, events in data selected by a jet triggers. Photon candidates in these events are required to pass the photon selection criteria described in Sec. 4.2.3, except for the $\sigma_{i\eta i\eta}$ requirement and I_{TRK} which is required to be in the range $2 \text{ GeV} < I_{TRK} - 0.001 \cdot E_T^{\gamma} - 0.0167(0.032) \cdot \rho < 5(3)$ GeV for photons in the barrel(endcap). This sideband requirement ensures that the contribution from genuine photons is negligible, while keeping the isolation requirements close to those for photon selection criteria. This allows to select jets with a large electromagnetic fraction that have properties similar to those of genuine photons. As shown in Figures 4.30 and 4.31, in simulated jet events $\sigma_{i\eta i\eta}$ is found to be largely uncorrelated with the isolation requirement. The background shape observed for jets with the sideband tracker isolation should therefore be the same as that for isolated jets.

The $\sigma_{i\eta i\eta}$ distribution in data are fit to

$$f(\sigma_{i\eta i\eta}) = N_S S(\sigma_{i\eta i\eta}) + N_B B(\sigma_{i\eta i\eta}), \tag{4.11}$$

where N_S and N_B are the expected number of signal and background candidates. $S(\sigma_{i\eta i\eta})$ and $B(\sigma_{i\eta i\eta})$ are the signal and background component 'templates'. The 'templates' are smoothed using kernel density estimation [28] or direct interpolation, in the case of high template statistics. This allows to perform unbinned fits of the $\sigma_{i\eta i\eta}$ distribution of selected photons, preserving the performance of the fit in low statistics scenarios.

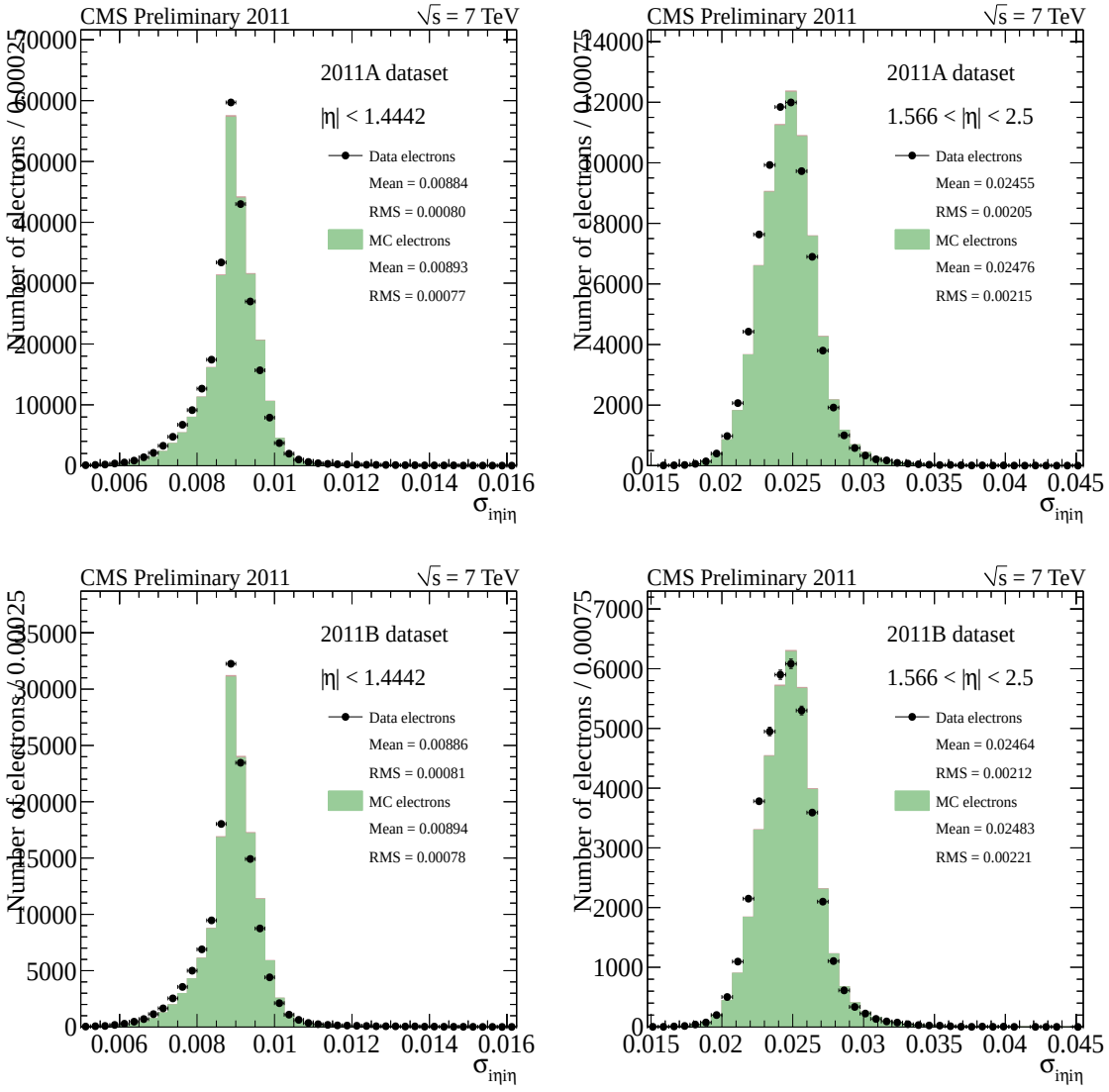

Figure 4.28: The $\sigma_{i\eta i\eta}$ distributions for barrel (left) and endcap (right). The difference of mean values between simulation (filled green histograms) and data (black dots) are accounted for by shifting the simulation signal shapes.

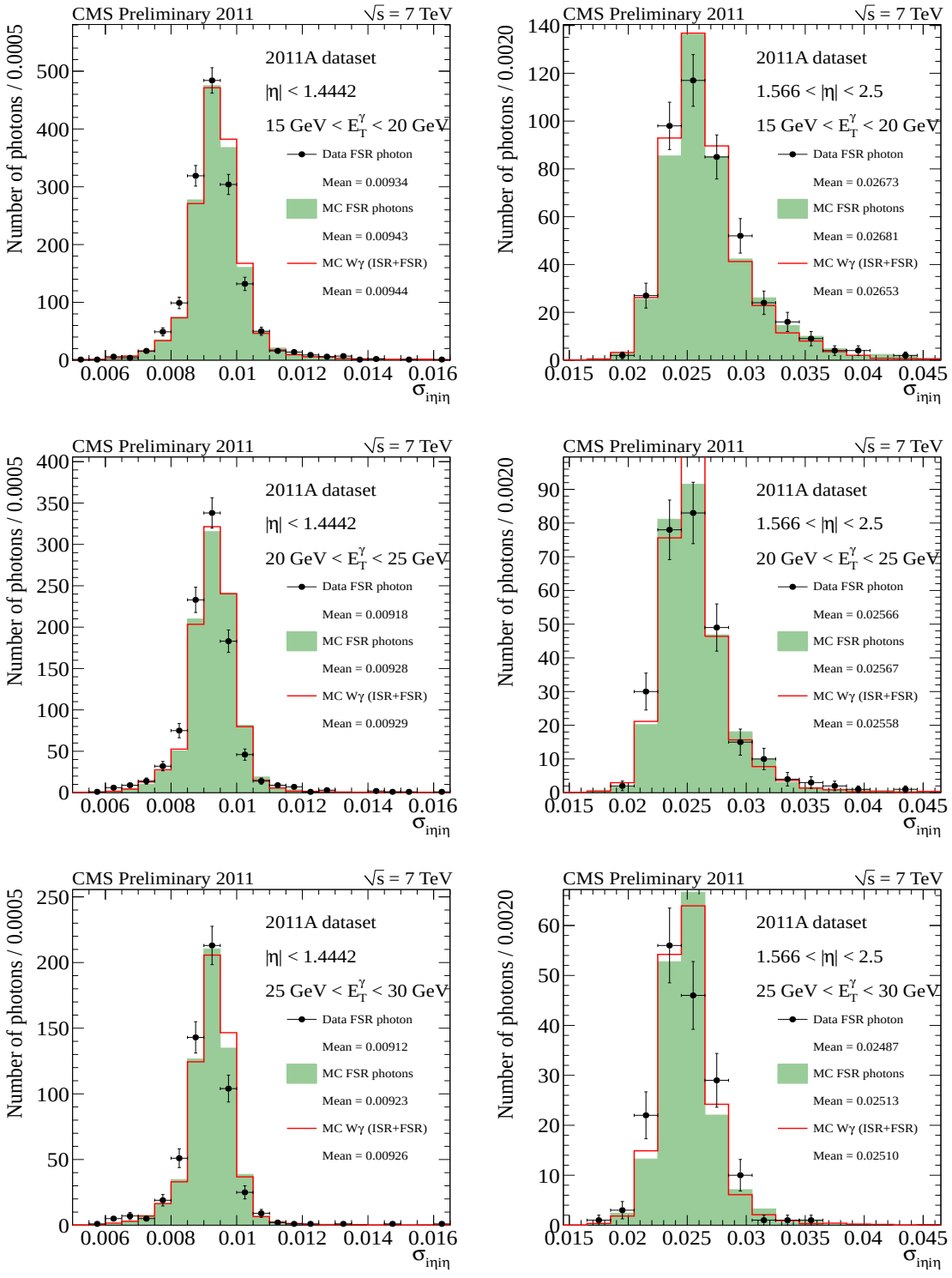

Figure 4.29: The $\sigma_{i\eta i\eta}$ distributions for barrel (left) and endcap (right) in different E_T^γ bins ($15-20$ GeV, $20-25$ GeV, and $25-30$ GeV). Data FSR photon is shown in black dots, simulated FSR photon is shown in filled green histogram, and photon from simulation $W\gamma$ is shown in red histogram.

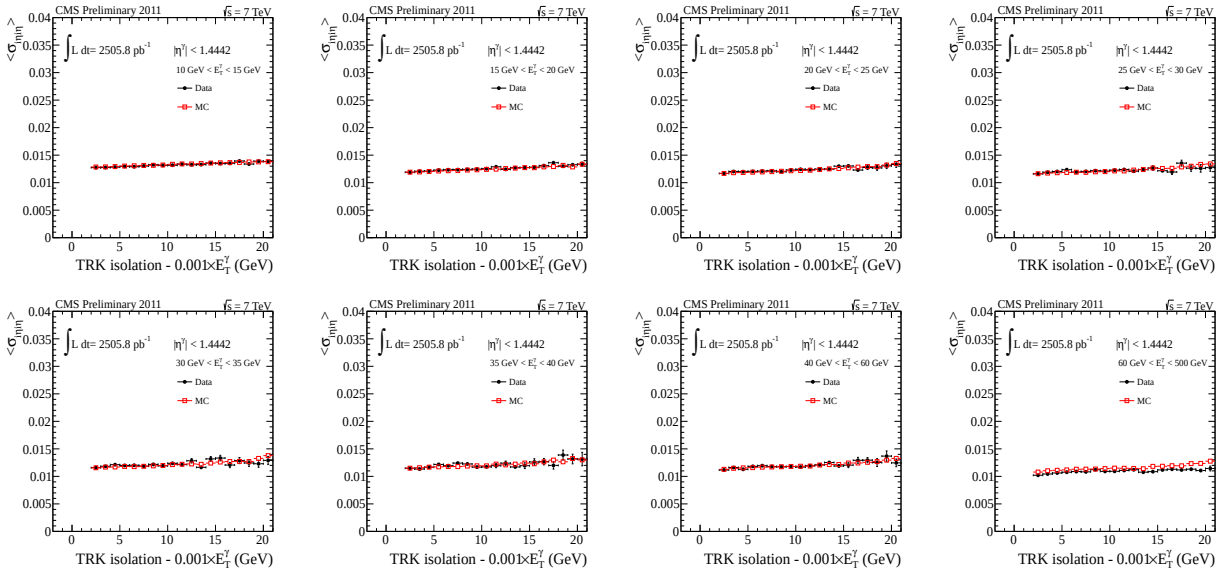

Figure 4.30: The correlation between $< \sigma_{i\eta i\eta} >$ and Iso_{TRK} for each E_{T}^{γ} bin in the barrel region.

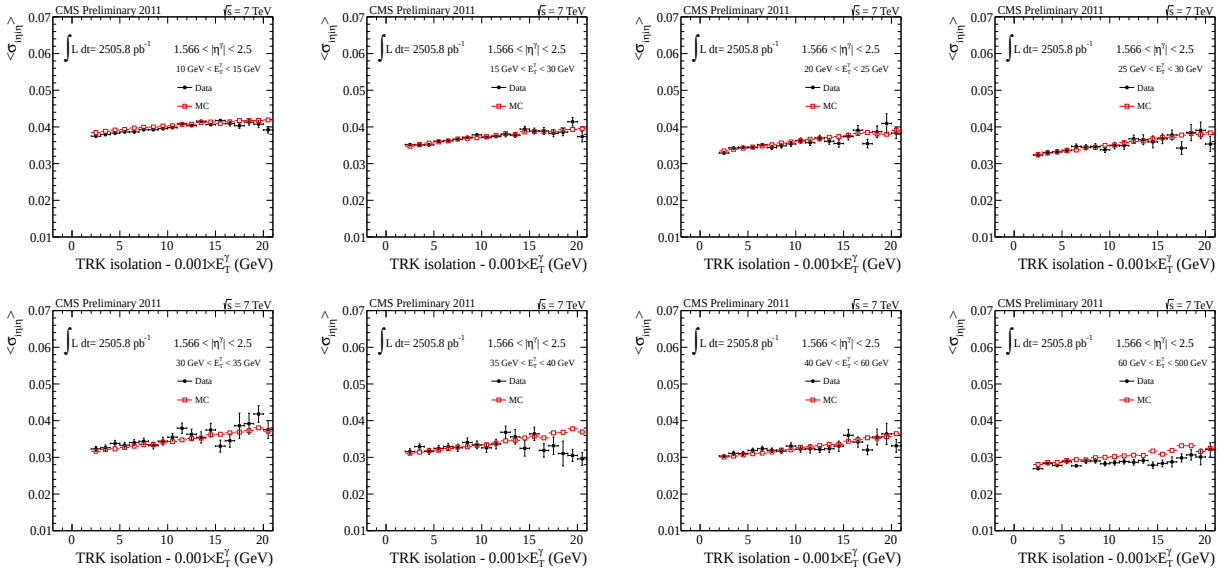

Figure 4.31: The correlation between $<\sigma_{i\eta i\eta}>$ and Iso_{TRK} for each E_{T}^{γ} bin in the endcap region.

The fit is performed by using an unbinned extended maximum likelihood, by minimizing:

$$-\ln L = (N_S + N_B) - N\ln(N_S S(\sigma_{i\eta i\eta}) + N_B B(\sigma_{i\eta i\eta})). \tag{4.12}$$

where N is the total number of data events in the given E_{T}^{γ} bin.

The unbinned fit results for the lowest and statisticaly most important E_{T}^{γ} bin, 15-20 GeV, are shown in Figure 4.32 for photon candidates in the barrel and in the endcaps.

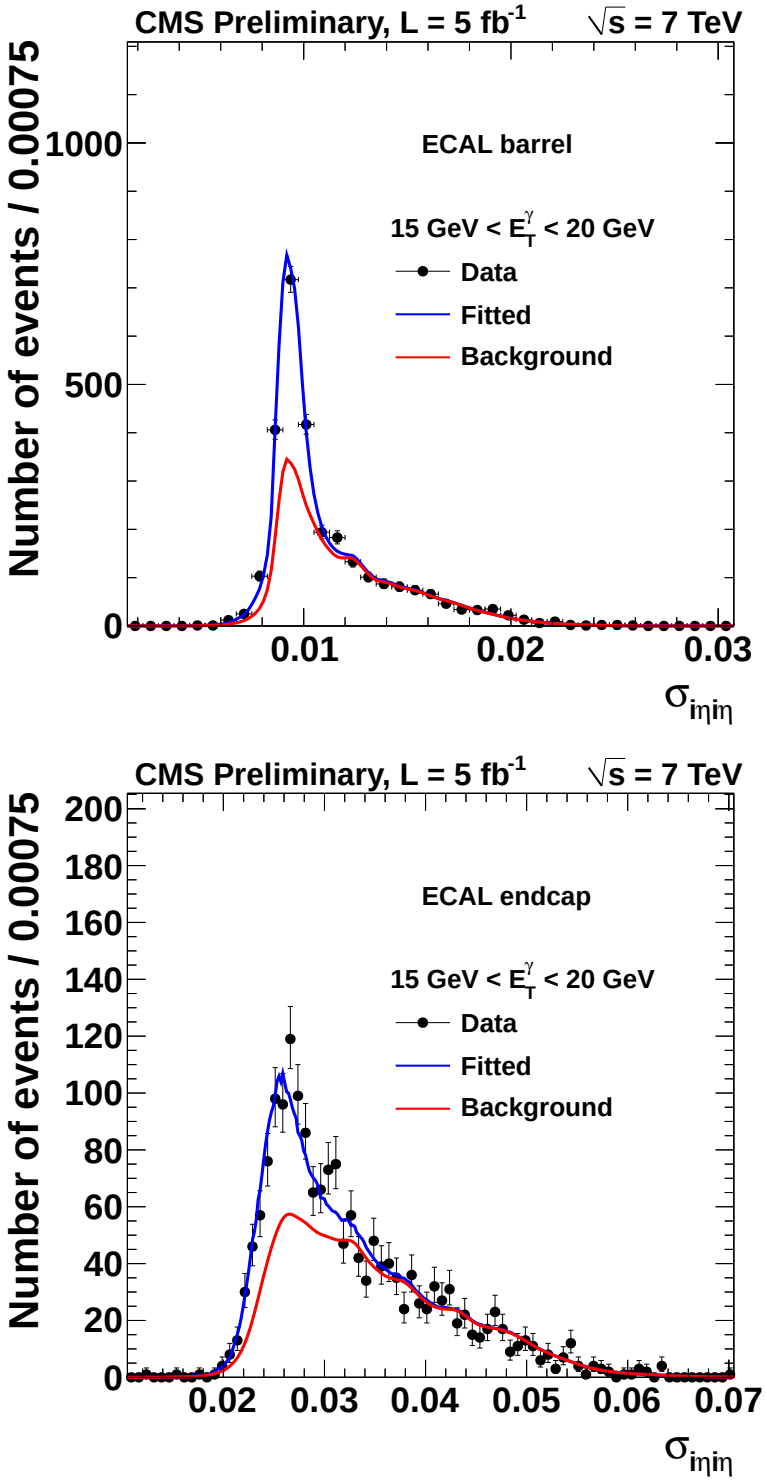

Figure 4.32: The $\sigma_{i\eta i\eta}$ distributions for the selected $W\gamma \to \mu\nu\gamma$ events in data (black squares) with photon candidates identified in the barrel (upper plot) and in the endcap (lower plot) for 2011A+2011B with the E_{T}^{γ} of 15-20 GeV. The unbinned fit result is shown by the blue solid line, and the background component is shown in red.

'Ratio method'

A second method refereed to as the 'ratio method' is used to infer the jet misidentification background as a cross-check to the results of the 'template method' at high $E_{\mathrm{T}}^{\gamma} > 60$ GeV where the 'template method' is subject to larger systematic uncertainties. This method takes advantage of the relatively high statistics in the $\gamma + jets$ data sample and the expected similarity between the misidentification rate for jets in $\gamma + jets$ sample and $W + jets$. This method can thus provide a higher precision estimate of the misidentified jet background at large E_{T}^{γ}.

This method exploits a category of jets that have similar properties to electromagnetic objects in the ECAL; these jets are called 'photon-like jets' ('plJets'). 'Photon-like jets' are selected by identifying a reconstructed photon which fails the photon isolation or the $\sigma_{i\eta i\eta}$ requirements of the final photon selection ('tight photon'), but are more isolated and have a higher electromagnetic fraction than most hadronic jets. The 'ratio method' measures the ratio R_p:

$$R_p = \frac{\text{probability of a jet to pass the 'tight photon' criteria}}{\text{probability of a jet to pass the 'plJet' criteria}}. \tag{4.13}$$

Once R_p is known, the number of selected $W\gamma$ events where jets satisfy the final photon selection criteria, $N_{\mathrm{W+jet}}$, can be estimated as the product of R_p and the number of $W+$'plJets' counted in data:

$$N_{\mathrm{W+jet}} = R_p \cdot N_{\mathrm{W+plJet}}, \tag{4.14}$$

where $N_{\mathrm{W+plJet}}$ is the number of events in data with an identified W boson, passing W selection requirements, and at least one 'plJet'.

The R_p value depends on the calorimeter response (different for barrel and endcap), P_T of jet and jet type. It is expected to be different for gluon and quark jets due to the difference in typical shower width . Therefore R_p is measured for each E_{T}^{γ} bin separately for the ECAL barrel and endcaps. To be able to measure R_p for quark-to-gluon fraction in the $W + jet$ process, the R_p for $\gamma + jet$ and

$jet + jet$ processes are measured in data since, as shown in Figure 4.33 using the simulation, the R_p for $W + jet$ is between the two.

Since there are now two objects (γ and jet) in the event, the ratio method is expanded to the two object case. Having $\gamma + jet$ and $jet + jet$ processes, one can have two 'tight photons' reconstructed, or one 'tight photon' and one 'plJet' or two 'plJets'. There is one more process that can result with the same signatures, $\gamma + \gamma$.

Summary table can be found in Table 4.10, where g is probability of a true photon to pass the 'plJet' criteria and h probability to pass the 'tight photon' criteria. The R_p for the $\gamma + jet$ and the $jet + jet$ process can be written as:

$$R_p(\gamma + jet) = \frac{f'}{e'}, R_p(jet + jet) = \frac{f}{e}. \tag{4.15}$$

where $f(f')$ is the probability of a jet to pass the tight photon criteria and $e(e')$ is the probability of a jet to pass the 'plJet' criteria.

The number of events with two 'plJets' (N'_{plJplJ}), with one 'plJet' and one 'tight photon' (N'_{TplJ}) and with two 'tight photons' (N'_{TT}) are observed. Assuming $g = 0$, the number of $jet + jet$ resulting in two 'plJets' can be observed directly since there are no competing entries in the 'plJet'+'plJet' column. Contributions from different processes in the 'Tight'+'plJet' column can be separated with a one dimensional $\sigma_{i\eta i\eta}$ template fit on the 'tight' photon. The jet $\sigma_{i\eta i\eta}$ 'templates' are constructed out of the 'plJets' in data and the photon 'templates' taken are from simulation. Separating the 'Tight'+'Tight' column into its elements can be done using a two dimensional $\sigma_{i\eta i\eta}$ template fit. A ratio that targets the fake rate from $jet + jet$ can be constructed without using 2D template fitting:

$$R_p(jet + jet) = \frac{f}{e} = \frac{1}{2} \cdot \frac{2feN_{JJ}}{e^2 N_{JJ}}, \tag{4.16}$$

and with the 2D 'template' fitting one can target the fake rate from $\gamma + jet$:

$$R_p(\gamma + jet) = \frac{f'}{e'} = \frac{f'hN_{\gamma J}}{e'hN_{\gamma J}} \tag{4.17}$$

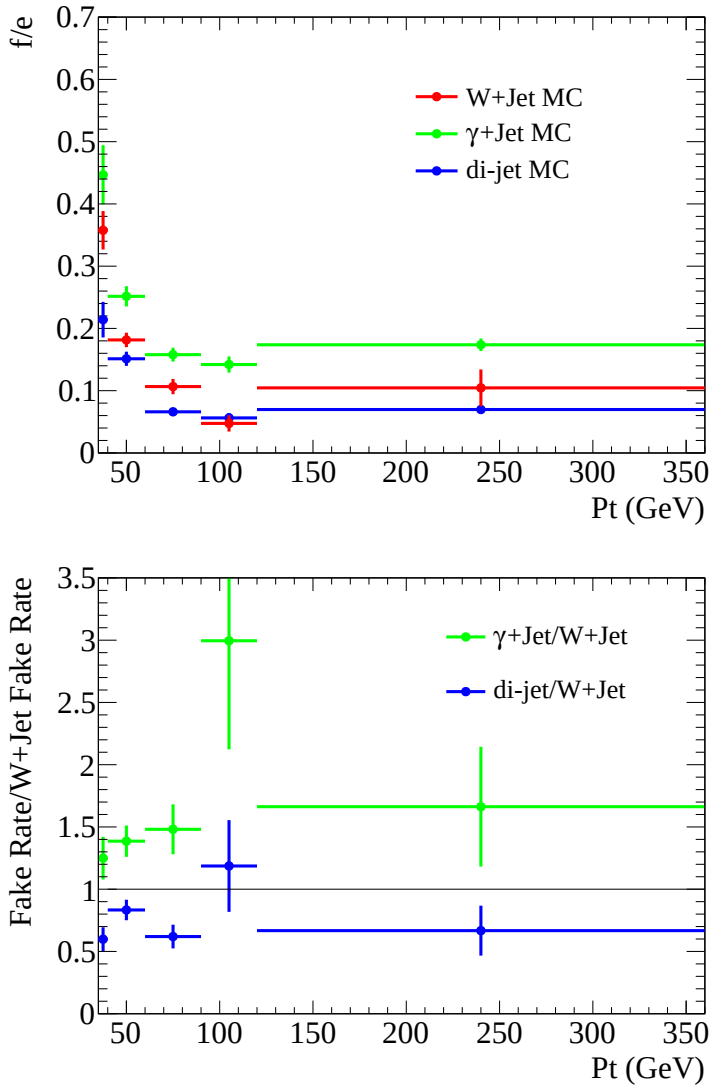

Figure 4.33: Above: Comparison of the fake rates for $W + jet$, $\gamma + jet$ and $jet + jet$ in simulation. The $\gamma + jet$ and $W + jet$ fake rates are not identical. Instead the $W + jet$ fake rate lies between that of $\gamma + jet$ and $jet + jet$. Below: Correction factors to adjust the $\gamma + jet$ and $jet + jet$ fake rate curves to emulate the $W + jet$ fake rate.

To measure the R_p value for a given bin of E_{T}^{γ} two electromagnetic objects are required to be both either in barrel or endcap, and to have E_{T} in the same bin.

		'Tight'+'Tight'	'Tight'+'plJet'	'plJet'+'plJet'	Other
		N'_{TT}	N'_{TplJ}	N'_{plJplJ}	
$\gamma+\gamma$	$N_{\gamma\gamma}$	$n_{\gamma\gamma-to-TT}$ $= h^2 N_{\gamma\gamma}$	$n_{\gamma\gamma-to-TplJ}$ $= 2gh \approx 0$	$n_{\gamma\gamma-to-plJplJ}$ $= g^2 N_{JJ} \approx 0$	>0
γ+Jet	$N_{\gamma J}$	$n_{\gamma J-to-TT}$ $= f'hN_{\gamma J}$	$n_{\gamma J-to-TplJ}$ $(+\, n_{\gamma J-to-plJT})$ $= e'h\ (+\, f'g \approx 0)N_{\gamma J}$	$n_{\gamma J-to-plJplJ}$ $= e'gN_{\gamma J} \approx 0$	$>>0$
Jet+Jet	N_{JJ}	$n_{JJ-to-TT}$ $= f^2 N_{JJ}$	$n_{JJ-to-TplJ}$ $= 2feN_{JJ}$	$n_{JJ-to-plJplJ}$ $= e^2 N_{JJ} \approx N'_{plJplJ}$	$>>0$

Table 4.10: Summary of probabilities for the two particle case.

In addition a correction factor $\alpha \approx 5-10\%$ is applied to account for the case where genuine photons satisfy 'plJet' definitions. The correction is derived from simulation and checked using Z$\rightarrow$ *ee* data and simulation.

The measured R_p values for the ECAL barrel are given in Figure 4.34. Simulation is used to compare the expected R_p values in $W+jet$, $\gamma+jet$ and $jet+jet$ processes. Using the compaison shown in Figure 4.33 measured R_p values for $\gamma+jet$ and $jet+jet$ processes are corrected for the difference to match the $W+jet$ process.

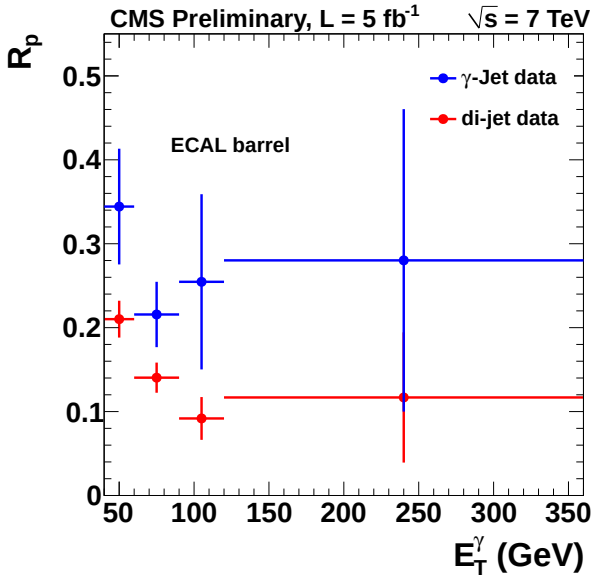

Figure 4.34: R_p as a function of photon candidate E_{T}^{γ} for barrel ECAL in $\gamma+jet$ and multijet QCD sample ($jet+jet$). The difference in R_p values between two processes is due to the fact that jets in $\gamma+jet$ process are dominated by quark fragmentation, while those in $jet+jet$ are dominated by gluon fragmentation.

The result of the 'ratio method' has a greater reliance on simulation than the 'template method'. It is found to be in agreement with the 'template method'. The 'ratio method' is therefore used in this study as an estimate for systematic uncertainty rather than as a direct estimation of the background.

Results

Table 4.11: Background from jets misidentified as photons for $W\gamma \to \mu\nu\gamma$ estimated with 'template method' for 2011A and 2011B.

E_{T}^{γ}, GeV	Background yields (2011A)	Background yields (2011B)
	Barrel	
15-20	834.8 ± 22.5(stat.) ± 28.7(syst.)	1006.4 ± 24.4(stat.) ± 40.7(syst.)
20-25	317 ± 15.5(stat.) ± 16.4(syst.)	348.1 ± 15.9(stat.) ± 21.2(syst.)
25-30	142.9 ± 10.4(stat.) ± 9.5(syst.)	164.8 ± 11.4(stat.) ± 12.3(syst.)
30-35	98.5 ± 8.6(stat.) ± 8.1(syst.)	120.4 ± 9.6(stat.) ± 11.9(syst.)
35-40	51.8 ± 6.5(stat.) ± 5(syst.)	66.9 ± 8.1(stat.) ± 7.4(syst.)
40-60	75.1 ± 8.4(stat.) ± 9.4(syst.)	105.4 ± 10.1(stat.) ± 13.7(syst.)
60-90	27.1 ± 5.2(stat.) ± 5.4(syst.)	41.6 ± 7.3(stat.) ± 8.6(syst.)
90-500	20.3 ± 6.8(stat.) ± 16.7(syst.)	34.5 ± 9.8(stat.) ± 28.5(syst.)
MET correlation	± 203.8(syst.)	± 245.4(syst.)
Δ(ratio vs template)	± 1.6 (syst.)	± 50.3(syst.)
Total	1567.5 ± 33.4(stat.) ± 207.9(syst.)	1888.1 ± 37.2(stat.) ± 257.5(syst.)
	Endcap	
15-20	417 ± 12.6(stat.) ± 29(syst.)	430.7 ± 12.4(stat.) ± 40.3(syst.)
20-25	185.1 ± 9.4(stat.) ± 15.3(syst.)	236.3 ± 10.4(stat.) ± 20.8(syst.)
25-30	81.6 ± 6.6(stat.) ± 9.1(syst.)	140.5 ± 9.3(stat.) ± 14.9(syst.)
30-35	56.2 ± 5.7(stat.) ± 7.4(syst.)	51 ± 5.8(stat.) ± 9.4(syst.)
35-40	44 ± 5.1(stat.) ± 4.9(syst.)	31 ± 4.9(stat.) ± 6.3(syst.)
40-60	40.3 ± 6.4(stat.) ± 7.6(syst.)	51.9 ± 7.1(stat.) ± 11.3(syst.)
60-90	18.2 ± 4.3(stat.) ± 4.3(syst.)	22.2 ± 5.3(stat.) ± 7.1(syst.)
90-500	7.3 ± 5.3(stat.) ± 12.3(syst.)	16.5 ± 6.6(stat.) ± 20.9(syst.)
MET correlation	± 59.5(syst.)	± 68.6(syst.)
Δ(ratio vs template)	± 13.4 (syst.)	± 21.3(syst.)
Total	849.7 ± 20.9(stat.) ± 72.0(syst.)	980.1 ± 23.0(stat.) ± 90.4(syst.)
	Barrel + Endcap	
15-20	1251.8 ± 25.8(stat.) ± 40.8(syst.)	1437.1 ± 27.4(stat.) ± 57.3(syst.)
20-25	502.1 ± 18.1(stat.) ± 22.4(syst.)	584.4 ± 19.0(stat.) ± 29.7(syst.)
25-30	224.5 ± 12.3(stat.) ± 13.2(syst.)	305.3 ± 14.7(stat.) ± 19.3(syst.)
30-35	154.7 ± 10.3(stat.) ± 11.0(syst.)	171.4 ± 11.2(stat.) ± 15.2(syst.)
35-40	95.8 ± 8.3(stat.) ± 7.0(syst.)	97.9 ± 9.5(stat.) ± 9.7(syst.)
40-60	115.4 ± 10.6(stat.) ± 12.1(syst.)	157.3 ± 12.3(stat.) ± 17.8(syst.)
60-90	45.3 ± 6.7(stat.) ± 6.9(syst.)	63.8 ± 9.0(stat.) ± 11.2(syst.)
90-500	27.6 ± 8.6(stat.) ± 20.7(syst.)	51 ± 11.8(stat.) ± 35.3(syst.)
MET correlation	± 212.3(syst.)	± 254.9(syst.)
Δ(ratio vs template)	± 11.8 (syst.)	± 71.5(syst.)
Total	2417.3 ± 39.4(stat.) ± 219.9(syst.)	2868.2 ± 43.7(stat.) ± 276.8(syst.)

The background estimation of jets misidentified as photons using the 'template method' and 'ratio method' for the $\mu\nu\gamma$ final state are shown in Figure 4.35. Results using the 'template method' are summarized in Table 4.11 and 4.12 including the systematic uncertainties described in Section 4.4.4. The estimated background is 2417.3 ± 39.4 (stat.) ± 219.9 (syst.) events in 2011A, 2868.2 ± 43.7 (stat.) ± 276.8 (syst.) events in 2011B and 5345.9 ± 58.2 (stat.) ± 482.6 (syst.) events in 2011A+2011B combined using the 'template method'.

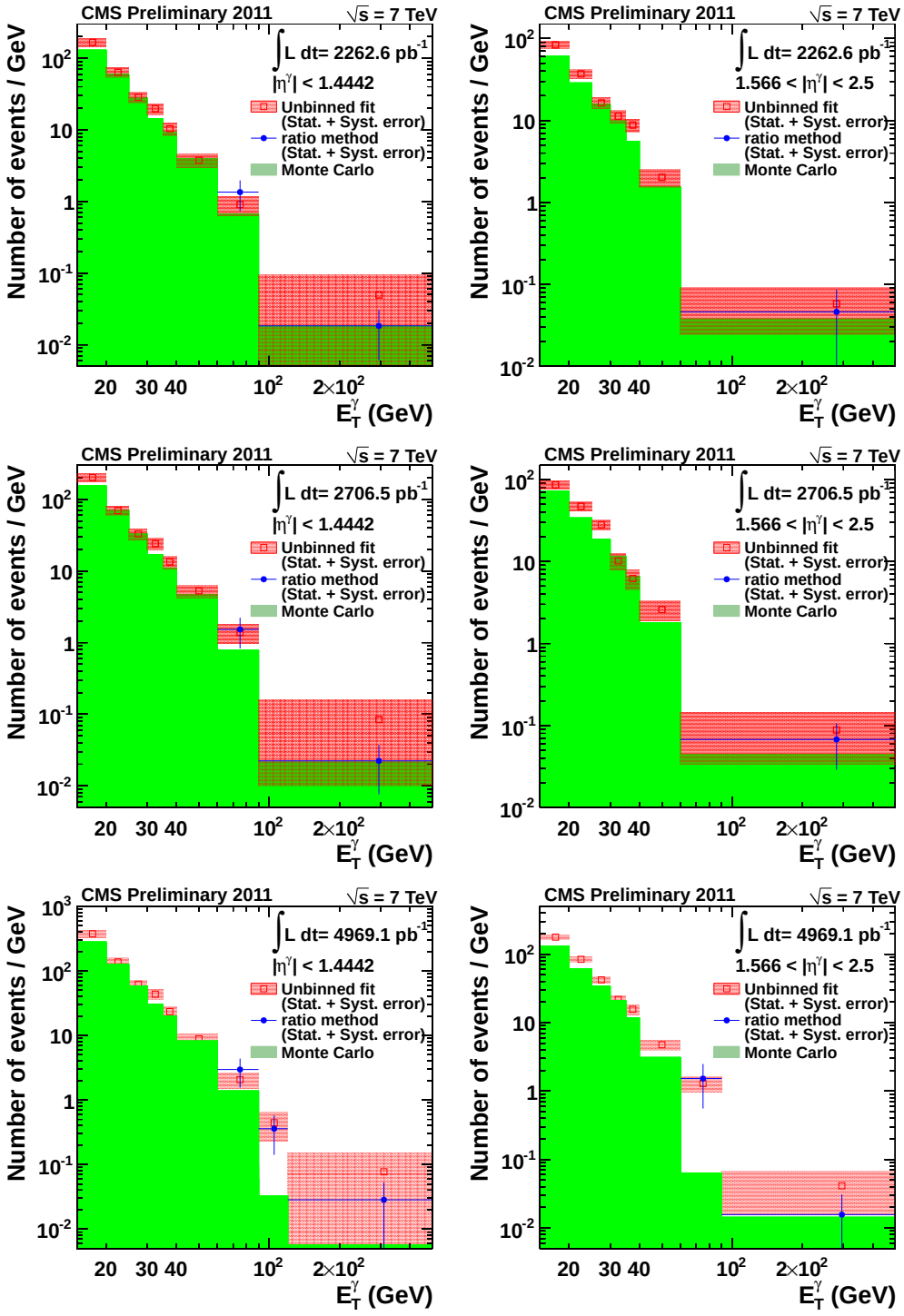

Figure 4.35: Estimated background from jets misidentified as photons for $W\gamma \to \mu\nu\gamma$ for the barrel (left) and endcap (right) photon candidates, for 2011A (top), 2011B (middle) and 2011A+2011B combined (bottom). The 'template method' fit results are shown in red, the 'ratio method' results in blue, and background prediction from simulation as filled histograms.

Table 4.12: Background from jets misidentified as photons for $W\gamma \to \mu\nu\gamma$ estimated with 'template method' for 2011A+2011B combined.

E_{T}^{γ} , GeV	Background yields (2011A+2011B)
Barrel	
15-20	1876.4 ± 32.4(stat.) ± 62.4(syst.)
20-25	688.2 ± 22.3(stat.) ± 37.8(syst.)
25-30	310.9 ± 15.3(stat.) ± 21.2(syst.)
30-35	217.6 ± 13(stat.) ± 17.4(syst.)
35-40	116.7 ± 10.4(stat.) ± 11.1(syst.)
40-60	177.5 ± 13.1(stat.) ± 22.1(syst.)
60-90	61.9 ± 7.8(stat.) ± 12.3(syst.)
90-120	13.3 ± 4.5(stat.) ± 4.2(syst.)
120-500	29.3 ± 10.2(stat.) ± 25.4(syst.)
MET correlation	± 453.9(syst.)
Δ(ratio vs template)	± 16.2 (syst.)
Total	3491.8 ± 49.1(stat.) ± 462.4(syst.)
Endcap	
15-20	886.5 ± 18(stat.) ± 36.4(syst.)
20-25	420.1 ± 14(stat.) ± 21.2(syst.)
25-30	210.7 ± 10.7(stat.) ± 16.3(syst.)
30-35	108.7 ± 8.4(stat.) ± 10.8(syst.)
35-40	78.1 ± 7.5(stat.) ± 8.8(syst.)
40-60	94.8 ± 10(stat.) ± 10.1(syst.)
60-90	38.6 ± 6.8(stat.) ± 6.3(syst.)
90-120	8.1 ± 4.7(stat.) ± 2.2(syst.)
120-500	8.8 ± 7.0(stat.) ± 5.6(syst.)
MET correlation	± 129.8(syst.)
Δ(ratio vs template)	± 9.2 (syst.)
Total	1854.4 ± 31.3(stat.) ± 139.1(syst.)
Barrel + Endcap	
15-20	2762.9 ± 37.1(stat.) ± 72.3(syst.)
20-25	1108.3 ± 26.3(stat.) ± 43.3(syst.)
25-30	521.6 ± 18.7(stat.) ± 26.7(syst.)
30-35	326.3 ± 15.5(stat.) ± 20.5(syst.)
35-40	194.8 ± 12.8(stat.) ± 14.2(syst.)
40-60	272.3 ± 16.5(stat.) ± 24.3(syst.)
60-90	100.5 ± 10.3(stat.) ± 13.8(syst.)
90-120	21.4 ± 6.5(stat.) ± 4.7(syst.)
120-500	38.1 ± 12.4(stat.) ± 26.0(syst.)
MET correlation	± 472.1(syst.)
Δ(ratio vs template)	± 7.0 (syst.)
Total	5345.9 ± 58.2(stat.) ± 482.6(syst.)

4.3.2 Background from electrons misidentified as photons

The criterion that allows to separate electrons from photons is the requirement of no pixel hit associated with the photon candidate. The probability P for an electron to have no pixel hit match is measured in a $Z \to ee$ data sample using the 'tag-and-probe' method. Fitting the dielectron invariant mass distribution with a convolution of a Breit–Wigner and Crystal Ball function to describe the signal and an 'exponential decay + error' function for the background, the efficiency of an electron to have associated pixel hit is obtained to be $P = 0.9858 \pm 0.002$ (syst.) for barrel and $P = 0.9710 \pm 0.004$ (syst.) for endcap in the 2011A data set, $P = 0.9873 \pm 0.003$ (syst.) for barrel and $P = 0.9727 \pm 0.003$ (syst.) for endcap in the 2011B data set, and $P = 0.014 \pm 0.003$ (syst.) for barrel and $P = 0.028 \pm 0.004$ (syst.) for endcap in 2011A+2011B combined. The difference between fitting and simple counting method results is assigned as systematic uncertainty. To estimate the background from electron misidentification in $W\gamma \to \mu\nu\gamma$ channel, events that pass the full selection criteria are selected, in which the photon candidate is however required to have associated pixel hit. This electron-like selection will yield $N_{\mu\nu e}$ selected events. Then the background contribution from genuine electrons misidentified as photons is calculated from:

$$N_{e\to\gamma} = N_{\mu\nu e} \times \frac{P}{1-P} \quad , \tag{4.18}$$

This background is found to be 44.0 ± 1.0 (stat.) ± 3.3 (syst.) in 2011A, 47.3 ± 1.0 (stat.) ± 3.40 (syst.) in 2011B and 91.4 ± 1.4 (stat.) ± 4.7 (syst.) in 2011A+2011B combined.

4.3.3 Summary of backgrounds

The expected background contributions from all considered sources for the $W\gamma \to \mu\mu\gamma$ final state is summarized in Table 4.13 for 2011A and 2011B and in Table 4.14 for 2011A+2011B data sets combined.

Table 4.13: Summary of background contributions in $W\gamma \to \mu\mu\gamma$ final state for 2011A and 2011B data set. The quoted fake photon background yield is determined by the 'template method'.

Background source	Background yield	
	2011A	2011B
Fake photons (misid. jets)	2417.3 ± 39.4 (stat.)± 219.9 (syst.)	2868.2 ± 43.7 (stat.) ± 276.8 (syst.)
Fake photons (misid. electrons)	44.0 ± 1.0 (stat.) ± 3.3 (syst.)	47.3 ± 1.0 (stat.) ± 3.4 (syst.)
Fake leptons	negligible	negligible
$W(\tau\nu)\gamma$	11.9 ± 1.9 (stat.) ± 1.1 (syst.)	18.0 ± 2.4 (stat.) ± 1.8 (syst.)
$Z\gamma$	149.8 ± 10.5 (stat.) ± 9.0 (syst.)	188.6 ± 11.6 (stat.) ± 11.3 (syst.)
$t\bar{t}\gamma$	16.9 ± 0.6 (stat.) ± 8.5 (syst.)	18.9 ± 0.7 (stat.) ± 9.5 (syst.)

Table 4.14: Summary of background contributions in $W\gamma \to \mu\mu\gamma$ final state for 2011A+2011B data sets combined. The quoted fake photon background yield is determined by the 'template method'.

Background source	Background yield
	2011A+2011B
Fake photons (misid. jets)	5345.9 ± 58.2 (stat.) ± 482.6 (syst.)
Fake photons (misid. electrons)	91.4 ± 1.4 (stat.) ± 4.7 (syst.)
Fake leptons	negligible
$W(\tau\nu)\gamma$	28.9 ± 3.4 (stat.) ± 2.7 (syst.)
$Z\gamma$	338.0 ± 18.3 (stat.) ± 20.3 (syst.)
$t\bar{t}\gamma$	35.9 ± 1.0 (stat.) ± 17.9 (syst.)

4.4 Systematic uncertainties

Systematic uncertainties are grouped into five categories:

- Uncertainties that affect the signal yield.
- Uncertainties that affect the acceptance and efficiency.
- Uncertainties that affect the efficiency correction factor.
- Uncertainties that affect the background yield.
- Uncertainties that affect the luminosity.

4.4.1 Uncertainties on signal yield

Uncertainties on the signal yield include uncertainties on muon and photon energy scales. Uncertainties on energy scales are determined using the Z resonance position measurements. For photons the energy scale is varied by 1% in the barrel and 3% in the endcaps. For muons, the P_T scale is varied by 0.2%. To estimate the systematic effect on the measured cross section N_{sig} is re-evaluated for variations of each source of systematic uncertainty. For the variation of the photon energy scale, the background subtraction is performed with signal and background 'templates' that are appropriately modified. This ensures that migrations of photons and misidentified jets across the low E_{T}^{γ} boundaries are properly accounted for when calculating this systematic uncertainty.

4.4.2 Uncertainties on acceptance and efficiency

The uncertainties that affect the product of the acceptance, reconstruction and identification efficiencies of final state objects are combined and determined from simulation. These include uncertainties on muon and photon energy resolution, effects from pile-up interactions, and uncertainties in the parton distribution functions (PDFs).

The combined acceptance times efficiency, $\mathscr{F} \equiv A \cdot \varepsilon_{\text{gen}}$, is determined from the simulation of the $W\gamma$ signal and is affected by the muon and photon energy resolution by way of migration of events in and out of acceptance. It is known that the resolution in simulation is better then the actual resolution in data. The energy in simulation is thus additionally smeared by a Gaussian function to match the resolution in data. The photon energy resolution is determined simultaneously with the photon energy scale in data following the method described in Sec. 4.2.4.

The number of PU interactions per event is estimated from data using a convolution procedure that extracts the estimated PU from the per-bunch instantaneous luminosity recorded by the luminosity monitors. This methodology uses the total inelastic pp scattering cross section, 68 ± 3.4 mb, to estimate the number of PU events in a given bunch crossing. The systematic uncertainty due to the modeling of PU interactions is estimated by varying the total inelastic cross section within its uncertainties, and estimate its effect on $\mathscr{F}$.

The uncertainties on parton distribution functions can alter the acceptance in simulation, especially for very forward, low x, $W\gamma$ events. To estimate the systematic effect on $\mathscr{F}$, LHAPDF [30] is used to generate per-event weights using variations along the 21 sets of eigenvectors of the CTEQ6L PDF set [31] following the procedure described in [32].

The uncertainty on signal modeling is taken from the $\mathscr{F}$ difference between different simulation generators.

4.4.3 Uncertainties on efficiency correction factor

Systematic uncertainties on the efficiency correction factor ρ_{eff} include uncertainties of muon trigger, muon and photon reconstruction and identification, and M_T^W selection efficiencies. The muon efficiencies are determined by the 'tag-and-probe' method in the same way for data and simulation, and the uncertainties are taken by varying the background modeling and fit range in the 'tag-and-probe' method. An additional uncertainty is added by taking into account the difference between the measured efficiency by 'tag-and-probe' and the true efficiency in simulation.

4.4.4 Uncertainties on background yield

This category comprises uncertainties on the background yield. These are dominated by the uncertainties on the estimations of background from jets misidentified as photons from data.

Uncertainties on the background from jets misidentified as photons

1. Signal 'template' shape:

   The signal $\sigma_{i\eta i\eta}$ 'template' in simulation needs to be corrected to match $\sigma_{i\eta i\eta}$ templates observed in data as described in Sec. 4.3.1. The difference in background estimate between measurements with corrected and uncorrected 'template' is used as systematic uncertainty.

2. Background 'template' shape:

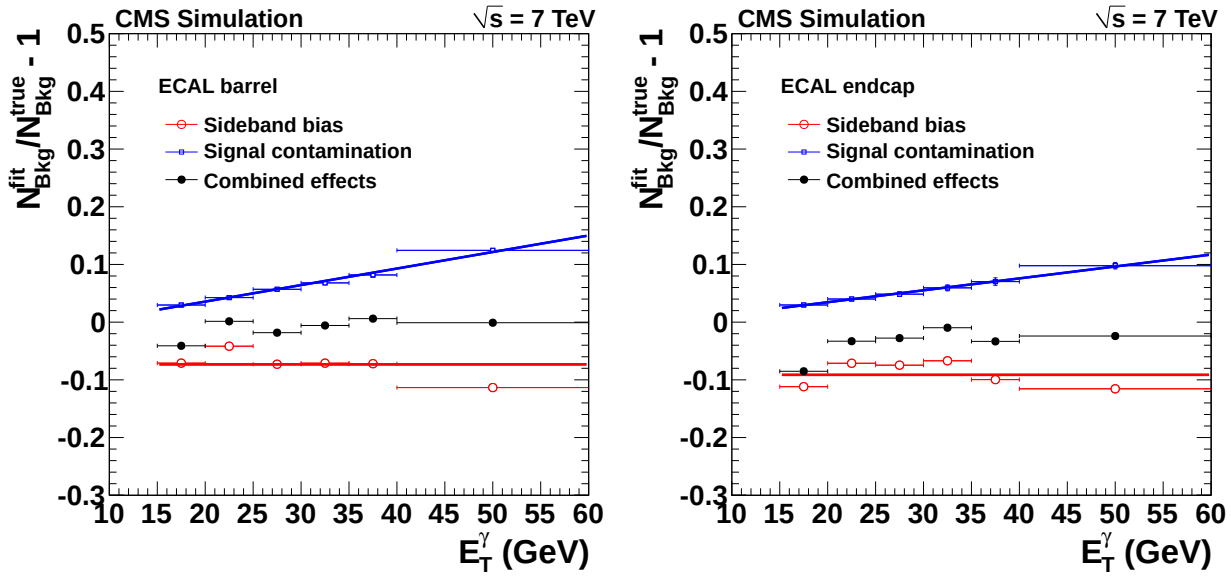

Figure 4.36: The uncertainty on background 'template' for barrel (left) and endcap (right). The change in the estimated number of background events due to anti-isolation requirement (sideband bias) is given as a function of E^{γ}_{T} as red circles, while the contamination from genuine photons are given as blue dots. The overall effect is given as red dots.

To obtain the background $\sigma_{i\eta i\eta}$ 'template' the photon-like jets from data selected by applying the tracker sideband requirement (anti-isolation requirement) are used. Using this 'template'

to infer the background from photon-like jets that pass the full photon isolation requirements can cause a bias if the $\sigma_{i\eta i\eta}$ template is correlated with tracker isolation. A contribution from genuine photons that pass anti-isolation requirement can also cause a bias in the estimation of the background. The effects from these sources are estimated in simulation where one can distinguish genuine photons from jets. The overall effect is found to be small (see Figure 4.36). For the sideband bias, signal 'templates' are from genuine photons from the simulation and background 'templates' are from genuine photon-like jets in simulation in sideband region. Pseudo photons, photons used to perform the fit on, are from simulation and pass photon selection without $\sigma_{i\eta i\eta}$ cut. For signal contamination, signal 'templates' are still from genuine photons and background templates are from photons in sideband region (contains genuine photons and genuine photon-like jets). Pseudo photons are from simulation. Selected genuine photons should pass photon selection without $\sigma_{i\eta i\eta}$ requirement, and selected genuine photon-like jets should pass the sideband selection.

Since smoothing is used to determine a continuous function that describes the $\sigma_{i\eta i\eta}$ distribution of the background, the effect of the statistical sampling of the background probability density function true underlying shape must be understood. To study this, a bootstrapping technique exploiting simulation is used. Using simulated events the random sample of events (where the number of events is the same as the number of events used in data to build the nominal template) are used to build the 'templates' which are then smoothed themselves and used to fit the background fraction in data. The results of each template distribution and fit are saved and the variance associated with the statistical fluctuation in the 'template' is recorded and taken as a systematic uncertainty.

It is noticed that the shape of the $\sigma_{i\eta i\eta}$ background 'template' is correlated with the presence of MET parallel to the photon-like jet. Since the $M_{\mathrm{T}}^{\mathrm{W}}$ requirement is used in $W\gamma$ selection, a presence of MET in the event can bias the background 'template' and affect the background estimate. To estimate this effect the background $\sigma_{i\eta i\eta}$ 'templates' for events where MET $>$ 10 GeV and MET is parallel to the direction of the photon-like jet are derived. Different 'templates' correspond to different $\Delta\phi(MET, \text{photon-like jet})$ requirements. The systematic uncertainty is estimated using the lowest E_T^γ bin only (15 GeV $< E_T^\gamma <$ 20 GeV), as this bin provides the largest background yield, and also it presents the largest control sample to

derive the background 'template'. The largest disagreement from the nominal yield are found to be 13% for barrel and 7% for endcap (as shown on Fig 4.37) and are used as systematic uncertainties.

3. Difference between 'ratio method' and 'template method' background estimates:

   The difference between the background estimation given by the two methods is taken as additional systematic uncertainty in the E_T^γ range where both methods are applicable, that is for $E_T^\gamma > 60$ GeV.

Values of the systematic uncertainties on the estimated background from jets misidentified as photons are summarized in Tables 4.15- 4.17. The largest systematic uncertainties come from the MET correlation. At high E_T^γ values the dominant uncertainty comes from the background 'template' shape.

Uncertainties on the background from electrons misidentified as photons

The systematic uncertainty on the electron misidentification includes the measured systematic uncertainty on the probability P for an electron to have no pixel hit match.

Uncertainties on other backgrounds derived from the simulation

The uncertainties on the smaller background contributions derived from the simulation include the statistical uncertainty of the simulation samples, the systematic uncertainties on the cross section, the photon energy resolution and the selection efficiency due to pile-up effect.

4.4.5 Uncertainties on luminosity

An additional uncertainty of 2.2% [33] due to the measurement of the integrated luminosity is considered.

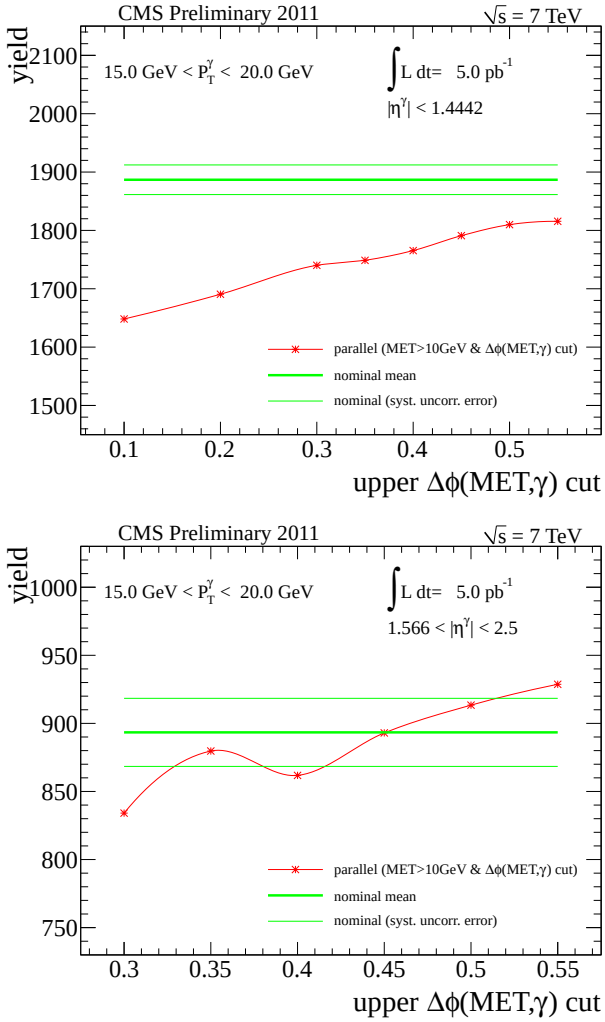

Figure 4.37: Template method background yields using different background templates as the function of upper $\Delta\phi(MET,\gamma)$ cut value.

Table 4.15: Systematic uncertainties on the background from jets misidentified as photons for $W\gamma \to \mu\nu\gamma$ for 2011A data set.

Photon E_T, GeV	Mean yield	Syst. from signal shape	Syst. from background shape	Syst. from sampling sampling of the distribution	Syst. from MET correlation	Syst. from Δ (ratio vs template)
Barrel						
15-20	834.8	7.1	23.8	14.5	108.5	-
20-25	317	5.3	13.6	7.6	41.2	-
25-30	142.9	2.0	8.2	4.5	18.6	-
30-35	98.5	1.6	7.0	3.8	12.8	-
35-40	51.8	0.3	4.4	2.3	6.7	-
40-60	75.1	0.1	9.1	2.4	9.8	1.0
60-90	27.1	0.0	5.2	1.2	3.5	0.4
90-500	20.3	0.3	16.7	0.4	2.6	0.3
Total	1567.5	9.2	35.7	17.7	203.8	1.6
Endcap						
15-20	417	4.3	24.5	15.0	29.2	-
20-25	185.1	2.0	12.6	8.5	13.0	-
25-30	81.6	1.4	7.1	5.4	5.7	-
30-35	56.2	0.8	5.9	4.4	3.9	-
35-40	44	0.0	3.7	3.3	3.1	-
40-60	40.3	0.2	7.3	2.2	2.8	8.2
60-90	18.2	0.7	4.0	1.4	1.3	3.7
90-500	7.3	0.9	12.2	0.4	0.5	1.5
Total	849.7	5.2	32.8	19.1	59.5	13.4
Barrel + Endcap						
15-20	1251.8	8.3	34.1	20.8	112.4	-
20-25	502.1	5.7	18.5	11.4	43.2	-
25-30	224.5	2.5	10.8	7.0	19.4	-
30-35	154.7	1.8	9.2	5.8	13.4	-
35-40	95.8	0.3	5.8	4.0	7.4	-
40-60	115.4	0.2	11.7	3.3	10.2	7.2
60-90	45.3	0.7	6.6	1.8	3.8	2.8
90-500	27.6	1.0	20.7	0.6	2.7	1.7
Total	2417.3	10.6	48.5	26.0	212.3	11.8
		219.9				

4.4.6 Summary of systematic uncertainties

A summary of all systematic uncertainties is given in Table 4.18. The dominant systematic uncertainties are the uncertainty on the 'template method' estimation and the uncertainty from signal modeling.

Table 4.16: Systematic uncertainties on the background from jets misidentified as photons for $W\gamma \to \mu\nu\gamma$ for 2011B data set.

Photon E_T, GeV	Mean yield	Syst. from signal shape	Syst. from background shape	Syst. from sampling sampling of the distribution	Syst. from MET correlation	Syst. from Δ (ratio vs template)
Barrel						
15-20	1006.4	9.5	28.7	27.3	130.8	-
20-25	348.1	3.4	14.9	14.8	45.3	-
25-30	164.8	1.3	9.4	7.8	21.4	-
30-35	120.4	1.2	8.6	8.2	15.7	-
35-40	66.9	2.7	5.7	3.8	8.7	-
40-60	105.4	0.0	12.8	4.8	13.7	29.2
60-90	41.6	1.5	8.0	2.5	5.4	11.5
90-500	34.5	2.5	28.4	0.5	4.5	9.6
Total	1888.1	11.0	47.7	33.7	245.4	50.3
Endcap						
15-20	430.7	4.0	29.5	27.1	30.2	-
20-25	236.3	1.1	13.8	15.6	16.5	-
25-30	140.5	2.5	8.2	12.2	9.8	-
30-35	51.0	0.2	7.3	5.9	3.6	-
35-40	31.0	1.1	4.7	4.1	2.2	-
40-60	51.9	0.4	10.2	4.8	3.6	12.2
60-90	22.2	0.3	6.2	3.5	1.6	5.2
90-500	16.5	1.6	20.8	0.7	1.2	3.9
Total	980.1	5.2	42.2	34.8	68.6	21.3
Barrel + Endcap						
15-20	1437.1	10.3	41.2	38.5	134.3	-
20-25	584.4	3.5	20.3	21.4	48.2	-
25-30	305.3	2.8	12.5	14.4	23.6	-
30-35	171.4	1.2	11.3	10.1	16.1	-
35-40	97.9	2.9	7.4	5.6	9.0	-
40-60	157.3	0.4	16.4	6.8	14.2	41.4
60-90	63.8	1.5	10.1	4.3	5.6	16.8
90-500	5.0	3.0	35.2	0.9	4.6	13.4
Total	2868.2	12.2	63.7	48.4	254.9	71.5
		276.8				

Table 4.17: Systematic uncertainties on the background from jets misidentified as photons for $W\gamma \to \mu\nu\gamma$ for 2011A+2011B combined data set.

Photon E_T, GeV	Mean yield	Syst. from signal shape	Syst. from background shape	Syst. from sampling sampling of the distribution	Syst. from MET correlation	Syst. from Δ (ratio vs template)
Barrel						
15-20	1876.4	20.0	59.2	25.4	243.9	-
20-25	688.2	19.2	32.5	13.8	89.5	-
25-30	310.9	8.4	19.5	8.0	40.4	-
30-35	217.6	3.1	17.1	7.1	28.3	-
35-40	116.7	2.4	10.8	4.1	15.2	-
40-60	177.5	0.6	22.1	4.7	23.1	10.2
60-90	61.9	0.8	12.3	2.8	8.1	3.6
90-120	13.3	2.0	3.7	0.5	1.7	0.8
120-500	29.3	1.9	25.4	0.7	3.8	1.7
Total	3491.8	29.4	81.5	31.6	453.9	16.2
Endcap						
15-20	886.5	4.4	36.1	25.0	62.1	-
20-25	420.1	3.0	21.0	12.8	29.4	-
25-30	210.7	4.1	15.7	11.7	14.8	-
30-35	108.7	1.1	10.8	8.5	7.6	-
35-40	78.1	1.5	8.7	6.7	5.5	-
40-60	94.8	0.5	10.1	4.2	6.6	5.8
60-90	38.6	0.2	6.3	2.6	2.7	2.4
90-120	8.1	1.2	1.9	0.7	0.6	0.5
120-500	8.8	0.8	5.6	0.3	0.6	0.5
Total	1854.4	7.1	48.5	72.5	129.8	9.2
Barrel + Endcap						
15-20	2762.9	20.5	59.4	35.6	251.7	-
20-25	1108.3	19.5	33.8	18.8	94.2	-
25-30	521.6	9.4	20.7	14.2	43.0	-
30-35	326.3	3.3	16.9	11.1	29.3	-
35-40	194.8	2.8	11.4	7.9	16.1	-
40-60	272.3	0.7	23.4	6.3	24.0	4.4
60-90	100.5	0.9	13.3	3.8	8.5	1.6
90-120	21.4	2.3	4.1	0.9	1.8	0.4
120-500	38.1	2.1	25.9	0.7	3.9	0.6
Total	5345.9	30.3	83.3	45.4	472.1	7.0
		482.6				

Table 4.18: Summary of systematic uncertainties for the $W\gamma \to \mu\nu\gamma$ cross section measurement.

		2011A	2011B	2011A+2011B
Source	Systematic uncertainty	Effect on N_{sig}		
Photon energy scale	1% (EB), 3% (EE)	3.7%	3.2%	2.9%
Muon P_T scale	0.2%	0.7%	0.8%	0.6%
Total uncertainty on N_{sig}		3.8%	3.3%	3.0%
Source	Systematic uncertainty	Effect on $\mathscr{F} = A \cdot \varepsilon_{gen}$		
Photon energy resolution	1% (EB), 3% (EE)	0.3%	0.1%	0.1%
Muon P_T resolution	0.6%	0.2%	0.1%	0.1%
Pile-up	Shift data PU distribution by $\pm$ 5%	0.6%	0.9%	0.8%
PDF	CTEQ6L reweighting	0.9%	0.9%	0.9%
Signal modeling	5%	5.0%	5.0%	5.0%
Total uncertainty on $\mathscr{F} = A \cdot \varepsilon_{gen}$		5.1%	5.2%	5.1%
Source	Systematic uncertainty	Effect on ρ_{eff}		
Muon trigger	1.5%	1.5%	1.5%	1.5%
Muon reconstruction	0.9%	0.9%	0.9%	0.9%
Muon ID and isolation	0.9%	0.9%	0.9%	0.9%
MET selection	1.1% (mu)	1.1%	1.5%	1.5%
Photon ID and isolation	0.5% (EB), 1.0% (EE)	0.5%	0.5%	0.5%
Total uncertainty on ρ_{eff}		2.3%	2.5%	2.5%
Source	Systematic uncertainty	Effect on background yield		
Template method		9.1%	9.7%	9.0%
Electron misidentification		7.5%	7.2%	5.2%
MC prediction		6.9%	6.6%	6.8%
Total uncertainty on background		8.3%	8.8%	8.3%
Source	Systematic uncertainty	Effect on luminosity		
Luminosity	2.2%	2.2%	2.2%	2.2%

4.5 Results

The number of signal events N_{sig} in 4.2 is obtained by subtracting the estimated number of background events N_{bkg} from the observed number of selected events N_{obs}. Equation 4.2 can therefore be rewritten as:

$$\sigma = \frac{N_{\text{obs}} - N_{\text{bkg}}}{\mathscr{F} \cdot \rho_{\text{eff}} \cdot \mathscr{L}}. \tag{4.19}$$

This is the equation used to measure the $W\gamma$ cross sections since it is well factorized in terms of the classes of systematic uncertainties.

The value of N_{sig} is obtained from the number of observed events and the estimated number of background events using the following relation:

$$N_{\text{sig}} = N_{\text{obs}} - N_{\text{bkg}}^{\text{misid. jets}} - N_{\text{bkg}}^{\text{misid. electrons}} - N_{\text{bkg}}^{\gamma+\text{jets}} - N_{\text{bkg}}^{\text{W}(\tau\nu)\gamma} - N_{\text{bkg}}^{\text{Z}\gamma} - N_{\text{bkg}}^{\text{t}\bar{\text{t}}\gamma}, \tag{4.20}$$

where N_{obs} is the number of selected events in data, $N_{\text{bkg}}^{\text{misid. jets}}$ is the estimated number of background events from jets misidentified as photons derived from data using the 'template method' described in Section 4.3.1, $N_{\text{bkg}}^{\text{misid. electrons}}$ is the estimated number of background events from electrons misidentified as photons derived from data using the method described in Section 4.3.2, $N_{\text{bkg}}^{\gamma+\text{jets}}$ is the estimated number of background events due to the $\gamma+$ *jets* process, $N_{\text{bkg}}^{W(\tau\nu)\gamma}$ is the estimated number of background events due to the $W(\tau\nu)\gamma$ process, $N_{\text{bkg}}^{Z\gamma}$ is the estimated number of background events due to the $Z\gamma$ process, and $N_{\text{bkg}}^{\text{t}\bar{\text{t}}\gamma}$ is the estimated number of background events due to the $\text{t}\bar{\text{t}}\gamma$ process. The last four sources of background result in small number of background events compared to $N_{\text{bkg}}^{\text{misid. jets}}$. They are estimated using the simulation.

After the full set of selection criteria 5014(5795) events are selected in the data set 2011A(2011B). Combining data sets 2011A+2011B, 10809 events are obtained corresponding to a luminosity of 4969.1 pb^{-1}. The full set of parameters used for the cross section measurement is listed in Tables 4.19 and 4.20.

The measured cross sections are:

$$\sigma(pp \to W\gamma \to \mu\nu\gamma)(2011A) = 37.4 \pm 1.3 \text{ (stat.)} \pm 4.3 \text{ (syst.)} \pm 0.8 \text{ (lumi.) pb.}$$

$$\sigma(pp \to W\gamma \to \mu\nu\gamma)(2011B) = 38.7 \pm 1.3 \text{ (stat.)} \pm 4.8 \text{ (syst.)} \pm 0.9 \text{ (lumi.) pb.}$$

$$\sigma(pp \to W\gamma \to \mu\nu\gamma)(2011A + 2011B) = 37.5 \pm 0.9 \text{ (stat.)} \pm 4.4 \text{ (syst.)} \pm 0.8 \text{ (lumi.) pb.}$$

The theoretical NLO cross section is 31.81 ± 1.8 pb., computed with the MCFM generator [34].

A comparison of several kinematic distributions between data and simulation after the full event selection is shown in Figures 4.38-4.40. The ratios of data to simulation for each variable are shown in Figures 4.41- 4.43. The simulated yields of background events are scaled to match the yields derived from data for background from jets misidentified as photons and for background from electrons misidentified as photons. The background distributions are scaled for all distributions except for histograms showing event yields after every selection criteria.

Figure 4.44 shows the cross section measurement results and theoretical NLO cross section.

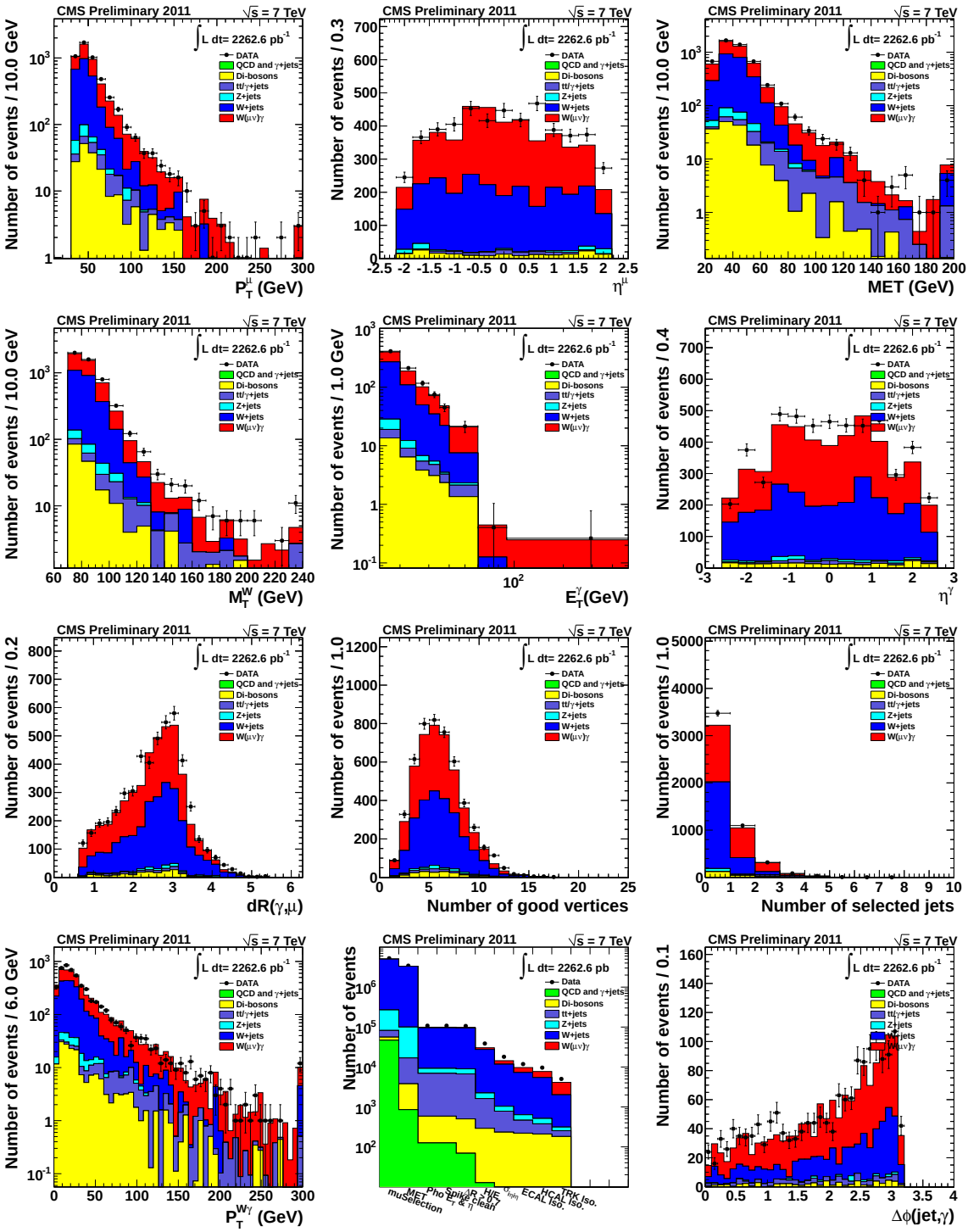

Figure 4.38: Muon candidate trensverse momentum (P_T^{μ}), pseudorapidity (η^{μ}), missing transverse energy (MET), invariant transverse mass of W (M_T^W), photon transverse energy E_T^{γ}, pseudorapidity (η^{γ}), $\Delta R(\mu,\gamma)$, number of good vertices, number of selected jets, $W\gamma$ candidate transverse momentum ($P_T^{W\gamma}$) , event yields after event selection and $\Delta\phi(leading\,jet,\gamma)$ overlaid distributions of the $W\gamma \to \mu\nu\gamma$ candidates in data, signal simulation, and background simulation for 2011A data set.

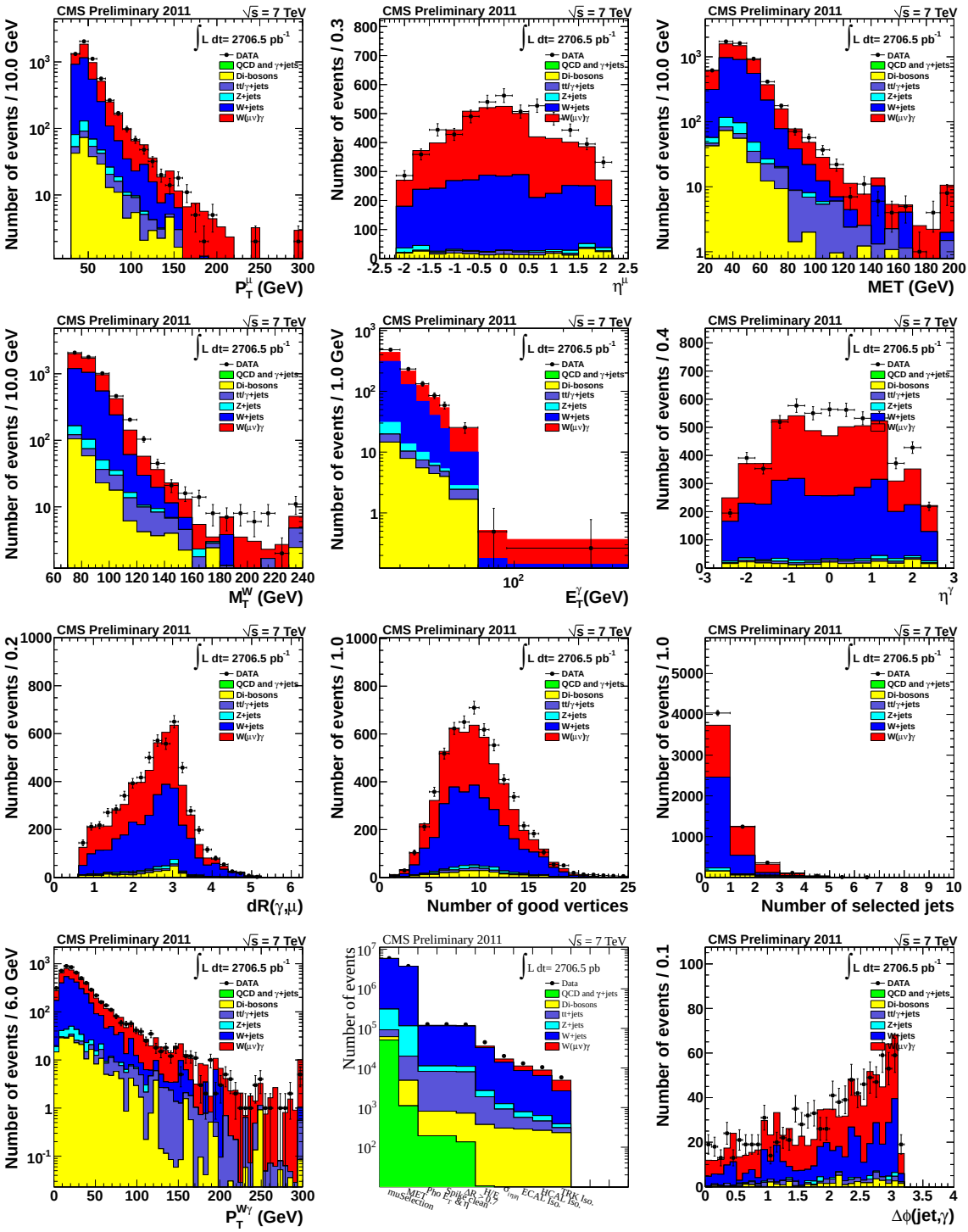

Figure 4.39: Muon candidate trensverse momentum (P_T^{μ}), pseudorapidity (η^{μ}), missing transverse energy (MET), invariant transverse mass of W (M_T^W), photon transverse energy E_T^{γ}, pseudorapidity (η^{γ}), $\Delta R(\mu,\gamma)$, number of good vertices, number of selected jets, $W\gamma$ candidate transverse momentum ($P_T^{W\gamma}$) , event yields after event selection and $\Delta\phi(leading\,jet,\gamma)$ overlaid distributions of the $W\gamma \to \mu\nu\gamma$ candidates in data, signal simulation, and background simulation for 2011B data set.

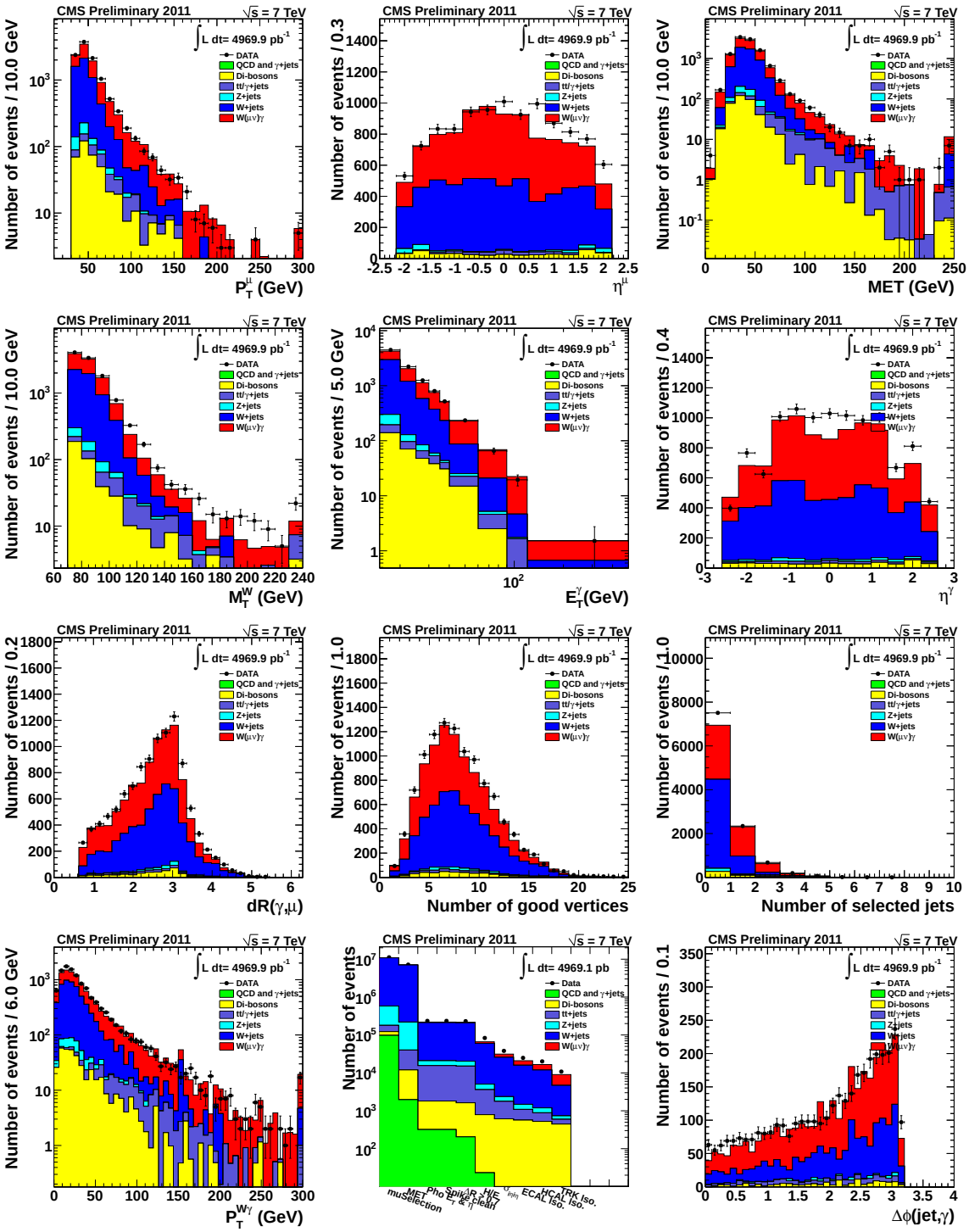

Figure 4.40: Muon candidate trensverse momentum (P_T^{μ}), pseudorapidity (η^{μ}), missing transverse energy (MET), invariant transverse mass of W (M_T^W), photon transverse energy E_T^{γ}, pseudorapidity (η^{γ}), $\Delta R(\mu,\gamma)$, number of good vertices, number of selected jets, $W\gamma$ candidate transverse momentum ($P_T^{W\gamma}$) , event yields after event selection and $\Delta\phi(leading\,jet,\gamma)$ overlaid distributions of the $W\gamma \to \mu\nu\gamma$ candidates in data, signal simulation, and background simulation for 2011A+2011B data sets combined.

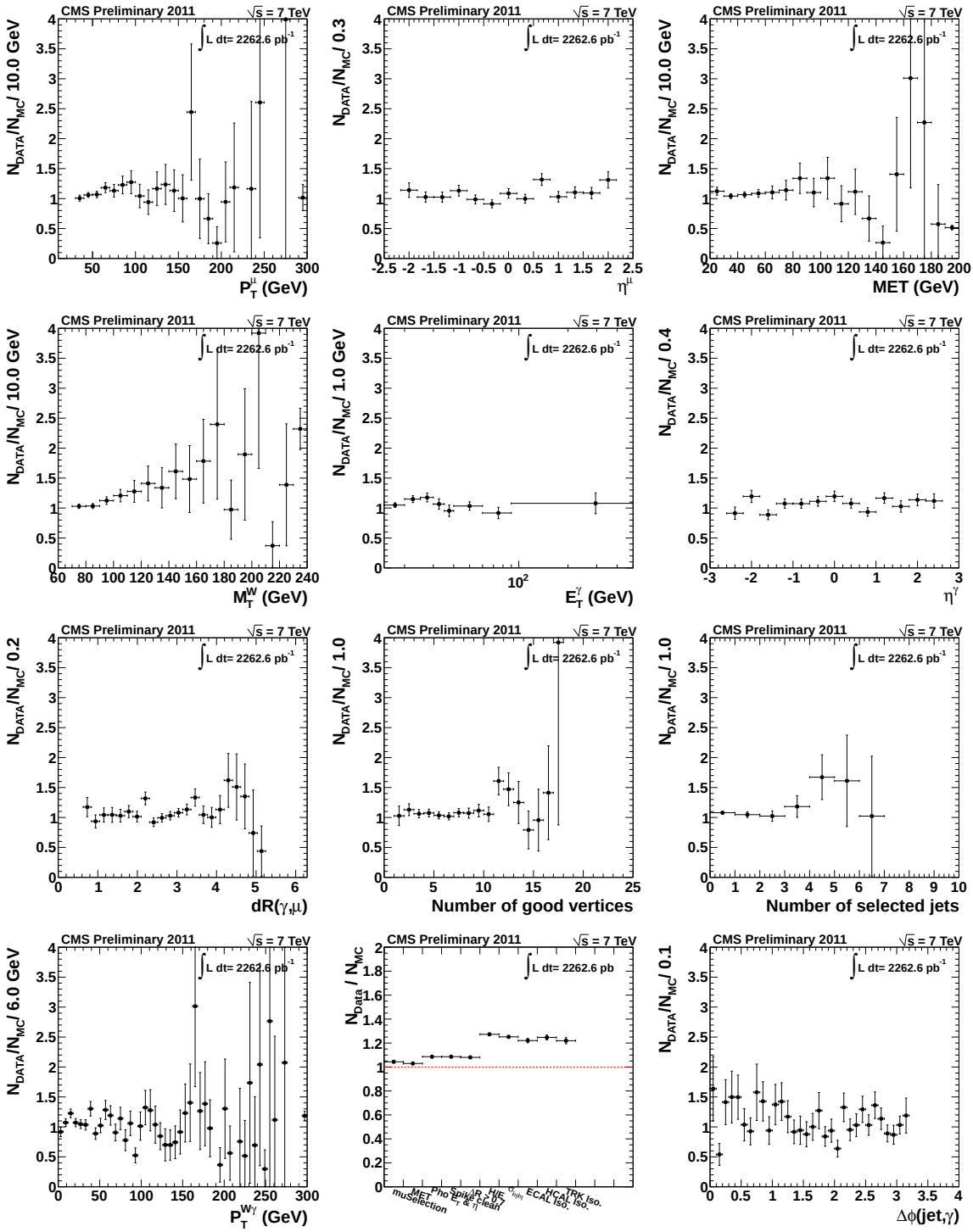

Figure 4.41: The ratio of data shape to simulation shape for muon candidate trensverse momentum (P_T^{μ}), pseudorapidity (η^{μ}), missing transverse energy (MET), invariant transverse mass of W (M_T^W), photon transverse energy E_T^{γ}, pseudorapidity (η^{γ}), $\Delta R(\mu,\gamma)$, number of good vertices, number of selected jets, $W\gamma$ candidate transverse momentum ($P_T^{W\gamma}$) , event yields after event selection and $\Delta\phi(leading\,jet,\gamma)$ of the $W\gamma \to \mu\nu\gamma$ candidates for 2011A data set.

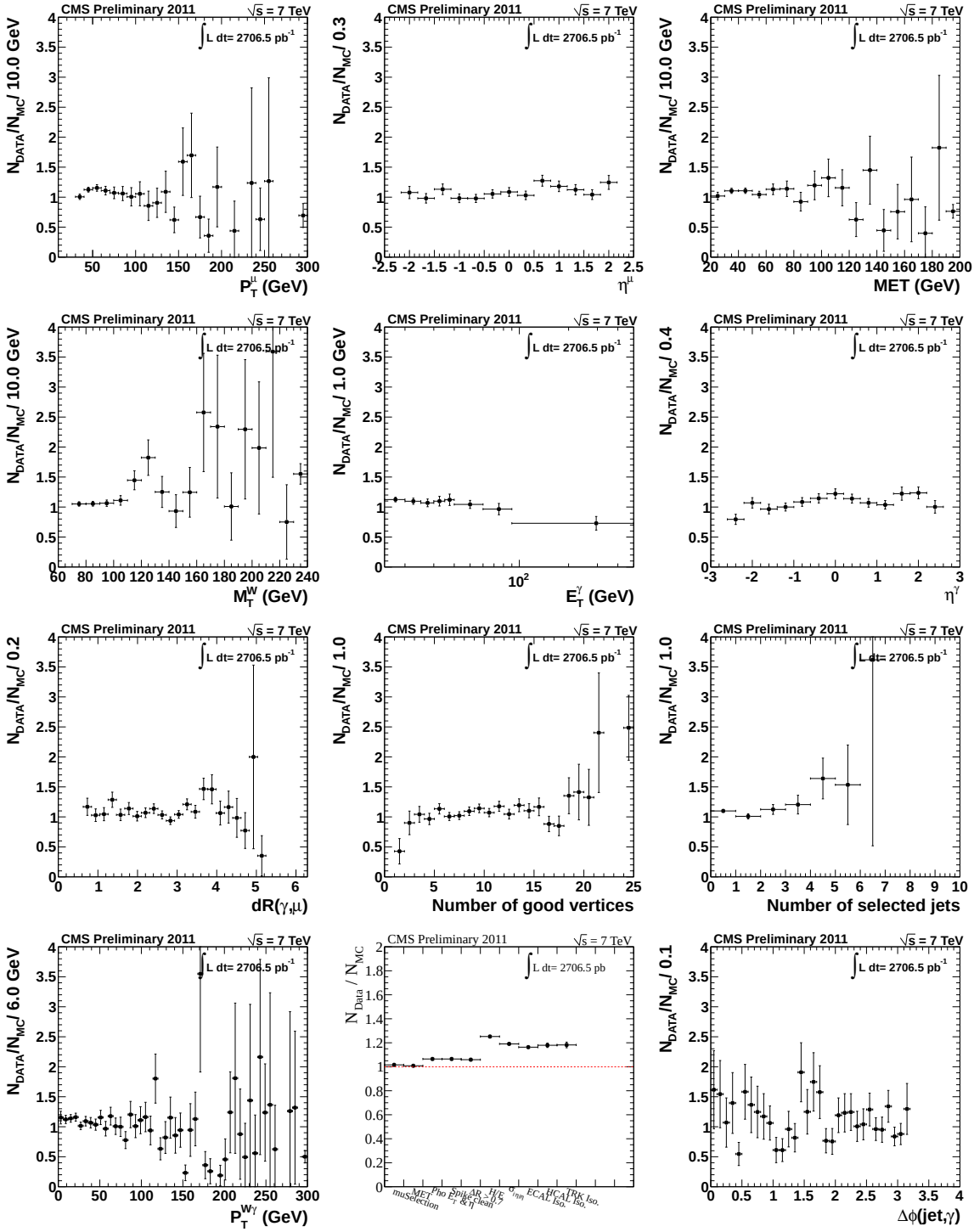

Figure 4.42: The ratio of data shape to simulation shape for muon candidate trensverse momentum (P_T^{μ}), pseudorapidity (η^{μ}), missing transverse energy (MET), invariant transverse mass of W (M_T^W), photon transverse energy E_T^{γ}, pseudorapidity (η^{γ}), $\Delta R(\mu,\gamma)$, number of good vertices, number of selected jets, $W\gamma$ candidate transverse momentum ($P_T^{W\gamma}$) , event yields after event selection and $\Delta\phi(leading\,jet,\gamma)$ of the $W\gamma \to \mu\nu\gamma$ candidates for 2011B data set.

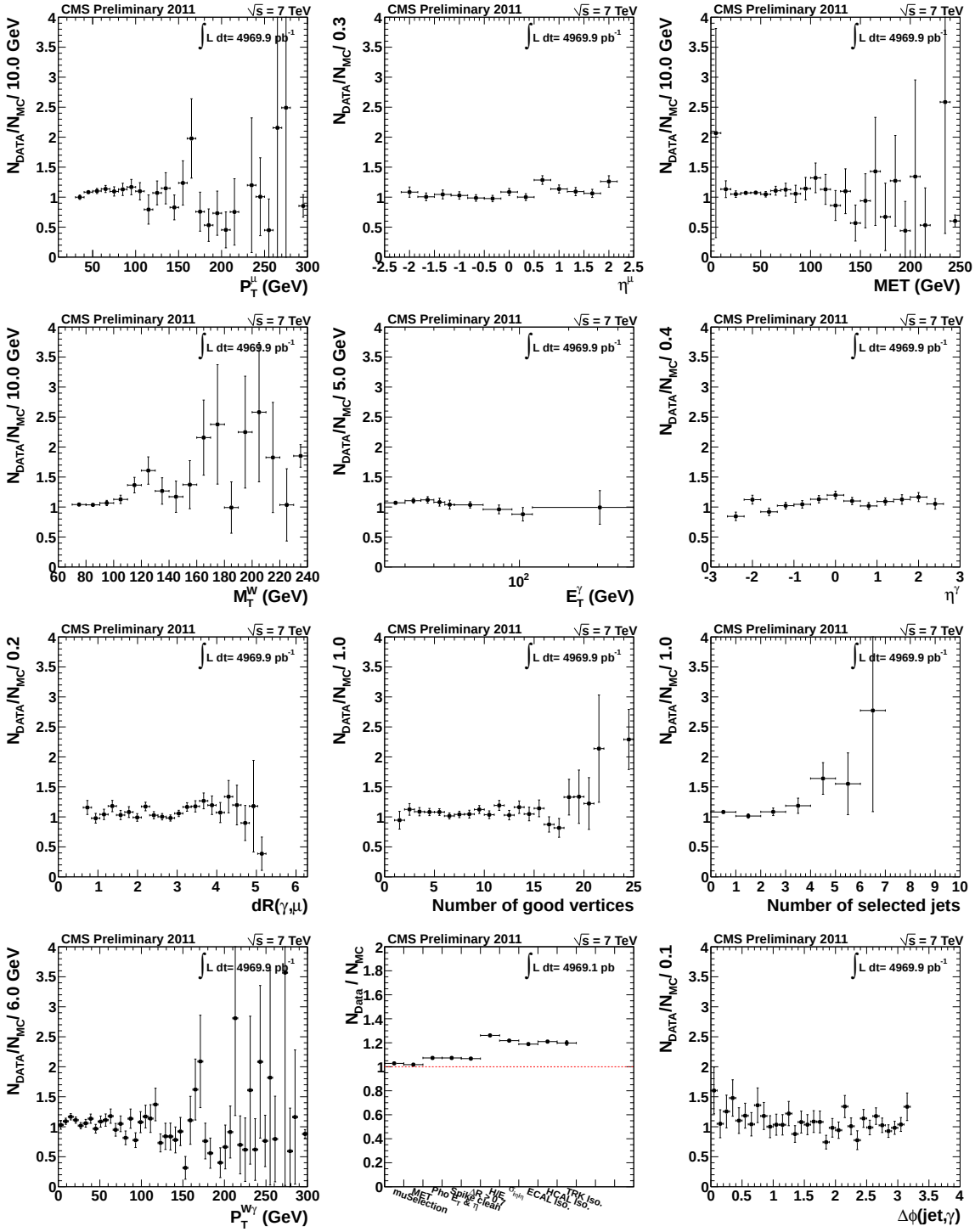

Figure 4.43: The ratio of data shape to simulation shape for muon candidate trensverse momentum (P_T^{μ}), pseudorapidity (η^{μ}), missing transverse energy (MET), invariant transverse mass of W (M_T^W), photon transverse energy E_T^{γ}, pseudorapidity (η^{γ}), $\Delta R(\mu,\gamma)$, number of good vertices, number of selected jets, $W\gamma$ candidate transverse momentum ($P_T^{W\gamma}$) , event yields after event selection and $\Delta\phi(leading\,jet,\gamma)$ of the $W\gamma \to \mu\nu\gamma$ candidates for 2011A+2011B data sets combined.

Table 4.19: Parameters used to calculate the $W\gamma \to \mu\nu\gamma$ cross section in 2011A and 2011B data sets.

Parameter	Number (2011A)	Number (2011B)
N_{events}	5014	5795
$N_{bkg}^{\text{misid. jets}}$	2417.3 ± 39.4 (stat.) ± 219.9 (syst.)	2868.2 ± 43.7 (stat.) ± 276.8 (syst.)
$N_{bkg}^{\text{misid. electrons}}$	44.0 ± 1.0 (stat.) ± 3.3 (syst.)	47.3 ± 1.0 (stat.) ± 3.4 (syst.)
$N_{bkg}^{\gamma+\text{jets}}$	negligible	negligible
$N_{bkg}^{W(\tau\nu)\gamma}$	11.9 ± 1.9 (stat.) ± 1.1 (syst.)	18.0 ± 2.4 (stat.) ± 1.8 (syst.)
$N_{bkg}^{Z\gamma}$	149.8 ± 10.5 (stat.) ± 9.0 (syst.)	188.6 ± 11.6 (stat.) ± 11.3 (syst.)
$N_{bkg}^{t\bar{t}\gamma}$	16.9 ± 0.6 (stat.) ± 8.5 (syst.)	18.9 ± 0.7 (stat.) ± 9.5 (syst.)
N_{bkg}	2639.9 ± 40.8 (stat.) ± 220.2 (syst.)	3141.0 ± 45.3 (stat.) ± 277.2 (syst.)
N_{sig}	2374.1 ± 81.7 (stat.) ± 238.0 (syst.)	2654.0 ± 88.6 (stat.) ± 290.7 (syst.)
$A \cdot \varepsilon_{gen}$	0.0286 ± 0.0015 (syst.)	0.0257 ± 0.0013 (syst.)
ρ_{eff}	0.9806 ± 0.0226 (syst.)	0.9865 ± 0.0247 (syst.)
$\int \mathscr{L}\, dt$	2262.6 ± 49.8 (syst.)	2706.5 ± 59.5 (syst.)

Table 4.20: Parameters used to calculate the $W\gamma \to \mu\nu\gamma$ cross section in 2011A+2011B data sets combined.

Parameter	Number (2011A+2011B)
N_{events}	10809
$N_{bkg}^{\text{misid. jets}}$	5345.9 ± 58.2 (stat.) ± 482.6 (syst.)
$N_{bkg}^{\text{misid. electrons}}$	91.4 ± 1.4 (stat.) ± 4.7 (syst.)
$N_{bkg}^{\gamma+\text{jets}}$	negligible
$N_{bkg}^{W(\tau\nu)\gamma}$	28.9 ± 3.4 (stat.) ± 2.7 (syst.)
$N_{bkg}^{Z\gamma}$	338.0 ± 18.3 (stat.) ± 20.3 (syst.)
$N_{bkg}^{t\bar{t}\gamma}$	35.9 ± 1.0 (stat.) ± 17.9 (syst.)
N_{bkg}	5840.1 ± 61.1 (stat.) ± 483.4 (syst.)
N_{sig}	4968.9 ± 120.6 (stat.) ± 505.8 (syst.)
$A \cdot \varepsilon_{gen}$	0.0270 ± 0.0014 (syst.)
ρ_{eff}	0.9898 ± 0.0247 (syst.)
$\int \mathscr{L}\, dt$	4969.1 ± 109.3 (syst.)

Besides measurement of cross section in the phase space $E_T^\gamma > 15$ GeV and $\Delta R(\mu,\gamma) > 0.7$ the measurements of the cross section is also performed for phase space regions restricted by higher E_T^γ thresholds, $E_T^\gamma > 60$ GeV and $E_T^\gamma > 90$ GeV. The $\Delta R(\mu,\gamma)$ requirement is the same, $\Delta R(\mu,\gamma) > 0.7$. The estimated cross section for photon $E_T > 60$ GeV is:

$$\sigma(pp \to W\gamma \to \mu\nu\gamma)(2011A+2011B) = 0.76 \pm 0.06\ (\text{stat.}) \pm 0.08\ (\text{syst.}) \pm 0.02\ (\text{lumi.})\ \text{pb}.$$

The theoretical NLO cross section for photon $E_T > 60$ GeV is 0.58 ± 0.08 pb.

The estimated cross section for photon $E_T > 90$ GeV is:

$$\sigma(pp \to W\gamma \to \mu\nu\gamma)(2011A+2011B) = 0.248 \pm 0.035\ (\text{stat.}) \pm 0.048\ (\text{syst.}) \pm 0.005\ (\text{lumi.})\ \text{pb}.$$

Table 4.21: Summary of systematic uncertainties for the Wγ cross section measurement ($E_T(\gamma) > 60.$ GeV and $E_T(\gamma) > 90.$ GeV) for 2011A+2011B data set.

		$E_T(\gamma) > 60.$ GeV	$E_T(\gamma) > 90.$ GeV
Source	Systematic uncertainty	Effect on N_{sig}	
Photon energy scale	1% (EB), 3% (EE)	5.5%	3.9%
Muon P_T scale	0.2%	0.2%	0.1%
Total uncertainty on N_{sig}		5.5%	3.9%
Source	Systematic uncertainty	Effect on $\mathscr{F} = A \cdot \varepsilon_{MC}$	
Photon energy resolution	1% (EB), 3% (EE)	0.8%	0.7%
Muon P_T resolution	0.6%	0.3%	0.1%
Pile-up	Shift data PU distribution by $\pm$ 5%	0.1%	1.0%
PDF	CTEQ6L reweighting	0.9%	0.9%
Signal modeling	5%	5.0%	5.0%
Total uncertainty on $\mathscr{F} = A \cdot \varepsilon_{MC}$		5.2%	5.2%
Source	Systematic uncertainty	Effect on ρ_{eff}	
Muon trigger	1.5%	1.5%	1.5%
Muon reconstruction	0.9%	0.9%	0.9%
Muon ID and isolation	0.9%	0.9%	0.9%
MET selection	1.4% (ele), 1.5% (mu)	1.5%	1.5%
Photon ID and isolation	0.5% (EB), 1.0% (EE)	0.5%	0.5%
Total uncertainty on ρ_{eff}		2.5%	2.5%
Source	Systematic uncertainty	Effect on background yield	
Template method		18.8%	44.6%
Electron misidentification		5.3%	5.2%
MC prediction		15.5%	17.0%
Total uncertainty on background		14.3%	32.2%
Source	Systematic uncertainty	Effect on luminosity	
Luminosity	2.2%	2.2%	2.2%

The theoretical NLO cross section for photon $E_T > 90$ GeV is 0.173 ± 0.026 pb.

Table 4.22 shows the summary of parameters for cross section measurement for photon $E_T >$ 60 GeV and $E_T > 90$ GeV. The corresponding systematic uncertainties are summarized in Table 4.21.

Table 4.22: Summary of parameters for the $W\gamma$ cross section measurement for photon $E_T > 60$ GeV and $E_T > 90$ GeV.

Parameters	$E_T^{\gamma} > 60$ GeV	$E_T^{\gamma} > 90$ GeV
N_{events}	610 $\pm$ 24.7 (stat.)	230 $\pm$ 15.2 (stat.)
$N_{bkg}^{misid.jets}$	159.9 $\pm$ 17.4 (stat.) $\pm$ 30.0 (syst.)	59.4 $\pm$ 14.0 (stat.) $\pm$ 26.5 (syst.)
$N_{bkg}^{misid.electrons}$	21.2 $\pm$ 0.6 (stat.) $\pm$ 1.1 (syst.)	7.2 $\pm$ 0.4 (stat.) $\pm$ 0.4 (syst.)
$N_{bkg}^{\gamma+\text{jets}}$	negligible	negligible
$N_{bkg}^{W(\tau\nu)\gamma}$	3.2 $\pm$ 1.2 (stat.) $\pm$ 0.3 (syst.)	.0 $\pm$ 0.0 (stat.) $\pm$ 0.0 (syst.)
$N_{bkg}^{Z\gamma}$	19.4 $\pm$ 4.4 (stat.) $\pm$ 1.2 (syst.)	10.9 $\pm$ 3.2 (stat.) $\pm$ 0.7 (syst.)
$N_{bkg}^{t\bar{t}\gamma}$	9.7 $\pm$ 0.5 (stat.) $\pm$ 4.9 (syst.)	5.3 $\pm$ 0.4 (stat.) $\pm$ 2.7 (syst.)
N_{sig}	396.7 $\pm$ 30.5 (stat.) $\pm$ 37.4 (syst.)	147.2 $\pm$ 20.9 (stat.) $\pm$ 27.2 (syst.)
$A \cdot \varepsilon_{MC,W\gamma\to\ell\nu\gamma}$	0.105 $\pm$ 0.005 (syst.)	0.120 $\pm$ 0.006 (syst.)
ρ_{eff}	0.993 $\pm$ 0.025 (syst.)	0.993 $\pm$ 0.025 (syst.)
$\int \mathscr{L}\, dt$	4969.1 $\pm$ 109.3 (syst.)	4969.1 $\pm$ 109.3 (syst.)

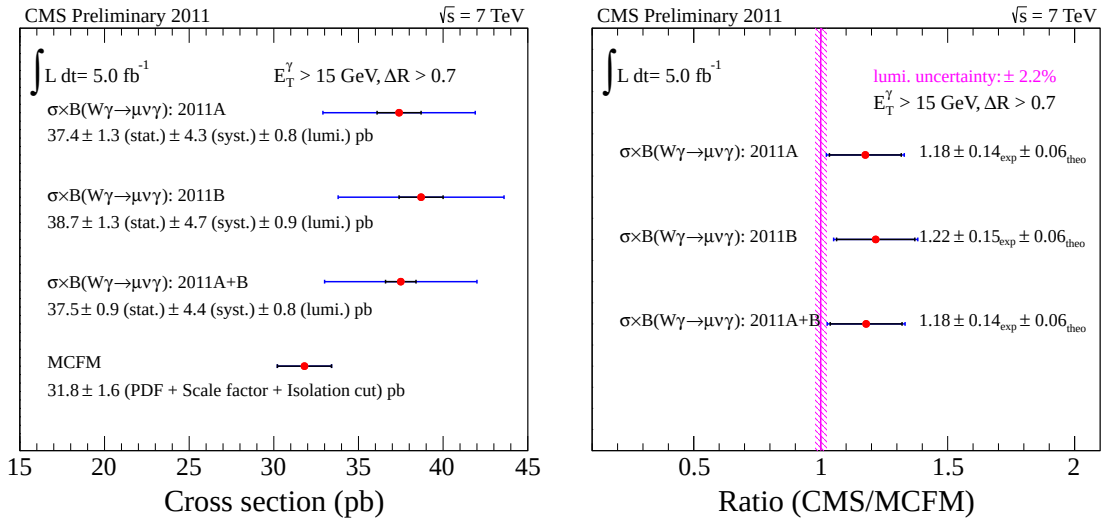

Figure 4.44: Measured cross sections for $W\gamma \to \mu\nu\gamma$ (left) and the ratio of measured cross section to MCFM prediction for $W\gamma \to \mu\nu\gamma$ (right).

4.6 Combined results with electron channel

The $W\gamma$ cross section has also been measured in the $e\nu\gamma$ final state. The results from the two channels are combined. The measured cross section in the electron channel is:

$$\sigma(pp \to \mathrm{W}\gamma \to e\nu\gamma) = 36.6 \pm 1.2\ (\mathrm{stat.}) \pm 4.3\ (\mathrm{syst.}) \pm 0.8\ (\mathrm{lumi.})\ \mathrm{pb}.$$

The combination of the cross sections in the muon and electron channels, performed using a Best Linear Unbiased Estimator (BLUE) [35], is:

$$\sigma(pp \to \mathrm{W}\gamma \to \ell\nu\gamma) = 37.0 \pm 0.8\ (\mathrm{stat.}) \pm 4.0\ (\mathrm{syst.}) \pm 0.8\ (\mathrm{lumi.})\ \mathrm{pb}.$$

Table 4.23: The summary of the cross section measurements and predictions for E_{T}^{γ} >60 and 90 GeV for $W\gamma$.

	Wγ	
	Electron Channel (pb)	Muon Channel (pb)
$E_{\mathrm{T}}^{\gamma} > 15$ GeV	36.6 ± 1.2(stat.) ± 4.3(syst.) ± 0.8(lumi.)	37.5 ± 0.9(stat.) ± 4.4(syst.) ± 0.8(lumi.)
Combination	37.0 ± 0.8(stat.) ± 4.0(syst.) ± 0.8(lumi.) pb	
Prediction	31.81 ± 1.80 (pb)	
$E_{\mathrm{T}}^{\gamma} > 60$ GeV	0.77 ± 0.07(stat.) ± 0.13(syst.) ± 0.02(lumi.)	0.76 ± 0.06(stat.) ± 0.08(syst.) ± 0.02(lumi.)
Combination	0.76 ± 0.05(stat.) ± 0.08(syst.) ± 0.02(lumi.) pb	
Prediction	0.58 ± 0.08 (pb)	
$E_{\mathrm{T}}^{\gamma} > 90$ GeV	0.173 ± 0.034(stat.) ± 0.037(syst.) ± 0.004(lumi.)	0.248 ± 0.035(stat.) ± 0.048(syst.) ± 0.005(lumi.)
Combination	0.200 ± 0.025(stat.) ± 0.038(syst.) ± 0.004(lumi.) pb	
Prediction	0.173 ± 0.026 pb	

Results for both electron and muon channels are shown in Figures 4.45- 4.47.

The estimated cross section for photon $E_T > 60$ GeV in the electron channel is:

$$\sigma(pp \to W\gamma \to e\nu\gamma)(2011A + 2011B) = 0.77 \pm 0.07\ (\mathrm{stat.}) \pm 0.13\ (\mathrm{syst.}) \pm 0.02\ (\mathrm{lumi.})\ \mathrm{pb}.$$

The combined cross section is:

$$\sigma(pp \to W\gamma \to \ell\nu\gamma)(2011A + 2011B) = 0.76 \pm 0.05\ (\mathrm{stat.}) \pm 0.08\ (\mathrm{syst.}) \pm 0.02\ (\mathrm{lumi.})\ \mathrm{pb}.$$

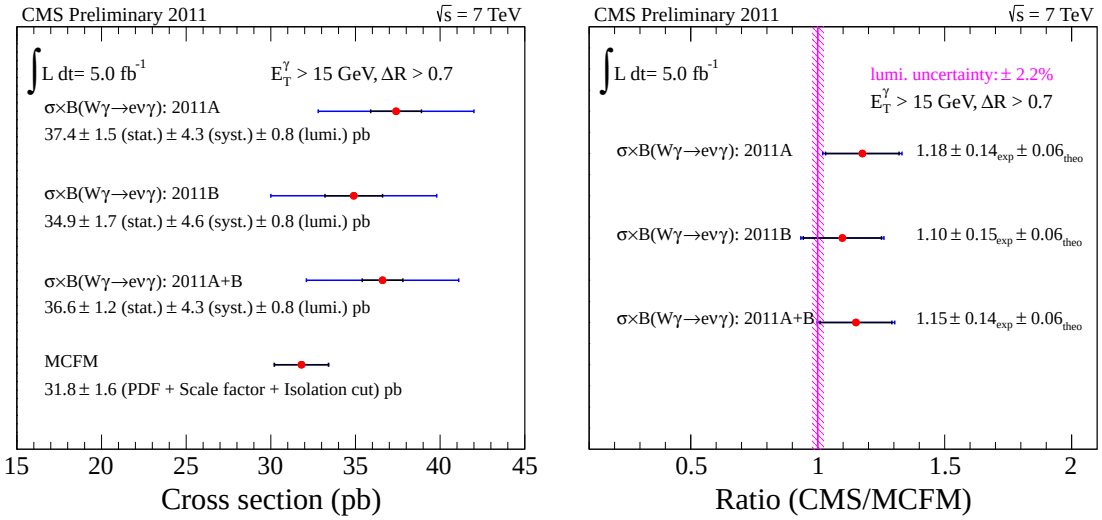

Figure 4.45: Measured cross sections for $W\gamma \rightarrow e\nu\gamma$ (left) and the ratio of measured cross section to MCFM prediction for $W\gamma \rightarrow e\nu\gamma$ (right).

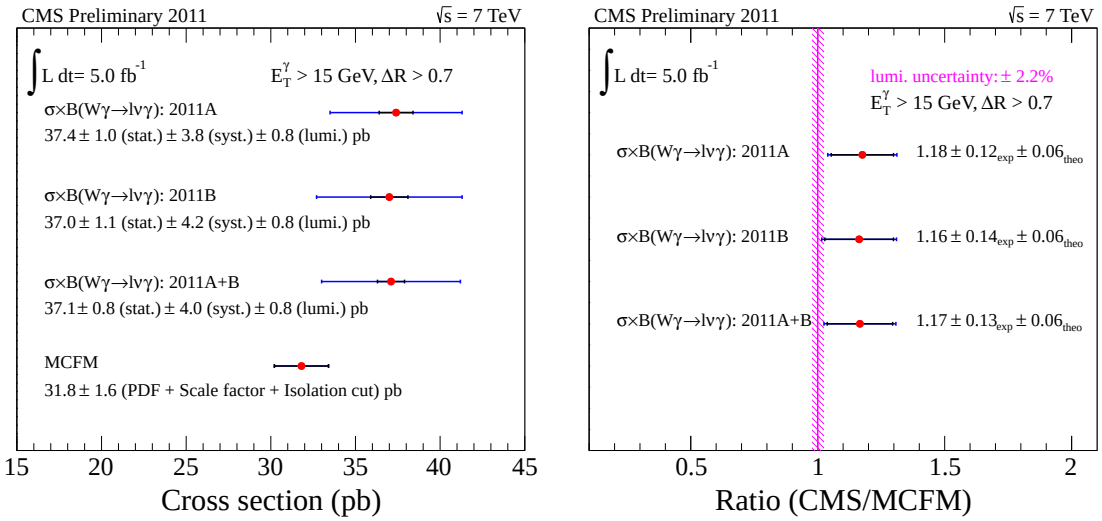

Figure 4.46: Measured cross sections for $W\gamma \rightarrow l\nu\gamma$ (left) and the ratio of measured cross section to MCFM prediction for $W\gamma \rightarrow l\nu\gamma$ (right). Measurements in electron and muon channel are combined.

The estimated cross section for photon $E_T > 90$ GeV in the electron channel is:

$$\sigma(pp \to W\gamma \to e\nu\gamma)(2011A + 2011B) = 0.173 \pm 0.034 \text{ (stat.)} \pm 0.037 \text{ (syst.)} \pm 0.004 \text{ (lumi.) pb.}$$

The combined cross section is:

$$\sigma(pp \to W\gamma \to \ell\nu\gamma)(2011A + 2011B) = 0.200 \pm 0.025 \text{ (stat.)} \pm 0.038 \text{ (syst.)} \pm 0.004 \text{ (lumi.) pb.}$$

The measured cross sections, predictions, and their uncertainties are summarized in Table 4.23 and in Figure 4.48.

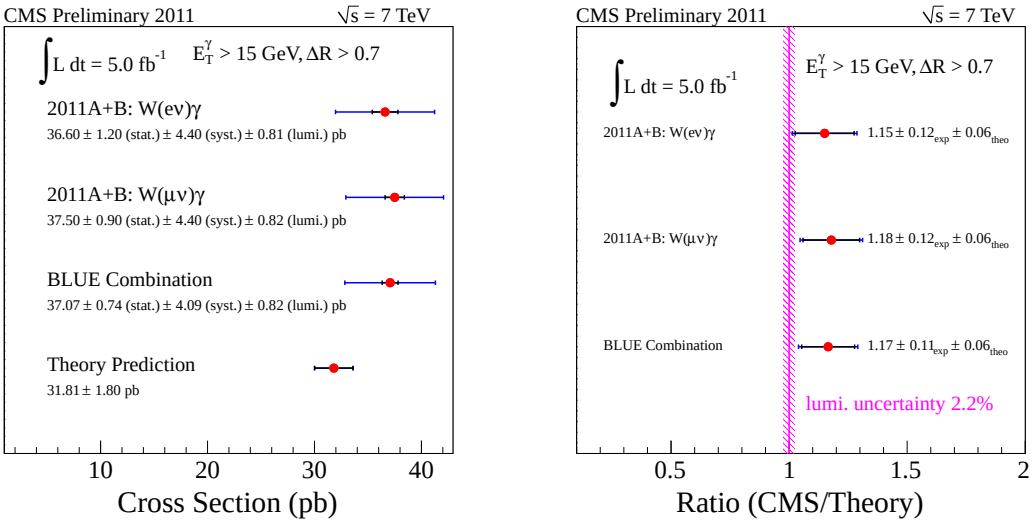

Figure 4.47: A summary of the measured cross sections and their combination for the Wγ analysis.

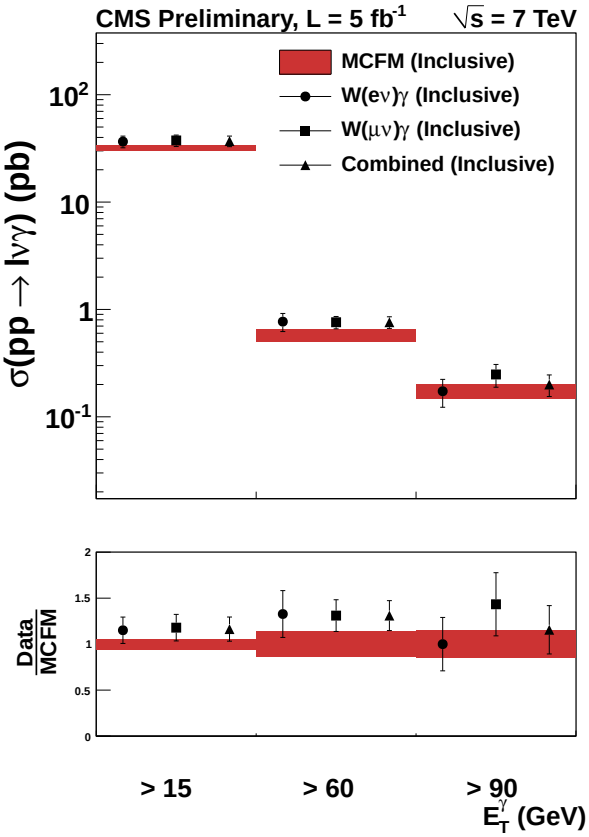

Figure 4.48: The summary of all cross section measurements and comparisons to theory for the Wγ measurement.

Chapter 5

Observation of $W\gamma$ radiation amplitude zero

To observe the radiation amplitude zero additional selection requirements on top of the selection used for the cross section measurement are needed. As discussed in Section 2.3 the additional selection consists in a jet veto. Events with jets reconstructed with "anti-k$_T$" algorithm [36] with $P_T^{jet} > 30$ GeV and $|\eta^{jet}| < 5$ are rejected. The second additional requirement consists in a transverse mass of $\mu MET\gamma$ ($\mu\nu\gamma$) system, $M_T^{\mu MET\gamma} > 110$ GeV.

5.1 Results

The charge-signed η distribution, $Q_l \times \Delta\eta$ where Q_l is the charge of the muon and $\Delta\eta$ is the difference in pseudorapidity between the muon and the photon of selected Wγ events for data sets 2011A+2011B combined and the corresponding ratios of data to simulation are shown in Figures 5.1 and 5.2. The dip around zero is clearly visible in data.

5.2 Combined results with electron channel

Figure 5.3 shows the charge-signed η distribution of selected Wγ events combined for electron and muon channel and demonstrates the radiation amplitude zero characteristic of Wγ production. The dip around value 0 is clearly visible.

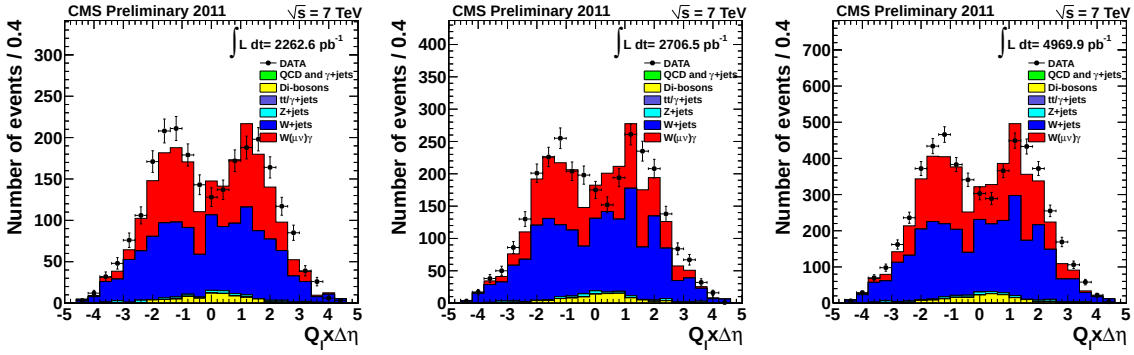

Figure 5.1: Charge-signed η distribution in data, signal simulation, and background simulation for $W\gamma \to \mu\nu\gamma$ for 2011A (left), 2011B (middle) and 2011A+2011B combined (right).

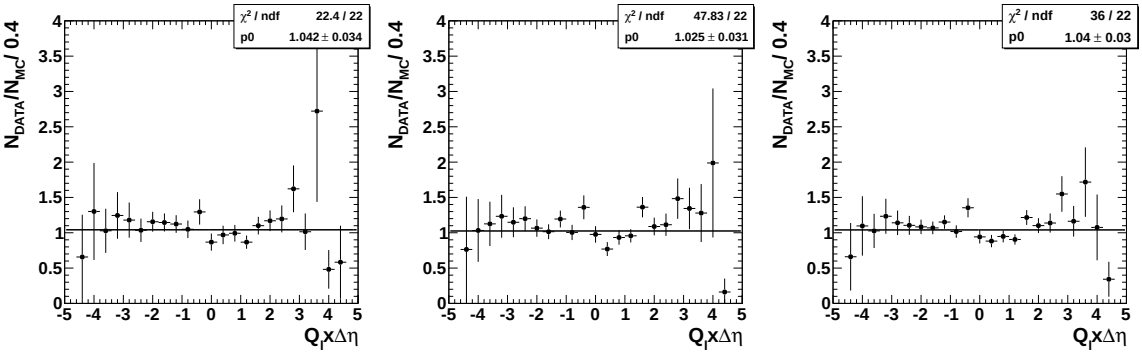

Figure 5.2: The ratio of data shape to simulated shape for charge-signed η distribution, for $W\gamma \to \mu\nu\gamma$ for 2011A (left), 2011B (middle) and 2011A+2011B combined (right).

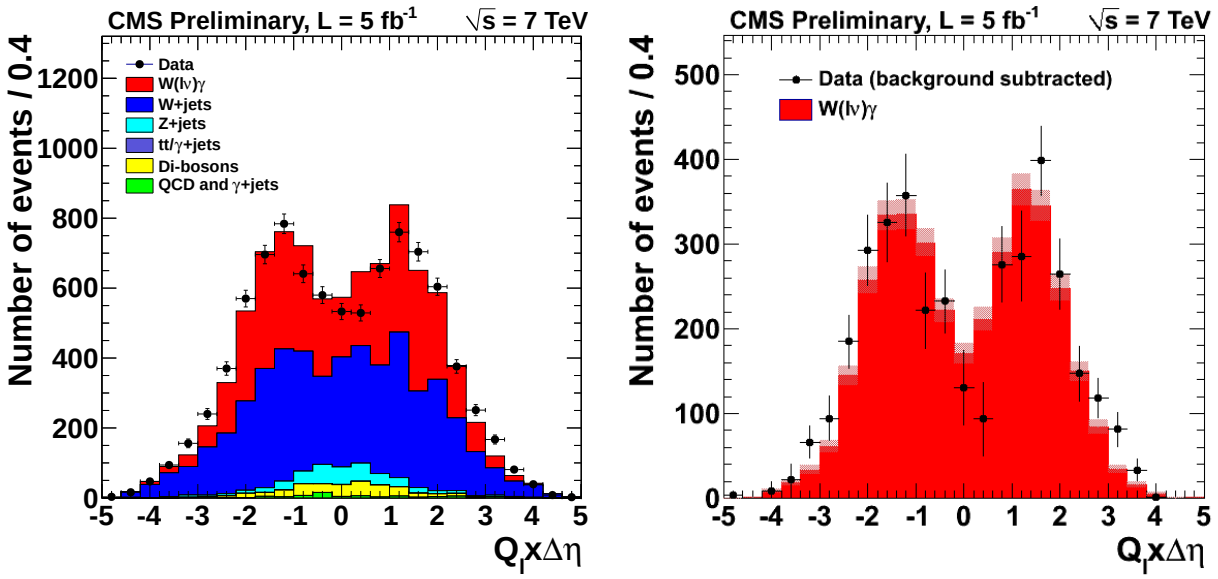

Figure 5.3: Charge-signed η distribution in data, signal simulation, and background simulation combined for $W\gamma \to \mu\nu\gamma$ and $W\gamma \to e\nu\gamma$ for 2011A+2011B data sets combined. Yield from signal simulation is scaled to data signal yield. The right plot is background subtracted, uncertainties include statistic and systematic uncertainties.

Chapter 6

Triple gauge coupling measurement

To look for anomalous couplings, an observable sensitive to aTGC is studied. One effect of introducing anomalous coupling parameters in the SM Lagrangian is an enhancement of the diboson production cross section when $\hat{s}$ is large. This results in an excess of events with high momentum bosons. The photon E_{T}^{γ} is used as observable to measure aTGC parameters, and the study is performed for $E_{\mathrm{T}}^{\gamma} > 40$ GeV. Distribution of sensitive observable in data is compared with predictions for different aTGC values. Limits on aTGC parameters are set using the formalism described below.

6.1 Likelihood Formalism

The aTGC results are interpreted by setting bounds on the ratio of the observed signal to that of the expected aTGC yield using the likelihood formalism described below. The probability of observing $\mathbf{X}$ events in a specific bin of E_{T}^{γ} for a given expectation value d is given by the Poisson distribution:

$$p(\mathbf{X};d) = \frac{d^{\mathbf{X}} e^{-d}}{\mathbf{X}!} \tag{6.1}$$

Here, d is comprised of both signal and background predictions that are modeled separately:

$$d = \mu \cdot \mathbf{s}(\vec{\alpha}, \vec{\theta}_s) + \mathbf{b}(\vec{\theta}_b), \tag{6.2}$$

where signal $\mathbf{s}(\vec{\alpha}, \vec{\theta}_s)$ and background $\mathbf{b}(\vec{\theta}_b)$ expectations are described in terms of the TGC parameter values $\vec{\alpha}$ and nuisance parameters $\vec{\theta}_s$ and $\vec{\theta}_b$. The parameter μ is the signal strength modifier.

The nuisance parameters are resolved into three contributions: systematic uncertainty on integrated luminosity $f_{\mathscr{L}}$, signal and background selection systematic uncertainties defined as $f_{Sig.}^{\text{Syst.}}$ and $f_{Bkg.}^{\text{Syst.}}$, respectively. Signal and background expectaions can be written as:

$$\mathbf{s}(\vec{\alpha}, \vec{\theta}_s) = f_{\mathscr{L}} \cdot f_{Sig.}^{\text{Syst.}} \cdot N^{\text{Sig.}} \vec{\alpha}, \tag{6.3}$$

$$\mathbf{b}(\vec{\theta}_b) = f_{Bkg.}^{\text{Syst.}} \cdot N^{\text{Bkg.}}. \tag{6.4}$$

Here, $N^{\text{Sig.}}$ and $N^{\text{Bkg.}}$ are the predicted signal and background event yields.

With this definition of d for each bin i of the E_{T}^{γ} distribution with data event yield N_i a likelihood function is constructed:

$$\text{L}(\mu, \vec{\alpha}, \vec{\theta}) = \prod_i Poisson(N_i, d_i(\mu, \vec{\alpha}, \vec{\theta})), \tag{6.5}$$

with the Poisson function defined in Eq. 6.1 and:

$$\vec{\theta} = (\vec{\theta}_s, \vec{\theta}_b). \tag{6.6}$$

The uncertainties on the quoted luminosity, signal, and background are assumed to be log-normally distributed.

The upper limits of TGCs are determined by using the following test statistics:

$$t_{\mu,\vec{\alpha}} = -2 \ln \lambda(\mu, \vec{\alpha}) \tag{6.7}$$

where $\lambda(\mu, \vec{\alpha})$ is the profile likelihood [1]:

$$\lambda(\mu,\vec{\alpha}) = \frac{\mathrm{L}(\mu,\vec{\alpha},\hat{\hat{\vec{\theta}}})}{\mathrm{L}(\hat{\mu},\vec{\alpha},\hat{\hat{\vec{\theta}}})} \tag{6.8}$$

with $\hat{\hat{\vec{\theta}}}$ being the conditional maximum-likelihood estimator of $\vec{\theta}$ and $\hat{\mu}$ and $\hat{\hat{\vec{\theta}}}$ being their maximum-likelihood estimators. The hypothesized values of TGCs are excluded based on whether the ratio of p-values:

$$CL_s = \frac{p_{s+b}}{1-p_b} \tag{6.9}$$

is less than a given threshold. More details can be found in [37]. This formalism is implemented in the ROOSTAT package.

6.2 Signal simulation

The aTGC signal for a grid of aTGC values is simulated using the SHERPA generator [3] interfaced with PYTHIA [4] for the detector simulation of the $W\gamma$+n jet (n $\leq$ 1) process. Two aTGC parameters, $\Delta\kappa_\gamma$ and λ_γ, are freely varied while g_1^Z is set to the SM value. The grid of aTGC values contains 49 points, 7 by 7, in $\Delta\kappa_\gamma$ and λ_γ space. The outermost points of the grid are $\Delta\kappa_\gamma = \pm 0.6$ and $\lambda_\gamma = \pm 0.06$. The samples for these aTGC points are fully simulated, to obtain the continuous signal description in aTGC parameters space the quadratic fit in every E_{T}^{γ} bin is performed.

6.3 Results

Figure 6.1 shows the photon E_{T}^{γ} distribution in data, background, and simulated signal overlaid as well as the background and the aTGC simulated signal for $\Delta\kappa_\gamma = 0.4$ and $\lambda_\gamma = 0.0$.

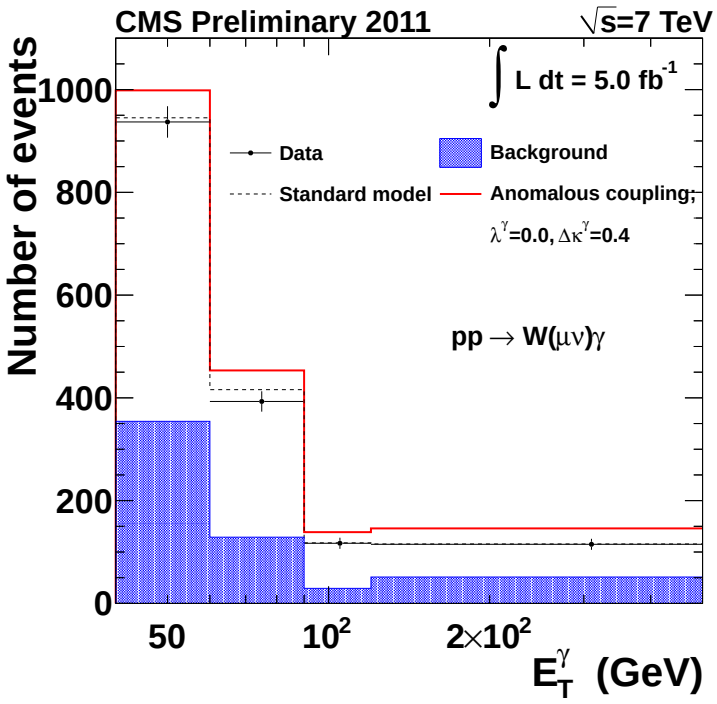

Figure 6.1: Photon E_{T}^{γ} distribution for data (black circles), background (blue filled histogram), simulated signal (black histogram), simulated signal with aTGC close to the excluded region $\Delta\kappa^{\gamma} = 0.4$ and $\lambda_{\gamma} = 0.0$ (red histogram). The last bin includes overflows.

No sizeable disagreement from the SM is observed, i.e. there is no signal of aTGC. Upper limits on aTGC parameters are therefore set. The 95% C.L. two-dimensional contours are shown in Figure 6.2. Corresponding one-dimensional limits are given in Figure 6.3 and 6.4 and in Table 6.1.

6.4 Combined results with electron channel

As for the cross section measurements, a search of aTGC is also performed in the electron channel. The results from the two channels are combined and shown in Figures 6.5-6.7 and in Table 6.1.

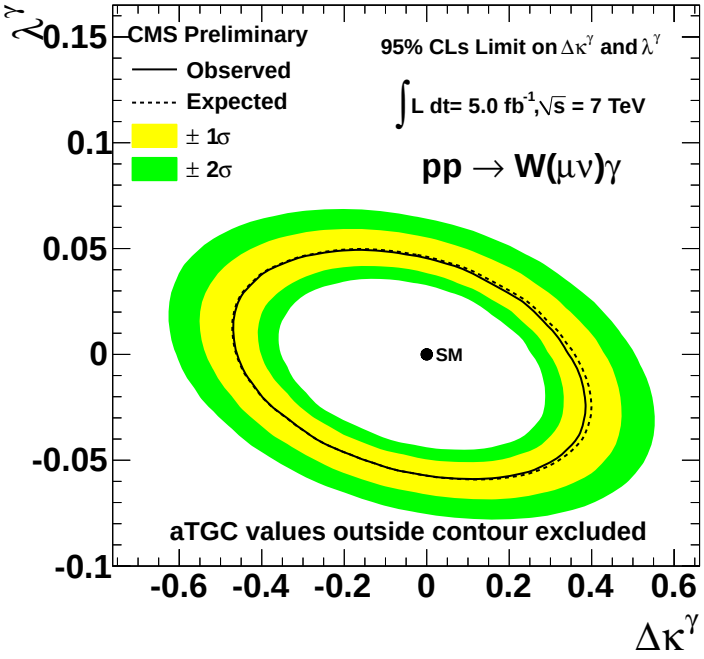

Figure 6.2: 2D 95% confidence level expected and observed contours for $WW\gamma$ coupling.

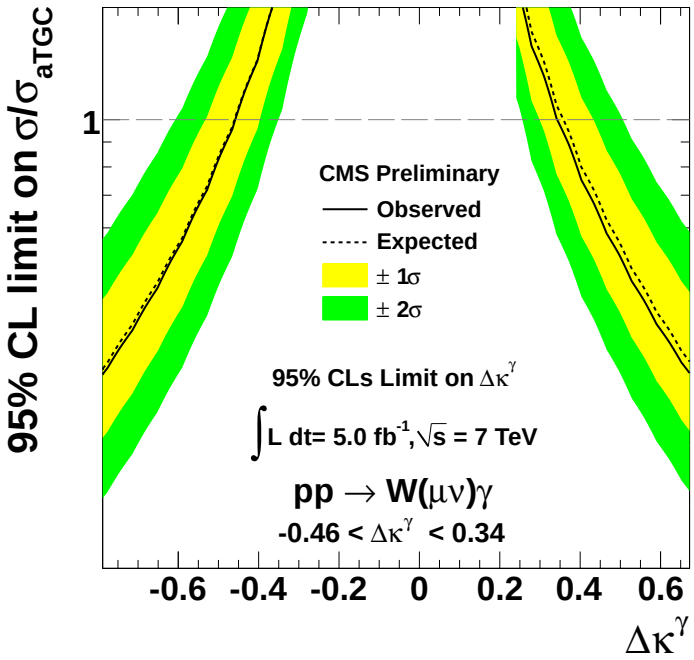

Figure 6.3: 1D 95% confidence level expected and observed limits for $\Delta\kappa^{\gamma}$ $WW\gamma$ coupling.

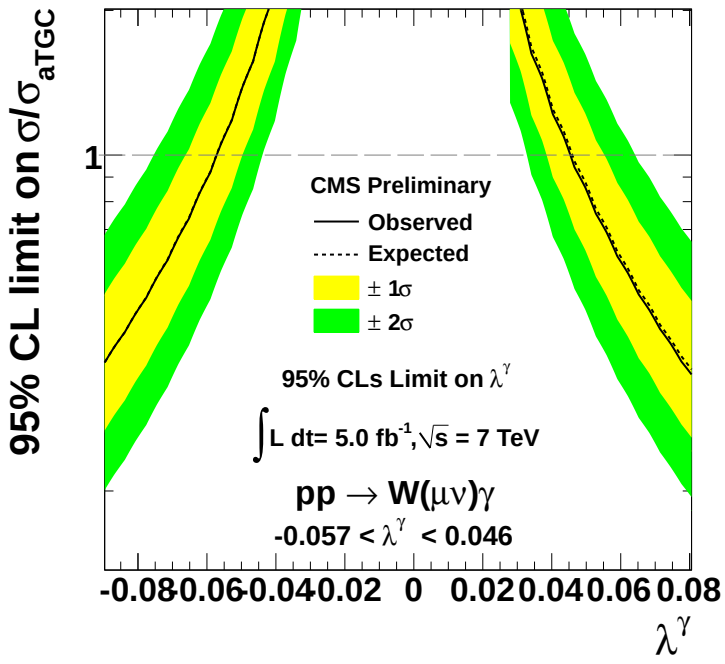

Figure 6.4: 1D 95% confidence level expected and observed limits for λ^{γ} $WW\gamma$ coupling.

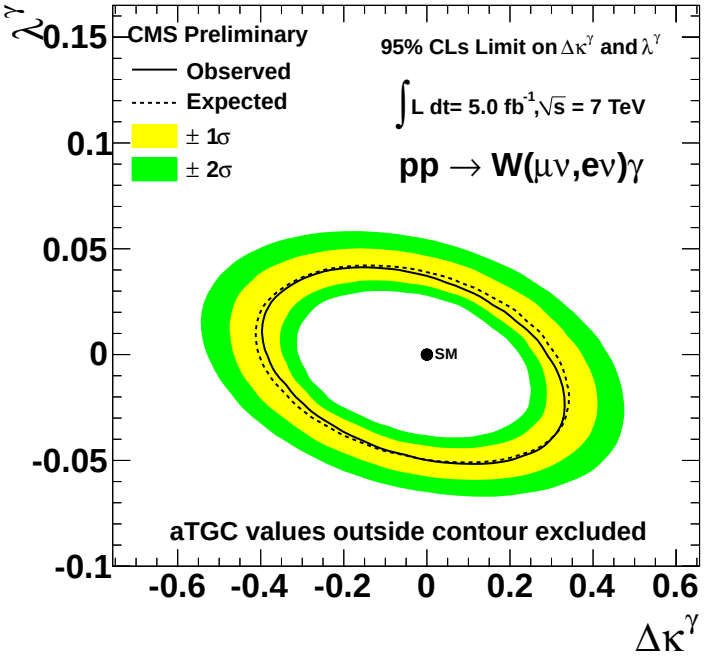

Figure 6.5: 2D 95% confidence level expected and observed contours for $WW\gamma$ coupling. Electron and muon channel combined.

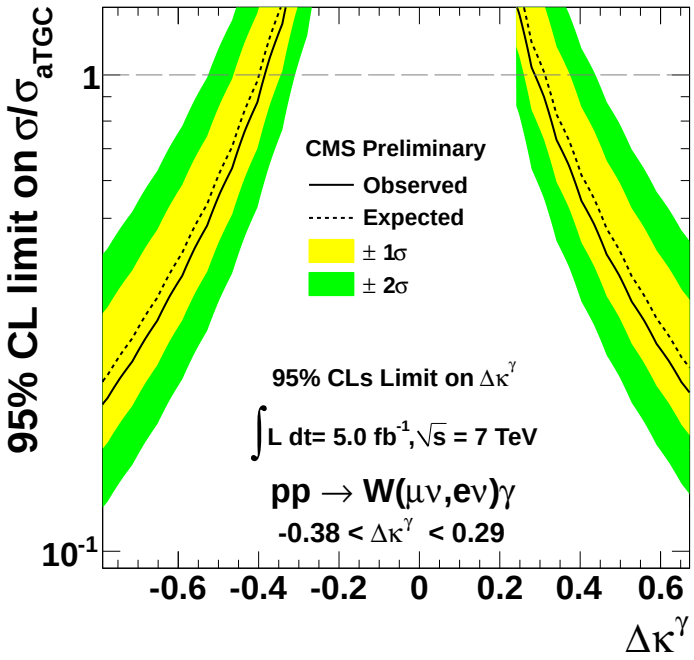

Figure 6.6: 1D 95% confidence level expected and observed limits for $\Delta\kappa^{\gamma}$ $WW\gamma$ coupling. Electron and muon channel combined.

Table 6.1: 1D 95% confidence level observed limits for $WW\gamma$ coupling. Electron and muon channel combined.

	$\Delta\kappa^{\gamma}$	λ^{γ}
$W\gamma \to e\nu\gamma$	[-0.45,0.37]	[-0.059,0.046]
$W\gamma \to \mu\nu\gamma$	[-0.46,0.34]	[-0.057,0.046]
$W\gamma \to l\nu\gamma$	[-0.38,0.29]	[-0.050,0.037]

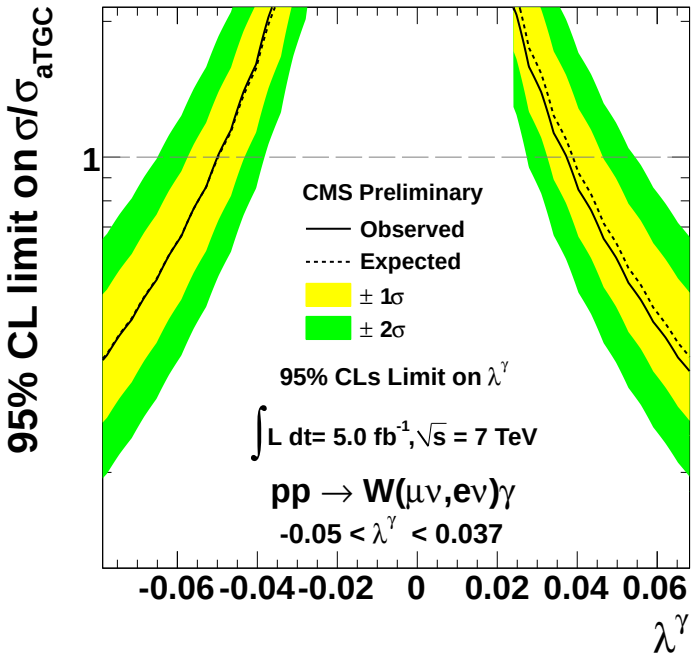

Figure 6.7: 1D 95% confidence level expected and observed limits for λ^{γ} $WW\gamma$ coupling. Electron and muon channel combined.

Chapter 7

Comparison with other results

The other general purpose detector at LHC, the ATLAS experiment, also performed a measurement of the $W\gamma$ process in proton-proton collisions at 7 TeV. The measurement was done with the luminosity of 1 fb^{-1} [38]. The selection criteria used by the ATLAS experiment are looser resulting in a larger number of selected events as well as signal events. Two measurements are performed, inclusive and exclusive (jet veto with $P_T^{jet} > 30$ GeV imposed) within the phase space: $P_T^l > 25$ GeV, $P_T^\nu > 25$ GeV, $|\eta^l| < 2.47, E_T^\gamma > 15/60/100$ GeV,$|\eta^\gamma| < 2.37$. Results are shown in Figure 7.1.

New results using 5 fb^{-1} [39] were recently presented. Figure 7.2 shows the measured cross sections compared to theory predictions.

As for the results presented in this work, the ATLAS results indicate that MCFM generator significantly disagrees with data for the $W\gamma$ inclusive cross section at higher E_T^γ values. Other generators like Sherpa [3] agree better with the data.

The measurement of TGC parameters is performed in a different way than in this work. The total number of signal events with $E_T^\gamma > 100$ GeV is used rather then the E_T^γ distribution to set the limits. The measurement is also performed using the exclusive sample of data, rather than inclusive. One dimensional limits on aTGC parameters using 1fb^{-1} of data are shown in Table 7.1, and using 5fb^{-1} of data in Figure 7.3. Results from ATLAS also do not show any indication of aTGC. Upper limits are set.

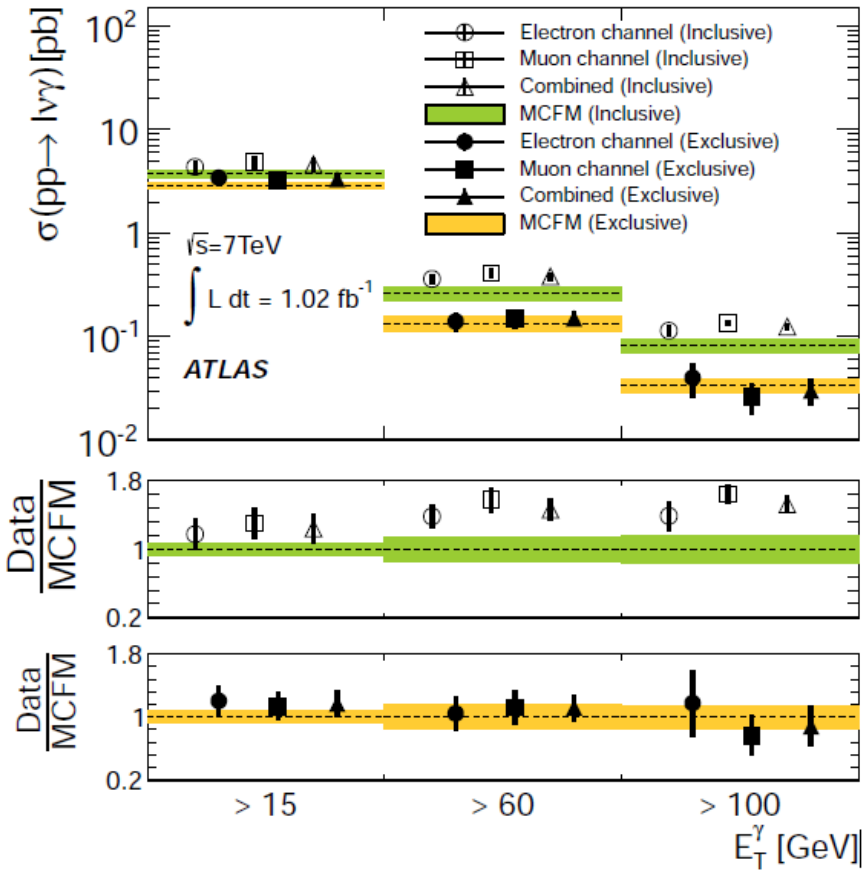

Figure 7.1: Measurements of $W\gamma$ cross section with ATLAS detector using 1 fb^{-1} of data.

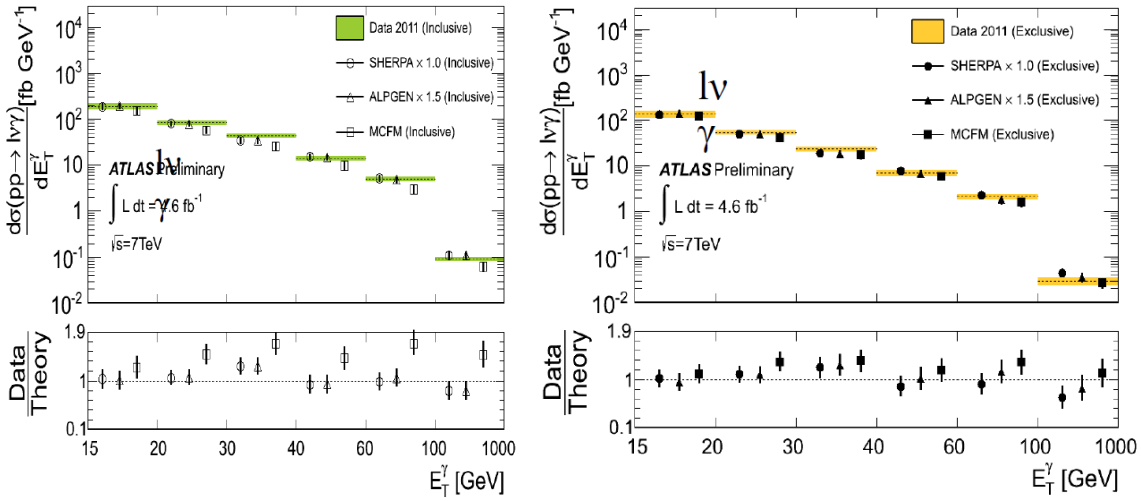

Figure 7.2: Measurements of $W\gamma$ cross section with ATLAS detector using 5 fb^{-1} of data. Left plot shows the results for inclusive and right plot for exclusive measurement.

Table 7.1: 1D limits on aTGC parameters from ATLAS experiment measurements using 1 fb^{-1} of data.

	Measured	Measured	Expected
Λ	2 TeV	∞	∞
$\Delta\kappa_\gamma$	[-0.36, 0.41]	[-0.33, 0.37]	[-0.33, 0.36]
λ_γ	[-0.079, 0.074]	[-0.060, 0.060]	[-0.063, -0.055]

Measurements of $W\gamma$ characteristics have also been performed at the Tevatron proton-antiproton collider at a center of mass energy $\sqrt{s} = 1.96$ TeV. The *D*0 and *CDF* experiments published several papers [40, 41, 42, 43] including $W\gamma$ cross section and aTGC measurements. The measured inclusive cross section is in good agreement with the NLO expectation . At Tevatron energies the NLO corrections are much smaller than at LHC. The paper [41] includes the RAZ observation.

The electron-positron collider at CERN, LEP, has also made di-boson measurements. At lower center of mass energy $\sqrt{s} \leq 209$ GeV limits on aTGC have been set. The summary of aTGC measurements from different experiments is shown in Table 7.2 and Figure 7.4. Results from measurements at different center of mass energies cannot be directly compared as well as measurements with and without form-factor formulation.

Table 7.2: Summary of limits on aTGC parameters from different experiments.

	ATLAS ($1fb^{-1}$ data) ($\sqrt{s} = 7$ TeV)	D0 (using form-factor formulation) ($\sqrt{s} = 1.96$ TeV)	LEP (combined) (68% CL) ($\sqrt{s} \leq 209$ GeV)	CMS (this work) ($\sqrt{s} = 7$ TeV)
$\Delta\kappa_\gamma$	[-0.33, 0.37]	[-0.29, 0.38]	[-0.072, 0.017]	[-0.38, 0.29]
λ_γ	[-0.060, 0.060]	[-0.08, 0.08]	[-0.049, -0.008]	[-0.050, 0.037]

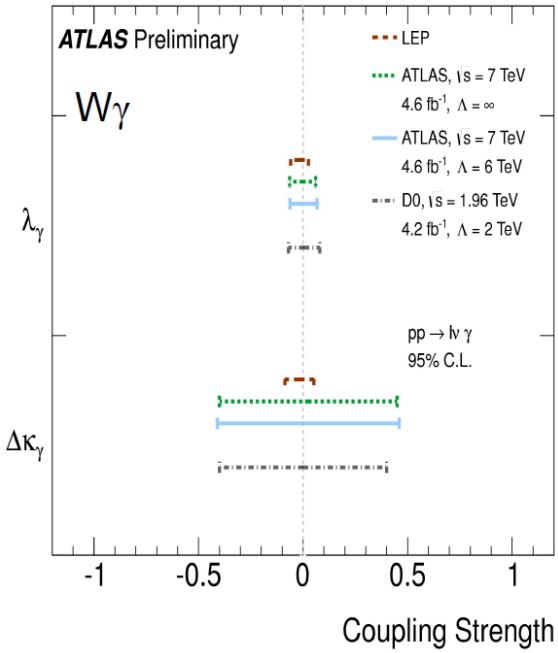

Figure 7.3: 1D limits on aTGC parameters from ATLAS experiment measurements using 5 fb^{-1} of data.

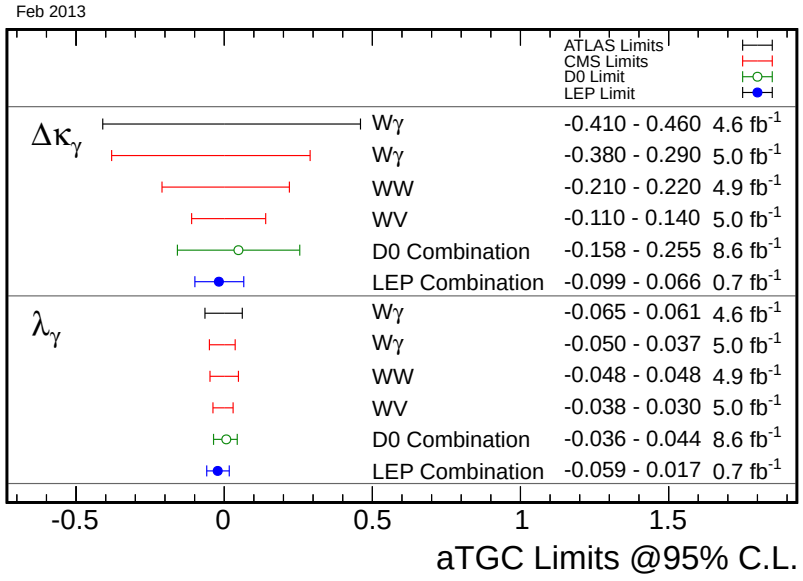

Figure 7.4: One-dimensional limits on aTGC parameters from different experiments.

Chapter 8

Conclusion

The inclusive cross section of $W\gamma \to \mu\nu\gamma$ using the full data set of 5.0 fb^{-1} collected in 2011 with the CMS detector has been measured. The measured cross section of 37.5 ± 0.9 (stat.) $\pm$ 4.4 (syst.) ± 0.8 (lumi.) pb is in agreement with results in the electron channel and about one sigma higher than the expectation from the MCFM generator. Recent measurements with the ATLAS experiment also show higher inclusive cross section than MCFM expectations. The exclusive measurement is however in agreement with expectations. These results indicate that next-to-leading order contribution are likely to be underestimated in the MCFM calculation.

The radiation amplitude zero is visible in the charge-signed η distribution after applying additional selection requiring jet veto and a high transverse mass of $\mu\nu\gamma$ system.

The aTGC signal is not observed so one and two dimensional upper limits on the parameters $\Delta\kappa^{\gamma}$ and λ_{γ} are set. One dimensional 95% C.L. limits $-0.46 < \Delta\kappa^{\gamma} < 0.34$ and $-0.057 < \lambda^{\gamma} < 0.046$ are in agreement with ATLAS measurements.

The cross section measurement of $W\gamma$ process using the full data set collected in 2012 will provide more precise measurement at high E_{T}^{γ} values. Besides inclusive measurement, the exclusive cross section measurement in jet multiplicity is very important to provide. As the sensitivity to aTGC increases with the increase of a center of mass energy, it is important to perform a search of aTGC using the data collected at a center of mass energy of 8 TeV.

Poglavlje 9

Prošireni sažetak: Mjerenje zajedničke produkcije W bozona i fotona i potraga za anomalnim vezanjem WW foton CMS detektorom

9.1 Uvod

Fizika elementarnih čestica desetljećima pokušava dati odgovore na nekoliko važnih pitanja. Kakva je fizika izvan Standardnog modela (SM)? Što je tamna tvar, tamna energija, kakva je priroda gravitacije? Postoji li Higgsov bozon? Želja za odgovorom na posljednje pitanje jedan je od glavnih razloga izgradnje nekoliko sudarivača i u sklopu njjih nekoliko detektorskih sustava. Na proton-antiproton sudarivaču na Fermilab-u u Sjedinjenim Američkim Državama dva detektora, D0 i CDF, mjerila su produkte sudara u periodu 1985-2011. Rezultati mjerenja bila su važna otkrića na energiji sudara od 2 TeV-a, ali Higgsov bozon nije otkriven. Prije nekoliko godina Veliki hadronski sudarivač (LHC, od engl. Large Hadron Collider) na CERN-u počinje s radom na energiji od 7 TeV-

a u sustavu centra mase dvaju protona. Dva detektora opće namjene, ATLAS i CMS, pokušavaju dati odgovor na pitanje postojanja Higgsovog bozona.

Jedan od osnovnih zahtjeva ATLAS i CMS detektora u procesu dizajniranja bio je precizno mjerenje produkata raspada Higgsovog bozona, leptona i fotona.

Osim potrage za Higgsovim bozonom i fizikom izvan SM, mjerenje SM procesa također je važan zadatak na LHC-u. Mjerenja SM procesa provjera su valjanosti SM-a na visokim energijama te također omogućavaju indirektnu potragu za fizikom izvan SM-a. U procesima s dva vektorska bozona u konačnom stanju, kao što je $W\gamma$, može su uz udarni presjek mjeriti i jakost trostrukih baždarnih vezanja (TGC, od engl. triple gauge coupling). U slučaju postojanja nove (još neotkrivene) fizike izvan SM-a jačina TGC-a bi bila veća što rezultira tzv. anomalnim doprinosima TGC-u (aTGC, od engl. anomalous triple gauge coupling). Jačine trostrukih baždarnih vezanja su najmanje precizno mjerene veličine elektroslabog sektora SM-a.

9.2 $W\gamma$ proces na LHC-u

9.2.1 Standardni Model

Standardni model [5] sadrži cjelokupno trenutno znanje o elementarnim česticama i njihovim interakcijama. Tijekom posljednjih nekoliko desetljeća, SM temeljito je testiran na svim energijama dostupnim u laboratoriju. S početkom rada LHC sudarivača na energiji od 7 TeV-a u sustavu centra mase dvaju protona jedan od prvih zadataka je bila provjera valjanosti SM-a.

Elektroslaba teorija Standardnog modela, koja obuhvaća elektromagnetsku i slabu interakciju, uključuje jedine masivne nosioce sila u teoriji, spontano lomljenje simetrije Higgsovim mehanizmom te V-A strukturu međudjelovanja. Zahtjevi na teoriju su da je to renormalizabilna lokalno invarijantna baždarna teorija. U elektroslaboj teoriji lagrangian je invarijantan na lokalne $SU(2)_L \otimes U(1)_Y$ transformacije, gdje L označava lijevi dublet a Y slabi hipernaboj.

Lagrangian slobodnog fermiona dan je s:

$$\begin{aligned} \mathscr{L}_1 &= \overline{\Psi}(i\gamma^\mu \partial_\mu - m)\Psi, \\ &= (\overline{L}+\overline{R})(i\gamma^\mu \partial_\mu - m)(L+R), \\ &= \overline{L}(i\gamma^\mu \partial_\mu)L + \overline{R}(i\gamma^\mu \partial_\mu)R - m(\overline{L}R + \overline{R}L) \end{aligned} \tag{9.1}$$

gdje je Ψ valna funkcija fermiona [6] a m masa. Ψ ima lijevu (L) i desnu (R) komponentu koje se različito transformiraju prilikom $SU(2)_L \otimes U(1)_Y$ transformacije:

$$\begin{aligned} L \to L' &= e^{i\overrightarrow{\alpha}(x)\cdot\overrightarrow{T} + i\beta(x)Y} L, \\ R \to R' &= e^{i\beta(x)Y} R \end{aligned} \tag{9.2}$$

gdje su $\overrightarrow{T}$ i Y generatori $SU(2)_L$ i $U(1)_Y$ grupa. L je izospinski dublet a R izospinski singlet. U slučaju leptona:

$$
\begin{aligned}
L &= \begin{pmatrix} \nu_e \\ e^- \end{pmatrix}_L, \begin{pmatrix} \nu_\mu \\ \mu^- \end{pmatrix}_L, \begin{pmatrix} \nu_\tau \\ \tau^- \end{pmatrix}_L, \\
R &= \left(e^-\right)_R, \left(\mu^-\right)_R, \left(\tau^-\right)_R.
\end{aligned} \tag{9.3}
$$

Kao što je rečeno, zahtjev na lagrangian 9.1 je invarijantnost na lokalne $SU(2)_L \otimes U(1)_Y$ transformacije. Za razliku od kvantne elektrodinamike dio lagrangiana koji sadrži fermionske mase nije invarijantan i zasada ćemo ga zanemariti. Invarijantnost preostalog dijela lagrangiana postiže se uvođenjem kovarijantne derivacije D_μ kojom se uvode i četiri vektorska bozonska polja:

$$
\text{za } L\text{: } D_\mu = \partial_\mu + ig\overrightarrow{T}\cdot\overrightarrow{W}_\mu + ig'\frac{Y}{2}B_\mu, \tag{9.4}
$$

$$
\text{za } R\text{: } D_\mu = \partial_\mu + ig'\frac{Y}{2}B_\mu. \tag{9.5}
$$

Korištenjem gornjih derivacija lagrangian postaje baždarno invarijantan:

$$
\begin{aligned}
\mathscr{L}_1 = {} & \overline{L}\gamma^\mu(i\partial_\mu - g\overrightarrow{T}\cdot\overrightarrow{W}_\mu - ig'\frac{Y}{2}B_\mu)L \\
& + \overline{R}\gamma^\mu(i\partial_\mu - ig'\frac{Y}{2}B_\mu)R
\end{aligned} \tag{9.6}
$$

Lagrangian 9.6 obuhvaća kinetičku energiju fermiona i njihovu interakciju s vektorskim bozonima W^1, W^2,W^3 i B koji pripadaju poljima $\overrightarrow{W}^\mu$ i B^μ. Pošto su uključena dodatna polja, u lagrangian treba uključiti i pripadajuće kinetičke energije bozona:

$$
\mathscr{L}_2 = -\frac{1}{4}\overrightarrow{W}_{\mu\nu}\overrightarrow{W}^{\mu\nu} - \frac{1}{4}B_{\mu\nu}B^{\mu\nu} \tag{9.7}
$$

gdje je:

$$
\overrightarrow{W}_{\mu\nu} = \partial_\mu\overrightarrow{W}_\nu - \partial_\nu\overrightarrow{W}_\mu - g\overrightarrow{W}_\mu \times \overrightarrow{W}_\nu, \tag{9.8}
$$

i

$$B_{\mu\nu} = \partial_\mu B_\nu - \partial_\nu B_\mu. \tag{9.9}$$

Posljednji član u 9.8 rezultat je neabelove strukture $SU(2)_L \otimes U(1)_Y$ grupe.

Poznato je da fermioni kao i elektroslabi bozoni $W^\pm$ i Z imaju masu različitu od nule dok je masa fotona jednaka nuli. Higgsov mehanizam [7, 8, 9] koristi se za generiranje masa bozona i fermiona a da istovremeno lagrangian ostaje baždarno invarijantan. U tu svrhu uvode se 4 dodatna realna skalarna polja Φ_i. Lagrangian skalarnog polja dan je izrazom:

$$\mathscr{L}_3 = (\partial_\mu \Phi)^\dagger (\partial^\mu \Phi) - V(\Phi), \tag{9.10}$$

gdje je $V(\Phi)$ potencijal polja. Potencijal $V(\Phi)$ ima oblik:

$$V(\Phi) = \mu^2 \Phi^\dagger \Phi + \lambda (\Phi^\dagger \Phi)^2. \tag{9.11}$$

Da bi lagrangian 9.10 bio lokalno baždarno invarijantan, Φ_i mora biti $SU(2)_L \otimes U(1)_Y$ multiplet te se mora koristiti kovarijantna derivacija 9.4.

Polja su izabrana tako da tvore izospinski dublet:

$$\Phi = \begin{pmatrix} \phi^+ \\ \phi^0 \end{pmatrix} \tag{9.12}$$

gdje je:

$$\phi^+ = \frac{\phi_1 + i\phi_2}{\sqrt{2}}, \tag{9.13}$$

$$\phi^0 = \frac{\phi_3 + i\phi_4}{\sqrt{2}}. \tag{9.14}$$

Ako su konstante μ i λ takve da je $\mu^2 < 0$ i $\lambda > 0$, potencijal ima oblik "Maksičkog šešira". Točka $\Phi = 0$ je nestabilna te postoji kontinuum točaka koje čine minimum:

$$\Phi^\dagger \Phi = -\frac{\mu^2}{2\lambda}. \tag{9.15}$$

Izborom jedne točke za minimum daje se vakuumu preferiran smjer u prostoru izospina, a simetrija je spontano slomljena. Minimum je izabran u točci:

$$\begin{aligned} \phi_1 = \phi_2 = \phi_4, \phi_3^2 = -\frac{\mu^2}{\lambda} \equiv v^2, \\ \Phi_0 = \frac{1}{\sqrt{2}} \begin{pmatrix} 0 \\ v \end{pmatrix}. \end{aligned} \tag{9.16}$$

Ovaj izbor za Φ_0 lomi $SU(2)$ i $U(1)_Y$ baždarne simetrije dok $U(1)_{em}$ ostaje sačuvana, što rezultira masivnim $W^\pm$ i Z vektorskim bozonima i bezmasenim fotonom.

Korištenjem kovarijantne derivacije lagrangian 9.10 je baždarno invarijantan:

$$\begin{aligned} \mathscr{L}_3 &= \Phi^\dagger (\partial_\mu - ig\overrightarrow{T}\cdot\overrightarrow{W}_\mu - ig'\frac{Y}{2}B_\mu)(\partial^\mu + ig\overrightarrow{T}\cdot\overrightarrow{W}^\mu + ig'\frac{Y}{2}B^\mu)\Phi - V(x) \\ &= \frac{1}{2}\begin{pmatrix} 0 & v \end{pmatrix}(\partial_\mu - ig\overrightarrow{T}\cdot\overrightarrow{W}_\mu - ig'\frac{1}{2}B_\mu)(\partial^\mu + ig\overrightarrow{T}\cdot\overrightarrow{W}^\mu + ig'\frac{1}{2}B^\mu)\begin{pmatrix} 0 \\ v \end{pmatrix} - V(x), \end{aligned} \tag{9.17}$$

gdje je korištena izabrana točka vakuuma 9.16 te odgovarajuća vrijednost hipernaboja $Y = 1$. Relevantni član za masu bozona je:

$$
\begin{aligned}
\mathscr{L}_3^{\text{član mase bozona}} =& \frac{1}{2}\begin{pmatrix}0 & v\end{pmatrix}(-ig\overrightarrow{T}\cdot\overrightarrow{W}_\mu - ig'\frac{1}{2}B_\mu)(ig\overrightarrow{T}\cdot\overrightarrow{W}^\mu + ig'\frac{1}{2}B^\mu)\begin{pmatrix}0\\ v\end{pmatrix} \\
=& \frac{1}{8}\begin{pmatrix}0 & v\end{pmatrix}\begin{pmatrix} gW_\mu^3 + g'B_\mu & gW_\mu^1 - igW_\mu^2 \\ gW_\mu^1 + igW_\mu^2 & -gW_\mu^3 + g'B_\mu\end{pmatrix} \\
& \begin{pmatrix} gW^{\mu 3} + g'B^\mu & gW^{\mu 1} - igW^{\mu 2} \\ gW^{\mu 1} + igW^{\mu 2} & -gW^{\mu 3} + g'B^\mu\end{pmatrix}\begin{pmatrix}0\\ v\end{pmatrix} \\
=& \frac{(vg)^2}{8}[(W_\mu^1)^2 + (W_\mu^2)^2] + \frac{(v)^2}{8}[-gW_\mu^3 + g'B_\mu]^2.
\end{aligned}
\tag{9.18}
$$

Za nabijene vektorske bozone očekuje se član oblika $M_X^2X^2$ dok se za neutralne bozone očekuje član oblika $\frac{1}{2}M_X^2X^2$. Miješanje polja $\overrightarrow{W}^\mu$ i B^μ nužno je za prepoznavanje fizikalnih vektorskih bozona $W^\pm$, Z i fotona. Koriste se slijedeći identiteti:

$$
\begin{aligned}
W_\mu^+ &= \frac{1}{\sqrt{2}}(W_\mu^1 - iW_\mu^2), \\
W_\mu^- &= \frac{1}{\sqrt{2}}(W_\mu^1 + iW_\mu^2), \\
Z_\mu &= \frac{1}{\sqrt{g^2+g'^2}}(gW_\mu^3 - g'B_\mu), \\
A_\mu &= \frac{1}{\sqrt{g^2+g'^2}}(g'W_\mu^3 + gB_\mu).
\end{aligned}
\tag{9.19}
$$

Sada se maseni član može pisati kao:

$$
\mathscr{L}_3^{\text{član mase bozona}} = \frac{(vg)^2}{4}W_\mu^+W^{\mu-} + \frac{(v)^2}{8}(g^2+g'^2)(Z_\mu)^2 + 0(A_\mu)^2, \tag{9.20}
$$

gdje se prepoznaju mase bozona:

$$
\begin{aligned}
M_W &= \frac{vg}{2}, \\
M_Z &= \frac{v}{2}\sqrt{g^2+g'^2}, \\
M_A &= 0.
\end{aligned}
\tag{9.21}
$$

Nadalje, Higgsov mehanizam koristi se za generiranje masa fermiona. Član lagrangiana koji predstavlja interakciju Higgsovog polja s fermionima može se napisati u obliku:

$$
\mathscr{L}_4 = -G_e(\overline{R}\Phi^{\dagger}L + \overline{L}\Phi R). \tag{9.22}
$$

Simetrija je spontano slomljena izborom točke vakuuma 9.16 i razvojem oko nje:

$$
\Phi(x) = \frac{1}{\sqrt{2}}\begin{pmatrix} 0 \\ v+h(x) \end{pmatrix}. \tag{9.23}
$$

U slučaju elektrona $\mathscr{L}_4$ poprima oblik:

$$
\begin{aligned}
\mathscr{L}_4 &= -\frac{G_e}{\sqrt{2}}[v(\overline{e_R}e_L + \overline{e_L}e_R) + h(x)(\overline{e_R}e_L + \overline{e_L}e_R)] \\
&= -\frac{G_e}{\sqrt{2}}[v(\overline{e}e) + h(x)(\overline{e}e)].
\end{aligned}
\tag{9.24}
$$

Uz jednakost:

$$
G_e = \sqrt{2}\frac{m_e}{v}, \tag{9.25}
$$

lagrangian 9.24 možemo napisati u obliku:

$$
\mathscr{L}_4 = -m_e\overline{e}e - \frac{m_e}{v}h(x)\overline{e}e, \tag{9.26}
$$

gdje prvi član definira masu elektrona a drugi član predstavlja vezanje Higgsovog bozona s elektronom. Mase kvarkova generiraju se na jednak način.

Sumiranjem svih članova dobiva se ukupni elektroslabi lagrangian:

$$\begin{aligned}\mathscr{L}_{ukupni} =& \Phi^{\dagger}(\partial_{\mu} - ig\overrightarrow{T}\cdot\overrightarrow{W}_{\mu} - ig'\frac{Y}{2}B_{\mu})(\partial^{\mu} + ig\overrightarrow{T}\cdot\overrightarrow{W}^{\mu} + ig'\frac{Y}{2}B^{\mu})\Phi - V(x) \\ & - G_1(\overline{R}\Phi^{\dagger}L + \overline{L}\Phi R) - G_2(\overline{R}\Phi_c^{\dagger}L + \overline{L}\Phi_c R) \\ & + \overline{L}\gamma^{\mu}(i\partial_{\mu} - g\overrightarrow{T}\cdot\overrightarrow{W}_{\mu} - ig'\frac{Y}{2}B_{\mu})L \\ & + \overline{R}\gamma^{\mu}(i\partial_{\mu} - ig'\frac{Y}{2}B_{\mu})R \\ & - \frac{1}{4}\overrightarrow{W}_{\mu\nu}\overrightarrow{W}^{\mu\nu} - \frac{1}{4}B_{\mu\nu}B^{\mu\nu}\end{aligned} \tag{9.27}$$

gdje je Φ_c novi Higgsov dublet korišten za generiranje masa gornjih članova u L dubletu:

$$\Phi_c = \begin{pmatrix} -\overline{\phi^0} \\ \phi^- \end{pmatrix}. \tag{9.28}$$

Prvi red u izrazu 9.27 predstavlja $W^{\pm}$, Z, γ i Higgs mase i vezanja, drugi red mase leptona i kvarkova i vezanja s Higgsovim bozonom, treći i četvrti red predstavljaju kinetičke energije leptona i kvarkova i njihove interakcije s vektorskim bozonima dok zadnji red predstavlja kinetičke energije vektorskih bozona i njihova međudjelovanja. Trostruka vezanja vektorskih bozona $WW\gamma$ i WWZ proizlaze iz zadnjeg člana u 9.8. Korištenjem identiteta 9.19 dio lagrangiana koji opisuje TGC jednak je:

$$\mathscr{L}_{TGC} = -ig_{WWV}[V^{\mu}(W^-_{\mu\nu}W^{+\nu} - W^+_{\mu\nu}W^{-\nu}) + W^+_{\mu}W^-_{\nu}V^{\mu\nu}], \tag{9.29}$$

gdje je V^{μ} jednak A^{μ} ili Z^{μ}, $g_{WWZ} = ecot\theta_W$, $g_{WW\gamma} = e$, a θ_W je slabi kut. Proizlazi da su TGC dozvoljena Standardnim modelom, $WW\gamma$ i WWZ.

9.2.2 $W\gamma$ proces

Produkcija para bozona omogućava proučavanje neabelove baždarne simetrije Standardnog modela. Odstupanja od predviđanja SM-a moguća su ako postoje anomalna vezanja ili se produciraju nove masivne čestice koje se raspadaju na parove bozona. Procesi s parovima bozona također predstavljaju veliki dio pozadine za mnoge signale fizike izvan SM.

Produkcija para vektorskih bozona $W\gamma$ u proton-proton sudarima u vodećem redu (LO, od engl. Leading Order) uključuje tri procesa prikazana na Slici 9.1. To su emisija fotona iz konačnog stanja, emisija fotona iz početnog stanja te trostruko baždarno vezanje $WW\gamma$. Postoji još jedan proces koji dominira na niskim energijama, $q_1 g \rightarrow V q_2$ gdje kvark u finalnom stanju emitira foton, tzv. zakočno zračenje fotona. Ovaj proces potisnut je zahtjevom da je foton izoliran.

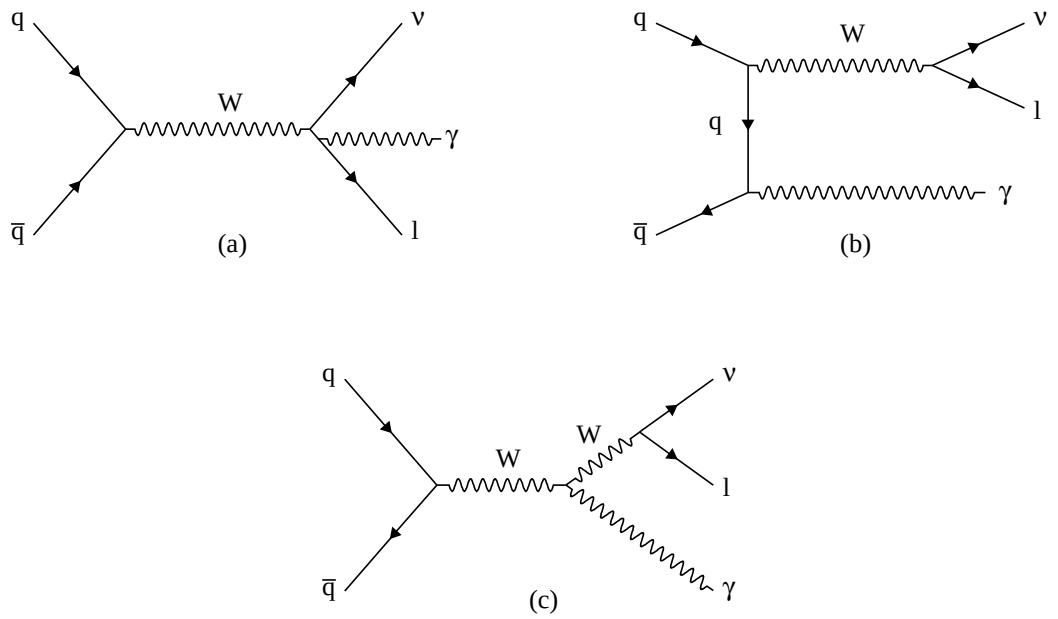

Slika 9.1: Feynmanovi dijagrami koji doprinose Wγ produkciji: emisija fotona iz konačnog (a) i početnog (b) stanja i WWγ trostruko baždarno vezanje (c).

U vodećem redu procesu produkcije doprinosi anihilacija kvarkova i antikvarkova, a u višem redu (NLO, od engl. Next to Leading Order) fuzija gluona i kvarkova. Na LHC-u NLO korekcije su vrlo velike zbog velike gustoće partona na visokim energijama.

Tablica 9.1: Omjeri grananja W^+ raspada [1].

Kanal raspada	Udio
$l^+\nu$	10.80 ± 0.09 %
$e^+\nu$	10.75 ± 0.13 %
$\mu^+\nu$	10.57 ± 0.15 %
hadrons	67.60 ± 0.27 %

Kanali raspada i pripadni omjeri grananja W^+ bozona dani su u Tablici 9.1.

9.2.3 Radijacijska amplituda vrijednosti nula

Istaknuta karakteristika $W\gamma$ produkcije u hadronskim sudarima je tzv. radijacijska amplituda vrijednosti nula (RAZ, od engl. Radiation Amplitude Zero), fenomen kada su sve amplitude heliciteta jednake nuli za određeni izlazni kut fotona u sustavu centra mase.

Poznato je da su sve amplitude heliciteta za procese $q_1\bar{q_2} \rightarrow W^{\pm}\gamma$ jednake nuli u sustavu centra mase za $\cos\theta^* = -\frac{Q_1+Q_2}{Q_1-Q_2}$ [10, 11], gdje je θ^* kut raspršenja fotona s obzirom na smjer kvarka q_1, Q_i (i = 1, 2) su naboji kvarkova u jedinicama naboja protona. U proton-proton sudarima dominantni proces produkcije $W^+\gamma$ je $u\bar{d} \rightarrow W^+\gamma$ gdje je amplituda jednaka nuli za $\cos\theta^* = -\frac{1}{3}$, a dominantan proces produkcije $W^-\gamma$ je $d\bar{u} \rightarrow W^-\gamma$ gdje je amplituda jednaka nuli za $\cos\theta^* = \frac{1}{3}$.

Iz više razloga ovu je pojavu potpunog poništenja amplitude teško opaziti. U realnom eksperimentu poništenje ampitude je uvijek djelomično i umjesto nule opaža se udubina u kutnoj raspodjeli. Dodatni procesi koji doprinose produkciji, QCD korekcije višeg reda, emisija fotona iz konačnog stanja, te konačna širina W bozona popunjavaju udubinu u kutnoj raspodjeli. Konačna rezolucija detektora dodatno otežava opažanje. Također nije moguće rekonstruirati sustav centra mase na hadronskim sudarivačima kao što je LHC pošto nije moguće jednoznačno odrediti longitudinalnu količinu gibanja neutrina. Kako nije moguće izvršiti mjerenje u sustavu centra mase potražene su osjetljive opservable u laboratorijskom sustavu. U sustavu centra mase, W bozon i foton, gibaju se u suprotnim smjerovima, stoga u raspodjeli rapiditeta W bozona isto kao i u razlici rapiditeta $y(\gamma)^* -$

$y(W)^*$ također postoji udubina.[1] Pošto je razlika rapiditeta invarijantna na longitudinalni potisak udubina se opaža i u razlici rapiditeta u laboratorijskom sustavu, $y(\gamma) - y(W)$. Kako longitudinalnu količinu gibanja za neutrino nije moguće eksperimentalno odrediti nije moguće odrediti rapiditet W bozona. U SM-u dominantan helicitet W bozona u $W^{\pm}\gamma$ produkciji je $\lambda_W = \pm 1$ [12]. To znači da je lepton iz W raspada dominantno emitiran u istom smjeru kao i W, tako da lepton odražava mnoga kinematska svojstva W bozona. Stoga je korelacija među rapiditetima W bozona i fotona prisutna i među rapiditetima leptona i fotona. U granici bezmasenih čestica rapiditet i pseudorapiditet su jednaki, stoga očekujemo da će RAZ udubina također biti prisutna u razlici pseudorapiditeta $\eta(\gamma) - \eta(l)$, što je veličina koja se može precizno mjeriti na CMS detektoru.[2]

Na LHC-u, RAZ učinak bi se mogao opaziti u $W\gamma$ produkciji kao udubina oko vrijednosti 0 u $\eta(\gamma) - \eta(l)$ raspodjeli, kao što je ilustrirano ns Slici 9.2 [2].

RAZ se može promatrati kao relativistička generalizacija odsutnosti električnog i magnetskog polja kod nerelativističkih sudara čestica s jednakim omjerom naboj/masa i g faktorom [13].

U selektiranim $W\gamma$ događajima moguće je dodatnim uvjetima postići lakše opažanje RAZ-a. Doprinos QCD korekcija višeg reda koje popunjavaju udubinu može se značajno smanjiti primjenom zahtjeva da u događaju ne postoji niti jedan hadronski mlaz s količinom gibanja većom od određenog P_T praga. Proces emisije fotona iz konačnog stanja također popunjava RAZ udubinu. Ovaj se doprinos može smanjiti postavljanjem zahtjeva na minimalnu vrijednost transverzalne mase $W\gamma$ sustava, $M_T^{(W\gamma)}$.

RAZ udubina je također osjetljiva na prisutnost anomalnih trostrukih baždarnih vezanja. aTGC će izmjeniti oblik $\eta(\gamma) - \eta(l)$ raspodjele te također popuniti RAZ udubinu, međutim ovo nije varijabla koja je najosjetljivija na prisutnost anomalnih vezanja u $W\gamma$ kanalu.

[1] Rapiditet čestice definiran je izrazom $y = \frac{1}{2}\ln\frac{E+p_Z}{E-p_Z}$, gdje je E energija čestice a p_Z komponenta količine gibanja u smjeru snopa.

[2] Pseudorapiditet čestice definiran je izrazom kao $\eta = -\ln\tan(\theta/2) = \frac{1}{2}\ln\frac{|\vec{p}|+p_Z}{|\vec{p}|-p_Z}$. θ je kut između smjera količine gibanja čestice $\vec{p}$ i osi snopa, a p_Z je komponenta količine gibanja u smjeru osi snopa.

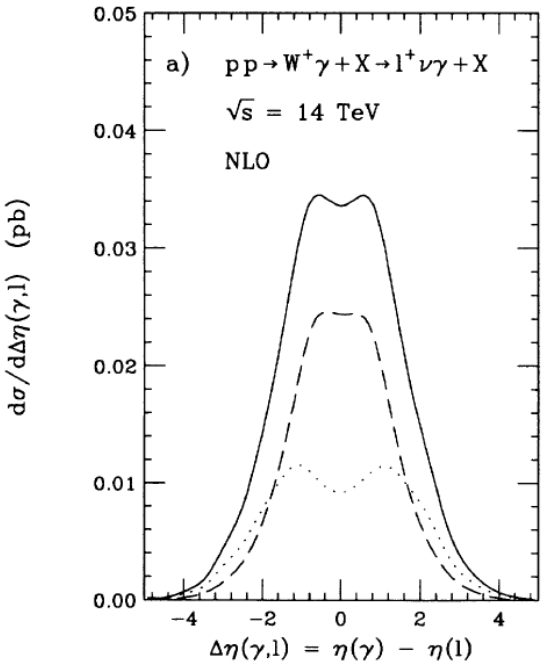

Slika 9.2: Diferencijalni udarni presjek razlike pseudorapiditeta fotona i leptona za proces $pp \to W^+\gamma \to l^+\nu\gamma$ pri $\sqrt{s} = 14$ TeV-a u SM. Inkluzivni NLO diferencijalni udarni presjek (puna linija), ekskluzivni diferencijalni udarni presjek događaja sa jednim mlazom (isprekidana linija), ekskluzivni diferencijalni udarni presjek događaja sa nula mlazeva (točkasta linija).

9.2.4 Trostruka baždarna vezanja

Ako postoje nove, još neotkrivene, čestice izvan Standardnog modela (kao naprimjer u teoriji Supersimetrija) s masama većim od $0.5 - 1$ TeV-a, tada se na nižim energijama generiraju anomalna vezanja.

Trostruka baždarna vezanja posljedica su neabelovog karaktera baždarne grupe elektroslabog sektora SM-a, a jakosti vezanja su jednoznačno određena. Mnoge teorije izvan SM-a predviđaju dodatne procese produkcije para bozona, stoga svako odstupanje mjerene vrijednosti od očekivanja SM-a može biti prvi znak fizike izvan SM-a na visokim energijama. Tako mjerenje aTGC-a može biti osjetljivo na nove fenomene na visokim energijama za koje je potrebna viša energija ili viši integrirani luminozitet za direktno opažanje.

Najopćenitiji efektivni lagrangian invarijantan na Lorentzove transformacije koji opisuje WWV vezanje ima 14 neovisnih parametara [15, 16], 7 parametara za WWZ i 7 parametara za $WW\gamma$ vezanje. Uz pretpostavku C i P sačuvanja u efektivnom lagrangianu ostaje samo 6 neovisnih parametara:

$$\frac{\mathscr{L}_{TGC}}{g_{WWV}} = ig_1^V(W^-_{\mu\nu}W^{+\mu}V^{\nu} - W^-_{\mu}V_{\nu}W^{+\mu\nu}) + i\kappa_V W^-_{\mu}W^+_{\nu}V^{\mu\nu} + \frac{i\lambda_V}{M_W^2}W^-_{\delta\mu}W^{+\mu}_{\nu}V^{\nu\delta}, \tag{9.30}$$

gdje je $V = \gamma$ ili Z, $g_{WW\gamma} = -e$ i $g_{WWZ} = -e\cot\theta_W$, θ_W je Weinbergov kut. Pretpostavivši elektromagnetsku baždarnu invarijantnost, $g_1^{\gamma} = 1$. Preostali parametri koji opisuju WWV vezanje su g_1^Z, κ_Z, κ_γ, λ_Z i λ_γ. Usporedbom sa 9.29 dobivaju se vrijednosti parametara u SM-u: $\lambda_Z = \lambda_\gamma = 0$ i $g_1^Z = \kappa_Z = \kappa_\gamma = 1$.

Preostalih pet parametara reducira se na tri neovisna parametra uz prepostavku da je lagrangian invarijantan na $SU(2)_L \otimes U(1)_Y$ transformacije:

$$\Delta\kappa_Z = \Delta g_1^Z - \Delta\kappa_\gamma \cdot \tan^2\theta_W, \;\; \lambda = \lambda_\gamma = \lambda_Z. \tag{9.31}$$

U ovom radu mjereni su parametri $\Delta\kappa_\gamma$ i λ_γ analizom procesa $pp \to W\gamma$.

Sva anomalna vezanja narušavaju unitarnost na visokim energijama. Iz tog razloga mjerenja aTGC-a na Tevatronu koriste pretpostavljenu $\hat{s}$-ovisnost parametara vezanja, tzv. form-faktor, da bi sačuvali unitarnost:

$$\alpha(\hat{s}) = \frac{\alpha_0}{(1+\hat{s}/\Lambda^2_{NP})^n}. \tag{9.32}$$

Ovdje je α_0 nisko-energijska aproksimacija vezanja $\alpha(\hat{s})$, $\hat{s}$ je kvadrat invarijantne mase dvobozonskog sustava, a Λ_{NP} je skala form-faktora i energija na kojoj fizika izvan SM poništava divergencije u aTGC vrhu. U ovom radu mjereni su aTGC parametri bez upotrebe form-faktora da se izbjegne pretpostavka o obliku ovisnosi parametara o energiji.

U konačnom stanju $W\gamma$, signal postojanja anomalnih trostrukih vezanja je povećan broj događaja koji sadrže fotone velikog transverzalnog impulsa E_T^γ kao što je prikazano na Slici 9.3. $W\gamma$ proces koji uključuje i anomalna trostruka vezanja simuliran je generatorima SHERPA [3] i PYTHIA [4].

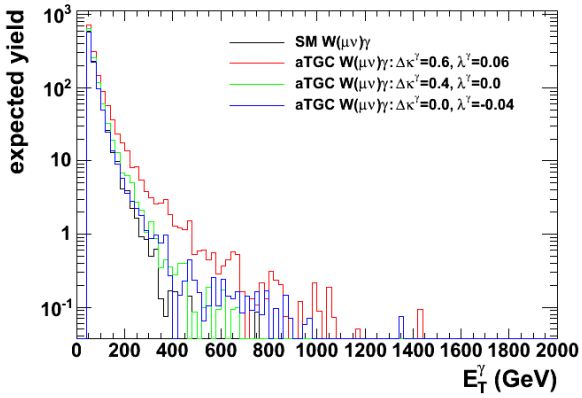

Slika 9.3: Simulirana raspodjela E_T^γ za $W\gamma$ proces, za različite vrijednosti aTGC parametara.

Različiti modeli fizike izvan SM-a predviđaju različite vrijednosti aTGC parametara. Dodatna generacija teških kvarkova i leptona rezultirala bi s vrijednostima reda $\approx 10^{-3}$ a Minimalni Supersimetričan SM (MSSM) [14] model s vrijednostima:

$$\begin{aligned} |\Delta\kappa_\gamma| &\leq 2\times 10^{-2}, \\ |\Delta\kappa_Z| &\leq 2\times 10^{-2}, \\ |\lambda_\gamma| &\leq 6\times 10^{-3}, \\ |\lambda_Z| &\leq 6\times 10^{-3}. \end{aligned} \tag{9.33}$$

9.3 LHC akcelerator i CMS detektor

9.3.1 LHC ubrzivač

Veliki hadronski sudarivač (LHC) [17] je najsnažniji ubrzivač čestica na svijetu u kojem se sudaraju protoni a započeo je radom 2009. godine. LHC je postavljen u tunelu opsega 26.7 km u kojem se nalazio LEP sudarivač. Tunel je smješten na dubini 45-170 m u blizini Švicarsko-Francuske granice i sastoji se od 8 ravnih dijelova povezanih s 8 lukova.

Korištenjem dva detektora opće namjene, CMS i ATLAS na LHC-u proučavaju se procesi Standardnog modela te provodi potraga za fizikom izvan Standardnog modela.

Shematski prikaz akceleratorskih sustava dan je na Slici 9.3.1.

Korištenje postojećeg LEP tunela predstavljalo je izazov, posebno pri dizajnu magneta za usmjeravanje LHC snopa. Budući da se isto magnetsko polje ne može koristiti za skretanje dva protonska snopa koji se gibaju u suprotnim smjerovima magneti imaju jedinstven dizajn prikazan na Slici 9.3.1. Magneti stvaraju suprotno usmjerena polja jakosti 8T.

9.3.2 CMS detektor

CMS je detektor opće namjene dizajniran za precizno mjerenje leptona i ostalih čestica koje se produciraju u visoko-energijskim proton-proton (pp) sudarima. Višeslojni dizajn CMS detektora prikazan je na Slici 9.6.

Najbliže točci sudara smješteni su silikonski piksel i trakasti detektori tragova, za identifikaciju i mjerenje tragova nabijenih čestica. Detektori tragova se zajedno s elektromagnetskim (ECAL) i hadronskim (HCAL) kalorimetrom nalaze u jakom magnetskom polju jakosti 3.8T. Kalorimetri mjere energiju čestica te sudjeluju u njihovoj identifikaciji. Izvan magneta nalaze se mionske komore pričvršćene na čeličnu konstrukciju koja služi za zatvaranje magnetskog polja. Detaljan opis detektora može se pronaći u [18].

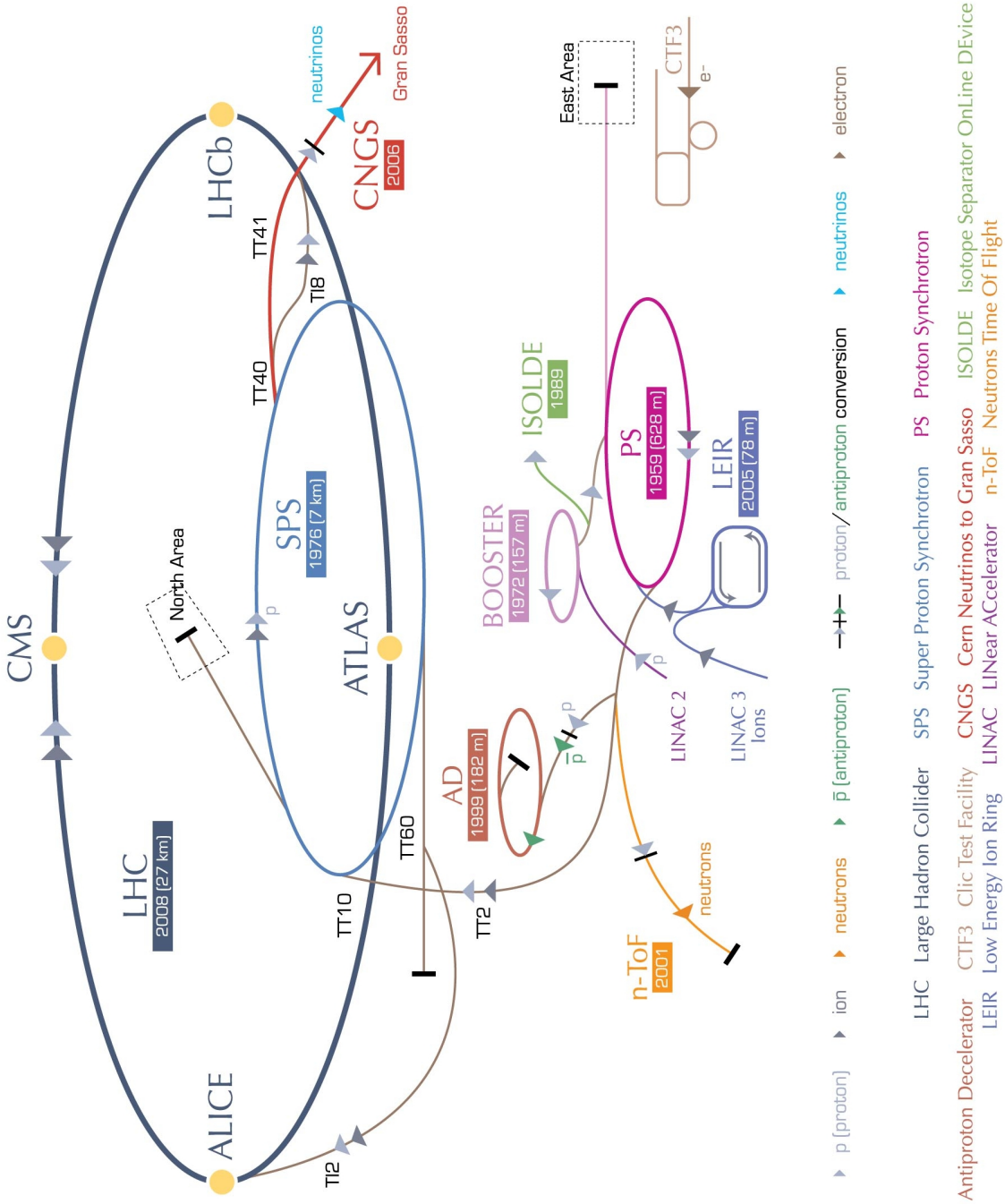

Slika 9.4: Shematski prikaz akceleratorskog sustava LHC-a.

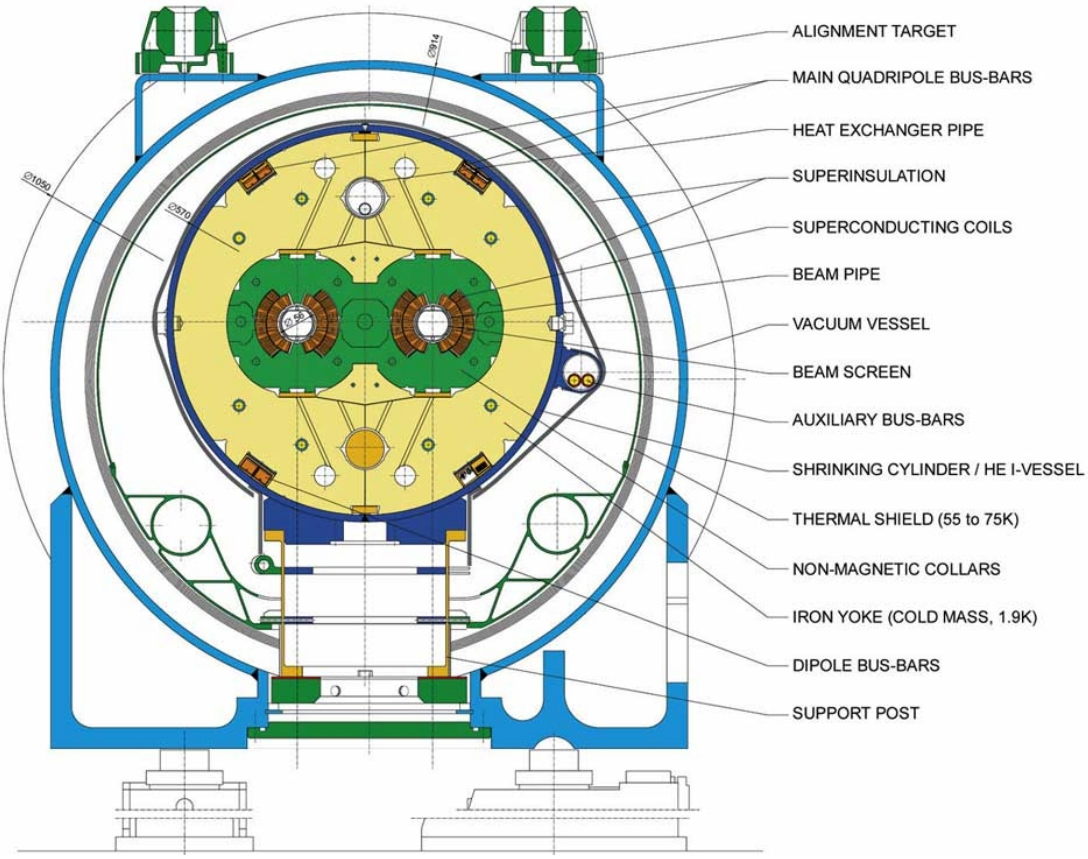

Slika 9.5: Shematski prikaz dipolnog magneta u LHC-u.

Koordinatni sustav

CMS detektor je cilindričnog oblika oko osi snopa, promjera 14.6m i duljine 21.6m. Sastoji se od centralnog i dvaju bočnih dijelova koji zatvaraju detektor. U eksperimentu se koristi desni kartezijev koordinatni sustav. U transverzalnoj ravnini (x-y) mjeri se azimutalni kut ϕ od x osi te radijalna udaljenost $r = \sqrt{x^2 + y^2}$. Polarni kut θ mjeri se od z osi, ali se za opis čestica češće koristi pseudorapiditet.

U neelastičnom sudaru protona međudjeluju dva partona (po jedan iz svakog protona) s određenim dijelom količine gibanja protona. Njihova količina gibanja je longitudinalna s zanemarivim doprinosom u trasnverzalnom smjeru. Zbog sačuvanja količine gibanja ukupna količina gibanja čestica iz sudara je također longitudinalna. Stoga se trajektorije novo nastalih čestica obično opisuju u

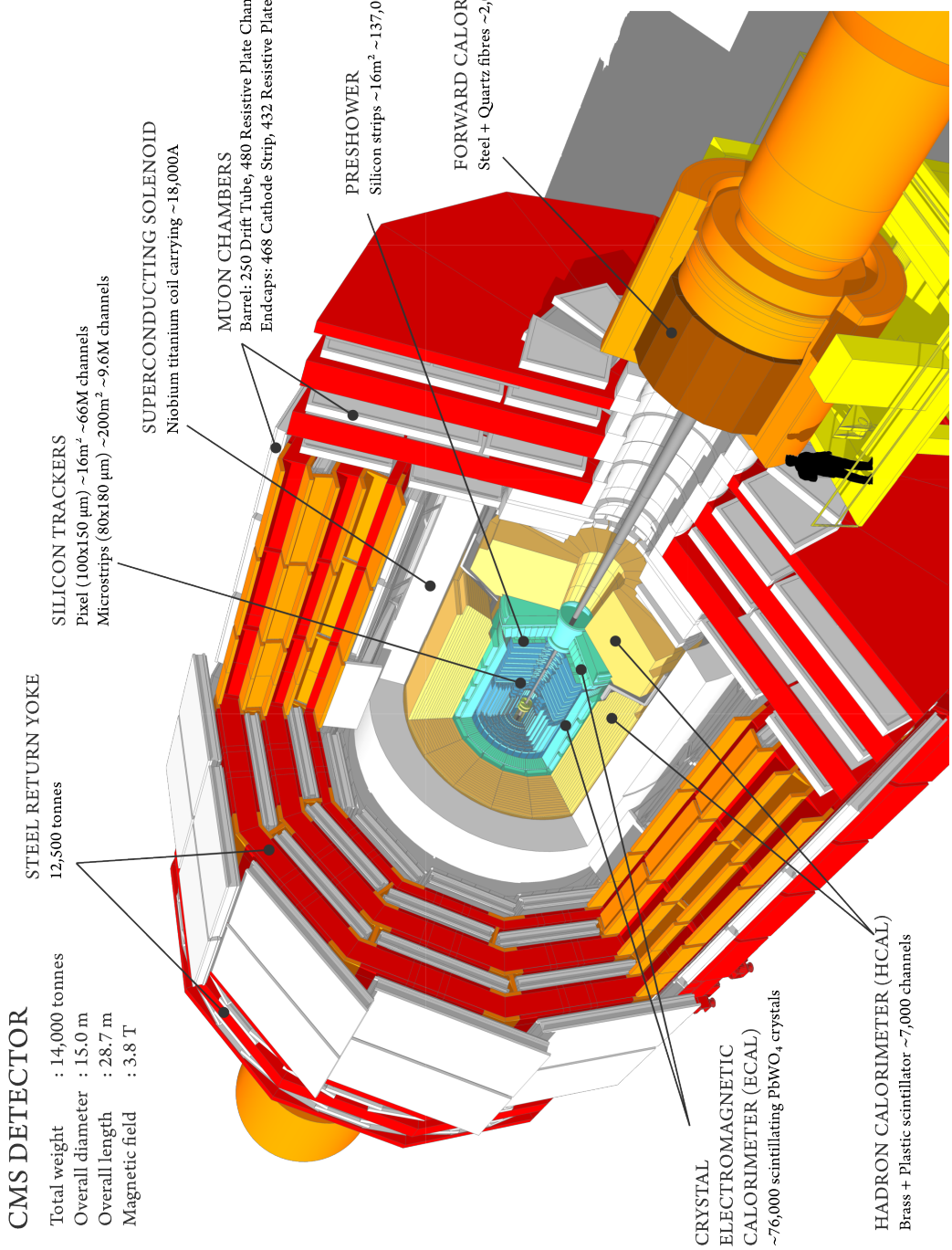

Slika 9.6: CMS detektor.

transverzalnoj ravnini. Čestice koje izlaze iz sudara nedetektirane, kao npr. neutrino, uzrokuje neravnotežu u ukupnoj transverzalnoj količini gibanja.

Detektor tragova

Detektor tragova smješten je najbliže točci sudara i sastoji se od silicijskih poluvodičkih komora. Unutarnji dio detektora odlikuje se vrlo finim piksel detektorima koji omogućuju identifikaciju višestrukih vrhova u sudarima. Tzv. primarni vrh odgovara točci interakcije protona. U jednom sudaru snopova protona može doći do interakcije više parova protona što rezultira s više primarnih vrhova (PU, od engl. pile up). U analizi se koristi zahtjev da je lepton pridružen primarnom verteksu čija je skalarna suma transverzalnih količina gibanja svih novo nastalih čestica maksimalna. Osim tri sloja piksel detektora dalje od točke sudara smješteni su silicijski trakasti detektori. Presjek detektora tragova prikazan je na Slici 9.7.

Rezolucija količine gibanja u centralnom dijelu detektora koji pokriva područje pseudorapiditeta $\mid \eta \mid \leq 1.6$ jednaka je:

$$\frac{\sigma_{p_T}}{p_T} = (15 p_T \oplus 0.5)\%(TeV), \tag{9.34}$$

dok je rezolucija u bočnim dijelovima za vrijednost pseudorapiditeta $\mid \eta \mid = 2.5$ jednaka:

$$\frac{\sigma_{p_T}}{p_T} = (60 p_T \oplus 0.5)\%(TeV). \tag{9.35}$$

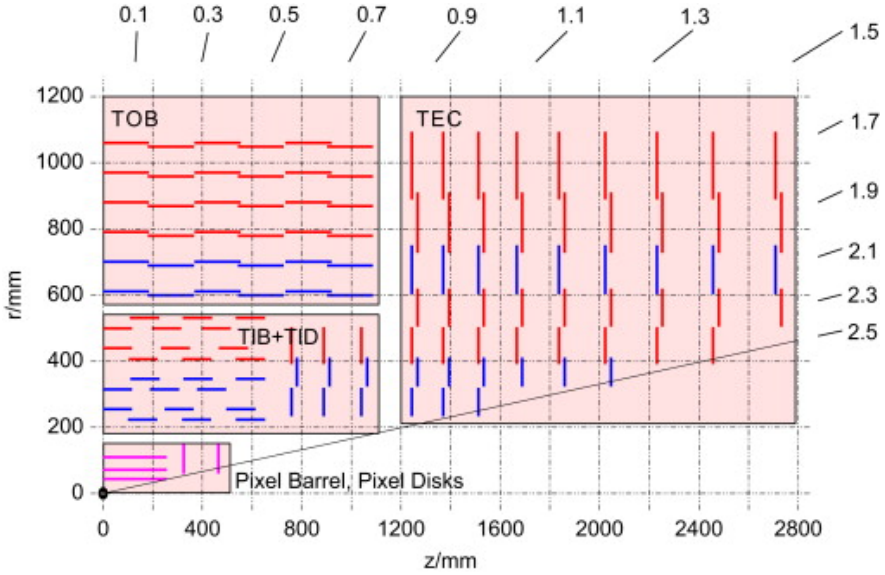

Slika 9.7: Presjek detektora tragova u CMS eksperimentu.

Elektromagnetski i hadronski kalorimetar

Elektromagnetski kalorimetar (ECAL, od engl. Electromagnetic calorimeter) dizajniran je za precizno mjerenje energije elektrona i fotona. ECAL je smješten unutar magneta stoga je vrlo kompaktan i izgrađen od materijala visoke prozirnosti i velike gustoće ($PbWO_4$). Velika gustoća (8.28 g/cm^{-3}), kratka radijacijska duljina (0.89 cm) i mali Molierov radijus (2.2 cm) omogućavaju apsorpciju elektronskog i fotonskog pljuska unutar kristala duljine samo 23 cm. Dobra separacija pljuskova omogućena je malim dimenzijama kristala od 2.2cm$\times$2.2cm.

Na slici 9.8 shematski je prikazan elektromagnetski kalorimetar.

Energijska rezolucija ECAL-a dana je izrazom:

$$\left(\frac{\sigma_E}{E}\right)^2 = \left(\frac{2.8\%}{\sqrt{E/GeV}}\right)^2 + \left(\frac{0.12}{E/GeV}\right)^2 + (0.3\%)^2 . \tag{9.36}$$

ECAL je okružen hadronskim kalorimetrom (HCAL, od engl. Hadronic calorimeter) dizajniranim za mjerenje energije čestica koje primarno interagiraju jakom nuklearnom silom. HCAL se sastoji

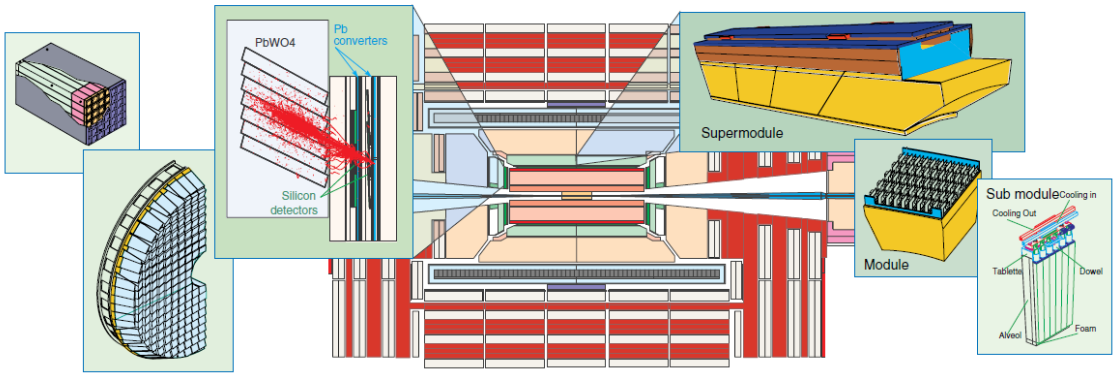

Slika 9.8: Prikaz elektromagnetskog kalorimetra u CMS eksperimentu.

od triju podsustava prikazanih na Slici 9.9. Detektori se sastoje od slojeva apsorpcijskog materijala (mjed/čelik) i materijala za detekciju. HCAL pokriva područje sve do $|\eta| \leq 5.0$, stoga igra važnu ulogu pri mjerenju ukupne nedostajuće transverzalne energije (MET, od engl. Missing transverse energy).

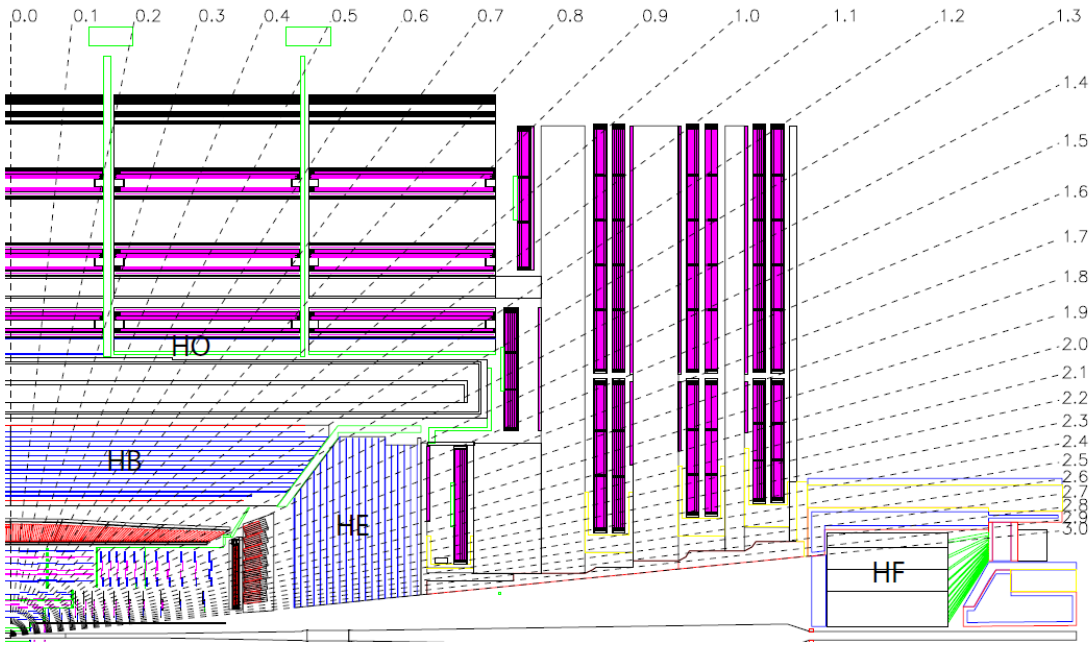

Slika 9.9: Shematski prikaz hadronskog kalorimetra.

Mionski sustav

Jedna od glavnih zadaća CMS detektora je efikasno i precizno mjerenje miona. Mioni nastali u sudaru registriraju se u detektoru tragova i u mionskim komorama smještenim izvan magneta.

Mionski sustav sastoji se od tri tipa komora koji su optimizirani za različita okruženja unutar CMS-a. U centralnom dijelu detektora nalaze se driftne komore (DT, od engl. Drift Tubes) koje pokrivaju područje pseudorapiditeta $\mid \eta \mid \leq 1.2$, dok se u bočnim dijelovima nalaze katodne trakaste komore (CSC, od engl. Chatode Strip Chambers) koje pokrivaju područje $\mid \eta \mid \leq 2.4$ i komore s otpornim pločama (RPC, od engl. Resistive Plate Chambers) koje pokrivaju područje $\mid \eta \mid \leq 1.6$. Mionski sustav prikazan je na Slici 9.10.

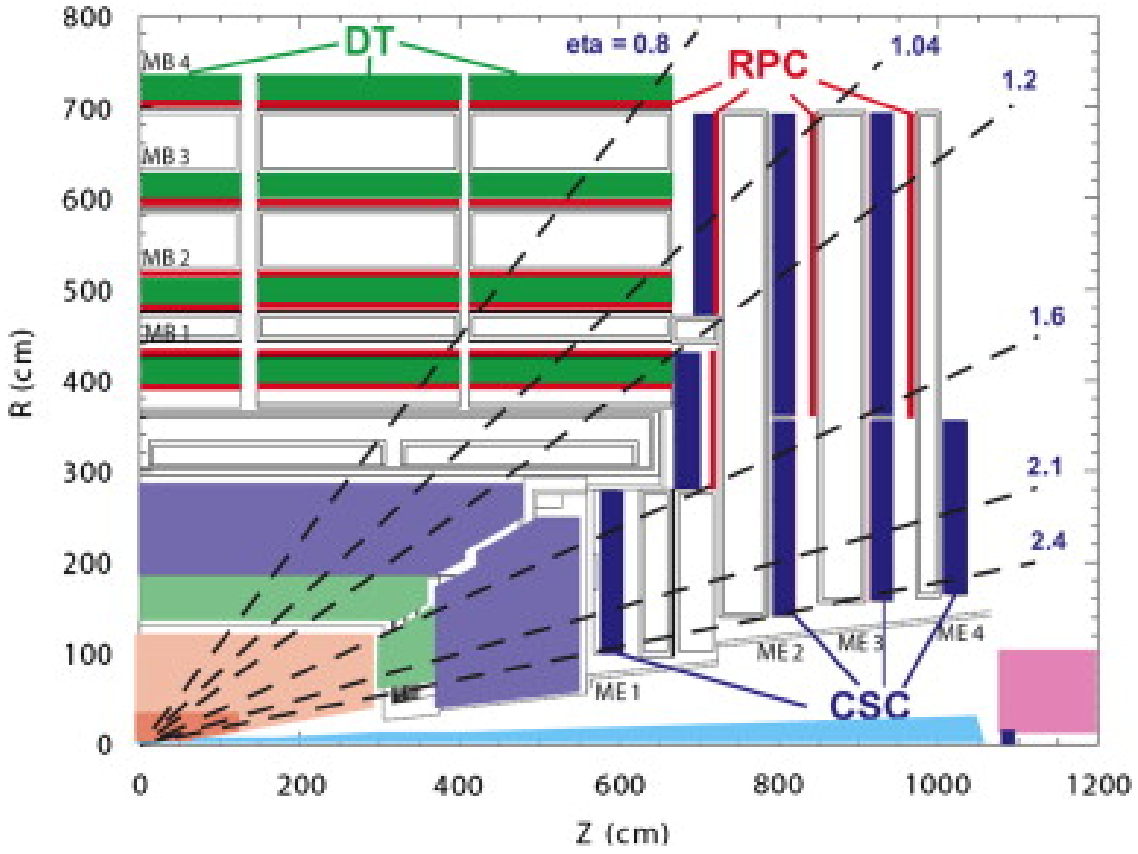

Slika 9.10: Mionski sustav eksperimenta CMS.

Prostorna rezolucija DT komora je 100 μm u r-ϕ ravnini i 150 μm u z smjeru, dok vremenska rezolucija iznosi 3.8 ns. Za CSC komore prostorna rezloucija je nešto slabija i iznosi 200 μm dok

je kutna rezolucija u ϕ reda 10 mrad. RPC komore se odlikuju odličnom vremenskom rezolucijom ($\approx$ 1 ns).

Rezolucija količine gibanja miona prikazana je na Slici 9.11.

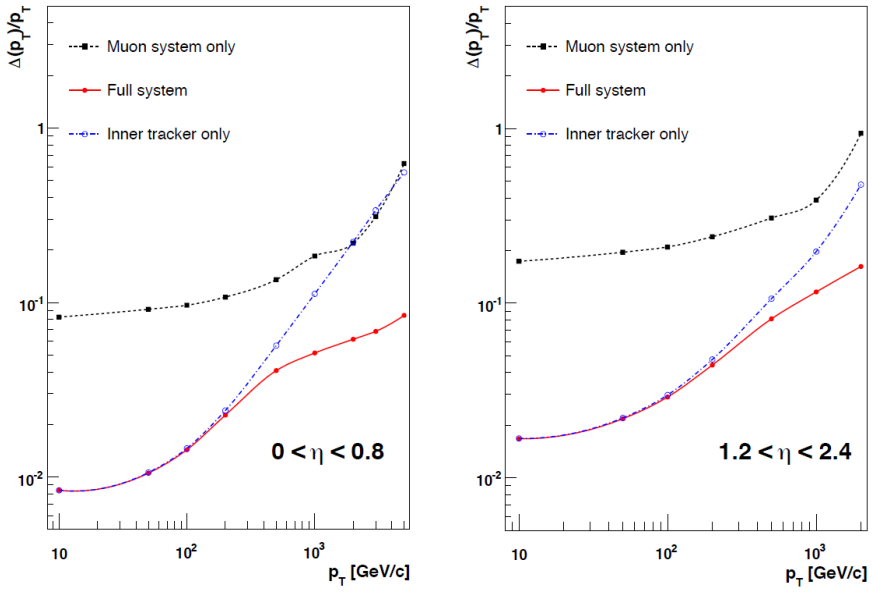

Slika 9.11: Rezolucija količine gibanja miona.

Postupak rekonstrukcije fizikalnih veličina i tragova čestica

Rekonstrukcija je proces dobivanja fizikalnih veličina i tragova čestica iz signala mjerenih u detektoru. Različite čestice ostavljaju rezličite signale u CMS detektoru (Slika 9.12). Mioni se mjere u detektoru tragova i u mionskim komorama te ostavljaju vrlo malo energije u kalorimetru. Elektroni ostavljaju trag u detektoru tragova i izazivaju elektromagnetski pljusak u ECAL-u, dok se fotoni mjere samo u ECAL-u.

Reconstrukcija miona Mioni (i antimioni) se detektiraju u području pseudorapiditeta $|\eta| < 2.4$ te se rekonstruiraju usklađivanjem traga u detektoru tragova s tragom u mionskim komorama. Konačna rezolucija količine gibanja je 1-5% za mione transverzalnog impulsa $p_T \leq 1$ TeV-a. Algoritam za rekonstrukciju detaljno je opisan u [19].

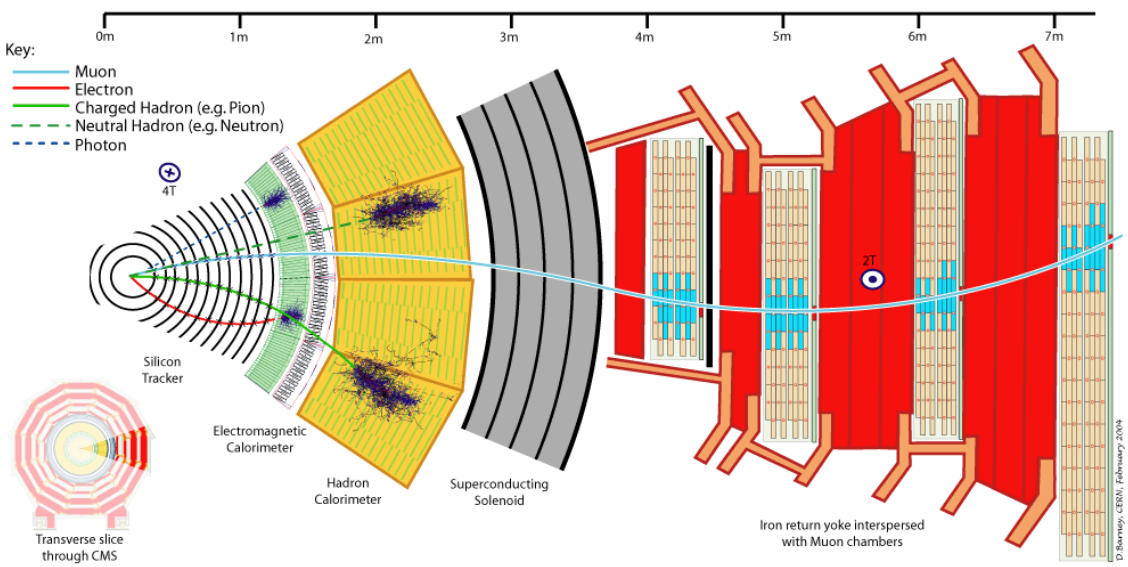

Slika 9.12: Transverzalni presjek CMS detektora s odgovarajućim potpisom različitih čestica.

Rekonstrukcija fotona Rekonstrukcija fotona bazira se na analizi energije deponirane u ECAL-u. Foton energije 1 GeV deponira 95% energije u polju ECAL kristala veličine 5×5. Približno 50% fotona će u interakciji s materijalom između točke sudara i ECAL-a konvertirati u e^+e^- par. Pošto se putanja nabijene čestice zakreće u magnetskom polju energija u ECAL-u pokrivat će veliko područje kuta ϕ.

Kristali s pripadajućom deponiranom energijom grupiraju se u veće skupine SC (od engl. Super Cluster) [20]. Centar elektromagnetskog pljuska određuje se izrazom:

$$x = \frac{\sum x_i W_i}{\sum W_i}, \text{ where } W_i = max\left(0, 4.7 + log\frac{E_i}{\sum E_j}\right) \tag{9.37}$$

gdje je E_i energija i^{tog} kristala u SC.

Rekonstrukcija nedostajuće transverzalne energije U konačnom stanju $W\gamma \to \l^{\pm}\nu\gamma$ neutrino nije detektiran što rezultira s neravnotežom u mjerenoj transverzalnoj energiji, MET. Ova se veličina određuje algoritmom opisanim u [21] koji rekonstruira kompletnu listu čestica proizašlih iz

sudara koristeći sve detektorske podsustave CMS eksperimenta. Za svaki događaj MET je određen kao negativna vrijednost vektorske sume transverzalnih energija svih rekonstruiranih čestica.

9.4 Mjerenje $W\gamma$ udarnog presjeka

U ovom radu prikazani su rezultati mjerenja udarnog presjeka procesa $pp \to W\gamma \to \mu\nu\gamma$ na energiji 7 TeV-a u sustavu centra mase dvaju protona. Kako udarni presjek $W\gamma$ procesa u vodećem redu divergira za fotone niske energije i fotone koji se gibaju u smjeru bliskom leptonu iz W raspada, mjerenje je izvršeno u kinematskom području definiranom zahtjevima:

- transverzalna energija fotona mora biti veća od 15 GeV-a.
- mion i foton moraju biti prostorno udaljeni $\Delta R(\mu,\gamma) \equiv \sqrt{(\Delta\phi)^2 + (\Delta\eta)^2} > 0.7$.

U analizi su korišteni podaci prikupljeni CMS detektorom tijekom 2011 godine.

Konačno stanje $W\gamma \to \mu\nu\gamma$ karakterizirano je izoliranim mionom visoke energije, značajnom nedostajućom transverzalnom energijom zbog nedetektiranog neutrina i izoliranim fotonom. Osim $W\gamma$ procesa postoje drugi procesi s identičnim konačnim stanjem ili procesi u kojima čestice konačnog stanja ostavljaju sličan potpis u detektoru. Da bi se smanjio doprinos ovih drugih procesa (pozadine) primjenjuju se zahtjevi (selekcija) na događaje.

Udarni presjek σ definiran je izrazom:

$$\sigma = \frac{N_{\text{sig}}}{A \cdot \varepsilon \cdot \mathscr{L}} \tag{9.38}$$

gdje je N_{sig} broj događaja signala u podacima , ε je efikasnost selekcije, $\mathscr{L}$ integrirani luminozitet, a A efikasnost detektora.

Produkt $A \cdot \varepsilon_{gen}$ određen je iz simulacija. Različita efikasnost u podacima i simulaciji korigira se faktorom $\rho_{\text{eff}} = \varepsilon/\varepsilon_{\text{gen}}$. Korekcijski faktor dobiva se mjerenjem efikasnosti u podacima i simulaciji na jednak način. Uz jednakost $\mathscr{F} \equiv A \cdot \varepsilon_{\text{gen}}$ izraz 9.38 može se napisati u obliku:

$$\sigma = \frac{N_{\text{sig}}}{A \cdot \varepsilon_{gen} \cdot \frac{\varepsilon}{\varepsilon_{gen}} \cdot \mathscr{L}} = \frac{N_{\text{sig}}}{\mathscr{F} \cdot \rho_{eff} \cdot \mathscr{L}}. \tag{9.39}$$

gdje je $\mathscr{F}$ definiran omjerom $\frac{N_{\text{accept}}}{N_{\text{gen,kin}}}$. N_{accept} je broj događaja u simulaciji koji prolaze selekciju, $N_{\text{gen,kin}}$ je broj simuliranih događaja s $E_T^{\gamma} > 15$ GeV-a i $\Delta R(\mu,\gamma) > 0.7$.

9.4.1 Podaci

U analizi su korišteni podaci koji odgovaraju integriranom luminozitetu od 5 fb^{-1} na energiji od 7 TeV-a u sustavu centra mase dvaju protona, prikupljeni tijekom 2011. godine. Tijekom 2011. godine mjerenja su izvršena u dva perioda s bitno različitim karakteristikama snopa. Prvi period odgovara integriranom luminozitetu od 2.2 fb^{-1} i naziva se 2011A. Drugi period koji se odlikuje većim brojem interakcija ("pile-up", PU), odgovara integriranom luminozitetu od 2.7 fb^{-1} i u radu se naziva 2011B. Mjerenje je izvršeno na ukupnom uzorku podataka 2011A+2011B, a za provjeru kompatibilnosti, i posebno na uzorcima 2011A i 2011B.

9.4.2 Selekcija događaja

Selekcijom događaja nastoji se minimizirati doprinos pozadina uz što manji gubitak signala.

Selekcija sustava okidača

Događaji $W\gamma \to \mu\nu\gamma$ selektirani su korištenjem okidača koji zahtjeva prisustvo miona u događaju, s transverzalnim impulsom P_T^{μ} iznad određenog praga. Korišten je okidač s najnižim pragom, $p_T^{\mu} \geq 30$ GeV-a.

Selekcija miona

Postupak odabira miona opisana je u [19], s time da je u analizi postavljen stroži rez na najbližu udaljenost između rekonstruiranog traga miona i primarnog vrha u transverzalnoj ravnini (d_0) i u z smjeru (d_z) [26]. Selektirani su mionski kandidati koji su rekonstruirani s dva algoritma, tzv.

Tablica 9.2: Selekcija miona.

Opis	selekcija
Kinematički	$p_{\mathrm{T}} > 35$ GeV i $\lvert\eta\rvert < 2.1$
Broj točaka u piksel komorama	> 0
Broj točaka u piksel i trakastim komorama	> 10
χ^2/n.d.f	< 10
Broj točaka u mionskim komorama	> 0
Broj mionskih komora s točkama	> 1
Vrh d_0	< 0.02 cm
Vrh d_z	< 0.1 cm
Relativna izolacija $\Delta R = 0.3$	< 0.1

"GlobalMuon" i "TrackerMuon". Prilikom selekcije zahtjeva se postojanje signala u piksel detektoru tragova, postojanje signala u većini slojeva trakastog detektora tragova i dobar χ^2 ukupne prilagodbe traga čestice na mjerenja u detektoru tragova i mionskim komorama.

Da bi se smanjila pozadina koja nastaje zbog pogrešno identificiranih piona i mlazeva koristi se zahtjev relativne izolacije, gdje suma transverzalnih količina gibanja svih rekonstruiranih čestica u konusu $\Delta R = 0.3$ oko miona, mora biti manja od 10% transverzalne količine gibanja miona.

Također se postavlja zahtjev na transverzalnu količinu gibanja miona, $p_T \geq$35 GeV-a i pseudorapiditet $|\eta| < 2.1$. Pregled svih selekcijskih uvijeta prikazan je u Tablici 9.2.

Selekcija fotona

Fotonski kandidati rekonstruirani su kao super-klasteri (SC, od engl. SuperClasters) transverzalne energije $E_{\mathrm{T}}^{\gamma} > 15$ GeV-a u ECAL-u. Da bi se smanjila pozadina, koju čine hadronski mlazevi, na rekonstruirane kandidate postavljaju se uvjeti:

- omjer energija u HCAL-u i ECAL-u u konusu $\Delta R = 0.15$ oko fotona mora biti manji od 0.05,
- $\sigma_{\mathrm{i}\eta\mathrm{i}\eta} \leq$0.011 u centralnom dijelu detektora i $\sigma_{i\eta i\eta} \leq 0.030$ u bočnim dijelovima.

Varijabla $\sigma_{i\eta i\eta}$ mjeri oblik super-klastera u smjeru pseudorapiditeta i definirana je izrazom:

$$\sigma^2_{i\eta i\eta} = \frac{\sum(\eta_i - \bar{\eta})^2 w_i}{\sum w_i},\ \bar{\eta} = \frac{\sum \eta_i w_i}{\sum w_i},\ w_i = \max(0, 4.7 + \log(E_i/E_{5\times5})), \tag{9.40}$$

gdje se sumira energija deponirana u kristalima koji čine polje veličine 5×5 oko kristala s najvećom energijom.

Pozadinu čine i elektroni. Njihov doprinos smanjuje se zahtjevom da fotonski kandidat nema pridruženu točku u piksel detektoru.

Izolacija fotona korigirana je za doprinos PU događaja [27] koristeći gustoću energije po površini, ρ. Pregled selekcijskih uvijeta prikazan je u Tablici 9.3.

Tablica 9.3: Selekcija fotona.

Opis	selekcija
Kinematički	$E_{\mathrm{T}} > 15$ GeV $\lvert\eta\rvert < 1.4442$ za centralni dio ($1.566 < \lvert\eta\rvert < 2.5$ za bočni dio)
HCAL/ECAL energija ; $\Delta R < 0.15$	< 0.05
$\sigma_{i\eta i\eta}$	$< 0.011(0.03)$
Pridružena točka piksel detektora	nema pridružene piksel točke
$Izolacija_{TRK}$; $\Delta R < 0.4$	$< 2.0 + 0.001 \cdot E_T + 0.0167(0.032) \cdot \rho$
$Izolacija_{ECAL}$; $\Delta R < 0.4$	$< 4.2 + 0.006 \cdot E_T + 0.183(0.090) \cdot \rho$
$Izolacija_{HCAL}$; $\Delta R < 0.4$	$< 2.2 + 0.0025 \cdot E_T + 0.062(0.180) \cdot \rho$

M_T^W selekcija

Za identifikaciju W bozona koristi se transverzalna masa, M_T^{W}, definirana izrazom:

$$M_T^{\mathrm{W}} = \sqrt{2 \times p_{\mathrm{T}}(\mu) \times \mathrm{MET} \times (1 - \cos\Delta\phi(\mu, \mathrm{MET}))}. \tag{9.41}$$

Zbog zahtjeva korištenog u okidaču u selekciji se koristi uvjet $M_T^W > 70$ GeV-a.

$W\gamma$ selekcija

U selekciji $W\gamma$ događaja zahtjeva se postojanje barem jednog mionskog kandidata transverzalnog impulsa $p_{\mathrm{T}} > 35$ GeV-a koji zadovoljava kriterije navedene u paragrafu 9.4.2. Ako postoji dodatni mionski kandidat transverzalne količine gibanja $p_{\mathrm{T}} > 10$ GeV-a i pseudorapiditeta $|\eta| < 2.4$ događaj se odbacuje kako bi se smanjila Drell-Yan pozadina.

Transverzalna masa W bozona mora zadovoljavati uvjet $M_T^W > 70$ GeV-a, i u događaju mora postojati barem jedan fotonski kandidat transverzalne energije $E_{\mathrm{T}} > 15$ GeV-a koji zadovoljava kriterije navedene u paragrafu 9.4.2. Ako postoji više fotonskih kandidata izabire se kandidat s najvećom energijom.

$W\gamma$ selekciju zadovoljava 5014(5795) događaja u uzorku podataka 2011A(2011B). Očekivani broj događaja u signalu i pozadini određen je pomoću simulacije i prikazan u Tablici 9.4.

Tablica 9.4: Broj selektiranih $W\gamma \to \mu\nu\gamma$ događaja u podacima i simulaciji za uzorak podataka 2011A (2.3 fb^{-1}), 2011B (2.7 fb^{-1}) i ukupni uzorak 2011A+2011B (5.0 fb^{-1}).

	udarni presjek(pb)	Broj događaja (2011A)	Broj događaja (2011B)	Broj događaja (2011A+2011B)
$W\gamma \to \mu\nu\gamma$	137.3	2097.4 ± 33.3	2252.5 ± 34.0	4341.7 ± 55.9
$W\gamma \to \tau\nu\gamma$	21.41	11.9 ± 1.9	18.0 ± 2.4	28.8 ± 3.5
W+mlazevi	31314	1701.4 ± 54.0	2261.3 ± 62.2	3945.9 ± 95.9
Z+mlazevi	3048	59.4 ± 4.9	78.4 ± 5.5	138.2 ± 8.6
$Z+\gamma \to ll\gamma$	41.37	154.7 ± 10.5	195.5 ± 11.6	349.2 ± 18.3
$t\bar{t}$+mlazevi	157.5	54.8 ± 3.4	59.0 ± 3.4	114.2 ± 5.6
$t\bar{t}\gamma$	0.444	17.2 ± 0.6	19.4 ± 0.6	36.7 ± 1.0
Incl. μ QCD	84679.3	0.0 ± 0.0	0.0 ± 0.0	0.0 ± 0.0
$\gamma+jets$	by $\hat{p_T}$	0.0 ± 0.0	0.0 ± 0.0	0.0 ± 0.0
WW	5.7	14.8 ± 0.6	15.7 ± 0.6	30.5 ± 1.0
WZ	0.6	0.2 ± 0.0	0.2 ± 0.0	0.4 ± 0.0
ZZ	0.06	0.0 ± 0.0	0.0 ± 0.0	0.0 ± 0.0
simulacija (ukupno)		4111.9 ± 64.6	4900.0 ± 72.2	8985.6 ± 113.0
podaci		5014	5795	10809

Efikasnost selekcije i geometrijski gubitci

Efikasnost selekcije i gubitci do kojih dolazi zbog konačne veličine detektora ($\mathscr{F} = A \cdot \varepsilon_{gen}$), određeni su analizom simuliranih $W\gamma$ događaja. Kako se efikasnost u podacima i simulaciji razlikuje, uvodi se korekcijski faktor $\rho_{eff} = \frac{\varepsilon}{\varepsilon_{gen}}$ kojom se ova razlika uzima u obzir.

Efikasnosti selekcije fotona i miona određene su iz mjerenih podataka tzv. 'tag-and-probe' metodom, dok je efikasnost zahtjeva $M_T^W > 70$ GeV-a određena metodom opisanom u [29].

9.4.3 Pozadinski događaji

Pozadinskim događajima koji zadovoljavaju $W\gamma \to \mu\nu\gamma$ selekciju, najviše doprinose događaji u kojima je hadronski mlaz pogrešno identificiran kao foton. Ovoj pozadini doprinose sljedeći procesi:

- W+mlazevi, gdje je mlaz pogrešno identificiran kao foton,
- Z+mlazevi, gdje jedan od leptona iz Z raspada nije detektiran, a mlaz je pogrešno identificiran kao foton,
- $t\bar{t}$+mlazevi, gdje se jedan od W bozona iz $t\bar{t}$ raspada leptonski, a mlaz je pogrešno identificiran kao foton.

Doprinos ovih hadronskih procesa procjenjen je iz podataka pomoću dvije metode, metode predložaka i metode omjera, koje su opisane u paragrafu 9.4.3.

Drugi procesi s dva bozona u konačnom stanju također mogu doprinjeti pozadini ukoliko je elektron pogrešno identificiran kao foton. Ova pozadina nije značajna i određena je iz podataka.

Pozadini doprinose i slijedeći procesi:

- krivo identificirani lepton iz γ+mlaz procesa,
- W$\gamma \to \tau\nu\gamma$ gdje se τ raspada na $\mu\nu\gamma$,
- Zγ događaji,
- $t\bar{t}\gamma$ događaji.

Njihov doprinos je puno manji od doprinosa procesa W+mlazevi, te je određen iz simulacije.

Pozadina od mlazeva pogrešno identificiranih kao fotoni

Dominantan dio pozadine $W\gamma \to \mu\nu\gamma$ procesa čine događaji u kojima je mlaz pogrešno identificiran kao foton. Ovoj pozadini najviše doprinosi proces W+mlazevi.

Metoda predložaka U metodi predloška koristi se $\sigma_{i\eta i\eta}$ raspodjela kao diskriminirajuća varijabla na kojoj se provodi dvokomponentna prilagodba signala i pozadine. Oblik raspodjele signala i pozadine određen je za različite vrijednosti transverzalne energije fotona, E_{T}^{γ}: $15-20$ GeV-a, $20-25$ GeV-a, $25-30$ GeV-a, $30-35$ GeV-a, $35-40$ GeV-a, $40-60$ GeV-a, $60-90$ GeV-a, i $90-500$ GeV-a za podatke 2011A i 2011B, te $90-120$ GeV-a i $120-500$ GeV-a za podatke 2011A+2011B. Oblici raspodjela posebno su određeni za fotone rekonstruirane u centralnom dijelu detektora ($|\eta| < 1.4442$) i u bočnim dijelovima ($1.556 < |\eta| < 2.5$).

Oblik raspodjela signala, određen je iz simuliranih $W\gamma$ događaja. Oblik raspodjele dobiven iz simulacije uspoređen je s oblikom $\sigma_{i\eta i\eta}$ raspodjele mjerenih $Z \to ee$ događaja. Usporedba je prikazana na Slici 9.13, gdje se uočava pomak između $\sigma_{i\eta i\eta}$ raspodjela u podacima i simulaciji. Stoga je $\sigma_{i\eta i\eta}$ raspodjela pravih fotona dobivena iz simulacije, pomaknuta prema manjim vrijednostima za iznos 0.9×10^{-4} (0.8×10^{-4}) i 2.1×10^{-4} (1.9×10^{-4}) u centralnom dijelu detektora i bočnim dijelovima u 2011A (2011B) uzorku podataka.

Oblici $\sigma_{i\eta i\eta}$ raspodjela za pozadinu, koju čine pogrešno identificirani hadronski mlazevi, dobiveni su iz podataka korištenjem događaja koji sadrže mlazeve. Fotonski kandidati selektirani su kao rekonstruirani fotoni koji prolaze selekciju definiranu u paragrafu 9.4.2 izuzev zahtjeva na $\sigma_{i\eta i\eta}$, te se za razliku od zahtjeva na izolaciju zahtjeva anti-izolacija u svrhu smanjenja doprinosa pravih fotona. Zahtjev anti-izolacije izabran je tako da nije koreliran sa $\sigma_{i\eta i\eta}$.

Na $\sigma_{i\eta i\eta}$ raspodjelu dobivenu iz podataka prilagođava se funkcija oblika:

$$f(\sigma_{i\eta i\eta}) = N_S S(\sigma_{i\eta i\eta}) + N_B B(\sigma_{i\eta i\eta}), \tag{9.42}$$

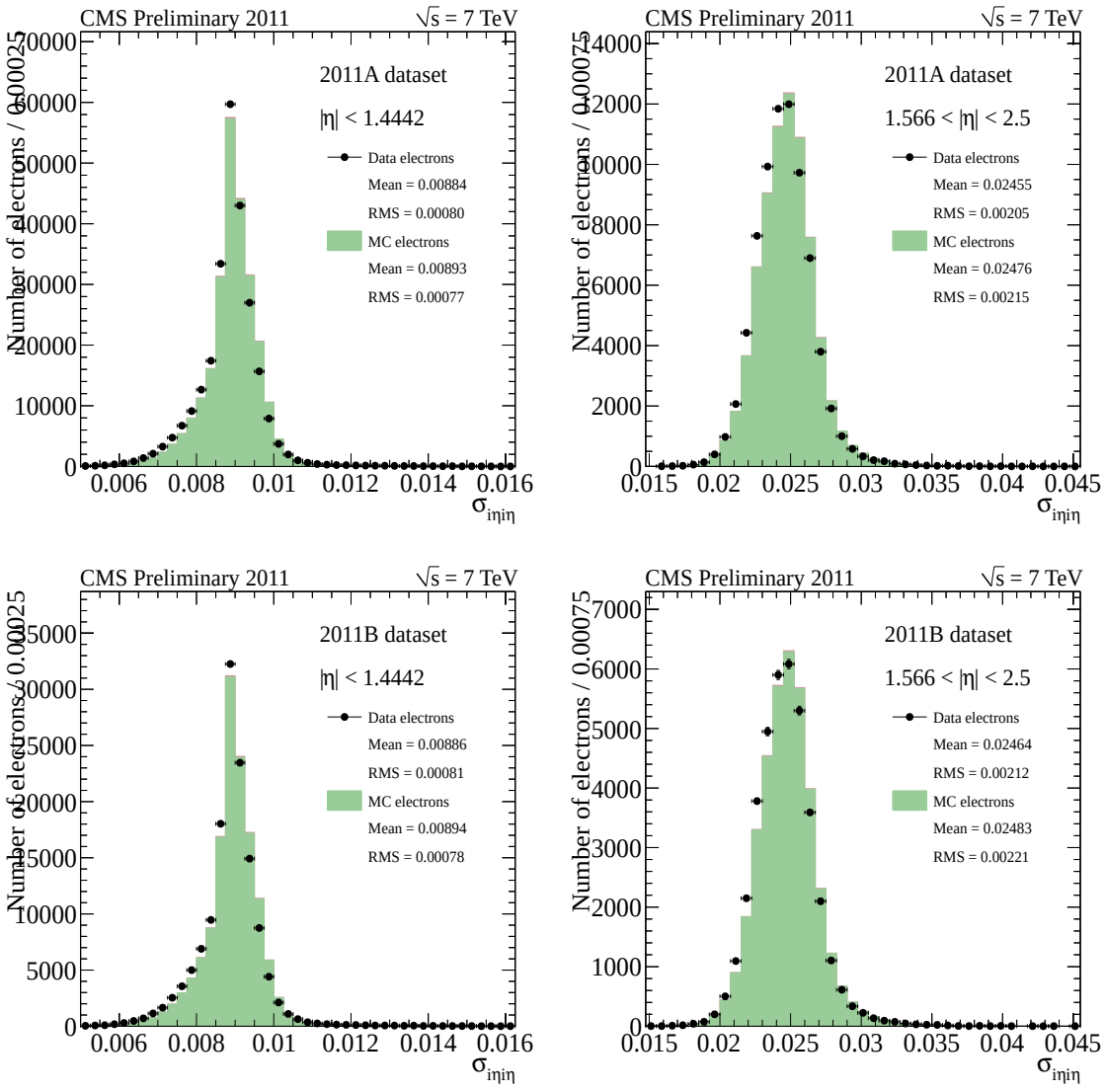

Slika 9.13: $\sigma_{i\eta i\eta}$ raspodjele za centralni (lijevo) i bočne dijelove detektora (desno) za simulirane (zeleni histogram) i mjerene događaje (točke) za uzorak 2011A (gore) i 2011B (dolje).

gdje su N_S i N_B očekivani doprinosi signala i pozadine, a $S(\sigma_{i\eta i\eta})$ i $B(\sigma_{i\eta i\eta})$ raspodjele signala i pozadine. Oblici raspodjela izglađeni su primjenom metode opisane u [28].

Vrijednosti parametara N_S i N_B dobivaju se minimiziranjem izraza:

$$-\ln L = (N_S + N_B) - N\ln(N_S S(\sigma_{i\eta i\eta}) + N_B B(\sigma_{i\eta i\eta})). \tag{9.43}$$

gdje je N ukupni broj događaja u podacima.

Rezultati prilagodbe za vrijednosti transverzalne energije fotona $15 \leq E_{\mathrm{T}}^{\gamma} \leq 20$ GeV-a prikazani su na Slici 9.14.

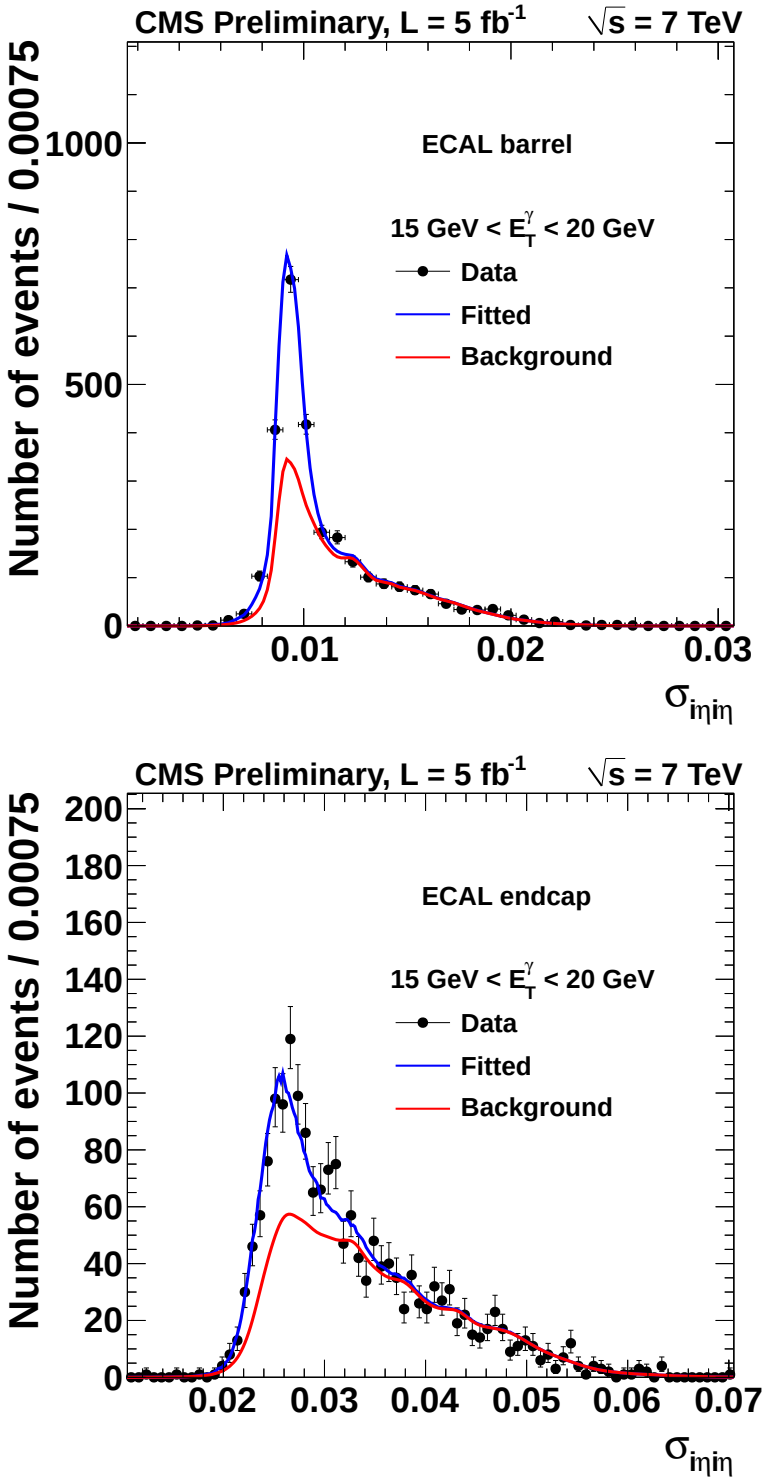

Slika 9.14: $\sigma_{i\eta i\eta}$ raspodjele za selektirane $W\gamma \to \mu\nu\gamma$ događaje u podacima (crne točke) za fotonske kandidate transverzalne enrgije $15 \leq E_{\mathrm{T}}^{\gamma} \leq 20$ GeV-a u centralnom (gore) i bočnim dijelovima detektora (dolje) za uzorak 2011A+2011B. Rezultati prilagodbe prikazani su plavom linijom dok je doprinos pozadine prikazan crvenom linijom.

Metoda omjera Metoda omjera korištena je za provjeru rezultata dobivenih metodom predložaka u području $E_{\mathrm{T}}^{\gamma} > 60$ GeV-a, u kojem je metoda predložaka podložna velikim statističkim pogreškama. Mlazevi s velikim udjelom elektromagnetskog signala koji ostavljaju sličan potpis u detektoru kao fotoni nazivaju se mlazevi slični fotonu (plJet, od engl. photon-like jet). Oni su selektirani kao fotonski kandidati koji ne zadovoljavaju izolacijski ili $\sigma_{i\eta i\eta}$ zahtjev a imaju veći udio elektromagnetskog doprinosa od većine mlazeva. U metodi se određuje omjer R_p:

$$R_p = \frac{\text{vjerojatnost da mlaz zadovoljava selekciju fotona}}{\text{vjerojatnost da mlaz zadovoljava selekciju plJet}}. \tag{9.44}$$

Doprinos pozadine mlazeva koji su pogrešno identificiranih kao fotoni, $N_{\text{W+mlazevi}}$, određuje se pomoću izraza:

$$N_{\text{W+mlazevi}} = R_p \cdot N_{\text{W+plJet}}, \tag{9.45}$$

gdje je $N_{\text{W+plJet}}$ broj događaja u podacima s identificiranim W bozonom i barem jednim "plJet" objektom.

Primjenom metode omjera i metode predložaka dobivaju se suglasni rezultati. Stoga je razlika rezultata dvije metode korištena kao dodatna sistematska pogreška na rezultat dobiven metodom predložaka.

Tablica 9.5: Broj pozadinskih događaja koji čine pogrešno identificiranih mlazeva određeni metodom predložaka za uzorke 2011A i 2011B.

E_{T}^{γ}, GeV	Procjenjena pozadina (2011A)	Procjenjena pozadina (2011B)
Centralni dio detektora		
15-20	834.8 ± 22.5(stat.) ± 28.7(syst.)	1006.4 ± 24.4(stat.) ± 40.7(syst.)
20-25	317 ± 15.5(stat.) ± 16.4(syst.)	348.1 ± 15.9(stat.) ± 21.2(syst.)
25-30	142.9 ± 10.4(stat.) ± 9.5(syst.)	164.8 ± 11.4(stat.) ± 12.3(syst.)
30-35	98.5 ± 8.6(stat.) ± 8.1(syst.)	120.4 ± 9.6(stat.) ± 11.9(syst.)
35-40	51.8 ± 6.5(stat.) ± 5(syst.)	66.9 ± 8.1(stat.) ± 7.4(syst.)
40-60	75.1 ± 8.4(stat.) ± 9.4(syst.)	105.4 ± 10.1(stat.) ± 13.7(syst.)
60-90	27.1 ± 5.2(stat.) ± 5.4(syst.)	41.6 ± 7.3(stat.) ± 8.6(syst.)
90-500	20.3 ± 6.8(stat.) ± 16.7(syst.)	34.5 ± 9.8(stat.) ± 28.5(syst.)
MET korelacija	± 203.8(syst.)	± 245.4(syst.)
Δ(metoda predložaka, metoda omjera)	± 1.6 (syst.)	± 50.3(syst.)
Ukupno	1567.5 ± 33.4(stat.) ± 207.9(syst.)	1888.1 ± 37.2(stat.) ± 257.5(syst.)
Bočni dijelovi detektora		
15-20	417 ± 12.6(stat.) ± 29(syst.)	430.7 ± 12.4(stat.) ± 40.3(syst.)
20-25	185.1 ± 9.4(stat.) ± 15.3(syst.)	236.3 ± 10.4(stat.) ± 20.8(syst.)
25-30	81.6 ± 6.6(stat.) ± 9.1(syst.)	140.5 ± 9.3(stat.) ± 14.9(syst.)
30-35	56.2 ± 5.7(stat.) ± 7.4(syst.)	51 ± 5.8(stat.) ± 9.4(syst.)
35-40	44 ± 5.1(stat.) ± 4.9(syst.)	31 ± 4.9(stat.) ± 6.3(syst.)
40-60	40.3 ± 6.4(stat.) ± 7.6(syst.)	51.9 ± 7.1(stat.) ± 11.3(syst.)
60-90	18.2 ± 4.3(stat.) ± 4.3(syst.)	22.2 ± 5.3(stat.) ± 7.1(syst.)
90-500	7.3 ± 5.3(stat.) ± 12.3(syst.)	16.5 ± 6.6(stat.) ± 20.9(syst.)
MET korelacija	± 59.5(syst.)	± 68.6(syst.)
Δ(metoda predložaka, metoda omjera)	± 13.4 (syst.)	± 21.3(syst.)
Ukupno	849.7 ± 20.9(stat.) ± 72.0(syst.)	980.1 ± 23.0(stat.) ± 90.4(syst.)
Centralni dio + bočni dijelovi detektora		
15-20	1251.8 ± 25.8(stat.) ± 40.8(syst.)	1437.1 ± 27.4(stat.) ± 57.3(syst.)
20-25	502.1 ± 18.1(stat.) ± 22.4(syst.)	584.4 ± 19.0(stat.) ± 29.7(syst.)
25-30	224.5 ± 12.3(stat.) ± 13.2(syst.)	305.3 ± 14.7(stat.) ± 19.3(syst.)
30-35	154.7 ± 10.3(stat.) ± 11.0(syst.)	171.4 ± 11.2(stat.) ± 15.2(syst.)
35-40	95.8 ± 8.3(stat.) ± 7.0(syst.)	97.9 ± 9.5(stat.) ± 9.7(syst.)
40-60	115.4 ± 10.6(stat.) ± 12.1(syst.)	157.3 ± 12.3(stat.) ± 17.8(syst.)
60-90	45.3 ± 6.7(stat.) ± 6.9(syst.)	63.8 ± 9.0(stat.) ± 11.2(syst.)
90-500	27.6 ± 8.6(stat.) ± 20.7(syst.)	51 ± 11.8(stat.) ± 35.3(syst.)
MET korelacija	± 212.3(syst.)	± 254.9(syst.)
Δ(metoda predložaka, metoda omjera)	± 11.8 (syst.)	± 71.5(syst.)
Ukupno	2417.3 ± 39.4(stat.) ± 219.9(syst.)	2868.2 ± 43.7(stat.) ± 276.8(syst.)

Rezultati Rezultati dobiveni primjenom metode predložaka i metode omjera prikazani su na Slici 9.15 i u Tablicama 9.5- 9.6. Broj pozadinskih događaja dobiven primjenom metode predložaka iznosi 2417.3 ± 39.4 (stat.) ± 219.9 (syst.) za uzorak 2011A, 2868.2 ± 43.7 (stat.) ± 276.8 (syst.) za uzorak 2011B i 5345.9 ± 58.2 (stat.) ± 482.6 (syst.) za uzorak 2011A+2011B.

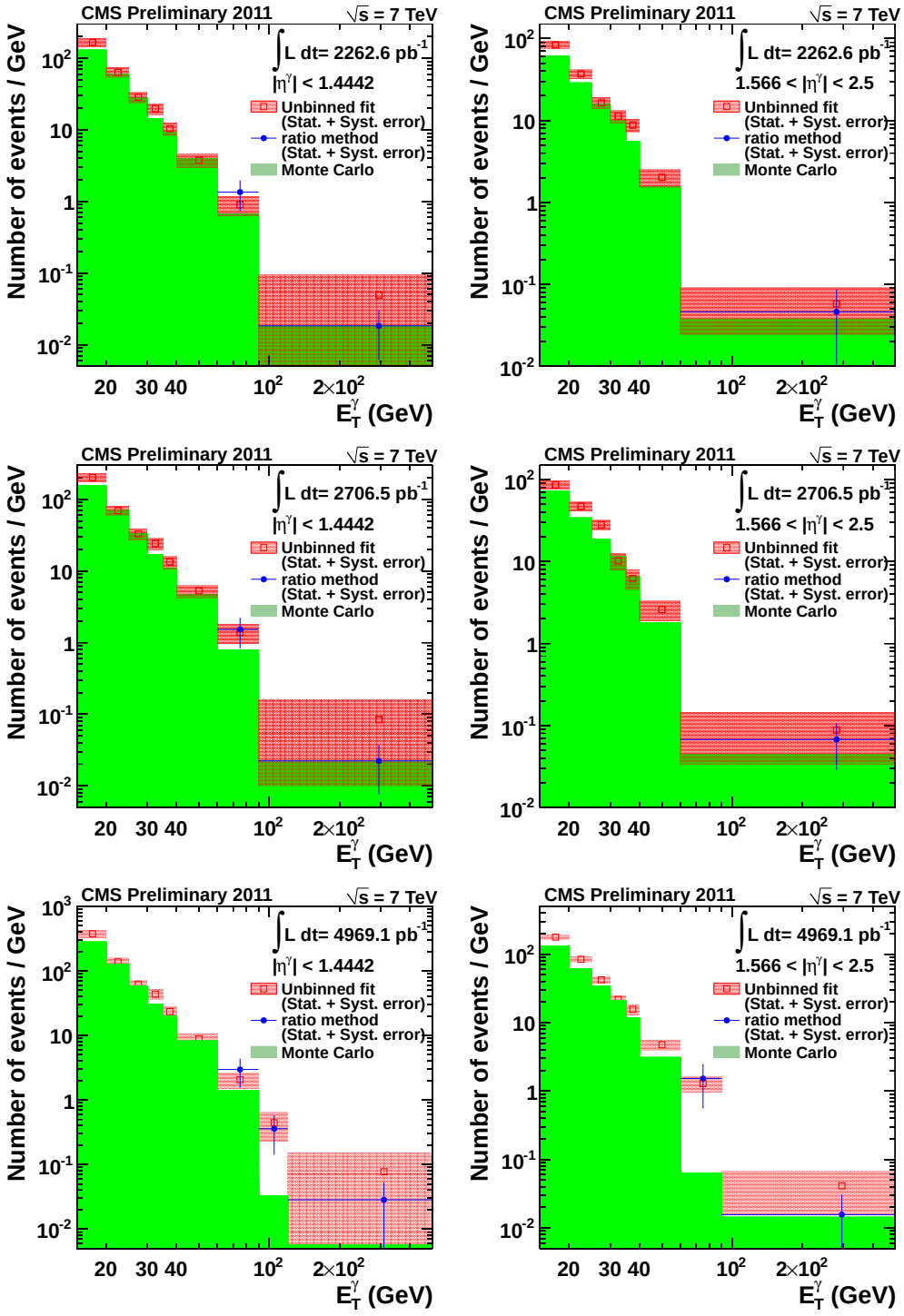

Slika 9.15: Broj pozadinskih događaja koje čine iz pogrešno identificirani mlazevi, za centralni (lijevo) i bočne dijelove detektora (desno). Rezultati dobiveni metodom predložaka i metodom omjera prikazani su crvenom odnosno plavom bojom. Zelenom bojom prikazan je broj pozadinskih događaja doiven iz simulacije.

Tablica 9.6: Broj pozadinskih događaja koji dolaze iz pogrešno identificiranih mlazeva određeni metodom predložaka za uzorak 2011A+2011B.

E_{T}^{γ} , GeV	Procjenjena pozadina (2011A+2011B)
Centralni dio detektora	
15-20	1876.4 $\pm$ 32.4(stat.) $\pm$ 62.4(syst.)
20-25	688.2 $\pm$ 22.3(stat.) $\pm$ 37.8(syst.)
25-30	310.9 $\pm$ 15.3(stat.) $\pm$ 21.2(syst.)
30-35	217.6 $\pm$ 13(stat.) $\pm$ 17.4(syst.)
35-40	116.7 $\pm$ 10.4(stat.) $\pm$ 11.1(syst.)
40-60	177.5 $\pm$ 13.1(stat.) $\pm$ 22.1(syst.)
60-90	61.9 $\pm$ 7.8(stat.) $\pm$ 12.3(syst.)
90-120	13.3 $\pm$ 4.5(stat.) $\pm$ 4.2(syst.)
120-500	29.3 $\pm$ 10.2(stat.) $\pm$ 25.4(syst.)
MET korelacija	$\pm$ 453.9(syst.)
Δ(metoda predložaka, metoda omjera)	$\pm$ 16.2 (syst.)
Ukupno	3491.8 $\pm$ 49.1(stat.) $\pm$ 462.4(syst.)
Bočni dijelovi detektora	
15-20	886.5 $\pm$ 18(stat.) $\pm$ 36.4(syst.)
20-25	420.1 $\pm$ 14(stat.) $\pm$ 21.2(syst.)
25-30	210.7 $\pm$ 10.7(stat.) $\pm$ 16.3(syst.)
30-35	108.7 $\pm$ 8.4(stat.) $\pm$ 10.8(syst.)
35-40	78.1 $\pm$ 7.5(stat.) $\pm$ 8.8(syst.)
40-60	94.8 $\pm$ 10(stat.) $\pm$ 10.1(syst.)
60-90	38.6 $\pm$ 6.8(stat.) $\pm$ 6.3(syst.)
90-120	8.1 $\pm$ 4.7(stat.) $\pm$ 2.2(syst.)
120-500	8.8 $\pm$ 7.0(stat.) $\pm$ 5.6(syst.)
MET korelacija	$\pm$ 129.8(syst.)
Δ(metoda predložaka, metoda omjera)	$\pm$ 9.2 (syst.)
Ukupno	1854.4 $\pm$ 31.3(stat.) $\pm$ 139.1(syst.)
Centralni + bočni dijelovi detektora	
15-20	2762.9 $\pm$ 37.1(stat.) $\pm$ 72.3(syst.)
20-25	1108.3 $\pm$ 26.3(stat.) $\pm$ 43.3(syst.)
25-30	521.6 $\pm$ 18.7(stat.) $\pm$ 26.7(syst.)
30-35	326.3 $\pm$ 15.5(stat.) $\pm$ 20.5(syst.)
35-40	194.8 $\pm$ 12.8(stat.) $\pm$ 14.2(syst.)
40-60	272.3 $\pm$ 16.5(stat.) $\pm$ 24.3(syst.)
60-90	100.5 $\pm$ 10.3(stat.) $\pm$ 13.8(syst.)
90-120	21.4 $\pm$ 6.5(stat.) $\pm$ 4.7(syst.)
120-500	38.1 $\pm$ 12.4(stat.) $\pm$ 26.0(syst.)
MET korelacija	$\pm$ 472.1(syst.)
Δ(metoda predložaka, metoda omjera)	$\pm$ 7.0 (syst.)
Ukupno	5345.9 $\pm$ 58.2(stat.) $\pm$ 482.6(syst.)

Pregled pozadina

Sve procjenjene pozadine sumirane su u Tablici 9.7 za uzorke 2011A i 2011B te u Tablici 9.8 za uzorak 2011A+2011B.

Tablica 9.7: Procjenjene pozadine u $W\gamma \to \mu\nu\gamma$ konačnom stanju za uzorke 2011A i 2011B.

Izvor pozadine	Procjenjena pozadina	
	2011A	2011B
Lažni fotoni (mlazevi)	2417.3 $\pm$ 39.4 (stat.)$\pm$ 219.9 (syst.)	2868.2 $\pm$ 43.7 (stat.) $\pm$ 276.8 (syst.)
Lažni fotoni (elektroni)	44.0 $\pm$ 1.0 (stat.) $\pm$ 3.3 (syst.)	47.3 $\pm$ 1.0 (stat.) $\pm$ 3.4 (syst.)
Lažni leptoni	zanemarivo	zanemarivo
$W(\tau\nu)\gamma$	11.9 $\pm$ 1.9 (stat.) $\pm$ 1.1 (syst.)	18.0 $\pm$ 2.4 (stat.) $\pm$ 1.8 (syst.)
$Z\gamma$	149.8 $\pm$ 10.5 (stat.) $\pm$ 9.0 (syst.)	188.6 $\pm$ 11.6 (stat.) $\pm$ 11.3 (syst.)
$t\bar{t}\gamma$	16.9 $\pm$ 0.6 (stat.) $\pm$ 8.5 (syst.)	18.9 $\pm$ 0.7 (stat.) $\pm$ 9.5 (syst.)

Tablica 9.8: Procjenjene pozadine u $W\gamma \to \mu\nu\gamma$ konačnom stanju za uzorak 2011A+2011B.

Izvor pozadine	Procjenjena pozadina
	2011A+2011B
Lažni fotoni (misid. mlazevi)	5345.9 $\pm$ 58.2 (stat.) $\pm$ 482.6 (syst.)
Lažni fotoni (misid. elektroni)	91.4 $\pm$ 1.4 (stat.) $\pm$ 4.7 (syst.)
Lažni leptoni	zanemarivo
$W(\tau\nu)\gamma$	28.9 $\pm$ 3.4 (stat.) $\pm$ 2.7 (syst.)
$Z\gamma$	338.0 $\pm$ 18.3 (stat.) $\pm$ 20.3 (syst.)
$t\bar{t}\gamma$	35.9 $\pm$ 1.0 (stat.) $\pm$ 17.9 (syst.)

9.4.4 Rezultati

Broj događaja u signalu N_{sig} u 9.39 određuje se kao broj selektiranih $W\gamma \to \mu\nu\gamma$ događaja u podacima N_{obs} umanjen za očekivani broj događaja pozadine N_{bkg} . Time se izraz za $W\gamma$ udarni presjek 9.39 može napisati u obliku:

$$\sigma = \frac{N_{\text{obs}} - N_{\text{bkg}}}{\mathscr{F} \cdot \rho_{\text{eff}} \cdot \mathscr{L}}. \tag{9.46}$$

Vrijednost N_{sig} određena je iz izraza:

$$N_{\text{sig}} = N_{\text{obs}} - N_{\text{bkg}}^{\text{mlazevi}} - N_{\text{bkg}}^{\text{elektroni}} - N_{\text{bkg}}^{\gamma+\text{mlazevi}} - N_{\text{bkg}}^{\text{W}(\tau\nu)\gamma} - N_{\text{bkg}}^{\text{Z}\gamma} - N_{\text{bkg}}^{\text{t}\bar{\text{t}}\gamma}, \tag{9.47}$$

gdje je $N_{\text{bkg}}^{\text{mlazevi}}$ pozadina koja dolazi od pogrešno identificiranih mlazeva određena metodom predložaka, $N_{\text{bkg}}^{\text{elektroni}}$ je pozadina koja dolazi od pogrešno identificiranih elektrona, $N_{\text{bkg}}^{\gamma+\text{mlazevi}}$ je pozadina od procesa $\gamma + jets$, $N_{\text{bkg}}^{W(\tau\nu)\gamma}$ pozadina od procesa $W(\tau\nu)\gamma$, $N_{\text{bkg}}^{Z\gamma}$ pozadina od procesa $Z\gamma$, a $N_{\text{bkg}}^{\text{t}\bar{\text{t}}\gamma}$ pozadina od procesa $\text{t}\bar{\text{t}}\gamma$.

$W\gamma \to \mu\nu\gamma$ selekciju zadovoljava 5014(5795) događaja u uzorku 2011A(2011B), te ukupno 10809 događaja u uzorku 2011A+2011B, što odgovara integriranom luminozitetu 4969.1 pb^{-1}.

Vrijednosti svih parametara korištenih pri određivanju udarnog presjeka prikazane su u Tablicama 9.9 i 9.10.

Dobivene mjerene vrijednosti udarnog presjeka iznose:

$$\sigma(pp \to W\gamma \to \mu\nu\gamma)(2011A) = 37.4 \pm 1.3\ (\text{stat.}) \pm 4.3\ (\text{syst.}) \pm 0.8\ (\text{lumi.})\ \text{pb}.$$

$$\sigma(pp \to W\gamma \to \mu\nu\gamma)(2011B) = 38.7 \pm 1.3\ (\text{stat.}) \pm 4.8\ (\text{syst.}) \pm 0.9\ (\text{lumi.})\ \text{pb}.$$

$$\sigma(pp \to W\gamma \to \mu\nu\gamma)(2011A + 2011B) = 37.5 \pm 0.9\ (\text{stat.}) \pm 4.4\ (\text{syst.}) \pm 0.8\ (\text{lumi.})\ \text{pb}.$$

Teorijski NLO udarni presjek određen MCFM generatorom [34] iznosi 31.81 ± 1.8 pb.

Usporedbe kinematičkih raspodjela u podacima i simulaciji nakon $W\gamma \to \mu\nu\gamma$ selekcije prikazane su na Slikama 9.16-9.18, dok su omjeri raspodjela prikazani na Slikama 9.19-9.21. Simulacija pozadine skalirana je na vrijednost određenu iz podataka.

Slika 9.22 pokazuje rezultate mjerenja udarnog presjeka u usporedbi s teorijski predviđenim udarnim presjekom u NLO redu.

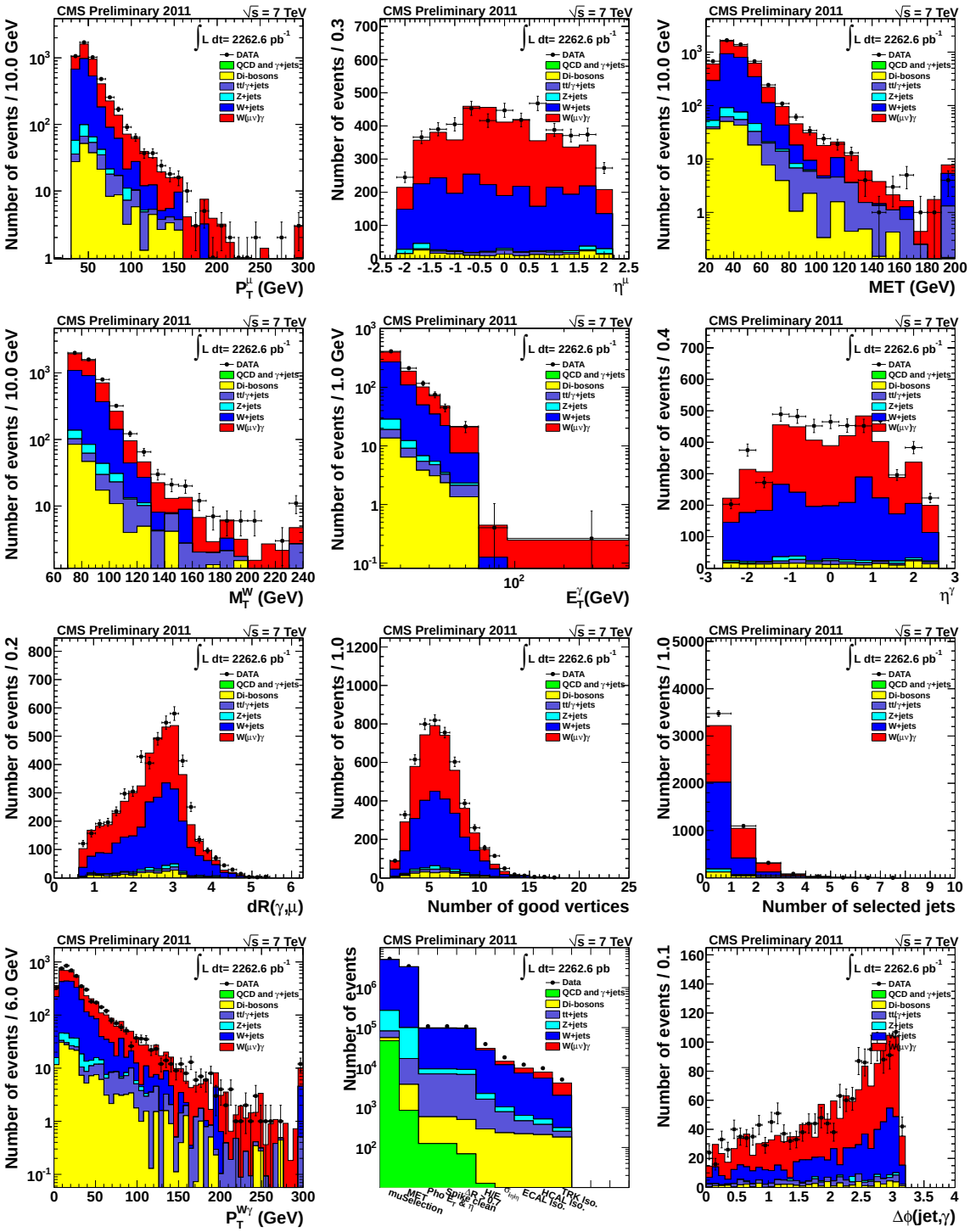

Slika 9.16: Raspodjela transverzalnog impulsa miona (P_T^{μ}), pseudorapiditeta miona (η^{μ}), nedostajuće transverzalne energije (MET), transverzalne mase W bozona (M_T^W), tranverzalne energije fotona (E_T^{γ}), pseudorapiditeta fotona (η^{γ}), prostorne udaljenosti fotona i miona ($dR(\gamma,\mu)$), broja primarnih vrhova u događaju (Number of good vertices), broja mlazeva u događaju (Number of selected jets), transverzalnog impulsa $W\gamma$ sustava ($P_T^{W\gamma}$), broja događaja koji prolaze niz selekcijskih zahtjeva i razlike u kutu ϕ između mlaza i fotona ($\Delta\phi(jet,\gamma)$) za događaje koji zadovoljavaju $W\gamma \to \mu\nu\gamma$ selekciju za simulirane (histogrami) i mjerene događaje (točke) za uzorak 2011A.

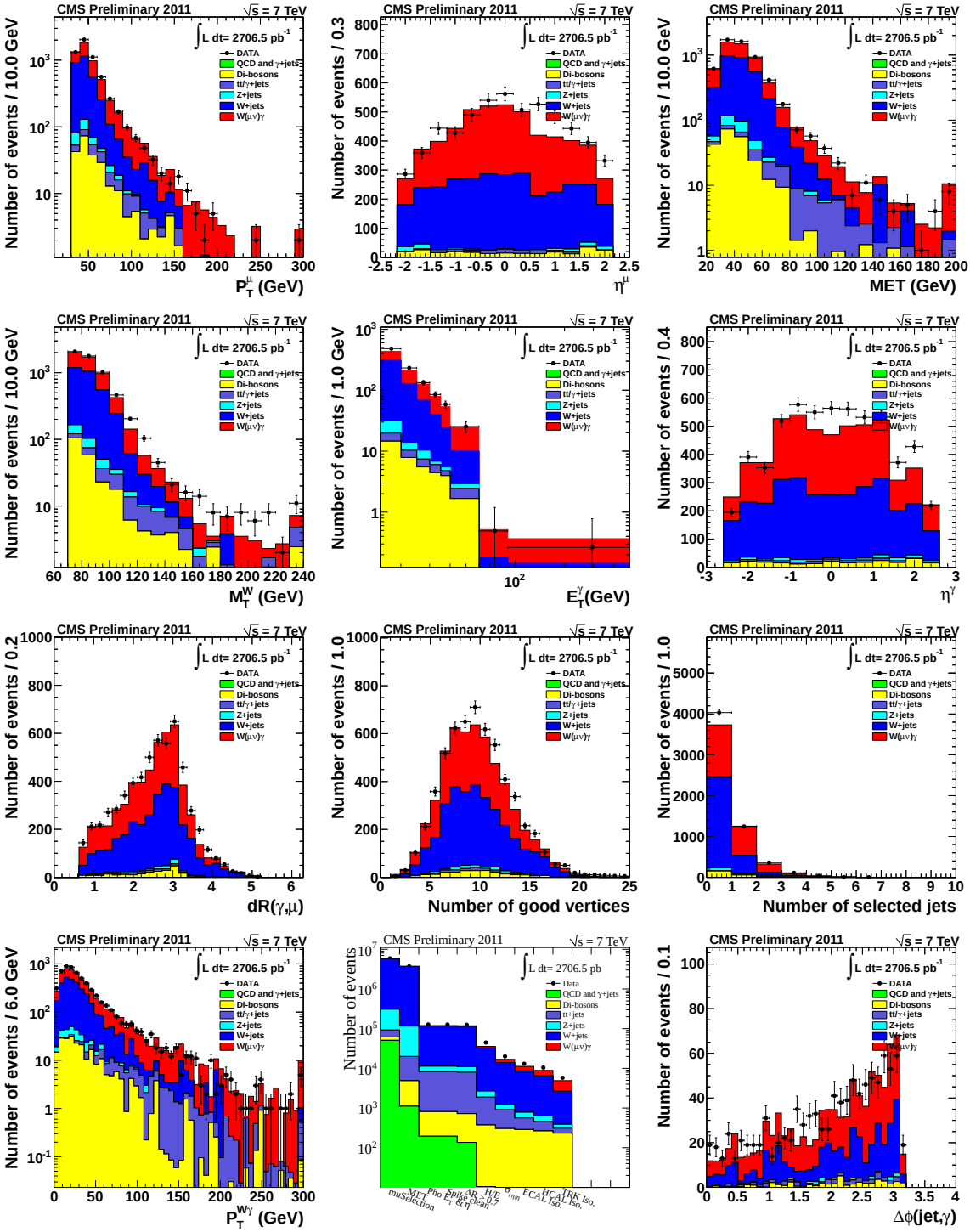

Slika 9.17: Raspodjela transverzalnog impulsa miona (P_T^{μ}), pseudorapiditeta miona (η^{μ}), nedostajuće transverzalne energije (MET), transverzalne mase W bozona (M_T^W), tranverzalne energije fotona (E_T^{γ}), pseudorapiditeta fotona (η^{γ}), prostorne udaljenosti fotona i miona ($dR(\gamma,\mu)$), broja primarnih vrhova u događaju (Number of good vertices), broja mlazeva u događaju (Number of selected jets), transverzalnog impulsa $W\gamma$ sustava ($P_T^{W\gamma}$), broja događaja koji prolaze niz selekcijskih zahtjeva i razlike u kutu ϕ između mlaza i fotona ($\Delta\phi(jet,\gamma)$) za događaje koji zadovoljavaju $W\gamma \to \mu\nu\gamma$ selekciju za simulirane (histogrami) i mjerene događaje (točke) za uzorak 2011B.

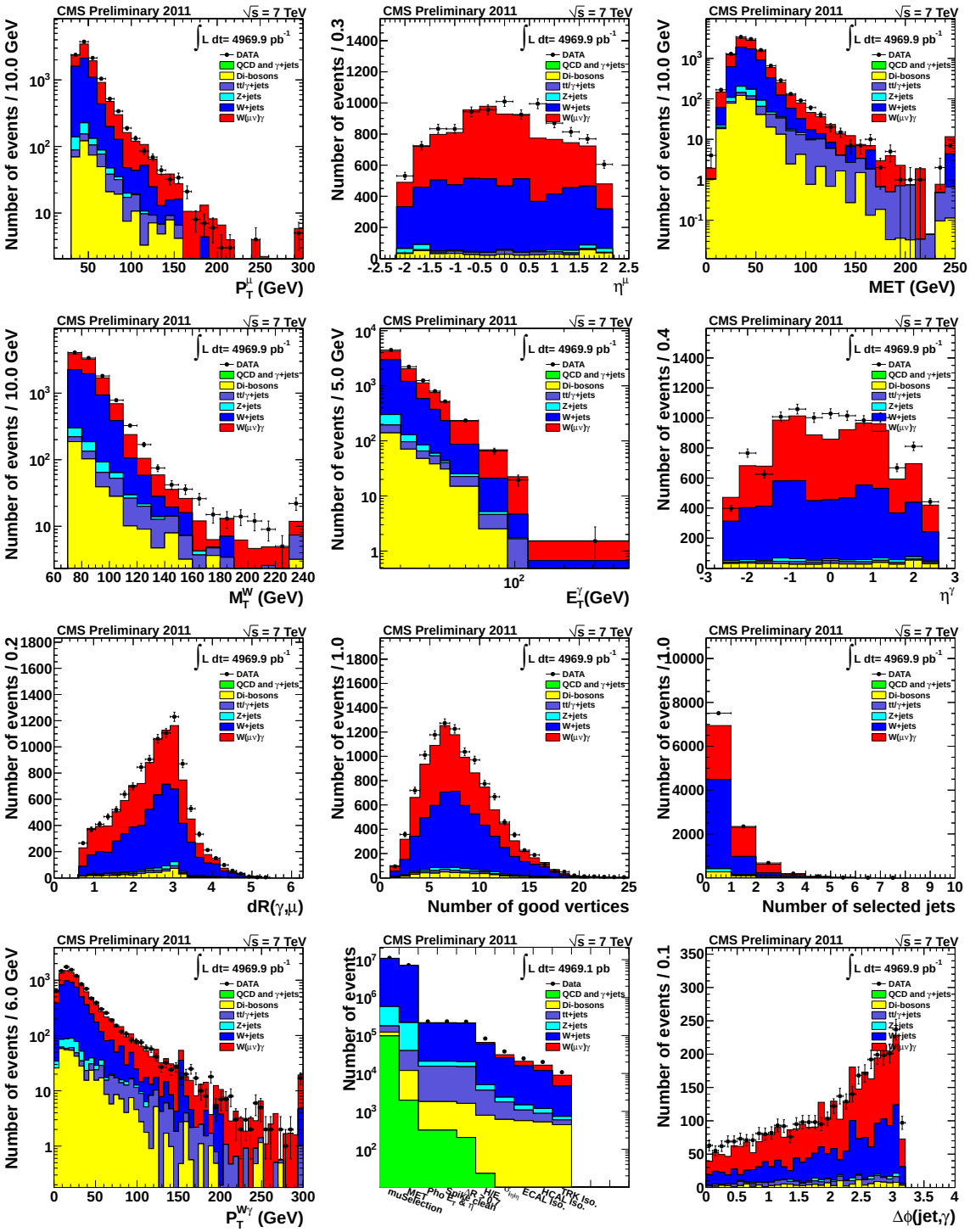

Slika 9.18: Raspodjela transverzalnog impulsa miona (P_T^{μ}), pseudorapiditeta miona (η^{μ}), nedostajuće transverzalne energije (MET), transverzalne mase W bozona (M_T^W), tranverzalne energije fotona (E_T^{γ}), pseudorapiditeta fotona (η^{γ}), prostorne udaljenosti fotona i miona ($dR(\gamma,\mu)$), broja primarnih vrhova u događaju (Number of good vertices), broja mlazeva u događaju (Number of selected jets), transverzalnog impulsa $W\gamma$ sustava ($P_T^{W\gamma}$), broja događaja koji prolaze niz selekcijskih zahtjeva i razlike u kutu ϕ između mlaza i fotona ($\Delta\phi(jet,\gamma)$) za događaje koji zadovoljavaju $W\gamma \to \mu\nu\gamma$ selekciju za simulirane (histogrami) i mjerene događaje (točke) za uzorak 2011A+2011B.

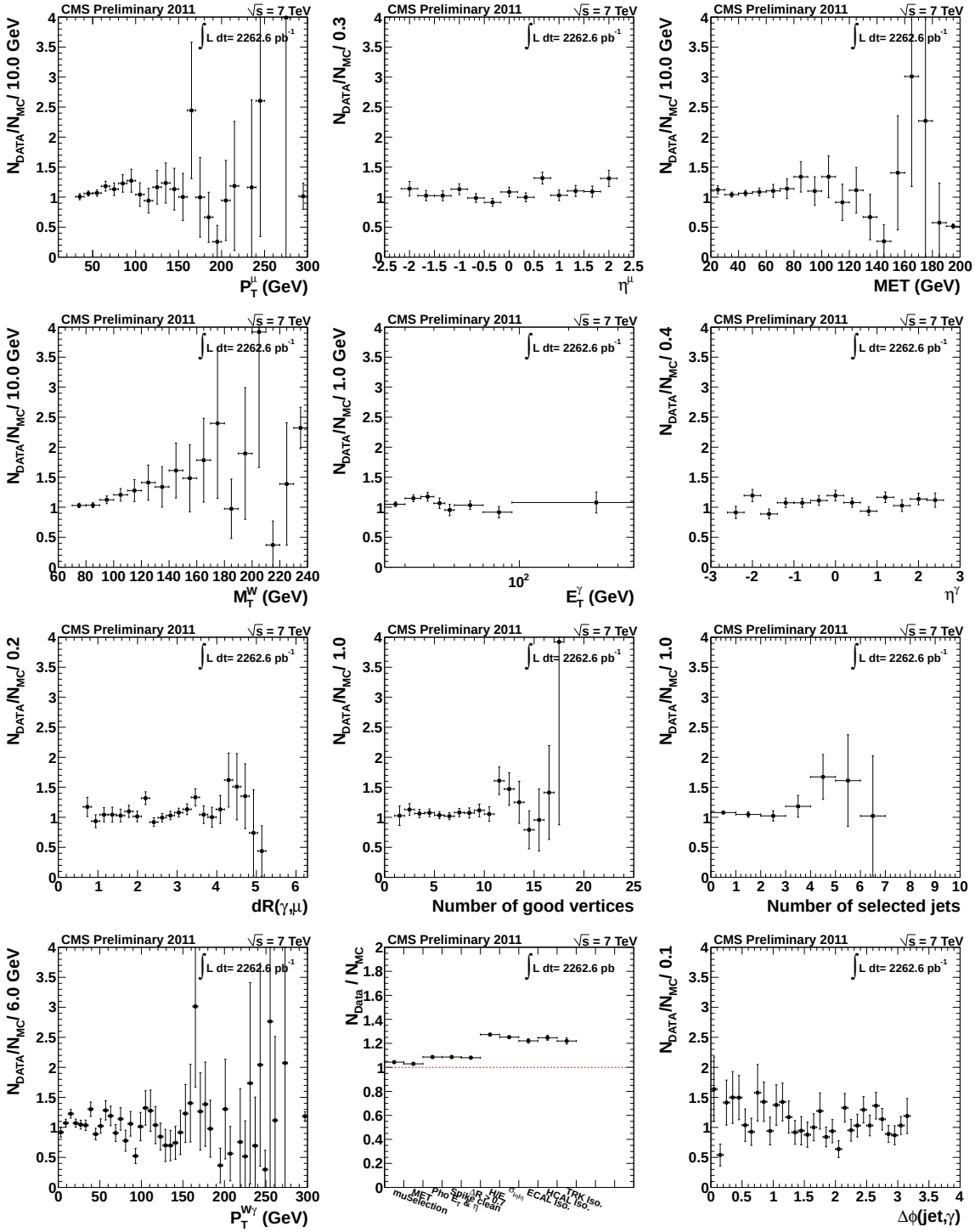

Slika 9.19: Omjeri raspodjela transverzalnog impulsa miona (P_T^{μ}), pseudorapiditeta miona (η^{μ}), nedostajuće transverzalne energije (MET), transverzalne mase W bozona (M_T^W), tranverzalne energije fotona (E_T^{γ}), pseudorapiditeta fotona (η^{γ}), prostorne udaljenosti fotona i miona ($dR(\gamma,\mu)$), broja primarnih vrhova u događaju (Number of good vertices), broja mlazeva u događaju (Number of selected jets), transverzalnog impulsa $W\gamma$ sustava ($P_T^{W\gamma}$), broja događaja koji prolaze niz selekcijskih zahtjeva i razlike u kutu ϕ između mlaza i fotona ($\Delta\phi(jet,\gamma)$) za događaje koji zadovoljavaju $W\gamma \to \mu\nu\gamma$ selekciju za mjerene i simulirane događaje za uzorak 2011A.

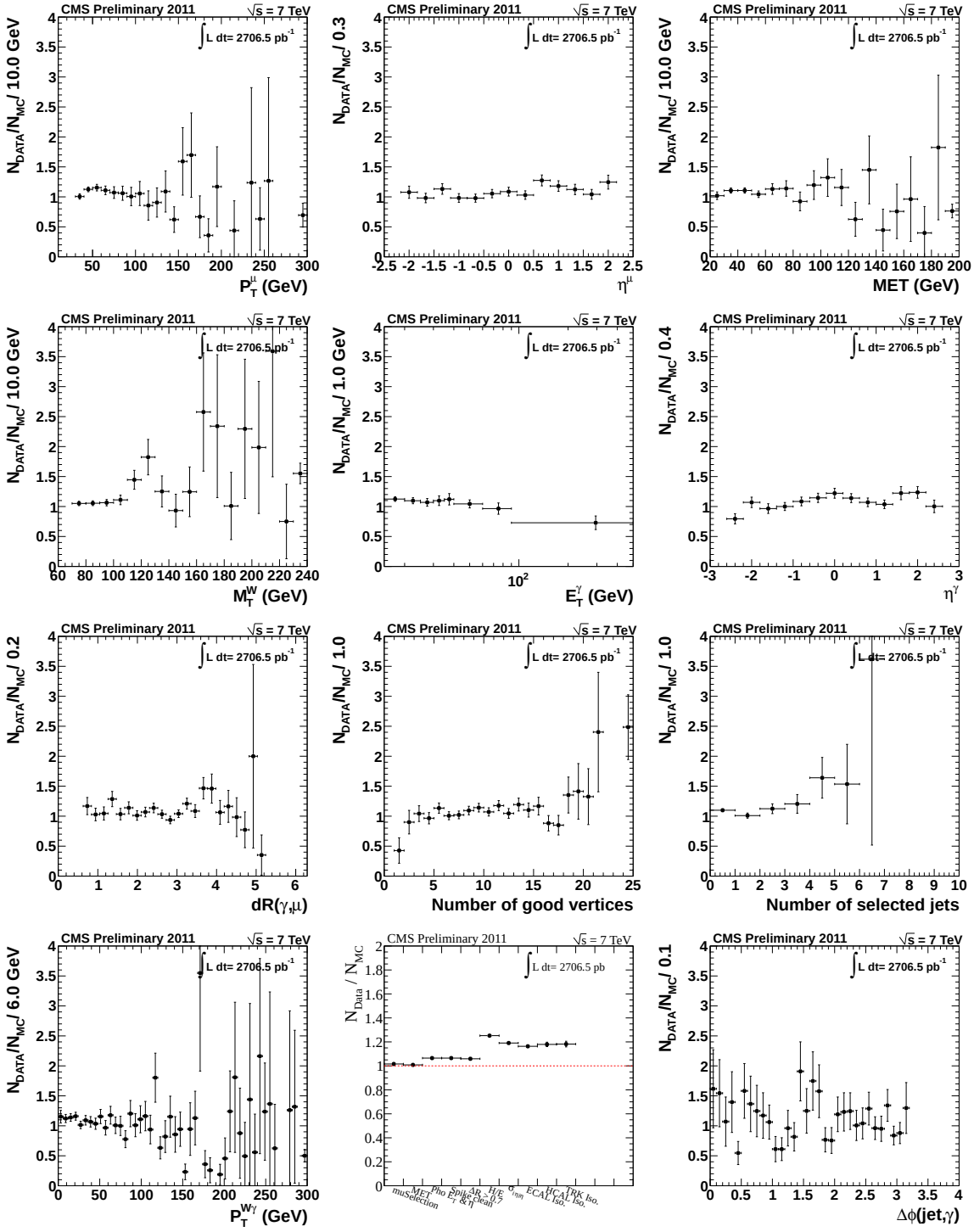

Slika 9.20: Omjeri raspodjela transverzalnog impulsa miona (P_T^{μ}), pseudorapiditeta miona (η^{μ}), nedostajuće transverzalne energije (MET), transverzalne mase W bozona (M_T^W), tranverzalne energije fotona (E_T^{γ}), pseudorapiditeta fotona (η^{γ}), prostorne udaljenosti fotona i miona ($dR(\gamma,\mu)$), broja primarnih vrhova u događaju (Number of good vertices), broja mlazeva u događaju (Number of selected jets), transverzalnog impulsa $W\gamma$ sustava ($P_T^{W\gamma}$), broja događaja koji prolaze niz selekcijskih zahtjeva i razlike u kutu ϕ između mlaza i fotona ($\Delta\phi(jet,\gamma)$) za događaje koji zadovoljavaju $W\gamma \to \mu\nu\gamma$ selekciju za mjerene i simulirane događaje za uzorak 2011B.

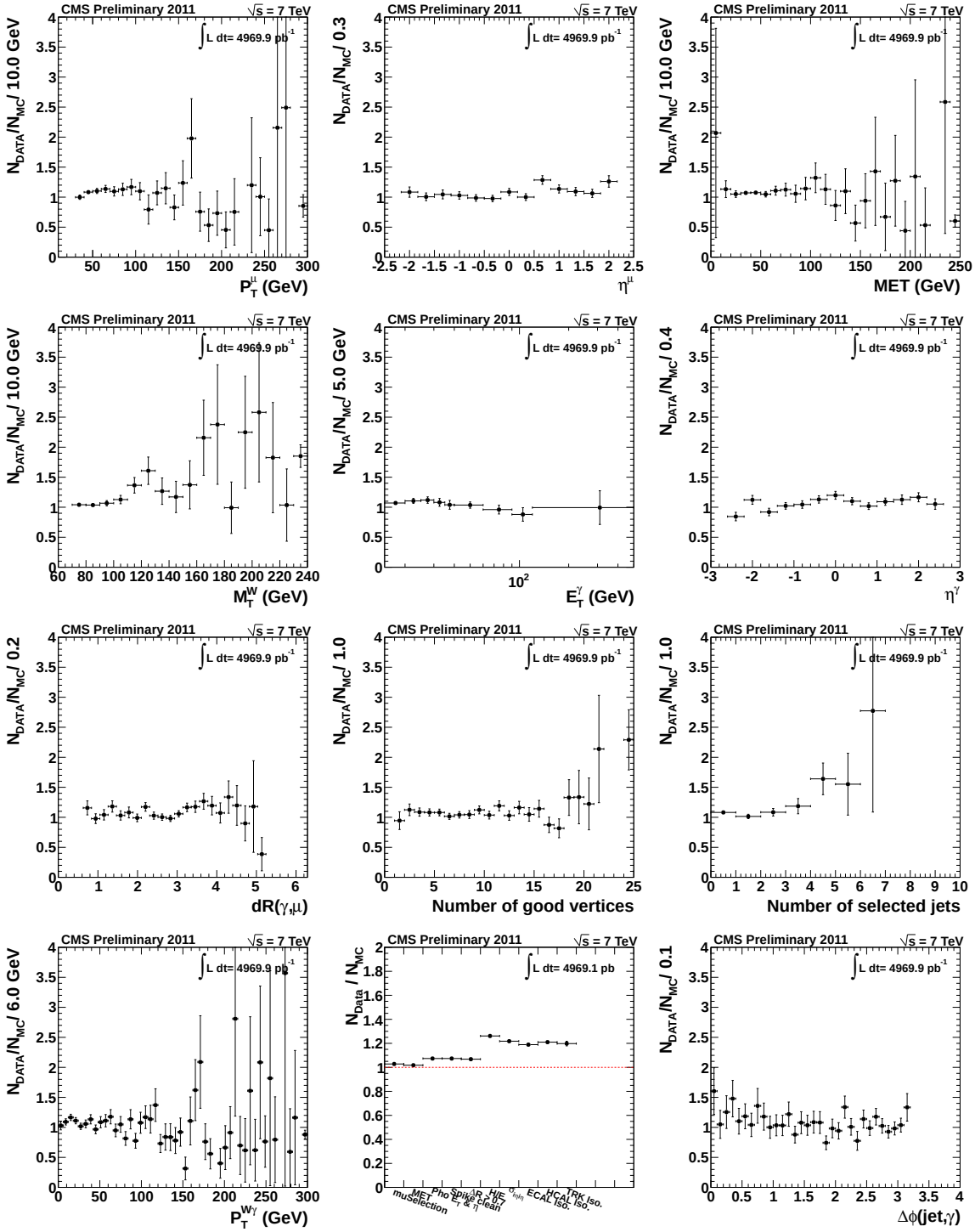

Slika 9.21: Omjeri raspodjela transverzalnog impulsa miona (P_T^{μ}), pseudorapiditeta miona (η^{μ}), nedostajuće transverzalne energije (MET), transverzalne mase W bozona (M_T^W), tranverzalne energije fotona (E_T^{γ}), pseudorapiditeta fotona (η^{γ}), prostorne udaljenosti fotona i miona ($dR(\gamma,\mu)$), broja primarnih vrhova u događaju (Number of good vertices), broja mlazeva u događaju (Number of selected jets), transverzalnog impulsa $W\gamma$ sustava ($P_T^{W\gamma}$), broja događaja koji prolaze niz selekcijskih zahtjeva i razlike u kutu ϕ između mlaza i fotona ($\Delta\phi(jet,\gamma)$) za događaje koji zadovoljavaju $W\gamma \to \mu\nu\gamma$ selekciju za mjerene i simulirane događaje za uzorak 2011A+2011B.

Tablica 9.9: Parametri korišteni pri određivanju udarnog presjeka $W\gamma \to \mu\nu\gamma$ za uzorke 2011A i 2011B.

Parametar	Iznos (2011A)	Iznos (2011B)
N_{events}	5014	5795
$N_{bkg}^{\text{misid. jets}}$	2417.3 ± 39.4 (stat.) ± 219.9 (syst.)	2868.2 ± 43.7 (stat.) ± 276.8 (syst.)
$N_{bkg}^{\text{misid. electrons}}$	44.0 ± 1.0 (stat.) ± 3.3 (syst.)	47.3 ± 1.0 (stat.) ± 3.4 (syst.)
$N_{bkg}^{\gamma+\text{jets}}$	negligible	negligible
$N_{bkg}^{W(\tau\nu)\gamma}$	11.9 ± 1.9 (stat.) ± 1.1 (syst.)	18.0 ± 2.4 (stat.) ± 1.8 (syst.)
$N_{bkg}^{Z\gamma}$	149.8 ± 10.5 (stat.) ± 9.0 (syst.)	188.6 ± 11.6 (stat.) ± 11.3 (syst.)
$N_{bkg}^{t\bar{t}\gamma}$	16.9 ± 0.6 (stat.) ± 8.5 (syst.)	18.9 ± 0.7 (stat.) ± 9.5 (syst.)
N_{bkg}	2639.9 ± 40.8 (stat.) ± 220.2 (syst.)	3141.0 ± 45.3 (stat.) ± 277.2 (syst.)
N_{sig}	2374.1 ± 81.7 (stat.) ± 238.0 (syst.)	2654.0 ± 88.6 (stat.) ± 290.7 (syst.)
$A \cdot \varepsilon_{gen}$	0.0286 ± 0.0015 (syst.)	0.0257 ± 0.0013 (syst.)
ρ_{eff}	0.9806 ± 0.0226 (syst.)	0.9865 ± 0.0247 (syst.)
$\int \mathscr{L}\, dt$	2262.6 ± 49.8 (syst.)	2706.5 ± 59.5 (syst.)

Tablica 9.10: Parametri korišteni pri određivanju udarnog presjeka $W\gamma \to \mu\nu\gamma$ za uzorak 2011A+2011B.

Parametar	Iznos (2011A+2011B)
N_{events}	10809
$N_{bkg}^{\text{misid. jets}}$	5345.9 ± 58.2 (stat.) ± 482.6 (syst.)
$N_{bkg}^{\text{misid. electrons}}$	91.4 ± 1.4 (stat.) ± 4.7 (syst.)
$N_{bkg}^{\gamma+\text{jets}}$	negligible
$N_{bkg}^{W(\tau\nu)\gamma}$	28.9 ± 3.4 (stat.) ± 2.7 (syst.)
$N_{bkg}^{Z\gamma}$	338.0 ± 18.3 (stat.) ± 20.3 (syst.)
$N_{bkg}^{t\bar{t}\gamma}$	35.9 ± 1.0 (stat.) ± 17.9 (syst.)
N_{bkg}	5840.1 ± 61.1 (stat.) ± 483.4 (syst.)
N_{sig}	4968.9 ± 120.6 (stat.) ± 505.8 (syst.)
$A \cdot \varepsilon_{gen}$	0.0270 ± 0.0014 (syst.)
ρ_{eff}	0.9898 ± 0.0247 (syst.)
$\int \mathscr{L}\, dt$	4969.1 ± 109.3 (syst.)

Osim mjerenja udarnog presjeka u kinematičkom području $E_T^\gamma > 15$ GeV-a i $\Delta R(\mu,\gamma) > 0.7$ analiza je provedena i u kinematskom području $E_T^\gamma > 60$ GeV-a i $E_T^\gamma > 90$ GeV-a.

Mjereni udarni presjek za $E_T^\gamma > 60$ GeV-a iznosi:

$$\sigma(pp \to W\gamma \to \mu\nu\gamma)(2011A+2011B) = 0.76 \pm 0.06\ (\text{stat.}) \pm 0.08\ (\text{syst.}) \pm 0.02\ (\text{lumi.})\ \text{pb}.$$

Teorijski NLO udarni presjek za $E_T^\gamma > 60$ GeV-a određen MCFM generatorom [34] iznosi 0.58 ± 0.08 pb.

Mjereni udarni presjek za $E_T^\gamma > 90$ GeV-a iznosi:

$$\sigma(pp \to W\gamma \to \mu\nu\gamma)(2011A+2011B) = 0.248 \pm 0.035\ (\text{stat.}) \pm 0.048\ (\text{syst.}) \pm 0.005\ (\text{lumi.})\ \text{pb}.$$

Teorijski NLO udarni presjek za $E_T^\gamma > 90$ GeV-a određen MCFM generatorom [34] iznosi 0.173 ± 0.026 pb.

Tablica 9.11: Parametri korišteni pri mjerenju udarnog presjeka $W\gamma \to \mu\nu\gamma$ za $E_T^\gamma > 60$ GeV-a i $E_T^\gamma > 90$ GeV-a za uzorak 2011A+2011B.

Parametar	$E_T^\gamma > 60$ GeV	$E_T^\gamma > 90$ GeV
N_{events}	610 ± 24.7 (stat.)	230 ± 15.2 (stat.)
$N_{bkg}^{mlazevi}$	159.9 ± 17.4 (stat.) ± 30.0 (syst.)	59.4 ± 14.0 (stat.) ± 26.5 (syst.)
$N_{bkg}^{elektroni}$	21.2 ± 0.6 (stat.) ± 1.1 (syst.)	7.2 ± 0.4 (stat.) ± 0.4 (syst.)
$N_{bkg}^{\gamma+\text{mlazevi}}$	zanemarivo	zanemarivo
$N_{bkg}^{W(\tau\nu)\gamma}$	3.2 ± 1.2 (stat.) ± 0.3 (syst.)	.0 ± 0.0 (stat.) ± 0.0 (syst.)
$N_{bkg}^{Z\gamma}$	19.4 ± 4.4 (stat.) ± 1.2 (syst.)	10.9 ± 3.2 (stat.) ± 0.7 (syst.)
$N_{bkg}^{t\bar{t}\gamma}$	9.7 ± 0.5 (stat.) ± 4.9 (syst.)	5.3 ± 0.4 (stat.) ± 2.7 (syst.)
N_{sig}	396.7 ± 30.5 (stat.) ± 37.4 (syst.)	147.2 ± 20.9 (stat.) ± 27.2 (syst.)
$A \cdot \varepsilon_{MC,W\gamma\to\ell\nu\gamma}$	0.105 ± 0.005 (syst.)	0.120 ± 0.006 (syst.)
ρ_{eff}	0.993 ± 0.025 (syst.)	0.993 ± 0.025 (syst.)
$\int \mathscr{L}\, dt$	4969.1 ± 109.3 (syst.)	4969.1 ± 109.3 (syst.)

Vrijednosti parametara korištenih pri mjerenju udarnog presjeka za $E_T^\gamma > 60$ GeV-a i $E_T^\gamma > 90$ GeV-a, prikazani su u Tablici 9.11.

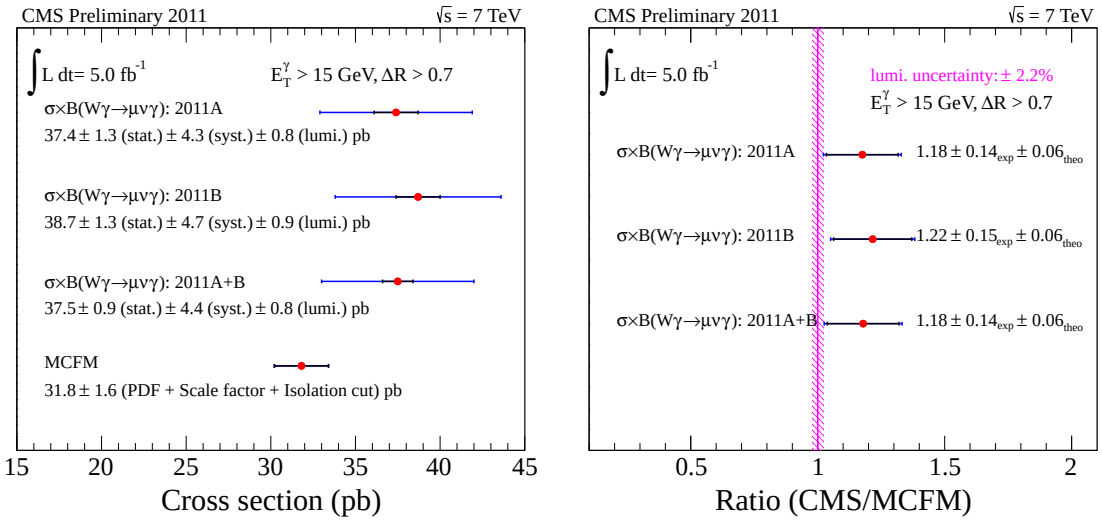

Slika 9.22: Mjereni udarni presjek $W\gamma \to \mu\nu\gamma$ (lijevo) te omjer mjerenog udarnog presjeka i udarnog presjeka predviđenog MCFM generatorom (desno).

9.4.5 Kombinacija rezultata s elektronskim kanalom

Paralelno s mjerenjem $W\gamma$ udarnog presjeka u mionskom kanalu koje je prikazano u ovom radu, izvršeno je i mjerenje udarnog presjeka u elektronskom kanalu. Mjereni udarni presjek u elektronskom kanalu iznosi:

$$\sigma(pp \to \mathrm{W}\gamma \to e\nu\gamma) = 36.6 \pm 1.2\ (\mathrm{stat.}) \pm 4.3\ (\mathrm{syst.}) \pm 0.8\ (\mathrm{lumi.})\ \mathrm{pb}.$$

Primjenom BLUE metode (od engl. Best Linear Unbiased Estimator) [35] određen je kombinirani udarni presjek:

$$\sigma(pp \to \mathrm{W}\gamma \to \ell\nu\gamma) = 37.0 \pm 0.8\ (\mathrm{stat.}) \pm 4.0\ (\mathrm{syst.}) \pm 0.8\ (\mathrm{lumi.})\ \mathrm{pb}.$$

Tablica 9.12: Prikaz mjerenih vrijednosti $W\gamma$ udarnog presjeka u mionskom i elektronskom kanalu.

	Wγ	
	Electronski kanal (pb)	Mionski kanal (pb)
$E_{\mathrm{T}}^{\gamma} > 15$ GeV	$36.6 \pm 1.2(\mathrm{stat.}) \pm 4.3(\mathrm{syst.}) \pm 0.8(\mathrm{lumi.})$	$37.5 \pm 0.9(\mathrm{stat.}) \pm 4.4(\mathrm{syst.}) \pm 0.8(\mathrm{lumi.})$
Kombinacija	$37.0 \pm 0.8(\mathrm{stat.}) \pm 4.0(\mathrm{syst.}) \pm 0.8(\mathrm{lumi.})$ pb	
NLO predviđeno	31.81 ± 1.80 (pb)	
$E_{\mathrm{T}}^{\gamma} > 60$ GeV	$0.77 \pm 0.07(\mathrm{stat.}) \pm 0.13(\mathrm{syst.}) \pm 0.02(\mathrm{lumi.})$	$0.76 \pm 0.06(\mathrm{stat.}) \pm 0.08(\mathrm{syst.}) \pm 0.02(\mathrm{lumi.})$
Kombinacija	$0.76 \pm 0.05(\mathrm{stat.}) \pm 0.08(\mathrm{syst.}) \pm 0.02(\mathrm{lumi.})$ pb	
NLO predviđeno	0.58 ± 0.08 (pb)	
$E_{\mathrm{T}}^{\gamma} > 90$ GeV	$0.173 \pm 0.034(\mathrm{stat.}) \pm 0.037(\mathrm{syst.}) \pm 0.004(\mathrm{lumi.})$	$0.248 \pm 0.035(\mathrm{stat.}) \pm 0.048(\mathrm{syst.}) \pm 0.005(\mathrm{lumi.})$
kombinacija	$0.200 \pm 0.025(\mathrm{stat.}) \pm 0.038(\mathrm{syst.}) \pm 0.004(\mathrm{lumi.})$ pb	
NLO predviđeno	0.173 ± 0.026 pb	

Svi rezultati mjerenja udarnog presjeka u elektronskom i mionskom kanalu prikazani su na Slikama 9.23- 9.25.

Mjereni udarni presjek za $E_T^{\gamma} > 60$ GeV-a u elektronskom kanalu iznosi:

$$\sigma(pp \to W\gamma \to e\nu\gamma)(2011A + 2011B) = 0.77 \pm 0.07\ (\mathrm{stat.}) \pm 0.13\ (\mathrm{syst.}) \pm 0.02\ (\mathrm{lumi.})\ \mathrm{pb},$$

dok kombinirani udarni presjek elektronskog i mionskog kanala iznosi:

$$\sigma(pp \to W\gamma \to \ell\nu\gamma)(2011A + 2011B) = 0.76 \pm 0.05\ (\mathrm{stat.}) \pm 0.08\ (\mathrm{syst.}) \pm 0.02\ (\mathrm{lumi.})\ \mathrm{pb}.$$

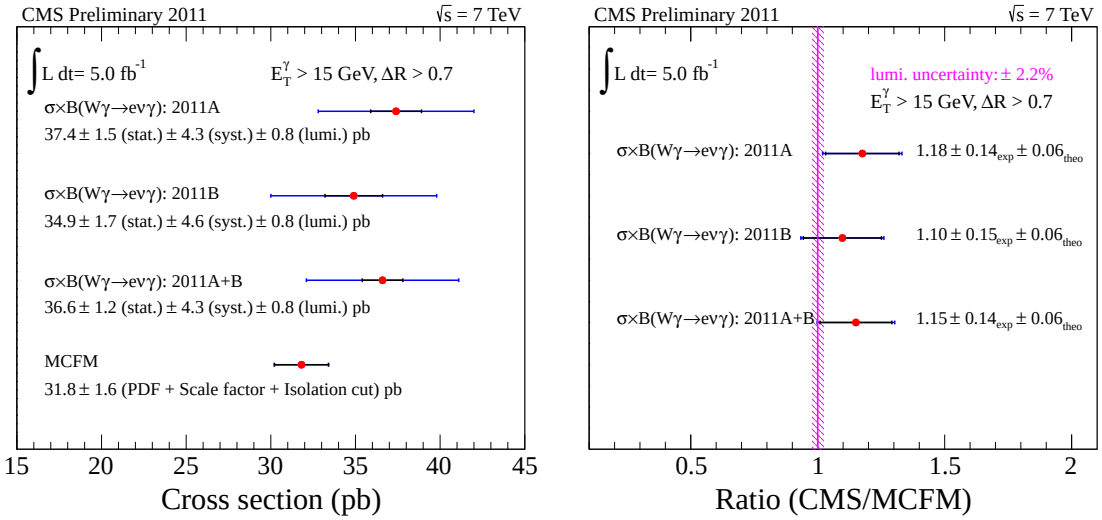

Slika 9.23: Mjereni udarni presjek $W\gamma \to e\nu\gamma$ (lijevo) te omjer mjerenog udarnog presjeka i udarnog presjeka predviđenog MCFM generatorom (desno).

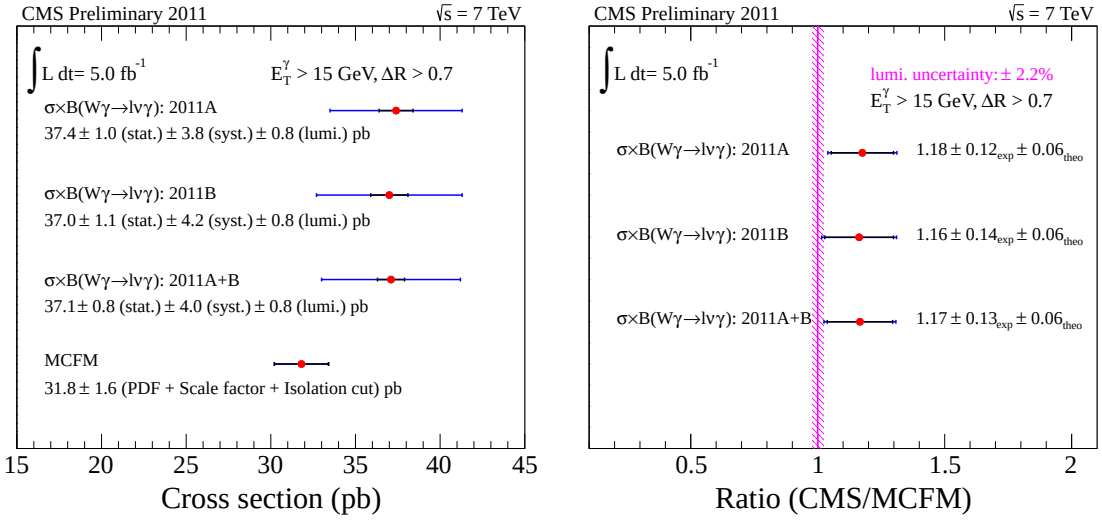

Slika 9.24: Mjereni udarni presjek $W\gamma \to l\nu\gamma$ (lijevo) te omjer mjerenog udarnog presjeka i udarnog presjeka predviđenog MCFM generatorom (desno) za kombinirani mionski i elektronski kanal.

Mjereni udarni presjek za $E_T^{\gamma} > 90$ GeV-a u elektronskom kanalu jednak je:

$$\sigma(pp \to W\gamma \to e\nu\gamma)(2011A + 2011B) = 0.173 \pm 0.034 \text{ (stat.)} \pm 0.037 \text{ (syst.)} \pm 0.004 \text{ (lumi.) pb.}$$

Udarni presjek dobiven kombinirenjem elektronskog i mionskog kanala jednak je:

$$\sigma(pp \to W\gamma \to \ell\nu\gamma)(2011A + 2011B) = 0.200 \pm 0.025 \text{ (stat.)} \pm 0.038 \text{ (syst.)} \pm 0.004 \text{ (lumi.) pb.}$$

Svi mjereni udarni presjeci s odgovarajućim pogreškama i teorijski predviđeni udarni presjeci prikazani su u Tablici 9.12 te na Slici 9.26.

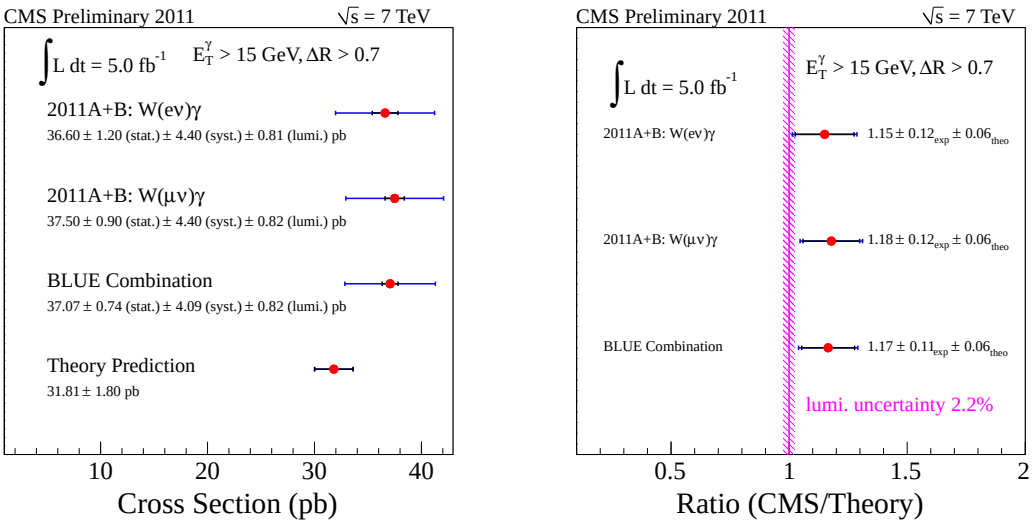

Slika 9.25: Pregled mjerenih udarnih presjeka $W\gamma$ procesa.

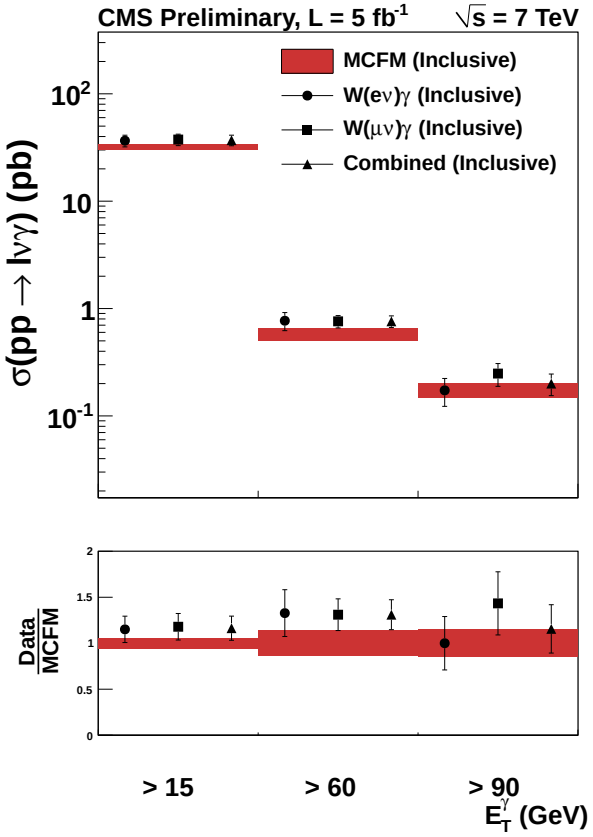

Slika 9.26: Mjereni i teorijski predviđeni udarni presjeci za $W\gamma$ proces.

9.5 Opažanje radijacijske amplitude vrijednosti nula u $W\gamma$ procesu

Za opažanje radijacijske amplitude vrijednosti nula potrebna je, uz selekcijske uvjete korištene pri mjerenju udarnog presjeka uvesti i dva dodatna zahtjeva. Kao što je spomenuto u paragrafu 9.2.3 korišten je zahtjev da u događaju ne postoji hadronski mlaz transverzalnog impulsa $p_T^{mlaz} > 30$ GeV-a, te zahjev da je transverzalna masa $\mu\text{MET}\gamma$ ($\mu\nu\gamma$) sustava veća od 110 GeV-a, $M_T^{\mu\text{MET}\gamma} > 110$ GeV-a.

9.5.1 Rezultati

Raspodjele $Q_l \times \Delta\eta$ za događaje koji zadovoljavaju $W\gamma \to \mu\nu\gamma$ selekciju za simulirane i mjerene događaje, te omjeri raspodjela za mjerene i simulirane događaje za uzorak 2011A+2011B prikazani su na Slikama 9.27 i 9.28. Q_l je naboj miona a $\Delta\eta$ razlika pseudorapiditeta fotona i miona. Udubina oko vrijednosti nula se jasno opaža u podacima.

9.5.2 Kombinacija rezultata s elektronskim kanalom

Raspodjele $Q_l \times \Delta\eta$, za događaje koji zadovoljavaju $W\gamma \to l\nu\gamma$ selekciju za simulirane i mjerene događaje za uzorak 2011A+2011B dobivene kombiniranjem mionskog i elektronskog kanala prikazani su na Slici 9.29. Udubina oko vrijednosti nula je jasno vidljiva.

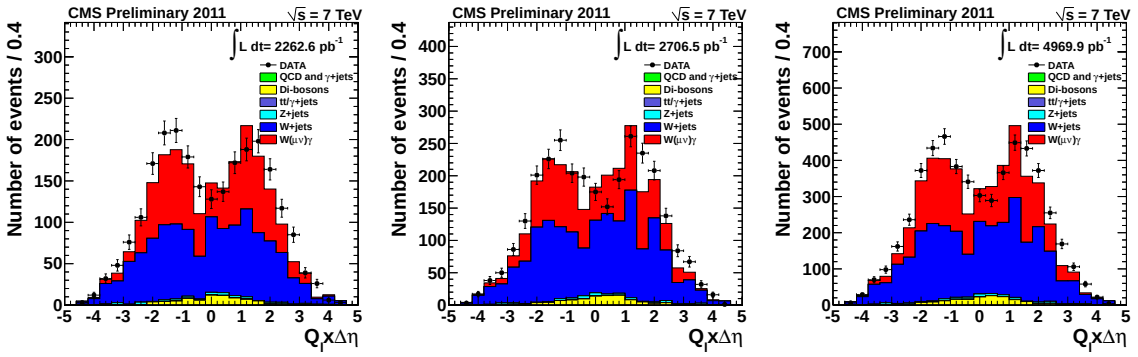

Slika 9.27: $Q_l \times \Delta\eta$ raspodjela za događaje koji zadovoljavaju $W\gamma \to \mu\nu\gamma$ selekciju za simulirane (histogrami) i mjerene događaje (točke) za uzorak 2011A (lijevo), uzrak 2011B (sredina) i uzorak 2011A+2011B (desno).

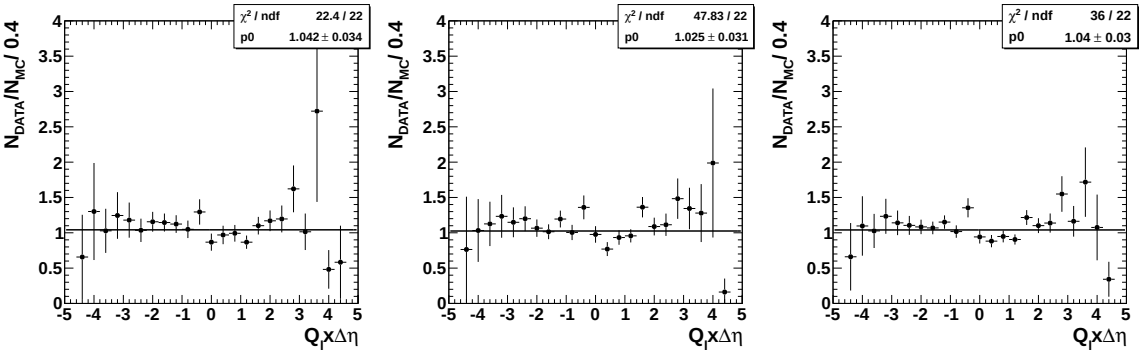

Slika 9.28: Omjer $Q_l \times \Delta\eta$ raspodjele za događaje koji zadovoljavaju $W\gamma \to \mu\nu\gamma$ selekciju za mjerene i simulirane događaje za uzorak 2011A (lijevo), uzorak 2011B (sredina) i uzorak 2011A+2011B (desno).

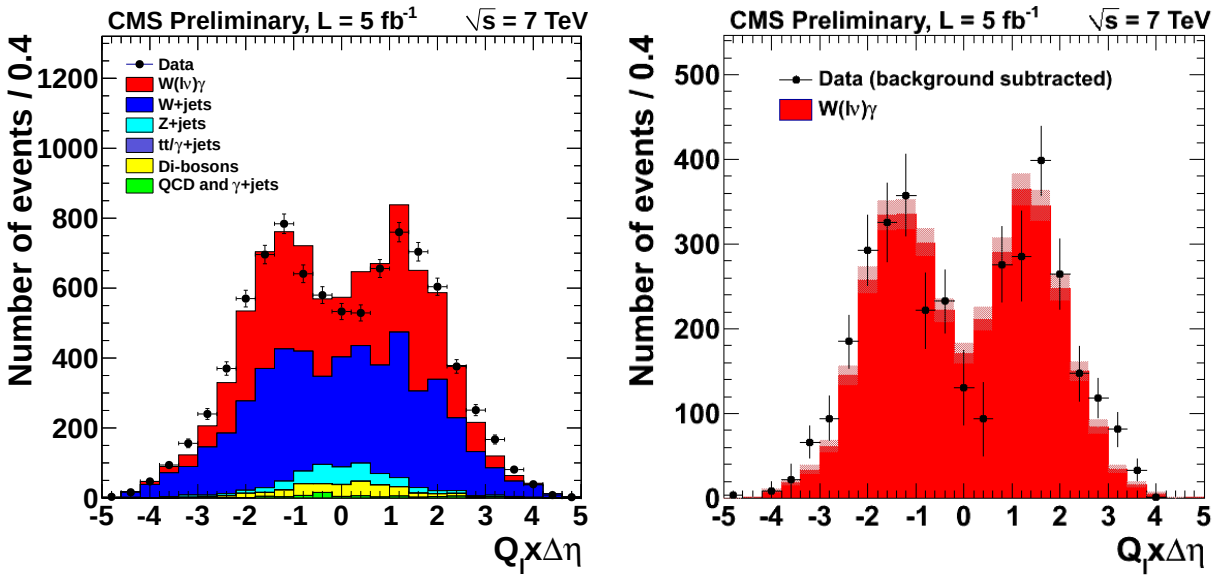

Slika 9.29: $Q_l \times \Delta\eta$ raspodjele dobivene kombiniranjem elektronskog i mionskog kanala za događaje koji zadovoljavaju $W\gamma \to l\nu\gamma$ selekciju za simulirane (histogrami) i mjerene događaje (točke) za uzorak 2011A+2011B. Broj simuliranih događaja u signalu skaliran je na mjereni broj događaja u signalu. Na desnoj raspodjeli oduzet je doprinos pozadine. Pogreške uključuju statističke i sistematske pogreške.

9.6 Trostuka baždarna vezanja

9.6.1 Statistički uvod

Jedan od efekata anomalnih trostrukih baždarnih vezanja je povećanje $W\gamma$ udarnog presjeka na velikim vrijednostima energije partona u sudaru $\hat{s}$. Rezultat je povećan broj događaja s bozonima s velikom količinom gibanja. Pošto je količina gibanja fotona opservabla osjetljiva na aTGC, raspodjela E_{T}^{γ} u području $E_{\mathrm{T}}^{\gamma} > 40$ GeV-a korištena je za mjerenje aTGC parametara. Postavljene su gornje granice na vrijednosti aTGC parametara uspoređujući mjerenu E_{T}^{γ} raspodjelu sa odgovarajućom E_{T}^{γ} raspodjelom simuliranom za različite vrijednosti aTGC parametara.

Vjerojatnost mjerenja N događaja uz očekivani broj događaja d dana je Poissonovom raspodjelom:

$$p(N;d) = \frac{d^N e^{-d}}{N!} \tag{9.48}$$

d je zbroj signala i pozadine koji su neovisno modelirani:

$$d = \mu \cdot \mathbf{s}(\vec{\alpha}, \vec{\theta}_s, \vec{\theta_{\mathscr{L}}}) + \mathbf{b}(\vec{\theta}_b), \tag{9.49}$$

gdje su vrijednosti signala $\mathbf{s}(\vec{\alpha}, \vec{\theta}_s, \vec{\theta_{\mathscr{L}}})$ i pozadine $\mathbf{b}(\vec{\theta}_b)$ određene s vrijednostima aTGC parametara $\vec{\alpha}$ i odgovarajućim pogrešakama signala $\vec{\theta}_s$, integriranog luminoziteta $\vec{\theta_{\mathscr{L}}}$, i pozadine $\vec{\theta}_b$. Parametar μ je tzv. jačina signala. aTGC signal dobiven je iz simulacije dok je pozadina određena iz podataka i simulacije kao što je opisano u paragrafu 9.4.3.

Vrijednosti signala i pozadine izražene su kao:

$$\mathbf{s}(\vec{\alpha}, \vec{\theta}_s, \vec{\theta_{\mathscr{L}}}) = f_{\mathscr{L}} \cdot f_{Sig}^{\mathrm{Syst}} \cdot N^{\mathrm{Sig}}(\vec{\alpha}), \tag{9.50}$$

$$\mathbf{b}(\vec{\theta}_b) = f_{Bkg}^{\mathrm{Syst}} \cdot N^{\mathrm{Bkg}}. \tag{9.51}$$

Ovdje su N^{Sig} i N^{Bkg} očekivani srednji broj događaja signala i pozadine, $f_{\mathscr{L}}$ je relativna vrijednost pogreške na integrirani luminozitet, f_{Sig}^{Syst} relativna pogreška na signal i f_{Bkg}^{Syst} relativna pogreška na pozadinu. Za pogreške je pretpostavljena log-normalna raspodjela.

Za svaki bin u E_{T}^{γ} raspodjeli s brojem mjerenja N_i funkcija vjerojatnosti definirana je kao produkt:

$$\mathrm{L}(\mu, \vec{\alpha}, \vec{\theta}) = \prod_i p(N_i, d_i(\mu, \vec{\alpha}, \vec{\theta})), \tag{9.52}$$

sa Poisson raspodjelom p definiranom u 9.48 i:

$$\vec{\theta} = (\vec{\theta}_s, \vec{\theta}_b). \tag{9.53}$$

Granice na aTGC parametre postavljene su korištenjem varijable:

$$t_{\mu,\vec{\alpha}} = -2\ln\lambda(\mu, \vec{\alpha}) \tag{9.54}$$

gdje je $\lambda(\mu, \vec{\alpha})$ definiran kao:

$$\lambda(\mu, \vec{\alpha}) = \frac{\mathrm{L}(\mu, \vec{\alpha}, \hat{\hat{\vec{\theta}}})}{\mathrm{L}(\hat{\mu}, \vec{\alpha}, \hat{\hat{\vec{\theta}}})}. \tag{9.55}$$

$\hat{\hat{\vec{\theta}}}$ je najvjerojatniji estimator od $\vec{\theta}$ za dani μ, a $\hat{\mu}$ i $\hat{\hat{\vec{\theta}}}$ su najvjerojatnini estimatori od μ i $\vec{\theta}$.

Hipoteza s određenom aTGC vrijednošću se isključuje ako je omjer p-vrijednosti:

$$CL_s = \frac{p_{s+b}}{1 - p_b} \tag{9.56}$$

manji od unaprijed zadane vrijednosti. Više detalja nalazi se u [37].

Tablica 9.13: Jednodimenzionalne 95% C.L. mjerene granice na parametre $WW\gamma$ vezanja uključujući kombinirane rezultate za elektronski i mionski kanal.

	$\Delta\kappa^{\gamma}$	λ^{γ}
$W\gamma \rightarrow e\nu\gamma$	[-0.45,0.37]	[-0.059,0.046]
$W\gamma \rightarrow \mu\nu\gamma$	[-0.46,0.34]	[-0.057,0.046]
$W\gamma \rightarrow l\nu\gamma$	[-0.38,0.29]	[-0.050,0.037]

9.6.2 Simulacija signala

aTGC signal simuliran je sa SHERPA [3] generatorom dok je za simulaciju $W\gamma$+n mlazeva (n ≤ 1) procesa u detektoru korišten PYTHIA [4] generator. Dva aTGC parametra, $\Delta\kappa_{\gamma}$ i λ_{γ}, varirana su dok je za g_1^Z parametar korištena vrijednost predviđena Standardnim modelom.

9.6.3 Rezultati

Slika 9.30 prikazuje raspodjelu transverzalne mase fotona E_{T}^{γ} u podacima i simulaciji te očekivani izgled signala za vrijednosti aTGC parametara $\Delta\kappa_{\gamma} = 0.4$ i $\lambda_{\gamma} = 0.0$.

Podaci ne pokazuju značajno odstupanje od očekivanja SM-a. Kako aTGC signal nije opažen postavljene su gornje granice na vrijednosti aTGC parametara. Dvodimenzionalne 95% C.L. granice prikazane su na Slici 9.31. Pripadajuće jednodimenzionalne granice prikazane su na Slikama 9.32 i 9.33 te u Tablici 9.13.

9.6.4 Kombinacija rezultata s elektronskim kanalom

Kao i kod mjerenja udarnog presjeka, mjerenje aTGC parametara osim u mionskom izvršeno je i u elektronskom kanalu. Rezultati dobiveni kombiniranjem dvaju kanala prikazani su na Slikama 9.34- 9.36 i u Tablici 9.13.

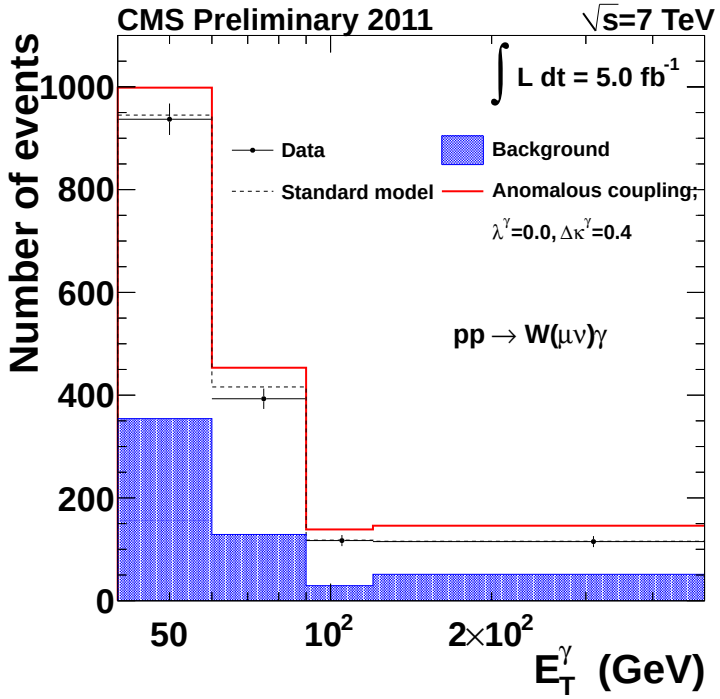

Slika 9.30: Raspodjela transverzalne mase fotona (E_{T}^{γ}) za događaje koji zadovoljavaju $W\gamma \to \mu\nu\gamma$ selekciju za pozadinu (puni histogram), simulirane $W\gamma$ događaje (crni isprekidani histogram), simulirani aTGC signal za vrijednosti parametara $\Delta\kappa^{\gamma} = 0.4$ i $\lambda_{\gamma} = 0.0$ (crveni histogram) i mjerene događaje (točke) za uzorak 2011A+2011B. Posljednji bin uključuje događaje s velikim E_{T}^{γ} vrijednostima.

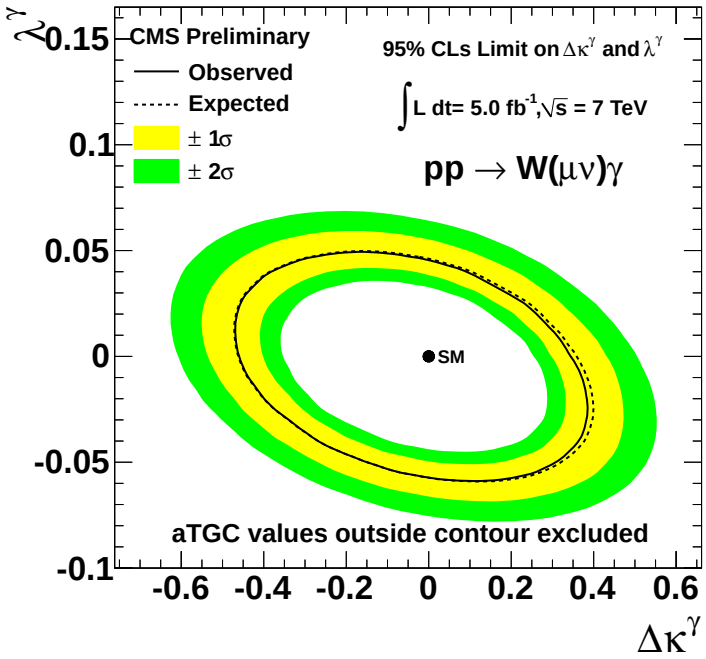

Slika 9.31: Dvodimenzionalne 95% C.L. očekivane i mjerene granice na parametre $WW\gamma$ vezanja.

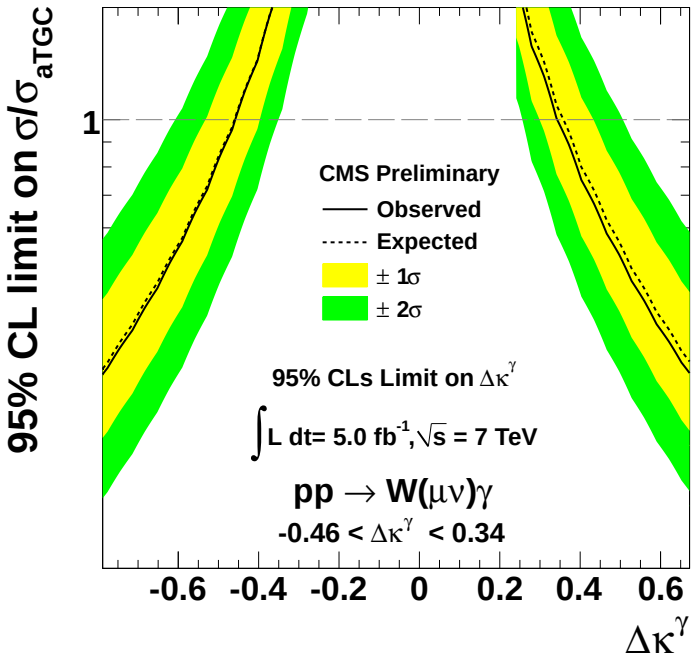

Slika 9.32: Jednodimenzionalne 95% C.L. očekivane i mjerene granice na parametar $\Delta\kappa^{\gamma}$ $WW\gamma$ vezanja.

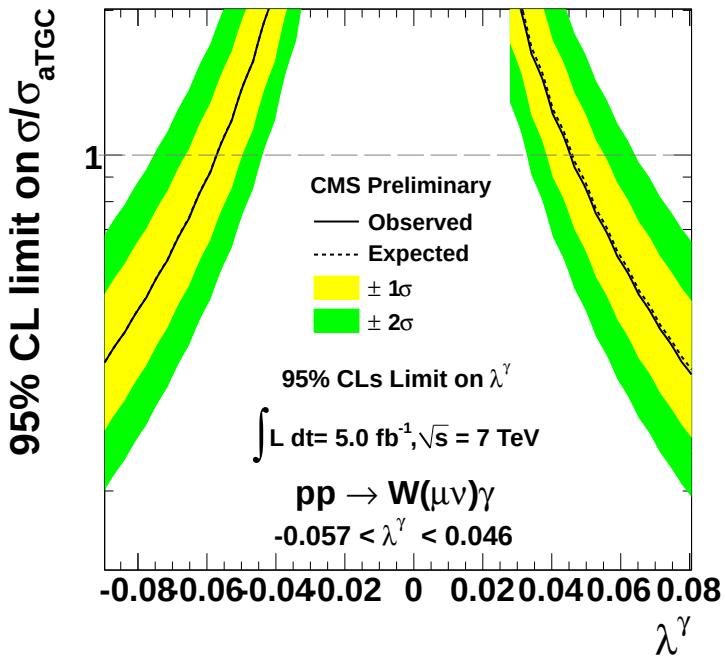

Slika 9.33: Jednodimenzionalne 95% C.L. očekivane i mjerene granice na parametar λ_γ $WW\gamma$ vezanja.

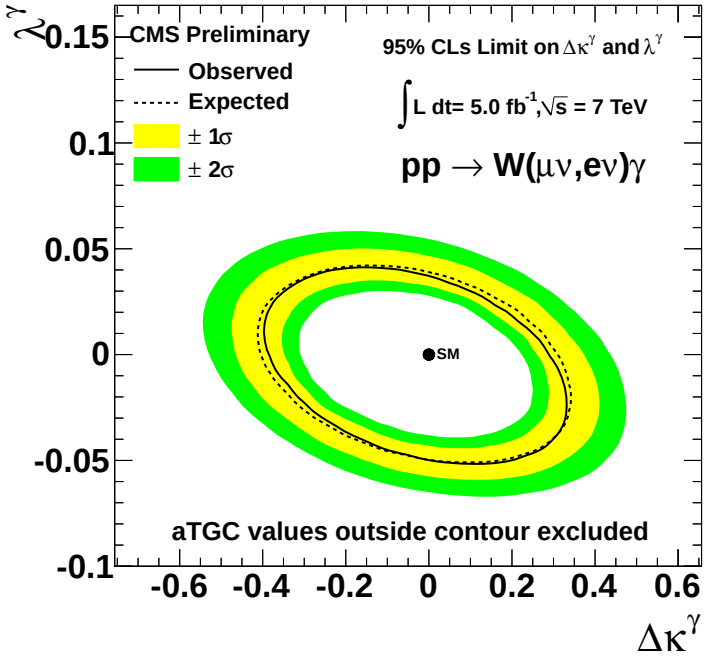

Slika 9.34: Dvodimenzionalne 95% C.L. očekivane i mjerene granice na parametre $WW\gamma$ vezanja. Kombinirani rezultati za elektronski i mionski kanal.

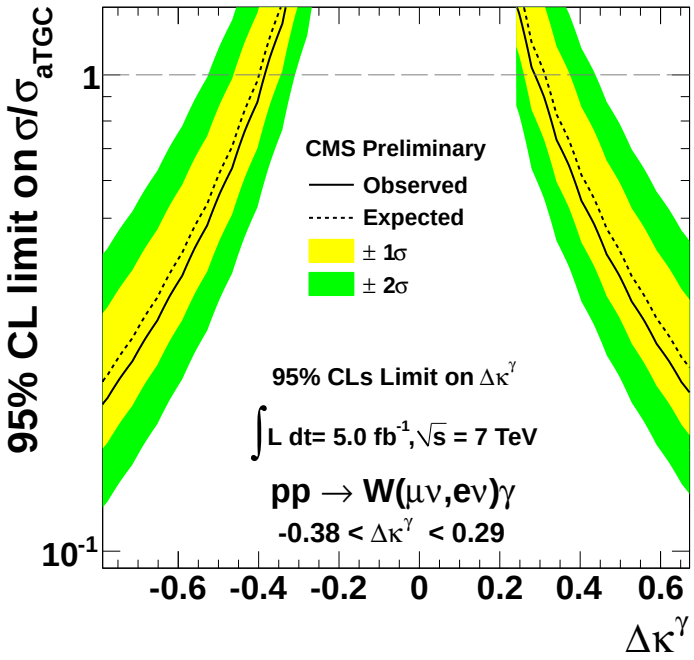

Slika 9.35: Jednodimenzionalne 95% C.L. očekivane i mjerene granice na parametar $\Delta\kappa^{\gamma}$ $WW\gamma$ vezanja. Kombinirani rezultati za elektronski i mionski kanal.

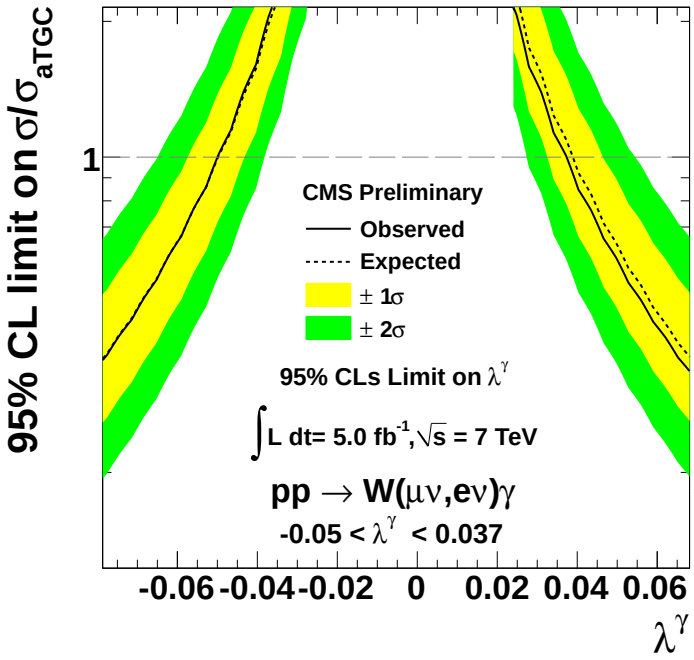

Slika 9.36: Jednodimenzionalne 95% C.L. očekivane i mjerene granice na parametar λ^{γ} $WW\gamma$ vezanja. Kombinirani rezultati za elektronski i mionski kanal.

9.7 Usporedba s drugim rezultatima

Drugi detektor opće namjene na LHC-u, ATLAS, također je mjerio $W\gamma$ proces u proton-proton sudarima na 7 TeV-a. Rezultati objavljeni 2012. godine na podacima integriranog luminoziteta 1 fb^{-1} [38], dobiveni su za dva različita mjerenja, inkluzivno i ekskluzivno. Pri mjerenju ekskluzivnog udarnog presjeka iz analize su isključeni događaji koji sadrže barem jedan mlaz trnsverzalnog impulsa $p_T^{mlaz} > 30$ GeV-a. Udarni presjek mjeren je u faznom prostoru $p_T^l > 25$ GeV-a, $p_T^\nu > 25$ GeV-a, $|\eta^l| < 2.47, E_T^\gamma > 15/60/100$ GeV-a, $|\eta^\gamma| < 2.37$. Rezultati mjerenja prikazani su na Slici 9.37. Nedavno objavljeni novi ATLAS rezultati s podacima od 5 fb^{-1} [39] prikazani su na Slici 9.38.

Rezultati ATLAS eksperimenta, kao i rezultati dobiveni u ovom radu, pokazuju značajno odstupanje od teorijskih predviđanja MCFM generatora u slučaju inkluzivnog udarnog presjeka $W\gamma$ na višim vrijednostima E_T^γ. Drugi generatori kao što je na primjer Sherpa [3] pokazuju bolje slaganje s podacima.

Mjerenje aTGC parametara u ATLAS eksperimentu provedeno je na drugačiji način od mjerenja provedenog u CMS eksperimentu. Umjesto E_T^γ raspodjele za postavljanje granica na aTGC parametre korišten je ukupan broj događaja selektiran kao signal u području transverzalne energije $E_T^\gamma > 100$ GeV-a. Mjerenje je izvršeno koristeći inkluzivne, a ne ekskluzivne događaje. Jednodimenzionalne granice na aTGC parametre koristeći podatke integriranog luminoziteta $1 fb^{-1}$ i $5 fb^{-1}$ prikazane su u Tablici 9.14 i Slici 9.39. Kao i u CMS eksperimentu nije uočen aTGC signal, stoga su postavljene gornje granice na vrijednosti parametara.

Tablica 9.14: Jednodimenzionalne 95% C.L. granice na parametre $WW\gamma$ vezanja ATLAS eksperimenta, dobivene analizom podataka integriranog luminoziteta $1 fb^{-1}$.

	Measured	Measured	Expected
Λ	2 TeV	∞	∞
$\Delta\kappa_\gamma$	[-0.36, 0.41]	[-0.33, 0.37]	[-0.33, 0.36]
λ_γ	[-0.079, 0.074]	[-0.060, 0.060]	[-0.063, -0.055]

Mjerenja $W\gamma$ procesa provedena su također i na Tevatronu, u proton-antiproton sudarima na energiji sustava centra mase $\sqrt{s} = 1.96$ TeV-a. Eksperimenti $D0$ i CDF objavili su više članaka [40, 41, 42,

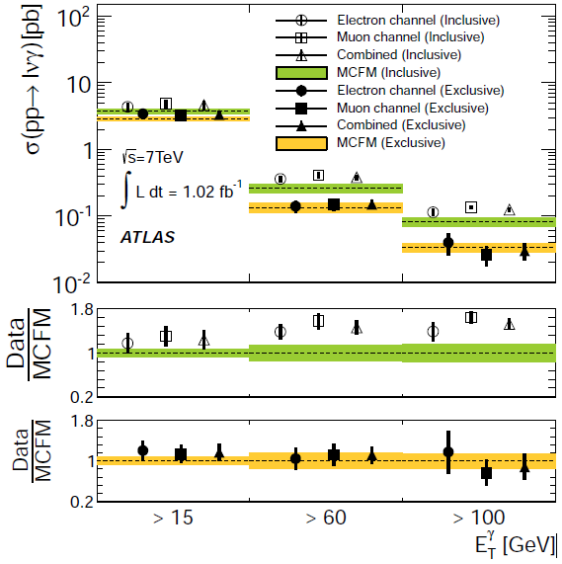

Slika 9.37: Rezultati mjerenja $W\gamma$ udarnog presjeka ATLAS detektorom koristeći podatke koji odgovaraju integriranom luminozitetu 1 fb^{-1}.

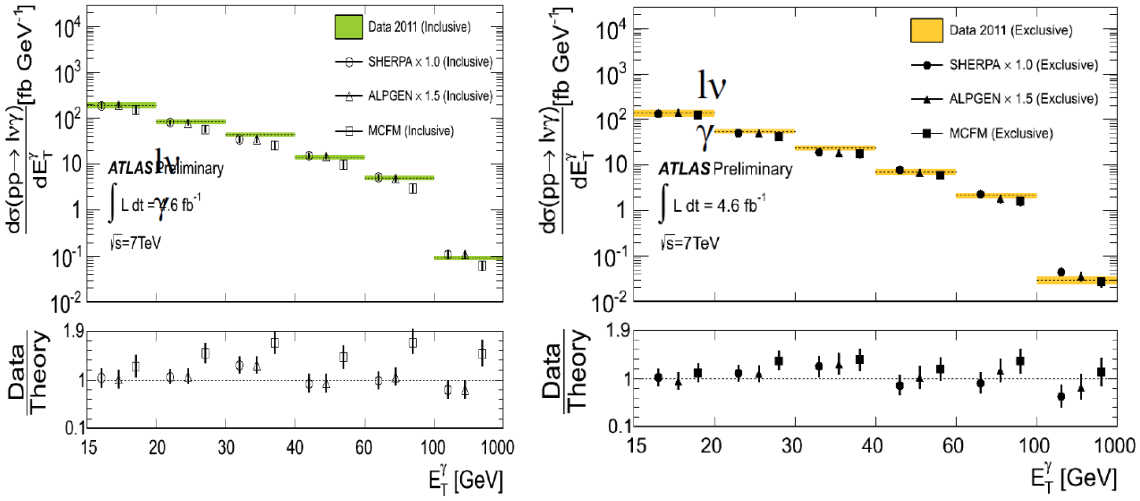

Slika 9.38: Rezultati inkluzivnog (lijevo) i ekskluzivnog (desno) mjerenja $W\gamma$ udarnog presjeka ATLAS detektorom koristeći podatke koji odgovaraju integriranom luminozitetu 5 fb^{-1}.

43] koji uključuju mjerenja udarnog presjeka i aTGC parametara. Mjerenja inkluzivnog udarnog presjeka u dobrom su slaganju s NLO očekivanjima. Na Tevatron energijama NLO korekcije su mnogo manje nego na LHC energijama. Članak [41] uključuje i opažanje RAZ signala.

Elektron-pozitron sudarivač na CERN-u, LEP, također je mjerio produkciju parova bozona. Na nižoj energiji u sustavu centra mase od $\sqrt{s} \leq 209$ GeV-a također su postavljene granice na aTGC parametre. Pregled aTGC rezultata iz različitih eksperimenata nalazi se u Tablici 9.15 i na Slici 9.40. Rezultati mjerenja na različitim enegijama kao i rezultati u kojima je korišten ili nije korišten form-faktor ne mogu se direktno usporediti.

Tablica 9.15: Rezultati mjerenja aTGC parametara u različitim eksperimentima.

	ATLAS ($1 fb^{-1}$ data) ($\sqrt{s} = 7$ TeV)	D0 (korišten form-faktor) ($\sqrt{s} = 1.96$ TeV)	LEP (kombinirano) (68% CL) ($\sqrt{s} \leq 209$ GeV)	CMS (ovaj rad) ($\sqrt{s} = 7$ TeV)
$\Delta\kappa_\gamma$	[-0.33, 0.37]	[-0.29, 0.38]	[-0.072, 0.017]	[-0.38, 0.29]
λ_γ	[-0.060, 0.060]	[-0.08, 0.08]	[-0.049, -0.008]	[-0.050, 0.037]

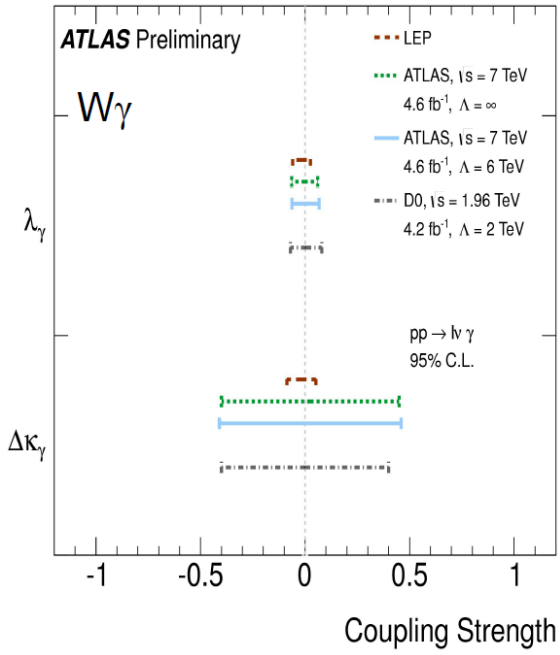

Slika 9.39: Jednodimenzionalne 95% C.L. granice na parametre $WW\gamma$ vezanja ATLAS eksperimenta. Rezultati su prikazani za mjerenje koristeći podatke integriranog luminoziteta $5fb^{-1}$.

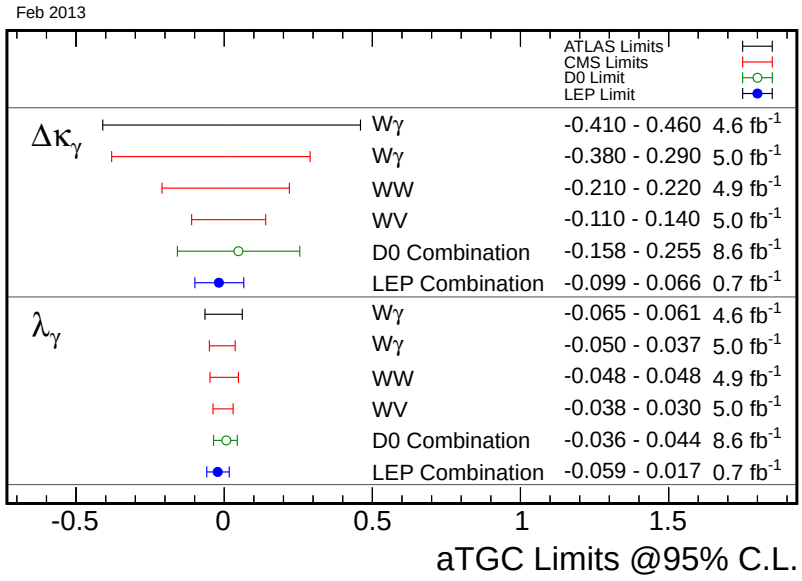

Slika 9.40: Rezultati mjerenja aTGC parametara u različitim eksperimentima.

9.8 Zaključak

U ovom radu prezentirani su rezultati mjerenja inkluzivnog udarnog presjeka $W\gamma \to \mu\nu\gamma$ koristeći podatke prikupljene CMS detektorom integriranog luminoziteta 5.0 fb^{-1}. Mjereni udarni presjek, 37.5 ± 0.9 (stat.) ± 4.4 (syst.) ± 0.8 (lumi.) pb, u slaganju je s mjerenjem u elektronskom kanalu $W\gamma \to e\nu\gamma$ te je za jednu standardnu devijaciju veći od predviđanja MCFM generatora. Nedavno objavljeni rezultati ATLAS eksperimenta također pokazuju veći inkluzivni udarni presjek od predviđenog MCFM generatora dok je ekskluzivno mjerenje u sukladu s očekivanjima. Ovi rezultati pokazuju da je NLO korekcija podcjenjena u izračunu MCFM generatora.

Efekt radijacijske amplitude vrijednosti nula uočen je u raspodjeli $Q_l \times \Delta\eta$ nakon primjene dodatne selekcije u kojoj se zahtjeva 0 hadronoskih mlazeva i visoka transverzalna masa sustava $\mu\nu\gamma$ u $W\gamma \to \mu\nu\gamma$ događaju.

U podacima nema vidljivog signala kao posljedice anomalnih trostrukih baždarnih vezanja, stoga su postavljene gornje granice na vrijednosti parametara $\Delta\kappa^\gamma$ i λ_γ. Jednodimenzionalne 95% C.L. granice, $-0.46 < \Delta\kappa^\gamma < 0.34$ i $-0.057 < \lambda^\gamma < 0.046$, u slaganju su s mjerenjima ATLAS eksperimenta.

Bibliography

[1] Particle Data Group Collaboration. Review of Particle Physics. *J. Phys.*, G37:075021, 2010.

[2] U. Baur, S. Errede, G. L. Landsberg. Rapidity correlations in $w\gamma$ production at hadron colliders. *Phys.Rev.*, D50:1917, 1994.

[3] T. Gleisberg et al. Event generation with sherpa 1.1. *JHEP*, 02:007, 2009.

[4] T. Sjostrand, S. Mrenna, and P. Skands. Pythia 6.4 physics and manual. *JHEP*, 05:026, 2006.

[5] S. Weinberg. A Model of Leptons. *Phys. Rev. Lett.*, 19:1264–1266, 1967.

[6] Steven Weinberg. *The Quantum Theory of Fields (Volume 1)*. Cambridge University Press, 1995.

[7] Peter W. Higgs. Spontaneous Symmetry Breakdown without Massless Bosons. *Phys.Rev.*, 145:1156–1163, 1966.

[8] F. Englert and R. Brout. Broken symmetry and the mass of gauge vector mesons. *Phys.Rev.Lett.*, 13:321–323, 1964.

[9] G. S. Guralnik, C. R. Hagen, and T. W. B. Kibble. Global Conservation Laws and Massless Particles. *Phys.Rev.Lett.*, 13:585–587, 1964.

[10] R. W. Brown et al. $W^{\pm}Z$ and $W^{\pm}\gamma$ Pair Production in Neutrino e, p p, and anti-p p Collisions. *Phys.Rev.*, D20:1164, 1979.

[11] K. O. Mikaelian et al. The Magnetic Moment of Weak Bosons Produced in p p and p anti-p Collisions. *Phys.Rev.Lett.*, 43:746, 1979.

[12] C. L. Bilchak, R. W. Brown and J. Stroughair. W and z polarization in pair production: Dominant helicities. *Phys.Rev.*, D29:375, 1984.

[13] CMS Collaboration. Measurement of the Differential Cross Section for Isolated Prompt Photon Production in pp Collisions at 7 TeV. *Phys.Rev.*, D84:052011, 2011.

[14] S. Martin. A supersymmetry primer. 1997.

[15] K. Hagiwara, R.D. Peccei, and D. Zeppenfeld. Probing the weak boson sector in $e^+e^- \rightarrow W^+W^-$. *Nucl. Phys.*, B282:253, 1987.

[16] K. Hagiwara, J. Woodside, and D. Zeppenfeld. Measuring the WWZ coupling at the Tevatron. *Phys. Rev.*, D41:2113, 1990.

[17] L. R. Evans and P. Bryant. LHC Machine. *JINST 3*, S08001:164, 2008.

[18] CMS Collaboration. The CMS experiment at the CERN LHC. *JINST*, 3:S08004, 2008.

[19] CMS Collaboration. Performance of CMS muon reconstruction in pp collision events at $\sqrt{s}$ = 7 TeV. 2012.

[20] Anderson, M. et al. Review of clustering algorithms and energy corrections in ECAL. 2008.

[21] CMS Collaboration. Particle-flow commissioning with muons and electrons from J/Psi, and W events at 7 TeV. *CMS PAS*, PFT-2010-003, 2010.

[22] . Metropolis and S. Ulam. The Monte Carlo Method. *Journal of the American Statistical Association 44*, 247:335, 1949.

[23] A. Moraes, C. Buttar, and I. Dawson. Prediction for minimum bias and the underlying event at lhc energies. *Eur. Phys. J.*, C50:435–466, 2007.

[24] S. Agostinelli et al. Geant4 — a simulation toolkit. *Nuclear Instruments and Methods in Physics Research Section A: Accelerators, Spectrometers, Detectors and Associated Equipment*, 506:250–303, 2003.

[25] J. Allison et al. Geant4 developments and applications. *Nuclear Science, IEEE Transactions on*, 53:270–278, 2006.

[26] J. Alcaraz Maestre *et al.* Updated measurements of the inclusive W and Z cross sections at 7 TeV. *CMS Note*, 2010/264, 2010.

[27] Matteo Cacciari. FastJet: A Code for fast k_t clustering, and more. pages 487–490, 2006.

[28] Kyle S. Cranmer. Kernel estimation in high-energy physics. *Comput. Phys. Commun.*, 136:198–207, 2001.

[29] CMS Collaboration. Missing transverse energy performance of the CMS detector. *JINST 6*, 09001, 2011.

[30] D Bourilkov, R C Group, and M R Whalley. LHAPDF: PDF use from the Tevatron to the LHC. 2006.

[31] J. Pumplin, D.R. Stump, J. Huston, H.L. Lai, Pavel M. Nadolsky, et al. New generation of parton distributions with uncertainties from global QCD analysis. *JHEP*, 0207:012, 2002.

[32] J.M. Campbell, J.W. Huston, W.J. Stirling. Hard interactions of quarks and gluons: a primer for lhc physics. *Rept.Prog.Phys*, 70:89, 2007.

[33] The CMS Collaboration. Absolute Calibration of the Luminosity Measurement at CMS : Winter 2012 Update. 2012.

[34] J.M. Campbell, R.K. Ellis, and C. Williams. Vector boson pair production at the LHC. *JHEP*, 1107:018, 2011.

[35] L. Lyons, G. Gibaut, and P. Clifford. How to combine correlated estimates of a single physical quantity. *Nucl. Instrum. Meth.*, A270:110, 1988.

[36] M. Cacciari, G. P. Salam, G. Soyez. The anti-kt jet clustering algorithm. *JHEPpa*, 0804:063, 2008.

[37] G. Cowan, K. Cranmer, E. Gross, O. Vitells. Asymptotic formulae for likelihood-based tests of new physics. *Eur.Phys.J.*, C71:1554, 2011.

[38] ATLAS Collaboration. Measurement of $w\gamma$ and $z\gamma$ production cross sections in pp collisions at $\sqrt{s} = 7$ tev and limits on anomalous triple couplings with the atlas detector. *Phys. Lett.*, B701:535, 2012.

[39] ATLAS Collaboration. Measurements of Wgamma and Zgamma production in pp collisions at sqrts= 7 TeV with the ATLAS detector at the LHC. 2013.

[40] D0 Collaboration. Measurement of $p\bar{p} \rightarrow W\gamma + X$ cross section at $\sqrt{s} = 1.96$ TeV and $WW\gamma$ anomalous coupling limits. *Phys. Rev.*, D71:091108, 2005.

[41] D0 Collaboration. First study of radiation-amplitude zero in $W\gamma$ production and limits on anomalous $WW\gamma$ couplings at $\sqrt{s} = 1.96$ TeV. *Phys. Rev. Lett.*, 100:241805, 2008.

[42] D0 Collaboration. Combined measurements of anomalous charged trilinear gauge-boson couplings from diboson production in p-pbar collisions at $\sqrt{(s)} = 1.96$ TeV. 2009.

[43] D0 Collaboration. Wγ production and limits on anomalous WWγ couplings in $p\bar{p}$ collisions. *Phys. Rev. Lett.*, 107:241803, 2011.

Curriculum vitae

Senka ĐURIĆ

Date and place of birth:	June 2 1982 in Čakovec, Croatia
Citizenship:	Croatian
Gender:	Female
Address:	Ruđer Bošković Institute Bijenička cesta 54, P.O.Box 180 10002 Zagreb (Croatia)
Telephone:	+385 1 457 1317
Mobile:	+385 95 80 93 785
E-mail:	senka.duric@cern.ch
Languages:	Fluent English; Basic German; Mother tongue Croatian

EDUCATION

2008. -	PhD studies, expecting to finish in May 2013. Department of Physics, Faculty of Science, University of Zagreb, Croatia Thesis title: "Measurement of associated $W\gamma$ production and search for anomalous $WW\gamma$ couplings with the CMS detector" Thesis advisors: Dr. Vuko Brigljević and Dr. Krešo Kadija 2001. - 2007.
Master studies	
	Department of Physics, Faculty of Science, University of Zagreb, Croatia Diploma thesis title: "Triple boson gauge couplings at LHC" Diploma thesis advisor: Dr. Vuko Brigljević
1997. - 2001.	Gymnasium school in Čakovec, Croatia

RESEARCH EXPERIENCE

From June 2007: Research assistant at the Ruđer Bošković Institute, Zagreb, Croatia in the group of dr. Krešo Kadija and dr. Vuko Brigljević, working on electroweak measurements at the CMS experiment at CERN (where I spent approximately 1.5 years in total)

- One of main contributors to $W\gamma$ cross section and triple gauge boson coupling measurement on the full 2011 data set. Measurement was done in collaboration with dr. Yurii Maravin, dr. Chia Ming Kuo and dr. Vuko Brigljević.
- Contribution to WW triple gauge boson coupling measurement.
- One of main contributors to $W\gamma$ triple gauge boson coupling measurement using the full 2010 data set.
- Contribution to WZ cross section measurement preparation using simulations.
- Contribution to the central on-line CMS data quality monitoring by performing several weeks of shifts per year.
- Cosmic muon analysis to estimate rates of cosmic muons accepted by the muon reconstruction used in proton-proton collisions. Summer Student Program (2005.) at CERN
- Working on alignment system for muon chambers on ATLAS detector.

AWARDS AND RECOGNITIONS

- Grant for PhD student project from the National science foundation of Croatia (2012.) to work at CERN on measurement of triple gauge coupling and $W\gamma$ cross section with CMS detector
- Member of graduate student counsel at Ruđer Bošković Institute (2007.-2010.)
- Rector's award (2005.) from the University of Zagreb for the best student research work for "Coalescence model application for Θ^{+} and Φ^{--} pentaquarks production in protonproton collisions at 17.3 GeV".

OTHER ACTIVITIES AND RESPONSIBILITIES

- Teaching assistant at CMSDASia, CMS Data Analysis School, Taipei, Taiwan (2012.)
- Popularisation of science:

  Lectures, articles and discussions to primary and high school pupils

  Set up an experiment to demonstrate cosmic rays for Ruđer Bošković Institute Open Days (2010., 2008.)

COMPUTING EXPERIENCE

- Knowledge of programming languages (C++, ROOT), Unix/Linux/Windows environment.

TALKS AT CONFERENCES

- Talk on “Diboson Physics at CMS” at “Results and Perspectives in Particle Physics” conference, La Thuile, Italy (2013.)

ATTENDED CONFERENCES

- "LHC days", Split, Croatia (2010.)
- "Physics at LHC", Split, Croatia (2008.)
- International Conference for Physics Students, Odense, Denmark (2003.)
- International meteor conference, Frombork, Poland (2002.)

PUBLICATIONS

1. **“Multiplicity and transverse-momentum dependence of two- and four-particle correlations in pPb and PbPb collisions”**
   S. Chatrchyan *et al.* [CMS Collaboration].
   arXiv:1305.0609 [nucl-ex]

2. **“Searches for long-lived charged particles in pp collisions at sqrt(s)=7 and 8 TeV”**
   S. Chatrchyan *et al.* [CMS Collaboration].
   arXiv:1305.0491 [hep-ex]

3. **“Measurement of the ratio of the inclusive 3-jet cross section to the inclusive 2-jet cross section in pp collisions at $\sqrt{s}$ = 7 TeV and first determination of the strong coupling constant in the TeV range”**
   S. Chatrchyan *et al.* [CMS Collaboration].
   arXiv:1304.7498 [hep-ex]

4. **“Measurement of the Lambda(b)0 lifetime in pp collisions at sqrt(s) = 7 TeV”**
   S. Chatrchyan *et al.* [CMS Collaboration].
   arXiv:1304.7495 [hep-ex]

5. **“Measurement of masses in the $t\bar{t}$ system by kinematic endpoints in pp collisions at $\sqrt{s}$=7 TeV”**
   S. Chatrchyan *et al.* [CMS Collaboration].
   arXiv:1304.5783 [hep-ex]

6. **“Search for a standard-model-like Higgs boson with a mass of up to 1 TeV at the LHC”**
   S. Chatrchyan *et al.* [CMS Collaboration].
   arXiv:1304.0213 [hep-ex]

7. **"Measurement of the Y(1S), Y(2S), and Y(3S) cross sections in pp collisions at $\sqrt{s}$ = 7 TeV"**
S. Chatrchyan *et al.* [CMS Collaboration].
arXiv:1303.5900 [hep-ex]

8. **"Search for microscopic black holes in pp collisions at sqrt(s) = 8 TeV"**
S. Chatrchyan *et al.* [CMS Collaboration].
arXiv:1303.5338 [hep-ex]

9. **"Studies of jet mass in dijet and W/Z+jet events"**
S. Chatrchyan *et al.* [CMS Collaboration].
arXiv:1303.4811 [hep-ex]

10. **"Observation of a new boson with mass near 125 GeV in pp collisions at sqrt(s) = 7 and 8 TeV"**
S. Chatrchyan *et al.* [CMS Collaboration].
arXiv:1303.4571 [hep-ex]

11. **"A new boson with a mass of 125-GeV observed with the CMS experiment at the Large Hadron Collider"**
S. Chatrchyan *et al.* [CMS Collaboration].
10.1126/science.1230816
Science **338**, 1569 (2012).

12. **"Measurement of associated production of vector bosons and top quark-antiquark pairs at sqrt(s) = 7 TeV"**
S. Chatrchyan *et al.* [CMS Collaboration].
arXiv:1303.3239 [hep-ex]
10.1103/PhysRevLett.110.172002
Phys. Rev. Lett. **110**, 172002 (2013)

13. **"Search for supersymmetry in hadronic final states with missing transverse energy using the variables α_T and b-quark multiplicity in pp collisions at $\sqrt{s}$ = 8 TeV"**
S. Chatrchyan *et al.* [CMS Collaboration].
arXiv:1303.2985 [hep-ex]

14. **"Search for the standard model Higgs boson produced in association with a top-quark pair in pp collisions at the LHC"**
S. Chatrchyan *et al.* [CMS Collaboration].
arXiv:1303.0763 [hep-ex]

15. **"Search for narrow resonances using the dijet mass spectrum in pp collisions at sqrt(s) = 8 TeV"**
S. Chatrchyan *et al.* [CMS Collaboration].
arXiv:1302.4794 [hep-ex]

16. **"Measurement of the X(3872) production cross section via decays to J/psi pi pi in pp collisions at sqrt(s) = 7 TeV"**
S. Chatrchyan *et al.* [CMS Collaboration].
arXiv:1302.3968 [hep-ex]

17. **"Search for a Higgs boson decaying into a b-quark pair and produced in association with b quarks in proton-proton collisions at 7 TeV"**
S. Chatrchyan *et al.* [CMS Collaboration].
arXiv:1302.2892 [hep-ex]

18. **"Search for new physics in final states with a lepton and missing transverse energy in pp collisions at the LHC"**
S. Chatrchyan *et al.* [CMS Collaboration].
arXiv:1302.2812 [hep-ex]
10.1103/PhysRevD.87.072005
Phys. Rev. D **87**, 072005 (2013)

19. **"Study of the underlying event at forward rapidity in pp collisions at $\sqrt{s}$ = 0.9, 2.76, and 7 TeV"**
S. Chatrchyan *et al.* [CMS Collaboration].
arXiv:1302.2394 [hep-ex]
10.1007/JHEP04(2013)072
JHEP **1304**, 072 (2013)

20. **"Searches for Higgs bosons in pp collisions at sqrt(s) = 7 and 8 TeV in the context of four-generation and fermiophobic models"**
S. Chatrchyan *et al.* [CMS Collaboration].
arXiv:1302.1764 [hep-ex]

21. **"Search for pair-produced dijet resonances in four-jet final states in pp collisions at sqrt(s) = 7 TeV"**
S. Chatrchyan *et al.* [CMS Collaboration].
arXiv:1302.0531 [hep-ex]
10.1103/PhysRevLett.110.141802
Phys. Rev. Lett. **110**, 141802 (2013)

22. **"Measurement of the ttbar production cross section in the all-jet final state in pp collisions at sqrt(s) = 7 TeV"**
S. Chatrchyan *et al.* [CMS Collaboration].
arXiv:1302.0508 [hep-ex]

23. **"Measurement of the top-antitop production cross section in the tau+jets channel in pp collisions at sqrt(s) = 7 TeV"**
S. Chatrchyan *et al.* [CMS Collaboration].
arXiv:1301.5755 [hep-ex]

24. **"Search for contact interactions using the inclusive jet pT spectrum in pp collisions at sqrt(s) = 7 TeV"**
S. Chatrchyan *et al.* [CMS Collaboration].
arXiv:1301.5023 [hep-ex]
10.1103/PhysRevD.87.052017
Phys. Rev. D **87**, 052017 (2013)

25. **"Measurement of W+W- and ZZ production cross sections in pp collisions at sqrt(s) = 8 TeV"**

S. Chatrchyan *et al.* [CMS Collaboration].
arXiv:1301.4698 [hep-ex]
10.1016/j.physletb.2013.03.027
Phys. Lett. B **721**, 190 (2013)

26. **"Search for physics beyond the standard model in events with tau leptons, jets, and large transverse momentum imbalance in pp collisions at sqrt(s) = 7 TeV"**
S. Chatrchyan *et al.* [CMS Collaboration].
arXiv:1301.3792 [hep-ex]

27. **"Interpretation of searches for supersymmetry with simplified models"**
S. Chatrchyan *et al.* [CMS Collaboration].
arXiv:1301.2175 [hep-ex]

28. **"Event shapes and azimuthal correlations in Z + jets events in pp collisions at $\sqrt{s} = 7$ TeV"**
S. Chatrchyan *et al.* [CMS Collaboration].
arXiv:1301.1646 [hep-ex]

29. **"Search for supersymmetry in events with opposite-sign dileptons and missing transverse energy using an artificial neural network"**
S. Chatrchyan *et al.* [CMS Collaboration].
arXiv:1301.0916 [hep-ex]
10.1103/PhysRevD.87.072001
Phys. Rev. D **87**, 072001 (2013)

30. **"Search for supersymmetry in pp collisions at $\sqrt{s} = 7$ TeV in events with a single lepton, jets, and missing transverse momentum"**
S. Chatrchyan *et al.* [CMS Collaboration].
arXiv:1212.6428 [hep-ex]

31. **"On the mass and spin-parity of the Higgs boson candidate via its decays to Z boson pairs"**
S. Chatrchyan *et al.* [CMS Collaboration].
arXiv:1212.6639 [hep-ex]

Phys. Rev. Lett. **110**, 081803 (2013)

32. **"Measurements of differential jet cross sections in proton-proton collisions at $\sqrt{s} = 7$ TeV with the CMS detector"**
S. Chatrchyan *et al.* [CMS Collaboration].
arXiv:1212.6660 [hep-ex]

33. **"Measurement of the $t\bar{t}$ production cross section in pp collisions at $\sqrt{s} = 7$ TeV with lepton + jets final states"**
S. Chatrchyan *et al.* [CMS Collaboration].
arXiv:1212.6682 [hep-ex]
10.1016/j.physletb.2013.02.021
Phys. Lett. B **720**, 83 (2013)

34. **"Inclusive search for supersymmetry using the razor variables in pp collisions at $\sqrt{s} = 7$ TeV"**
S. Chatrchyan *et al.* [CMS Collaboration].
arXiv:1212.6961 [hep-ex]

35. **"Search for new physics in events with same-sign dileptons and b jets in pp collisions at $\sqrt{s} = 8$ TeV"**
S. Chatrchyan *et al.* [CMS Collaboration].
arXiv:1212.6194 [hep-ex]
10.1007/JHEP03(2013)037
JHEP **1303**, 037 (2013)

36. **"Search for heavy narrow dilepton resonances in pp collisions at $\sqrt{s} = 7$ TeV and $\sqrt{s} = 8$ TeV"**
S. Chatrchyan *et al.* [CMS Collaboration].
arXiv:1212.6175 [hep-ex]
10.1016/j.physletb.2013.02.003
Phys. Lett. B **720**, 63 (2013)

37. **"Search for contact interactions in opposite-sign dimuon events in pp collisions at $\sqrt{s} = 7$ TeV"**
S. Chatrchyan *et al.* [CMS Collaboration].
arXiv:1212.4563 [hep-ex]
10.1103/PhysRevD.87.032001
Phys. Rev. D **87**, 032001 (2013)

38. **"Search for heavy resonances in the W/Z-tagged dijet mass spectrum in pp collisions at 7 TeV"**
S. Chatrchyan *et al.* [CMS Collaboration].
arXiv:1212.1910 [hep-ex]

39. **"Search for long-lived particles decaying to photons and missing energy in proton-proton collisions at $\sqrt{s} = 7$ TeV"**
S. Chatrchyan *et al.* [CMS Collaboration].
arXiv:1212.1838 [hep-ex]

40. **"Search for exotic resonances decaying into WZ/ZZ in pp collisions at $\sqrt{s} = 7$ TeV"**
S. Chatrchyan *et al.* [CMS Collaboration].
arXiv:1211.5779 [hep-ex]
10.1007/JHEP02(2013)036
JHEP **1302**, 036 (2013)

41. **"Measurement of the ZZ production cross section and search for anomalous couplings in 2 l2l ' final states in pp collisions at $\sqrt{s} = 7$ TeV"**
S. Chatrchyan *et al.* [CMS Collaboration].
arXiv:1211.4890 [hep-ex]
10.1007/JHEP01(2013)063
JHEP **1301**, 063 (2013)

42. **"Search for new physics in events with photons, jets, and missing transverse energy in pp collisions at $\sqrt{s} = 7$ TeV"**
S. Chatrchyan *et al.* [CMS Collaboration].
arXiv:1211.4784 [hep-ex]
10.1007/JHEP03(2013)111
JHEP **1303**, 111 (2013)

43. **"Identification of b-quark jets with the CMS experiment"**
S. Chatrchyan *et al.* [CMS Collaboration].
arXiv:1211.4462 [hep-ex]
10.1088/1748-0221/8/04/P04013
JINST **8**, P04013 (2013)

44. **"Search for Z ' resonances decaying to $t\bar{t}$ in dilepton+jets final states in pp collisions at $\sqrt{s} = 7$ TeV"**
S. Chatrchyan *et al.* [CMS Collaboration].
arXiv:1211.3338 [hep-ex]
10.1103/PhysRevD.87.072002
Phys. Rev. D **87**, 072002 (2013)

45. **"Search for supersymmetry in final states with a single lepton, b-quark jets, and missing transverse energy in proton-proton collisions at $\sqrt{s} = 7$ TeV"**
S. Chatrchyan *et al.* [CMS Collaboration].
arXiv:1211.3143 [hep-ex]
10.1103/PhysRevD.87.052006
Phys. Rev. D **87**, 052006 (2013)

46. **"Search in leptonic channels for heavy resonances decaying to long-lived neutral particles"**
S. Chatrchyan *et al.* [CMS Collaboration].
arXiv:1211.2472 [hep-ex]
10.1007/JHEP02(2013)085
JHEP **1302**, 085 (2013)

47. **"Measurement of differential top-quark pair production cross sections in pp colisions at $\sqrt{s} = 7$ TeV"**
S. Chatrchyan *et al.* [CMS Collaboration].
arXiv:1211.2220 [hep-ex]
10.1140/epjc/s10052-013-2339-4
Eur. Phys. J. C **73**, 2339 (2013)

48. **"Search for supersymmetry in final states with missing transverse energy and 0, 1, 2, or at least 3 b-quark jets in 7 TeV pp collisions using the variable alphaT"**
S. Chatrchyan *et al.* [CMS Collaboration].
arXiv:1210.8115 [hep-ex]
10.1007/JHEP01(2013)077
JHEP **1301**, 077 (2013)

49. **"Search for a non-standard-model Higgs boson decaying to a pair of new light bosons in four-muon final states"**

S. Chatrchyan *et al.* [CMS Collaboration].
arXiv:1210.7619 [hep-ex]

50. **"Measurement of the sum of WW and WZ production with $W+$dijet events in pp collisions at $\sqrt{s} = 7$ TeV"**
S. Chatrchyan *et al.* [CMS Collaboration].
arXiv:1210.7544 [hep-ex]
10.1140/epjc/s10052-013-2283-3
Eur. Phys. J. C **73**, 2283 (2013)

51. **"Search for heavy quarks decaying into a top quark and a W or Z boson using lepton + jets events in pp collisions at $\sqrt{s} = 7$ TeV"**
S. Chatrchyan *et al.* [CMS Collaboration].
arXiv:1210.7471 [hep-ex]

JHEP **01**, 154 (2013)

52. **"Measurement of the inelastic proton-proton cross section at $\sqrt{s} = 7$ TeV"**
S. Chatrchyan *et al.* [CMS Collaboration].
arXiv:1210.6718 [hep-ex]
10.1016/j.physletb.2013.03.024
Phys. Lett. B **722**, 5 (2013)

53. **"Search for pair production of third-generation leptoquarks and top squarks in pp collisions at $\sqrt{s} = 7$ TeV"**
S. Chatrchyan *et al.* [CMS Collaboration].
arXiv:1210.5629 [hep-ex]
10.1103/PhysRevLett.110.081801
Phys. Rev. Lett. **110**, 081801 (2013)

54. **"Search for third-generation leptoquarks and scalar bottom quarks in pp collisions at $\sqrt{s} = 7$ TeV"**
S. Chatrchyan *et al.* [CMS Collaboration].
arXiv:1210.5627 [hep-ex]
10.1007/JHEP12(2012)055
JHEP **1212**, 055 (2012)

55. **"Observation of long-range near-side angular correlations in proton-lead collisions at the LHC"**
S. Chatrchyan *et al.* [CMS Collaboration].
arXiv:1210.5482 [nucl-ex]
10.1016/j.physletb.2012.11.025
Phys. Lett. B **718**, 795 (2013)

56. **"Observation of Z decays to four leptons with the CMS detector at the LHC"**
S. Chatrchyan *et al.* [CMS Collaboration].
arXiv:1210.3844 [hep-ex]
10.1007/JHEP12(2012)034
JHEP **1212**, 034 (2012)

57. **"Search for excited leptons in pp collisions at $\sqrt{s} = 7$ TeV"**
S. Chatrchyan *et al.* [CMS Collaboration].
arXiv:1210.2422 [hep-ex]
10.1016/j.physletb.2013.02.031
Phys. Lett. B **720**, 309 (2013)

58. **"Search for heavy neutrinos and W[R] bosons with right-handed couplings in a left-right symmetric model in pp collisions at sqrt(s) = 7 TeV"**
S. Chatrchyan *et al.* [CMS Collaboration].
arXiv:1210.2402 [hep-ex]
10.1103/PhysRevLett.109.261802
Phys. Rev. Lett. **109**, 261802 (2012)

59. **"Search for narrow resonances and quantum black holes in inclusive and b-tagged dijet mass spectra from pp collisions at $\sqrt{s} = 7$ TeV"**
S. Chatrchyan *et al.* [CMS Collaboration].
arXiv:1210.2387 [hep-ex]
10.1007/JHEP01(2013)013
JHEP **1301**, 013 (2013)

60. **"Search for fractionally charged particles in pp collisions at $\sqrt{s} = 7$ TeV"**
S. Chatrchyan *et al.* [CMS Collaboration].
arXiv:1210.2311 [hep-ex]

61. **"Search for supersymmetry in events with photons and low missing transverse energy in pp collisions at $\sqrt{s} = 7$ TeV"**
S. Chatrchyan *et al.* [CMS Collaboration].
arXiv:1210.2052 [hep-ex]
10.1016/j.physletb.2012.12.055
Phys. Lett. B **719**, 42 (2013)

62. **"Search for heavy lepton partners of neutrinos in proton-proton collisions in the context of the type III seesaw mechanism"**
S. Chatrchyan *et al.* [CMS Collaboration].
arXiv:1210.1797 [hep-ex]
10.1016/j.physletb.2012.10.070
Phys. Lett. B **718**, 348 (2012)

63. **"Measurement of the relative prompt production rate of chi(c2) and chi(c1) in pp collisions at $\sqrt{s} = 7$ TeV"**
S. Chatrchyan *et al.* [CMS Collaboration].
arXiv:1210.0875 [hep-ex]
10.1140/epjc/s10052-012-2251-3
Eur. Phys. J. C **72**, 2251 (2012)

64. **"Search for anomalous production of highly boosted Z bosons decaying to dimuons in pp collisions at $\sqrt{s} = 7$ TeV"**
S. Chatrchyan *et al.* [CMS Collaboration].
arXiv:1210.0867 [hep-ex]

10.1016/j.physletb.2013.03.037
Phys. Lett. B **722**, 28 (2013)

65. **"Search for electroweak production of charginos and neutralinos using leptonic final states in pp collisions at $\sqrt{s} = 7$ TeV"**
S. Chatrchyan *et al.* [CMS Collaboration].
arXiv:1209.6620 [hep-ex]
10.1007/JHEP11(2012)147
JHEP **1211**, 147 (2012)

66. **"Measurement of the single-top-quark t-channel cross section in pp collisions at $\sqrt{s} = 7$ TeV"**
S. Chatrchyan *et al.* [CMS Collaboration].
arXiv:1209.4533 [hep-ex]
10.1007/JHEP12(2012)035
JHEP **1212**, 035 (2012)

67. **"Search for resonant $t\bar{t}$ production in lepton+jets events in pp collisions at $\sqrt{s} = 7$ TeV"**
S. Chatrchyan *et al.* [CMS Collaboration].
arXiv:1209.4397 [hep-ex]
10.1007/JHEP12(2012)015
JHEP **1212**, 015 (2012)

68. **"Search for the standard model Higgs boson produced in association with W and Z bosons in pp collisions at $\sqrt{s} = 7$ TeV"**
S. Chatrchyan *et al.* [CMS Collaboration].
arXiv:1209.3937 [hep-ex]
10.1007/JHEP11(2012)088
JHEP **1211**, 088 (2012)

69. **"Search for a narrow spin-2 resonance decaying to a pair of Z vector bosons in the semileptonic final state"**
S. Chatrchyan *et al.* [CMS Collaboration].
arXiv:1209.3807 [hep-ex]
10.1016/j.physletb.2012.11.063
Phys. Lett. B **718**, 1208 (2013)

70. **"Evidence for associated production of a single top quark and W boson in pp collisions at 7 TeV"**
S. Chatrchyan *et al.* [CMS Collaboration].
arXiv:1209.3489 [hep-ex]
10.1103/PhysRevLett.110.022003
Phys. Rev. Lett.

71. **"Measurement of the Y1S, Y2S and Y3S polarizations in pp collisions at $\sqrt{s} = 7$ TeV"**
S. Chatrchyan *et al.* [CMS Collaboration].
arXiv:1209.2922 [hep-ex]
10.1103/PhysRevLett.110.081802
Phys. Rev. Lett.

72. **"Measurement of the top-quark mass in $t\bar{t}$ events with dilepton final states in pp collisions at $\sqrt{s} = 7$ TeV"**
S. Chatrchyan *et al.* [CMS Collaboration].
arXiv:1209.2393 [hep-ex]
10.1140/epjc/s10052-012-2202-z
Eur. Phys. J. C **72**, 2202 (2012)

73. **"Measurement of the top-quark mass in $t\bar{t}$ events with lepton+jets final states in pp collisions at $\sqrt{s} = 7$ TeV"**
S. Chatrchyan *et al.* [CMS Collaboration].
arXiv:1209.2319 [hep-ex]
10.1007/JHEP12(2012)105
JHEP **1212**, 105 (2012)

74. **"Observation of a diffractive contribution to dijet production in proton-proton collisions at $\sqrt{s} = 7$ TeV"**
S. Chatrchyan *et al.* [CMS Collaboration].
arXiv:1209.1805 [hep-ex]
10.1103/PhysRevD.87.012006
Phys. Rev. D **87**, 012006 (2013)

75. **"Search for exclusive or semi-exclusive photon pair production and observation of exclusive and semi-exclusive electron pair production in pp collisions at $\sqrt{s} = 7$ TeV"**
S. Chatrchyan *et al.* [CMS Collaboration].
arXiv:1209.1666 [hep-ex]
10.1007/JHEP11(2012)080
JHEP **1211**, 080 (2012)

76. **"Combined search for the quarks of a sequential fourth generation"**
S. Chatrchyan *et al.* [CMS Collaboration].
arXiv:1209.1062 [hep-ex]
10.1103/PhysRevD.86.112003
Phys. Rev. D **86**, 112003 (2012)

77. **"Search for pair produced fourth-generation up-type quarks in pp collisions at $\sqrt{s} = 7$ TeV with a lepton in the final state"**
S. Chatrchyan *et al.* [CMS Collaboration].
arXiv:1209.0471 [hep-ex]
10.1016/j.physletb.2012.10.038
Phys. Lett. B **718**, 307 (2012)

78. **"Search for supersymmetry in events with b-quark jets and missing transverse energy in pp collisions at 7 TeV"**
S. Chatrchyan *et al.* [CMS Collaboration].
arXiv:1208.4859 [hep-ex]
10.1103/PhysRevD.86.072010
Phys. Rev. D **86**, 072010 (2012)

79. **"Study of the dijet mass spectrum in $pp \to W+$ jets events at $\sqrt{s} = 7$ TeV"**
S. Chatrchyan *et al.* [CMS Collaboration].

arXiv:1208.3477 [hep-ex]
10.1103/PhysRevLett.109.251801
Phys. Rev. Lett. **109**, 251801 (2012)

80. **"Search for three-jet resonances in pp collisions at $\sqrt{s} = 7$ TeV"**
S. Chatrchyan *et al.* [CMS Collaboration].
arXiv:1208.2931 [hep-ex]
10.1016/j.physletb.2012.10.048
Phys. Lett. B **718**, 329 (2012)

81. **"Observation of sequential Upsilon suppression in PbPb collisions"**
S. Chatrchyan *et al.* [CMS Collaboration].
arXiv:1208.2826 [nucl-ex]
10.1103/PhysRevLett.109.222301
Phys. Rev. Lett. **109**, 222301 (2012)

82. **"Measurement of the $t\bar{t}$ production cross section in the dilepton channel in pp collisions at $\sqrt{s} = 7$ TeV"**
S. Chatrchyan *et al.* [CMS Collaboration].
arXiv:1208.2671 [hep-ex]
10.1007/JHEP11(2012)067
JHEP **1211**, 067 (2012)

83. **"Measurement of the azimuthal anisotropy of neutral pions in PbPb collisions at $\sqrt{s_{NN}} = 2.76$ TeV"**
S. Chatrchyan *et al.* [CMS Collaboration].
arXiv:1208.2470 [nucl-ex]

84. **"Search for flavor changing neutral currents in top quark decays in pp collisions at 7 TeV"**
S. Chatrchyan *et al.* [CMS Collaboration].
arXiv:1208.0957 [hep-ex]
10.1016/j.physletb.2012.12.045
Phys. Lett. B **718**, 1252 (2013)

85. **"Search for a W ' boson decaying to a bottom quark and a top quark in pp collisions at $\sqrt{s} = 7$ TeV"**
S. Chatrchyan *et al.* [CMS Collaboration].
arXiv:1208.0956 [hep-ex]
10.1016/j.physletb.2012.12.008
Phys. Lett. B **718**, 1229 (2013)

86. **"Observation of a new boson at a mass of 125 GeV with the CMS experiment at the LHC"**
S. Chatrchyan *et al.* [CMS Collaboration].
arXiv:1207.7235 [hep-ex]
10.1016/j.physletb.2012.08.021
Phys. Lett. B **716**, 30 (2012)

87. **"Search for heavy Majorana neutrinos in $\mu^+\mu^+[\mu^-\mu^-]$ and $e^+e^+[e^-e^-]$ events in pp collisions at $\sqrt{s} = 7$ TeV"**
S. Chatrchyan *et al.* [CMS Collaboration].
arXiv:1207.6079 [hep-ex]
10.1016/j.physletb.2012.09.012
Phys. Lett. B **717**, 109 (2012)

88. **"Search for pair production of first- and second-generation scalar leptoquarks in pp collisions at $\sqrt{s} = 7$ TeV"**
S. Chatrchyan *et al.* [CMS Collaboration].
arXiv:1207.5406 [hep-ex]
10.1103/PhysRevD.86.052013
Phys. Rev. D **86**, 052013 (2012)

89. **"Study of the inclusive production of charged pions, kaons, and protons in pp collisions at $\sqrt{s} = 0.9$, 2.76, and 7 TeV"**
S. Chatrchyan *et al.* [CMS Collaboration].
arXiv:1207.4724 [hep-ex]
10.1140/epjc/s10052-012-2164-1
Eur. Phys. J. C **72**, 2164 (2012)

90. **"Forward-backward asymmetry of Drell-Yan lepton pairs in pp collisions at $\sqrt{s} = 7$ TeV"**
S. Chatrchyan *et al.* [CMS Collaboration].
arXiv:1207.3973 [hep-ex]
10.1016/j.physletb.2012.10.082
Phys. Lett. B **718**, 752 (2013)

91. **"A search for a doubly-charged Higgs boson in pp collisions at $\sqrt{s} = 7$ TeV"**
S. Chatrchyan *et al.* [CMS Collaboration].
arXiv:1207.2666 [hep-ex]
10.1140/epjc/s10052-012-2189-5
Eur. Phys. J. C **72**, 2189 (2012)

92. **"Measurement of the underlying event activity in pp collisions at $\sqrt{s} = 0.9$ and 7 TeV with the novel jet-area/median approach"**
S. Chatrchyan *et al.* [CMS Collaboration].
arXiv:1207.2392 [hep-ex]
10.1007/JHEP08(2012)130
JHEP **1208**, 130 (2012)

93. **"Search for new physics in the multijet and missing transverse momentum final state in proton-proton collisions at $\sqrt{s} = 7$ TeV"**
S. Chatrchyan *et al.* [CMS Collaboration].
arXiv:1207.1898 [hep-ex]
10.1103/PhysRevLett.109.171803
Phys. Rev. Lett. **109**, 171803 (2012)

94. **"Search for supersymmetry in hadronic final states using MT2 in pp collisions at $\sqrt{s} = 7$ TeV"**

S. Chatrchyan *et al.* [CMS Collaboration].
arXiv:1207.1798 [hep-ex]
10.1007/JHEP10(2012)018
JHEP **1210**, 018 (2012)

95. **"Search for a fermiophobic Higgs boson in pp collisions at $\sqrt{s} = 7$ TeV"**
S. Chatrchyan *et al.* [CMS Collaboration].
arXiv:1207.1130 [hep-ex]
10.1007/JHEP09(2012)111
JHEP **1209**, 111 (2012)

96. **"Search for new physics with long-lived particles decaying to photons and missing energy in pp collisions at $\sqrt{s} = 7$ TeV"**
S. Chatrchyan *et al.* [CMS Collaboration].
arXiv:1207.0627 [hep-ex]
10.1007/JHEP11(2012)172
JHEP **1211**, 172 (2012)

97. **"Search for stopped long-lived particles produced in pp collisions at $\sqrt{s} = 7$ TeV"**
S. Chatrchyan *et al.* [CMS Collaboration].
arXiv:1207.0106 [hep-ex]
10.1007/JHEP08(2012)026
JHEP **1208**, 026 (2012)

98. **"Inclusive and differential measurements of the $t\bar{t}$ charge asymmetry in proton-proton collisions at 7 TeV"**
S. Chatrchyan *et al.* [CMS Collaboration].
arXiv:1207.0065 [hep-ex]
10.1016/j.physletb.2012.09.028
Phys. Lett. B **717**, 129 (2012)

99. **"Search for a light pseudoscalar Higgs boson in the dimuon decay channel in pp collisions at $\sqrt{s} = 7$ TeV"**
S. Chatrchyan *et al.* [CMS Collaboration].
arXiv:1206.6326 [hep-ex]
10.1103/PhysRevLett.109.121801
Phys. Rev. Lett. **109**, 121801 (2012)

100. **"Search for dark matter and large extra dimensions in monojet events in pp collisions at $\sqrt{s} = 7$ TeV"**
S. Chatrchyan *et al.* [CMS Collaboration].
arXiv:1206.5663 [hep-ex]
10.1007/JHEP09(2012)094
JHEP **1209**, 094 (2012)

101. **"Performance of CMS muon reconstruction in pp collision events at $\sqrt{s} = 7$ TeV"**
S. Chatrchyan *et al.* [CMS Collaboration].
arXiv:1206.4071 [physics.ins-det]
10.1088/1748-0221/7/10/P10002
JINST **7**, P10002 (2012)

102. **"Search for new physics in events with opposite-sign leptons, jets, and missing transverse energy in pp collisions at $\sqrt{s} = 7$ TeV"**
S. Chatrchyan *et al.* [CMS Collaboration].
arXiv:1206.3949 [hep-ex]
10.1016/j.physletb.2012.11.036
Phys. Lett. B **718**, 815 (2013)

103. **"Search for charge-asymmetric production of W ' bosons in top pair + jet events from pp collisions at $\sqrt{s} = 7$ TeV"**
S. Chatrchyan *et al.* [CMS Collaboration].
arXiv:1206.3921 [hep-ex]
10.1016/j.physletb.2012.09.048
Phys. Lett. B **717**, 351 (2012)

104. **"Measurement of the electron charge asymmetry in inclusive W production in pp collisions at $\sqrt{s} = 7$ TeV"**
S. Chatrchyan *et al.* [CMS Collaboration].
arXiv:1206.2598 [hep-ex]
10.1103/PhysRevLett.109.111806
Phys. Rev. Lett. **109**, 111806 (2012)

105. **"Search for narrow resonances in dilepton mass spectra in pp collisions at $\sqrt{s} = 7$ TeV"**
S. Chatrchyan *et al.* [CMS Collaboration].
arXiv:1206.1849 [hep-ex]
10.1016/j.physletb.2012.06.051
Phys. Lett. B **714**, 158 (2012)

106. **"Search for high mass resonances decaying into τ^- lepton pairs in pp collisions at $\sqrt{s} = 7$ TeV"**
S. Chatrchyan *et al.* [CMS Collaboration].
arXiv:1206.1725 [hep-ex]
10.1016/j.physletb.2012.07.062
Phys. Lett. B **716**, 82 (2012)

107. **"Search for a W' or Techni-ρ Decaying into WZ in pp Collisions at $\sqrt{s} = 7$ TeV"**
S. Chatrchyan *et al.* [CMS Collaboration].
arXiv:1206.0433 [hep-ex]
10.1103/PhysRevLett.109.141801
Phys. Rev. Lett. **109**, 141801 (2012)

108. **"Search for new physics with same-sign isolated dilepton events with jets and missing transverse energy"**
S. Chatrchyan *et al.* [CMS Collaboration].
arXiv:1205.6615 [hep-ex]
10.1103/PhysRevLett.109.071803
Phys. Rev. Lett. **109**, 071803 (2012)

109. **"Study of W boson production in PbPb and pp collisions at $\sqrt{s_{NN}} = 2.76$ TeV"**
S. Chatrchyan *et al.* [CMS Collaboration].

arXiv:1205.6334 [nucl-ex]
10.1016/j.physletb.2012.07.025
Phys. Lett. B **715**, 66 (2012)

110. **"Measurement of jet fragmentation into charged particles in pp and PbPb collisions at $\sqrt{s_{NN}} = 2.76$ TeV"**
S. Chatrchyan *et al.* [CMS Collaboration].
arXiv:1205.5872 [nucl-ex]
10.1007/JHEP10(2012)087
JHEP **1210**, 087 (2012)

111. **"Search for a light charged Higgs boson in top quark decays in pp collisions at $\sqrt{s} = 7$ TeV"**
S. Chatrchyan *et al.* [CMS Collaboration].
arXiv:1205.5736 [hep-ex]
10.1007/JHEP07(2012)143
JHEP **1207**, 143 (2012)

112. **"Search for new physics in events with same-sign dileptons and b-tagged jets in pp collisions at $\sqrt{s} = 7$ TeV"**
S. Chatrchyan *et al.* [CMS Collaboration].
arXiv:1205.3933 [hep-ex]
10.1007/JHEP08(2012)110
JHEP **1208**, 110 (2012)

113. **"Measurement of the pseudorapidity and centrality dependence of the transverse energy density in PbPb collisions at $\sqrt{s_{NN}} = 2.76$ TeV"**
S. Chatrchyan *et al.* [CMS Collaboration].
arXiv:1205.2488 [nucl-ex]
10.1103/PhysRevLett.109.152303
Phys. Rev. Lett. **109**, 152303 (2012)

114. **"Measurement of the $Lambda_b$ cross section and the $\bar{\Lambda}(\ b^{)}$ to $Lambda_b$ ratio with $Lambda_b$ to J/Psi Λ decays in pp collisions at $\sqrt{s} = 7$ TeV"**
S. Chatrchyan *et al.* [CMS Collaboration].
arXiv:1205.0594 [hep-ex]
10.1016/j.physletb.2012.05.063
Phys. Lett. B **714**, 136 (2012)

115. **"Search for heavy long-lived charged particles in pp collisions at $\sqrt{s} = 7$ TeV"**
S. Chatrchyan *et al.* [CMS Collaboration].
arXiv:1205.0272 [hep-ex]
10.1016/j.physletb.2012.06.023
Phys. Lett. B **713**, 408 (2012)

116. **"Studies of jet quenching using isolated-photon+jet correlations in PbPb and pp collisions at $\sqrt{s_{NN}} = 2.76$ TeV"**
S. Chatrchyan *et al.* [CMS Collaboration].
arXiv:1205.0206 [nucl-ex]

10.1016/j.physletb.2012.11.003
Phys. Lett. B **718**, 773 (2013)

117. **"Observation of a new Xi(b) baryon"**
S. Chatrchyan *et al.* [CMS Collaboration].
arXiv:1204.5955 [hep-ex]
10.1103/PhysRevLett.108.252002
Phys. Rev. Lett. **108**, 252002 (2012)

118. **"Search for anomalous production of multilepton events in pp collisions at $\sqrt{s} = 7$ TeV"**
S. Chatrchyan *et al.* [CMS Collaboration].
arXiv:1204.5341 [hep-ex]
10.1007/JHEP06(2012)169
JHEP **1206**, 169 (2012)

119. **"Search for leptonic decays of W ' bosons in pp collisions at $\sqrt{s} = 7$ TeV"**
S. Chatrchyan *et al.* [CMS Collaboration].
arXiv:1204.4764 [hep-ex]
10.1007/JHEP08(2012)023
JHEP **1208**, 023 (2012)

120. **"Search for physics beyond the standard model in events with a Z boson, jets, and missing transverse energy in pp collisions at $\sqrt{s} = 7$ TeV"**
S. Chatrchyan *et al.* [CMS Collaboration].
arXiv:1204.3774 [hep-ex]
10.1016/j.physletb.2012.08.026
Phys. Lett. B **716**, 260 (2012)

121. **"Shape, transverse size, and charged hadron multiplicity of jets in pp collisions at 7 TeV"**
S. Chatrchyan *et al.* [CMS Collaboration].
arXiv:1204.3170 [hep-ex]
10.1007/JHEP06(2012)160
JHEP **1206**, 160 (2012)

122. **"Measurement of the mass difference between top and antitop quarks"**
S. Chatrchyan *et al.* [CMS Collaboration].
arXiv:1204.2807 [hep-ex]
10.1007/JHEP06(2012)109
JHEP **1206**, 109 (2012)

123. **"Search for anomalous t t-bar production in the highly-boosted all-hadronic final state"**
S. Chatrchyan *et al.* [CMS Collaboration].
arXiv:1204.2488 [hep-ex]
10.1007/JHEP09(2012)029
JHEP **1209**, 029 (2012)

124. **"Azimuthal anisotropy of charged particles at high transverse momenta in PbPb collisions at $\sqrt{s_{NN}} = 2.76$ TeV"**
S. Chatrchyan *et al.* [CMS Collaboration].

arXiv:1204.1850 [nucl-ex]
10.1103/PhysRevLett.109.022301
Phys. Rev. Lett. **109**, 022301 (2012)

125. **"Measurement of the Z/gamma*+b-jet cross section in pp collisions at 7 TeV"**
S. Chatrchyan *et al.* [CMS Collaboration].
arXiv:1204.1643 [hep-ex]
10.1007/JHEP06(2012)126
JHEP **1206**, 126 (2012)

126. **"Measurement of the elliptic anisotropy of charged particles produced in PbPb collisions at nucleon-nucleon center-of-mass energy = 2.76 TeV"**
S. Chatrchyan *et al.* [CMS Collaboration].
arXiv:1204.1409 [nucl-ex]
10.1103/PhysRevC.87.014902
Phys. Rev. C **87**, 014902 (2013)

127. **"Measurement of the underlying event in the Drell-Yan process in proton-proton collisions at $\sqrt{s} = 7$ TeV"**
S. Chatrchyan *et al.* [CMS Collaboration].
arXiv:1204.1411 [hep-ex]
10.1140/epjc/s10052-012-2080-4
Eur. Phys. J. C **72**, 2080 (2012)

128. **"Search for heavy bottom-like quarks in 4.9 inverse femtobarns of pp collisions at $\sqrt{s} = 7$ TeV"**
S. Chatrchyan *et al.* [CMS Collaboration].
arXiv:1204.1088 [hep-ex]
10.1007/JHEP05(2012)123
JHEP **1205**, 123 (2012)

129. **"Search for Dark Matter and Large Extra Dimensions in pp Collisions Yielding a Photon and Missing Transverse Energy"**
S. Chatrchyan *et al.* [CMS Collaboration].
arXiv:1204.0821 [hep-ex]
10.1103/PhysRevLett.108.261803
Phys. Rev. Lett. **108**, 261803 (2012)

130. **"Ratios of dijet production cross sections as a function of the absolute difference in rapidity between jets in proton-proton collisions at $\sqrt{s} = 7$ TeV"**
S. Chatrchyan *et al.* [CMS Collaboration].
arXiv:1204.0696 [hep-ex]
10.1140/epjc/s10052-012-2216-6
Eur. Phys. J. C **72**, 2216 (2012)

131. **"Measurement of the top quark pair production cross section in pp collisions at $\sqrt{s} = 7$ TeV in dilepton final states containing a τ"**
S. Chatrchyan *et al.* [CMS Collaboration].
arXiv:1203.6810 [hep-ex]

10.1103/PhysRevD.85.112007
Phys. Rev. D **85**, 112007 (2012)

132. **"Search for heavy, top-like quark pair production in the dilepton final state in pp collisions at $\sqrt{s} = 7$ TeV"**
S. Chatrchyan *et al.* [CMS Collaboration].
arXiv:1203.5410 [hep-ex]
10.1016/j.physletb.2012.07.059
Phys. Lett. B **716**, 103 (2012)

133. **"Search for $B_s^0 to \mu^+ \mu^-$ and $B^0 to \mu^+ \mu^-$ decays"**
S. Chatrchyan *et al.* [CMS Collaboration].
arXiv:1203.3976 [hep-ex]
10.1007/JHEP04(2012)033
JHEP **1204**, 033 (2012)

134. **"Measurement of the cross section for production of bb^- bar X, decaying to muons in pp collisions at $\sqrt{s} = 7$ TeV"**
S. Chatrchyan *et al.* [CMS Collaboration].
arXiv:1203.3458 [hep-ex]
10.1007/JHEP06(2012)110
JHEP **1206**, 110 (2012)

135. **"Search for microscopic black holes in pp collisions at $\sqrt{s} = 7$ TeV"**
S. Chatrchyan *et al.* [CMS Collaboration].
arXiv:1202.6396 [hep-ex]
10.1007/JHEP04(2012)061
JHEP **1204**, 061 (2012)

136. **"Search for quark compositeness in dijet angular distributions from pp collisions at $\sqrt{s} = 7$ TeV"**
S. Chatrchyan *et al.* [CMS Collaboration].
arXiv:1202.5535 [hep-ex]
10.1007/JHEP05(2012)055
JHEP **1205**, 055 (2012)

137. **"Jet momentum dependence of jet quenching in PbPb collisions at $\sqrt{s_{NN}} = 2.76$ TeV"**
S. Chatrchyan *et al.* [CMS Collaboration].
arXiv:1202.5022 [nucl-ex]
10.1016/j.physletb.2012.04.058
Phys. Lett. B **712**, 176 (2012)

138. **"Inclusive b-jet production in pp collisions at $\sqrt{s} = 7$ TeV"**
S. Chatrchyan *et al.* [CMS Collaboration].
arXiv:1202.4617 [hep-ex]
10.1007/JHEP04(2012)084
JHEP **1204**, 084 (2012)

139. **"Search for the standard model Higgs boson decaying to bottom quarks in pp collisions at $\sqrt{s} = 7$ TeV"**

S. Chatrchyan *et al.* [CMS Collaboration].
arXiv:1202.4195 [hep-ex]
10.1016/j.physletb.2012.02.085
Phys. Lett. B **710**, 284 (2012)

140. **"Search for neutral Higgs bosons decaying to τ pairs in pp collisions at $\sqrt{s} = 7$ TeV"**
S. Chatrchyan *et al.* [CMS Collaboration].
arXiv:1202.4083 [hep-ex]
10.1016/j.physletb.2012.05.028
Phys. Lett. B **713**, 68 (2012)

141. **"Search for large extra dimensions in dimuon and dielectron events in pp collisions at $\sqrt{s} = 7$ TeV"**
S. Chatrchyan *et al.* [CMS Collaboration].
arXiv:1202.3827 [hep-ex]
10.1016/j.physletb.2012.03.029
Phys. Lett. B **711**, 15 (2012)

142. **"Search for the standard model Higgs boson in the H to ZZ to 2 $\ell 2\nu$ channel in pp collisions at $\sqrt{s} = 7$ TeV"**
S. Chatrchyan *et al.* [CMS Collaboration].
arXiv:1202.3478 [hep-ex]
10.1007/JHEP03(2012)040
JHEP **1203**, 040 (2012)

143. **"Search for the standard model Higgs boson in the H to ZZ to $\ell\ell\tau\tau$ decay channel in pp collisions at $\sqrt{s} = 7$ TeV"**
S. Chatrchyan *et al.* [CMS Collaboration].
arXiv:1202.3617 [hep-ex]
10.1007/JHEP03(2012)081
JHEP **1203**, 081 (2012)

144. **"Study of high-pT charged particle suppression in PbPb compared to pp collisions at $\sqrt{s_{NN}} = 2.76$ TeV"**
S. Chatrchyan *et al.* [CMS Collaboration].
arXiv:1202.2554 [nucl-ex]
10.1140/epjc/s10052-012-1945-x
Eur. Phys. J. C **72**, 1945 (2012)

145. **"Search for the standard model Higgs boson in the decay channel H to ZZ to 4 leptons in pp collisions at $\sqrt{s} = 7$ TeV"**
S. Chatrchyan *et al.* [CMS Collaboration].
arXiv:1202.1997 [hep-ex]
10.1103/PhysRevLett.108.111804
Phys. Rev. Lett. **108**, 111804 (2012)

146. **"Search for the standard model Higgs boson decaying to a W pair in the fully leptonic final state in pp collisions at $\sqrt{s} = 7$ TeV"**
S. Chatrchyan *et al.* [CMS Collaboration].

arXiv:1202.1489 [hep-ex]
10.1016/j.physletb.2012.02.076
Phys. Lett. B **710**, 91 (2012)

147. **"Combined results of searches for the standard model Higgs boson in pp collisions at $\sqrt{s} = 7$ TeV"**
S. Chatrchyan *et al.* [CMS Collaboration].
arXiv:1202.1488 [hep-ex]
10.1016/j.physletb.2012.02.064
Phys. Lett. B **710**, 26 (2012)

148. **"Search for the standard model Higgs boson decaying into two photons in pp collisions at $\sqrt{s} = 7$ TeV"**
S. Chatrchyan *et al.* [CMS Collaboration].
arXiv:1202.1487 [hep-ex]
10.1016/j.physletb.2012.03.003
Phys. Lett. B **710**, 403 (2012)

149. **"Search for a Higgs boson in the decay channel H to ZZ(*) to q qbar ℓ^- l+ in pp collisions at $\sqrt{s} = 7$ TeV"**
S. Chatrchyan *et al.* [CMS Collaboration].
arXiv:1202.1416 [hep-ex]
10.1007/JHEP04(2012)036
JHEP **1204**, 036 (2012)

150. **"Measurement of the inclusive production cross sections for forward jets and for dijet events with one forward and one central jet in pp collisions at $\sqrt{s} = 7$ TeV"**
S. Chatrchyan *et al.* [CMS Collaboration].
arXiv:1202.0704 [hep-ex]
10.1007/JHEP06(2012)036
JHEP **1206**, 036 (2012)

151. **"Suppression of non-prompt J/ψ, prompt J/ψ, and Y(1S) in PbPb collisions at $\sqrt{s_{NN}} =$ 2.76 TeV"**
S. Chatrchyan *et al.* [CMS Collaboration].
arXiv:1201.5069 [nucl-ex]
10.1007/JHEP05(2012)063
JHEP **1205**, 063 (2012)

152. **"Centrality dependence of dihadron correlations and azimuthal anisotropy harmonics in PbPb collisions at $\sqrt{s_{NN}} = 2.76$ TeV"**
S. Chatrchyan *et al.* [CMS Collaboration].
arXiv:1201.3158 [nucl-ex]
10.1140/epjc/s10052-012-2012-3
Eur. Phys. J. C **72**, 2012 (2012)

153. **"Measurement of isolated photon production in pp and PbPb collisions at $\sqrt{s_{NN}} = 2.76$ TeV"**
S. Chatrchyan *et al.* [CMS Collaboration].

arXiv:1201.3093 [nucl-ex]
10.1016/j.physletb.2012.02.077
Phys. Lett. B **710**, 256 (2012)

154. **"Measurement of the charge asymmetry in top-quark pair production in proton-proton collisions at $\sqrt{s} = 7$ TeV"**
S. Chatrchyan *et al.* [CMS Collaboration].
arXiv:1112.5100 [hep-ex]
10.1016/j.physletb.2012.01.078
Phys. Lett. B **709**, 28 (2012)

155. **"Search for signatures of extra dimensions in the diphoton mass spectrum at the Large Hadron Collider"**
S. Chatrchyan *et al.* [CMS Collaboration].
arXiv:1112.0688 [hep-ex]
10.1103/PhysRevLett.108.111801
Phys. Rev. Lett. **108**, 111801 (2012)

156. **"Exclusive photon-photon production of muon pairs in proton-proton collisions at $\sqrt{s} =$ 7 TeV"**
S. Chatrchyan *et al.* [CMS Collaboration].
arXiv:1111.5536 [hep-ex]
10.1007/JHEP01(2012)052
JHEP **1201**, 052 (2012)

157. **"J/ψ and ψ_{2S} production in pp collisions at $\sqrt{s} = 7$ TeV"**
S. Chatrchyan *et al.* [CMS Collaboration].
arXiv:1111.1557 [hep-ex]
10.1007/JHEP02(2012)011
JHEP **1202**, 011 (2012)

158. **"Measurement of the Production Cross Section for Pairs of Isolated Photons in pp collisions at $\sqrt{s} = 7$ TeV"**
S. Chatrchyan *et al.* [CMS Collaboration].
arXiv:1110.6461 [hep-ex]
10.1007/JHEP01(2012)133
JHEP **1201**, 133 (2012)

159. **"Measurement of the Rapidity and Transverse Momentum Distributions of Z Bosons in pp Collisions at $\sqrt{s} = 7$ TeV"**
S. Chatrchyan *et al.* [CMS Collaboration].
arXiv:1110.4973 [hep-ex]
10.1103/PhysRevD.85.032002
Phys. Rev. D **85**, 032002 (2012)

160. **"Jet Production Rates in Association with W and Z Bosons in pp Collisions at $\sqrt{s} = 7$ TeV"**
S. Chatrchyan *et al.* [CMS Collaboration].
arXiv:1110.3226 [hep-ex]

10.1007/JHEP01(2012)010
JHEP **1201**, 010 (2012)

161. **"Measurement of the weak mixing angle with the Drell-Yan process in proton-proton collisions at the LHC"**
S. Chatrchyan *et al.* [CMS Collaboration].
arXiv:1110.2682 [hep-ex]
10.1103/PhysRevD.84.112002
Phys. Rev. D **84**, 112002 (2011)

162. **"Measurement of energy flow at large pseudorapidities in pp collisions at $\sqrt{s} = 0.9$ and 7 TeV"**
S. Chatrchyan *et al.* [CMS Collaboration].
arXiv:1110.0211 [hep-ex]
10.1007/JHEP11(2011)148, 10.1007/JHEP02(2012)055
JHEP **1111**, 148 (2011), [Erratum-ibid. **1202**, 055 (2012)]

163. **"Forward Energy Flow, Central Charged-Particle Multiplicities, and Pseudorapidity Gaps in W and Z Boson Events from pp Collisions at 7 TeV"**
S. Chatrchyan *et al.* [CMS Collaboration].
arXiv:1110.0181 [hep-ex]
10.1140/epjc/s10052-011-1839-3
Eur. Phys. J. C **72**, 1839 (2012)

164. **"Performance of tau-lepton reconstruction and identification in CMS"**
C. Collaboration *et al.* [CMS Collaboration].
arXiv:1109.6034 [physics.ins-det]
10.1088/1748-0221/7/01/P01001
JINST **7**, P01001 (2012)

165. **"Search for a Vector-like Quark with Charge 2/3 in t + Z Events from pp Collisions at $\sqrt{s} = 7$ TeV"**
S. Chatrchyan *et al.* [CMS Collaboration].
arXiv:1109.4985 [hep-ex]
10.1103/PhysRevLett.107.271802
Phys. Rev. Lett. **107**, 271802 (2011)

166. **"Search for Supersymmetry at the LHC in Events with Jets and Missing Transverse Energy"**
S. Chatrchyan *et al.* [CMS Collaboration].
arXiv:1109.2352 [hep-ex]
10.1103/PhysRevLett.107.221804
Phys. Rev. Lett. **107**, 221804 (2011)

167. **"Measurement of the t** $\bar{t}ProductionCrossSectioninppCollisionsat7TeVinLepton + JetsEventsUsingb-quarkJetIdentification''$
$S.Chatrchyanetal.[CMSCollaboration]$.
$arXiv:1108.3773[hep-ex]$
$10.1103/PhysRevD.84.092004$
$Phys.Rev.D$**84**$,092004(2011)$

168. **"Measurement of the Differential Cross Section for Isolated Prompt Photon Production in pp Collisions at 7 TeV"**
S. Chatrchyan *et al.* [CMS Collaboration].
arXiv:1108.2044 [hep-ex]
10.1103/PhysRevD.84.052011
Phys. Rev. D **84**, 052011 (2011)

169. **"Measurement of the Drell-Yan Cross Section in pp Collisions at $\sqrt{s} = 7$ TeV"**
S. Chatrchyan *et al.* [CMS Collaboration].
arXiv:1108.0566 [hep-ex]
10.1007/JHEP10(2011)007
JHEP **1110**, 007 (2011)

170. **"Search for B(s) and B to dimuon decays in pp collisions at 7 TeV"**
S. Chatrchyan *et al.* [CMS Collaboration].
arXiv:1107.5834 [hep-ex]
10.1103/PhysRevLett.107.191802
Phys. Rev. Lett. **107**, 191802 (2011)

171. **"Search for Resonances in the Dijet Mass Spectrum from 7 TeV pp Collisions at CMS"**
S. Chatrchyan *et al.* [CMS Collaboration].
arXiv:1107.4771 [hep-ex]
10.1016/j.physletb.2011.09.015
Phys. Lett. B **704**, 123 (2011)

172. **"Measurement of the Inclusive W and Z Production Cross Sections in pp Collisions at $\sqrt{s} = 7$ TeV"**
S. Chatrchyan *et al.* [CMS Collaboration].
arXiv:1107.4789 [hep-ex]
10.1007/JHEP10(2011)132
JHEP **1110**, 132 (2011)

173. **"Dependence on pseudorapidity and centrality of charged hadron production in PbPb collisions at a nucleon-nucleon centre-of-mass energy of 2.76 TeV"**
S. Chatrchyan *et al.* [CMS Collaboration].
arXiv:1107.4800 [nucl-ex]
10.1007/JHEP08(2011)141
JHEP **1108**, 141 (2011)

174. **"Determination of Jet Energy Calibration and Transverse Momentum Resolution in CMS"**
S. Chatrchyan *et al.* [CMS Collaboration].
arXiv:1107.4277 [physics.ins-det]
10.1088/1748-0221/6/11/P11002
JINST **6**, P11002 (2011)

175. **"Search for Three-Jet Resonances in pp Collisions at $\sqrt{s} = 7$ TeV"**
S. Chatrchyan *et al.* [CMS Collaboration].
arXiv:1107.3084 [hep-ex]

10.1103/PhysRevLett.107.101801
Phys. Rev. Lett. **107**, 101801 (2011)

176. **"Search for supersymmetry in pp collisions at $\sqrt{s} = 7$ TeV in events with a single lepton, jets, and missing transverse momentum"**
S. Chatrchyan *et al.* [CMS Collaboration].
arXiv:1107.1870 [hep-ex]
10.1007/JHEP08(2011)156
JHEP **1108**, 156 (2011)

177. **"A search for excited leptons in pp Collisions at $\sqrt{s} = 7$ TeV"**
S. Chatrchyan *et al.* [CMS Collaboration].
arXiv:1107.1773 [hep-ex]
10.1016/j.physletb.2011.09.021
Phys. Lett. B **704**, 143 (2011)

178. **"Inclusive search for squarks and gluinos in pp collisions at $\sqrt{s} = 7$ TeV"**
S. Chatrchyan *et al.* [CMS Collaboration].
arXiv:1107.1279 [hep-ex]
10.1103/PhysRevD.85.012004
Phys. Rev. D **85**, 012004 (2012)

179. **"Measurement of the Underlying Event Activity at the LHC with $\sqrt{s} = 7$ TeV and Comparison with $\sqrt{s} = 0.9$ TeV"**
S. Chatrchyan *et al.* [CMS Collaboration].
arXiv:1107.0330 [hep-ex]
10.1007/JHEP09(2011)109
JHEP **1109**, 109 (2011)

180. **"Missing transverse energy performance of the CMS detector"**
S. Chatrchyan *et al.* [CMS Collaboration].
arXiv:1106.5048 [physics.ins-det]
10.1088/1748-0221/6/09/P09001
JINST **6**, P09001 (2011)

181. **"Search for New Physics with a Mono-Jet and Missing Transverse Energy in pp Collisions at $\sqrt{s} = 7$ TeV"**
S. Chatrchyan *et al.* [CMS Collaboration].
arXiv:1106.4775 [hep-ex]
10.1103/PhysRevLett.107.201804
Phys. Rev. Lett. **107**, 201804 (2011)

182. **"Search for New Physics with Jets and Missing Transverse Momentum in pp collisions at $\sqrt{s} = 7$ TeV"**
S. Chatrchyan *et al.* [CMS Collaboration].
arXiv:1106.4503 [hep-ex]
10.1007/JHEP08(2011)155
JHEP **1108**, 155 (2011)

183. **"Measurement of the Strange B Meson Production Cross Section with J/Psi ϕ Decays in pp Collisions at $\sqrt{s} = 7$ TeV"**
S. Chatrchyan *et al.* [CMS Collaboration].
arXiv:1106.4048 [hep-ex]
10.1103/PhysRevD.84.052008
Phys. Rev. D **84**, 052008 (2011)

184. **"Search for Supersymmetry in Events with b Jets and Missing Transverse Momentum at the LHC"**
S. Chatrchyan *et al.* [CMS Collaboration].
arXiv:1106.3272 [hep-ex]
10.1007/JHEP07(2011)113
JHEP **1107**, 113 (2011)

185. **"Measurement of the t-channel single top quark production cross section in pp collisions at $\sqrt{s} = 7$ TeV"**
S. Chatrchyan *et al.* [CMS Collaboration].
arXiv:1106.3052 [hep-ex]
10.1103/PhysRevLett.107.091802
Phys. Rev. Lett. **107**, 091802 (2011)

186. **"Search for Light Resonances Decaying into Pairs of Muons as a Signal of New Physics"**
S. Chatrchyan *et al.* [CMS Collaboration].
arXiv:1106.2375 [hep-ex]
10.1007/JHEP07(2011)098
JHEP **1107**, 098 (2011)

187. **"Search for Same-Sign Top-Quark Pair Production at $\sqrt{s} = 7$ TeV and Limits on Flavour Changing Neutral Currents in the Top Sector"**
S. Chatrchyan *et al.* [CMS Collaboration].
arXiv:1106.2142 [hep-ex]
10.1007/JHEP08(2011)005
JHEP **1108**, 005 (2011)

188. **"Measurement of the Top-antitop Production Cross Section in pp Collisions at $\sqrt{s} = 7$ TeV using the Kinematic Properties of Events with Leptons and Jets"**
S. Chatrchyan *et al.* [CMS Collaboration].
arXiv:1106.0902 [hep-ex]
10.1140/epjc/s10052-011-1721-3
Eur. Phys. J. C **71**, 1721 (2011)

189. **"Search for Physics Beyond the Standard Model Using Multilepton Signatures in pp Collisions at $\sqrt{s} = 7$ TeV"**
S. Chatrchyan *et al.* [CMS Collaboration].
arXiv:1106.0933 [hep-ex]
10.1016/j.physletb.2011.09.047
Phys. Lett. B **704**, 411 (2011)

190. **"Measurement of the Ratio of the 3-jet to 2-jet Cross Sections in pp Collisions at $\sqrt{s} = 7$ TeV"**

S. Chatrchyan *et al.* [CMS Collaboration].
arXiv:1106.0647 [hep-ex]
10.1016/j.physletb.2011.07.067
Phys. Lett. B **702**, 336 (2011)

191. **"Measurement of the Inclusive Jet Cross Section in pp Collisions at $\sqrt{s} = 7$ TeV"**
S. Chatrchyan *et al.* [CMS Collaboration].
arXiv:1106.0208 [hep-ex]
10.1103/PhysRevLett.107.132001
Phys. Rev. Lett. **107**, 132001 (2011)

192. **"Measurement of the $t\bar{t}$ production cross section and the top quark mass in the dilepton channel in pp collisions at $\sqrt{s} = 7$ TeV"**
S. Chatrchyan *et al.* [CMS Collaboration].
arXiv:1105.5661 [hep-ex]
10.1007/JHEP07(2011)049
JHEP **1107**, 049 (2011)

193. **"Search for First Generation Scalar Leptoquarks in the evjj channel in pp collisions at $\sqrt{s} = 7$ TeV"**
S. Chatrchyan *et al.* [CMS Collaboration].
arXiv:1105.5237 [hep-ex]
10.1016/j.physletb.2011.07.089
Phys. Lett. B **703**, 246 (2011)

194. **"Indications of suppression of excited Υ states in PbPb collisions at $\sqrt{S_{NN}}$ = 2.76 TeV"**
S. Chatrchyan *et al.* [CMS Collaboration].
arXiv:1105.4894 [nucl-ex]
10.1103/PhysRevLett.107.052302
Phys. Rev. Lett. **107**, 052302 (2011)

195. **"Search for supersymmetry in events with a lepton, a photon, and large missing transverse energy in pp collisions at $\sqrt{s} = 7$ TeV"**
S. Chatrchyan *et al.* [CMS Collaboration].
arXiv:1105.3152 [hep-ex]
10.1007/JHEP06(2011)093
JHEP **1106**, 093 (2011)

196. **"Measurement of $W\gamma$ and $Z\gamma$ production in pp collisions at $\sqrt{s} = 7$ TeV"**
S. Chatrchyan *et al.* [CMS Collaboration].
arXiv:1105.2758 [hep-ex]
10.1016/j.physletb.2011.06.034
Phys. Lett. B **701**, 535 (2011)

197. **"Long-range and short-range dihadron angular correlations in central PbPb collisions at a nucleon-nucleon center of mass energy of 2.76 TeV"**
S. Chatrchyan *et al.* [CMS Collaboration].
arXiv:1105.2438 [nucl-ex]
10.1007/JHEP07(2011)076
JHEP **1107**, 076 (2011)

198. **"Charged particle transverse momentum spectra in pp collisions at $\sqrt{s} = 0.9$ and 7 TeV"**
S. Chatrchyan *et al.* [CMS Collaboration].
arXiv:1104.3547 [hep-ex]
10.1007/JHEP08(2011)086
JHEP **1108**, 086 (2011)

199. **"Measurement of the Polarization of W Bosons with Large Transverse Momenta in W+Jets Events at the LHC"**
S. Chatrchyan *et al.* [CMS Collaboration].
arXiv:1104.3829 [hep-ex]
10.1103/PhysRevLett.107.021802
Phys. Rev. Lett. **107**, 021802 (2011)

200. **"Search for new physics with same-sign isolated dilepton events with jets and missing transverse energy at the LHC"**
S. Chatrchyan *et al.* [CMS Collaboration].
arXiv:1104.3168 [hep-ex]
10.1007/JHEP06(2011)077
JHEP **1106**, 077 (2011)

201. **"Measurement of the B^0 production cross section in pp Collisions at $\sqrt{s} = 7$ TeV"**
S. Chatrchyan *et al.* [CMS Collaboration].
arXiv:1104.2892 [hep-ex]
10.1103/PhysRevLett.106.252001
Phys. Rev. Lett. **106**, 252001 (2011)

202. **"Measurement of the differential dijet production cross section in proton-proton collisions at $\sqrt{s} = 7$ TeV"**
S. Chatrchyan *et al.* [CMS Collaboration].
arXiv:1104.1693 [hep-ex]
10.1016/j.physletb.2011.05.027
Phys. Lett. B **700**, 187 (2011)

203. **"Measurement of the Inclusive Z Cross Section via Decays to Tau Pairs in pp Collisions at $\sqrt{s} = 7$ TeV"**
S. Chatrchyan *et al.* [CMS Collaboration].
arXiv:1104.1617 [hep-ex]
10.1007/JHEP08(2011)117
JHEP **1108**, 117 (2011)

204. **"Search for Neutral MSSM Higgs Bosons Decaying to Tau Pairs in pp Collisions at $\sqrt{s} = 7$ TeV"**
S. Chatrchyan *et al.* [CMS Collaboration].
arXiv:1104.1619 [hep-ex]
10.1103/PhysRevLett.106.231801
Phys. Rev. Lett. **106**, 231801 (2011)

205. **"Search for Large Extra Dimensions in the Diphoton Final State at the Large Hadron Collider"**

S. Chatrchyan *et al.* [CMS Collaboration].
arXiv:1103.4279 [hep-ex]
10.1007/JHEP05(2011)085
JHEP **1105**, 085 (2011)

206. **"Measurement of the lepton charge asymmetry in inclusive W production in pp collisions at $\sqrt{s} = 7$ TeV"**
S. Chatrchyan *et al.* [CMS Collaboration].
arXiv:1103.3470 [hep-ex]
10.1007/JHEP04(2011)050
JHEP **1104**, 050 (2011)

207. **"Search for Physics Beyond the Standard Model in Opposite-Sign Dilepton Events at $\sqrt{s} = 7$ TeV"**
S. Chatrchyan *et al.* [CMS Collaboration].
arXiv:1103.1348 [hep-ex]
10.1007/JHEP06(2011)026
JHEP **1106**, 026 (2011)

208. **"Search for Supersymmetry in pp Collisions at $\sqrt{s} = 7$ TeV in Events with Two Photons and Missing Transverse Energy"**
S. Chatrchyan *et al.* [CMS Collaboration].
arXiv:1103.0953 [hep-ex]
10.1103/PhysRevLett.106.211802
Phys. Rev. Lett. **106**, 211802 (2011)

209. **"Search for Resonances in the Dilepton Mass Distribution in pp Collisions at $\sqrt{(s)} = 7$ TeV"**
S. Chatrchyan *et al.* [CMS Collaboration].
arXiv:1103.0981 [hep-ex]
10.1007/JHEP05(2011)093
JHEP **1105**, 093 (2011)

210. **"Search for a W' boson decaying to a muon and a neutrino in pp collisions at $\sqrt{s} = 7$ TeV"**
S. Chatrchyan *et al.* [CMS Collaboration].
arXiv:1103.0030 [hep-ex]
10.1016/j.physletb.2011.05.048
Phys. Lett. B **701**, 160 (2011)

211. **"Measurement of W^+W^- Production and Search for the Higgs Boson in pp Collisions at $\sqrt{s} = 7$ TeV"**
S. Chatrchyan *et al.* [CMS Collaboration].
arXiv:1102.5429 [hep-ex]
10.1016/j.physletb.2011.03.056
Phys. Lett. B **699**, 25 (2011)

212. **"Study of Z boson production in PbPb collisions at nucleon-nucleon centre of mass energy = 2.76 TeV"**

S. Chatrchyan *et al.* [CMS Collaboration].
arXiv:1102.5435 [nucl-ex]
10.1103/PhysRevLett.106.212301
Phys. Rev. Lett. **106**, 212301 (2011)

213. **"Search for a Heavy Bottom-like Quark in pp Collisions at $\sqrt{s} = 7$ TeV"**
S. Chatrchyan *et al.* [CMS Collaboration].
arXiv:1102.4746 [hep-ex]
10.1016/j.physletb.2011.05.074
Phys. Lett. B **701**, 204 (2011)

214. **"Strange Particle Production in pp Collisions at $\sqrt{s} = 0.9$ and 7 TeV"**
V. Khachatryan *et al.* [CMS Collaboration].
arXiv:1102.4282 [hep-ex]
10.1007/JHEP05(2011)064
JHEP **1105**, 064 (2011)

215. **"Measurement of $B\bar{B}$ Angular Correlations based on Secondary Vertex Reconstruction at $\sqrt{s} = 7$ TeV"**
V. Khachatryan *et al.* [CMS Collaboration].
arXiv:1102.3194 [hep-ex]
10.1007/JHEP03(2011)136
JHEP **1103**, 136 (2011)

216. **"Measurement of Dijet Angular Distributions and Search for Quark Compositeness in pp Collisions at $sqrts = 7$ TeV"**
V. Khachatryan *et al.* [CMS Collaboration].
arXiv:1102.2020 [hep-ex]
10.1103/PhysRevLett.106.201804
Phys. Rev. Lett. **106**, 201804 (2011)

217. **"Observation and studies of jet quenching in PbPb collisions at nucleon-nucleon center-of-mass energy = 2.76 TeV"**
S. Chatrchyan *et al.* [CMS Collaboration].
arXiv:1102.1957 [nucl-ex]
10.1103/PhysRevC.84.024906
Phys. Rev. C **84**, 024906 (2011)

218. **"First Measurement of Hadronic Event Shapes in pp Collisions at $\sqrt{(}s) = 7$ TeV"**
V. Khachatryan *et al.* [CMS Collaboration].
arXiv:1102.0068 [hep-ex]
10.1016/j.physletb.2011.03.060
Phys. Lett. B **699**, 48 (2011)

219. **"Dijet Azimuthal Decorrelations in pp Collisions at $\sqrt{s} = 7$ TeV"**
V. Khachatryan *et al.* [CMS Collaboration].
arXiv:1101.5029 [hep-ex]
10.1103/PhysRevLett.106.122003
Phys. Rev. Lett. **106**, 122003 (2011)

220. **"Inclusive b-hadron production cross section with muons in pp collisions at $\sqrt{s} = 7$ TeV"**
V. Khachatryan *et al.* [CMS Collaboration].
arXiv:1101.3512 [hep-ex]
10.1007/JHEP03(2011)090
JHEP **1103**, 090 (2011)

221. **"Measurement of Bose-Einstein Correlations in pp Collisions at $\sqrt{s} = 0.9$ and 7 TeV"**
V. Khachatryan *et al.* [CMS Collaboration].
arXiv:1101.3518 [hep-ex]
10.1007/JHEP05(2011)029
JHEP **1105**, 029 (2011)

222. **"Search for Supersymmetry in pp Collisions at 7 TeV in Events with Jets and Missing Transverse Energy"**
V. Khachatryan *et al.* [CMS Collaboration].
arXiv:1101.1628 [hep-ex]
10.1016/j.physletb.2011.03.021
Phys. Lett. B **698**, 196 (2011)

223. **"Search for Heavy Stable Charged Particles in pp collisions at $\sqrt{s} = 7$ TeV"**
V. Khachatryan *et al.* [CMS Collaboration].
arXiv:1101.1645 [hep-ex]
10.1007/JHEP03(2011)024
JHEP **1103**, 024 (2011)

224. **"Measurement of the B^+ Production Cross Section in pp Collisions at $\sqrt{s} = 7$ TeV"**
V. Khachatryan *et al.* [CMS Collaboration].
arXiv:1101.0131 [hep-ex]
10.1103/PhysRevLett.106.112001
Phys. Rev. Lett. **106**, 112001 (2011)

225. **"Search for a heavy gauge boson W ' in the final state with an electron and large missing transverse energy in pp collisions at $\sqrt{s} = 7$ TeV"**
V. Khachatryan *et al.* [CMS Collaboration].
arXiv:1012.5945 [hep-ex]
10.1016/j.physletb.2011.02.048
Phys. Lett. B **698**, 21 (2011)

226. **"Measurement of the Inclusive υ production cross section in pp collisions at $\sqrt{s} = 7$ TeV"**
V. Khachatryan *et al.* [CMS Collaboration].
arXiv:1012.5545 [hep-ex]
10.1103/PhysRevD.83.112004
Phys. Rev. D **83**, 112004 (2011)

227. **"Search for Pair Production of First-Generation Scalar Leptoquarks in pp Collisions at $\sqrt{s} = 7$ TeV"**
V. Khachatryan *et al.* [CMS Collaboration].

arXiv:1012.4031 [hep-ex]
10.1103/PhysRevLett.106.201802
Phys. Rev. Lett. **106**, 201802 (2011)

228. **"Search for Pair Production of Second-Generation Scalar Leptoquarks in pp Collisions at $\sqrt{s} = 7$ TeV"**
V. Khachatryan *et al.* [CMS Collaboration].
arXiv:1012.4033 [hep-ex]
10.1103/PhysRevLett.106.201803
Phys. Rev. Lett. **106**, 201803 (2011)

229. **"Search for Microscopic Black Hole Signatures at the Large Hadron Collider"**
V. Khachatryan *et al.* [CMS Collaboration].
arXiv:1012.3375 [hep-ex]
10.1016/j.physletb.2011.02.032
Phys. Lett. B **697**, 434 (2011)

230. **"Measurements of Inclusive W and Z Cross Sections in pp Collisions at $\sqrt{s} = 7$ TeV"**
V. Khachatryan *et al.* [CMS Collaboration].
arXiv:1012.2466 [hep-ex]
10.1007/JHEP01(2011)080
JHEP **1101**, 080 (2011)

231. **"Measurement of the Isolated Prompt Photon Production Cross Section in pp Collisions at $\sqrt{s} = 7$ TeV"**
V. Khachatryan *et al.* [CMS Collaboration].
arXiv:1012.0799 [hep-ex]
10.1103/PhysRevLett.106.082001
Phys. Rev. Lett. **106**, 082001 (2011)

232. **"Charged particle multiplicities in pp interactions at $\sqrt{s} = 0.9$, 2.36, and 7 TeV"**
V. Khachatryan *et al.* [CMS Collaboration].
arXiv:1011.5531 [hep-ex]
10.1007/JHEP01(2011)079
JHEP **1101**, 079 (2011)

233. **"Search for Stopped Gluinos in pp collisions at $\sqrt{s} = 7$ TeV"**
V. Khachatryan *et al.* [CMS Collaboration].
arXiv:1011.5861 [hep-ex]
10.1103/PhysRevLett.106.011801
Phys. Rev. Lett. **106**, 011801 (2011)

234. **"Prompt and non-prompt J/ψ production in pp collisions at $\sqrt{s} = 7$ TeV"**
V. Khachatryan *et al.* [CMS Collaboration].
arXiv:1011.4193 [hep-ex]
10.1140/epjc/s10052-011-1575-8
Eur. Phys. J. C **71**, 1575 (2011)

235. **"First Measurement of the Cross Section for Top-Quark Pair Production in Proton-Proton Collisions at $\sqrt{s} = 7$ TeV"**

V. Khachatryan *et al.* [CMS Collaboration].
arXiv:1010.5994 [hep-ex]
10.1016/j.physletb.2010.11.058
Phys. Lett. B **695**, 424 (2011)

236. **"Search for Quark Compositeness with the Dijet Centrality Ratio in pp Collisions at $\sqrt{s} = 7$ TeV"**
V. Khachatryan *et al.* [CMS Collaboration].
arXiv:1010.4439 [hep-ex]
10.1103/PhysRevLett.105.262001
Phys. Rev. Lett. **105**, 262001 (2010)

237. **"Search for Dijet Resonances in 7 TeV pp Collisions at CMS"**
V. Khachatryan *et al.* [CMS Collaboration].
arXiv:1010.0203 [hep-ex]
10.1103/PhysRevLett.105.211801, 10.1103/PhysRevLett.106.029902
Phys. Rev. Lett. **105**, 211801 (2010)

238. **"Observation of Long-Range Near-Side Angular Correlations in Proton-Proton Collisions at the LHC"**
V. Khachatryan *et al.* [CMS Collaboration].
arXiv:1009.4122 [hep-ex]
10.1007/JHEP09(2010)091
JHEP **1009**, 091 (2010)

239. **"CMS Tracking Performance Results from early LHC Operation"**
V. Khachatryan *et al.* [CMS Collaboration].
arXiv:1007.1988 [physics.ins-det]
10.1140/epjc/s10052-010-1491-3
Eur. Phys. J. C **70**, 1165 (2010)

240. **"First Measurement of the Underlying Event Activity at the LHC with $\sqrt{s} = 0.9$ TeV"**
V. Khachatryan *et al.* [CMS Collaboration].
arXiv:1006.2083 [hep-ex]
10.1140/epjc/s10052-010-1453-9
Eur. Phys. J. C **70**, 555 (2010)

241. **"Measurement of the charge ratio of atmospheric muons with the CMS detector"**
V. Khachatryan *et al.* [CMS Collaboration].
arXiv:1005.5332 [hep-ex]
10.1016/j.physletb.2010.07.033
Phys. Lett. B **692**, 83 (2010)

242. **"Measurement of Bose-Einstein correlations with first CMS data"**
V. Khachatryan *et al.* [CMS Collaboration].
arXiv:1005.3294 [hep-ex]
10.1103/PhysRevLett.105.032001
Phys. Rev. Lett. **105**, 032001 (2010)

243. **"Transverse-momentum and pseudorapidity distributions of charged hadrons in pp collisions at $\sqrt{s} = 7$ TeV"**
V. Khachatryan *et al.* [CMS Collaboration].
arXiv:1005.3299 [hep-ex]
10.1103/PhysRevLett.105.022002
Phys. Rev. Lett. **105**, 022002 (2010)

244. **"Transverse momentum and pseudorapidity distributions of charged hadrons in pp collisions at $\sqrt{(s)}$ = 0.9 and 2.36 TeV"**
V. Khachatryan *et al.* [CMS Collaboration].
arXiv:1002.0621 [hep-ex]
10.1007/JHEP02(2010)041
JHEP **1002**, 041 (2010)

245. **"Commissioning and Performance of the CMS Pixel Tracker with Cosmic Ray Muons"**
SChatrchyan *et al.* [CMS Collaboration].
arXiv:0911.5434 [physics.ins-det]
10.1088/1748-0221/5/03/T03007
JINST **5**, T03007 (2010)

246. **"Performance of the CMS Level-1 Trigger during Commissioning with Cosmic Ray Muons"**
SChatrchyan *et al.* [CMS Collaboration].
arXiv:0911.5422 [physics.ins-det]
10.1088/1748-0221/5/03/T03002
JINST **5**, T03002 (2010)

247. **"Measurement of the Muon Stopping Power in Lead Tungstate"**
SChatrchyan *et al.* [CMS Collaboration].
arXiv:0911.5397 [physics.ins-det]
10.1088/1748-0221/5/03/P03007
JINST **5**, P03007 (2010)

248. **"Commissioning and Performance of the CMS Silicon Strip Tracker with Cosmic Ray Muons"**
SChatrchyan *et al.* [CMS Collaboration].
arXiv:0911.4996 [physics.ins-det]
10.1088/1748-0221/5/03/T03008
JINST **5**, T03008 (2010)

249. **"Performance of CMS Muon Reconstruction in Cosmic-Ray Events"**
SChatrchyan *et al.* [CMS Collaboration].
arXiv:0911.4994 [physics.ins-det]
10.1088/1748-0221/5/03/T03022
JINST **5**, T03022 (2010)

250. **"Performance of the CMS Cathode Strip Chambers with Cosmic Rays"**
SChatrchyan *et al.* [CMS Collaboration].
arXiv:0911.4992 [physics.ins-det]

10.1088/1748-0221/5/03/T03018
JINST **5**, T03018 (2010)

251. **"Performance of the CMS Hadron Calorimeter with Cosmic Ray Muons and LHC Beam Data"**
SChatrchyan *et al.* [CMS Collaboration].
arXiv:0911.4991 [physics.ins-det]
10.1088/1748-0221/5/03/T03012
JINST **5**, T03012 (2010)

252. **"Fine Synchronization of the CMS Muon Drift-Tube Local Trigger using Cosmic Rays"**
SChatrchyan *et al.* [CMS Collaboration].
arXiv:0911.4904 [physics.ins-det]
10.1088/1748-0221/5/03/T03004
JINST **5**, T03004 (2010)

253. **"Calibration of the CMS Drift Tube Chambers and Measurement of the Drift Velocity with Cosmic Rays"**
SChatrchyan *et al.* [CMS Collaboration].
arXiv:0911.4895 [physics.ins-det]
10.1088/1748-0221/5/03/T03016
JINST **5**, T03016 (2010)

254. **"Performance of the CMS Drift-Tube Local Trigger with Cosmic Rays"**
SChatrchyan *et al.* [CMS Collaboration].
arXiv:0911.4893 [physics.ins-det]
10.1088/1748-0221/5/03/T03003
JINST **5**, T03003 (2010)

255. **"Commissioning of the CMS High-Level Trigger with Cosmic Rays"**
SChatrchyan *et al.* [CMS Collaboration].
arXiv:0911.4889 [physics.ins-det]
10.1088/1748-0221/5/03/T03005
JINST **5**, T03005 (2010)

256. **"Identification and Filtering of Uncharacteristic Noise in the CMS Hadron Calorimeter"**
SChatrchyan *et al.* [CMS Collaboration].
arXiv:0911.4881 [physics.ins-det]
10.1088/1748-0221/5/03/T03014
JINST **5**, T03014 (2010)

257. **"Performance of CMS Hadron Calorimeter Timing and Synchronization using Test Beam, Cosmic Ray, and LHC Beam Data"**
SChatrchyan *et al.* [CMS Collaboration].
arXiv:0911.4877 [physics.ins-det]
10.1088/1748-0221/5/03/T03013
JINST **5**, T03013 (2010)

258. **"Performance of the CMS Drift Tube Chambers with Cosmic Rays"**
SChatrchyan *et al.* [CMS Collaboration].
arXiv:0911.4855 [physics.ins-det]
10.1088/1748-0221/5/03/T03015
JINST **5**, T03015 (2010)

259. **"Commissioning of the CMS Experiment and the Cosmic Run at Four Tesla"**
SChatrchyan *et al.* [CMS Collaboration].
arXiv:0911.4845 [physics.ins-det]
10.1088/1748-0221/5/03/T03001
JINST **5**, T03001 (2010)

260. **"CMS Data Processing Workflows during an Extended Cosmic Ray Run"**
SChatrchyan *et al.* [CMS Collaboration].
arXiv:0911.4842 [physics.ins-det]
10.1088/1748-0221/5/03/T03006
JINST **5**, T03006 (2010)

261. **"Aligning the CMS Muon Chambers with the Muon Alignment System during an Extended Cosmic Ray Run"**
SChatrchyan *et al.* [CMS Collaboration].
arXiv:0911.4770 [physics.ins-det]
10.1088/1748-0221/5/03/T03019
JINST **5**, T03019 (2010)

262. **"Performance Study of the CMS Barrel Resistive Plate Chambers with Cosmic Rays"**
SChatrchyan *et al.* [CMS Collaboration].
arXiv:0911.4045 [physics.ins-det]
10.1088/1748-0221/5/03/T03017
JINST **5**, T03017 (2010)

263. **"Time Reconstruction and Performance of the CMS Electromagnetic Calorimeter"**
SChatrchyan *et al.* [CMS Collaboration].
arXiv:0911.4044 [physics.ins-det]
10.1088/1748-0221/5/03/T03011
JINST **5**, T03011 (2010)

264. **"Alignment of the CMS Muon System with Cosmic-Ray and Beam-Halo Muons"**
SChatrchyan *et al.* [CMS Collaboration].
arXiv:0911.4022 [physics.ins-det]
10.1088/1748-0221/5/03/T03020
JINST **5**, T03020 (2010)

265. **"Precise Mapping of the Magnetic Field in the CMS Barrel Yoke using Cosmic Rays"**
SChatrchyan *et al.* [CMS Collaboration].
arXiv:0910.5530 [physics.ins-det]
10.1088/1748-0221/5/03/T03021
JINST **5**, T03021 (2010)

266. **"Performance and Operation of the CMS Electromagnetic Calorimeter"**
SChatrchyan *et al.* [CMS Collaboration].
arXiv:0910.3423 [physics.ins-det]
10.1088/1748-0221/5/03/T03010
JINST **5**, T03010 (2010)

267. **"Alignment of the CMS Silicon Tracker during Commissioning with Cosmic Rays"**
SChatrchyan *et al.* [CMS Collaboration].
arXiv:0910.2505 [physics.ins-det]
10.1088/1748-0221/5/03/T03009
JINST **5**, T03009 (2010)